

# **Nano-Scale Feature Profile Modeling of Plasma Material Processing**

**by  
Chad M. Huard**

A dissertation submitted in partial fulfillment  
of the requirements of the degree of  
Doctor of Philosophy  
(Electrical Engineering)  
in the University of Michigan  
2018

Doctoral Committee:

Professor Mark J. Kushner, Chair  
Professor John Foster  
Professor Rachel Goldman  
Professor Wei Lu  
Professor Fred Terry

Copyright © Chad Huard 2018

All rights reserved

ORCID: 0000-0002-8852-6343

chuard@umich.edu

For Wyatt and Evangeline.

## ACKNOWLEDGMENTS

I would like to acknowledge the wonderful support I have received over the years, without which I would have been unable to complete this endeavor.

Many thanks go to my wonderful wife, Emily. Without her unwavering support and assistance, I would be lost. She has tirelessly supported me, even when it was difficult to do so. Her love and devotion, to me and our family, are an inspiration and a joy to me each and every day.

My son, Wyatt, and daughter, Evangeline, give me purpose. I thank them for their unconditional love and support, without which I would not have had the fortitude to continue through some of the difficult times over the course of obtaining this degree.

My parents instilled in me a desire to understand the world around me, and the knowledge that I can accomplish anything I set my mind to. I thank them for their love and support.

I would also like to thank Prof. Mark Kushner, who has been both a professional and personal mentor to me. Prof. Kushner has the (rare) ability to lead-by-example, instilling a sense of professionalism, scientific integrity and attention to detail that will be with me for the rest of my life.

I would also like to acknowledge the efforts of Prof. Mark Ming-Cheng Cheng and Prof. L. Jay Guo, who gave me the opportunity to begin this journey. I also thank my fellow group members and collaborators, past and present, who have made the process so enjoyable.

## TABLE OF CONTENTS

|   |            |
|---|------------|
| <b>DEDICATION.....</b>  | <b>ii</b>  |
| <b>ACKNOWLEDGMENTS .....</b>  | <b>iii</b> |
| <b>LIST OF FIGURES .....</b>  | <b>vii</b> |
| <b>LIST OF TABLES .....</b>   | <b>xiv</b> |
| <b>LIST OF ABBREVIATIONS .....</b>  | <b>xv</b>  |
| <b>ABSTRACT.....</b>  | <b>xvi</b> |
| <b>Chapter 1 INTRODUCTION .....</b>   | <b>1</b>   |
| 1.1. Plasma Etching in Semiconductor Processing.....                            | 1          |
| 1.2. Plasma Physics Overview .....  | 2          |
| 1.2.1. Quasi-Neutral Plasma .....   | 3          |
| 1.2.2. Electron Impact Reactions .....  | 5          |
| 1.2.3. Formation of the Plasma Sheath and Anisotropic Acceleration of Ions..... | 8          |
| 1.2.4. Ion Energy Distributions and the Influence of RF Bias.....               | 10         |
| 1.3. Plasma Surface Interactions.....   | 12         |
| 1.3.1. Physical Sputtering .....  | 13         |
| 1.3.2. Surface Passivation and Chemical Sputtering .....                        | 14         |
| 1.3.3. Fluorocarbon Etching.....  | 17         |
| 1.4. Plasma Etching Challenges.....   | 19         |
| 1.5. Feature Scale Modeling .....   | 21         |
| 1.5.1. Goals for Feature Scale Modeling .....                                   | 23         |
| 1.6. Summary .....  | 24         |
| 1.7. Figures.....   | 27         |
| <b>Chapter 2 DESCRIPTION OF MODELS.....</b>                                     | <b>41</b>  |
| 2.1. Overview of Monte Carlo Feature Profile Model (MCFPM).....                 | 41         |
| 2.2. Reactor Scale Modeling.....  | 42         |
| 2.3. 3D Mesh.....   | 45         |
| 2.4. Simulation Time / Pulsing .....  | 46         |

|  |            |
|--|------------|
| 2.5. Pseudo-particle Behavior .....                              | 50         |
| 2.5.1. Pseudo-Particle Initialization .....                      | 50         |
| 2.5.2. Particle Trajectories .....                               | 52         |
| 2.5.3. Surface Normal Calculation.....                           | 55         |
| 2.5.4. Reflections: Specular and Diffusive .....                 | 57         |
| 2.5.5. Surface Reactions.....                                    | 60         |
| 2.5.6. Radical Diffusion Through Bulk Solids .....               | 62         |
| 2.5.7. Ion Implantation.....                                     | 64         |
| 2.5.8. Surface Diffusion of Adsorbed Particles .....             | 69         |
| 2.6. Code Layout / Parallelism.....                              | 73         |
| 2.7. MCFPM Validation .....                                      | 74         |
| 2.8. Figures.....  | 77         |
| <b>Chapter 3 SURFACE REACTION MECHANISMS .....</b>               | <b>85</b>  |
| 3.1. Introduction.....   | 85         |
| 3.2. Halogen Plasma Surface Reaction Mechanism .....             | 86         |
| 3.3. Fluorocarbon Plasma Surface Reaction Mechanism .....        | 89         |
| 3.4. Figures.....  | 95         |
| 3.5. Reaction Mechanism Tables .....                             | 96         |
| <b>Chapter 4 ASPECT RATIO DEPENDENCE OF PLASMA ETCHING .....</b> | <b>100</b> |
| 4.1. Introduction.....   | 100        |
| 4.2. Scaling of ARDE .....                                       | 104        |
| 4.3. Neutral to Ion Flux Ratios.....                             | 111        |
| 4.4. Chlorine Recombination .....                                | 115        |
| 4.5. Neutral Angular Distribution .....                          | 118        |
| 4.6. Ion Angular Distribution.....                               | 119        |
| 4.7. Dependence on Feature Width.....                            | 121        |
| 4.8. Parameters affecting ARDE.....                              | 122        |
| 4.9. Concluding Remarks.....                                     | 125        |
| 4.10. Figures.....   | 127        |
| <b>Chapter 5 ATOMIC LAYER ETCHING USING HALOGEN GASES .....</b>  | <b>145</b> |
| 5.1. Introduction.....   | 145        |
| 5.2. Characteristics of Ideal ALE.....                           | 149        |
| 5.3. ALE with Non-Ideal Reactant Fluxes .....                    | 152        |
| 5.3.1. Non-ideal Radical or Ion Fluxes .....                     | 152        |

|  |            |
|--|------------|
| 5.3.2. Controlling EPC and ALE synergy with pulse times .....        | 159        |
| 5.4. Gate Etch Using ALE .....                                       | 164        |
| 5.5. Concluding Remarks.....   | 167        |
| 5.6. Figures.....  | 169        |
| <b>Chapter 6 WAFER SCALE UNIFORMITY .....</b>                        | <b>184</b> |
| 6.1. Introduction.....   | 184        |
| 6.2. Scaling of ALE with Uniformity of Fluxes .....                  | 186        |
| 6.3. Concluding Remarks.....   | 196        |
| 6.4. Figures.....  | 197        |
| <b>Chapter 7 ATOMIC LAYER ETCHING USING FLUOROCARBON GASES ...</b>   | <b>202</b> |
| 7.1. Introduction.....   | 202        |
| 7.2. C <sub>4</sub> F <sub>8</sub> Inductively Coupled Plasmas ..... | 204        |
| 7.3. ALE blanket etching .....                                       | 207        |
| 7.4. Feature etching.....  | 217        |
| 7.5. Role of Polymer in Dielectric Plasma ALE.....                   | 220        |
| 7.6. Concluding Remarks.....   | 222        |
| 7.7. Figures.....  | 224        |
| <b>Chapter 8 SUMMARY AND FUTURE WORK.....</b>                        | <b>234</b> |
| 8.1. Summary .....   | 234        |
| 8.2. Future work.....  | 237        |
| 8.3. Concluding Remarks.....   | 238        |
| <b>REFERENCES.....</b>   | <b>241</b> |

## LIST OF FIGURES

- Fig. 1.1 Comparison of isotropic and anisotropic etching. Low aspect ratio features can be etched adequately by isotropic etching, while high aspect ratio features require an anisotropic etch profile. .... 27
- Fig. 1.2 Electron – Cl<sub>2</sub> collision cross section set. Cross sections for dissociative attachment ( $Q_{da}$ ), vibrational excitation ( $Q_v$ ), ion pair formation ( $Q_{ip}$ ), electronic excitation ( $Q_{exc}$ ), direct dissociation ( $Q_{diss}$ ), ionization ( $Q_{ion}$ ) and momentum transfer ( $Q_m$ ). Reproduced from Gregório et al..[9] ..... 28
- Fig. 1.3 Schematic example of the effect of applying a RF bias to a wafer in a (a) symmetric and (b) asymmetric reactors..... 29
- Fig. 1.4 Ion energy distributions for different values of  $\tau_{ion}/\tau_{rf}$ . The curve marked 1 is the lowest  $\tau_{ion}/\tau_{rf}$  and 5 is the highest. The lack of a low frequency peak is due to an assumption that the sheath width is constant, and is not typical of experiment. Reproduced from Tsui.[11] ..... 30
- Fig. 1.5 Ion energy distribution function for several values of RF frequency. Lower frequency results in wider bi-modal distributions, while higher frequencies converge on a single peak distribution. Reproduced from Kawamura et al.[10] ..... 31
- Fig. 1.6 Ion energy distribution for several ions with different masses. Reproduced from Coburn and Kay.[12] ..... 32
- Fig. 1.7 Two different three body collision cascades which result in sputtering. Target atom 2 undergoes a collision with the incoming ion, then a second collision with target atom 1 before being ejected from the solid. Target atom 3 undergoes a collision with the incoming ion, then transfers (some of) the kinetic energy from the ion collision to atom 4, which is ejected from the solid. Reproduced from Sigmund.[13] ..... 33
- Fig. 1.8 Two cross sectional scanning electron microscope images of the gate structure in Intel’s 10 nm process. In order to take these images, the transistors were cut using focused ion beam milling to expose the cross-sectional view. Reproduced from Auth et al..[65] ..... 34
- Fig. 1.9 Etch rate of silicon exposed to XeF<sub>2</sub> only, XeF<sub>2</sub>/Ar<sup>+</sup> and Ar<sup>+</sup> only. The dramatic increase in etch rate when XeF<sub>2</sub> is combined with Ar<sup>+</sup> exposure is due to the reduced surface binding energy of fluorinated silicon. Reproduced from Coburn and Winters.[21] ..... 35
- Fig. 1.10 Etch yield per Ar<sup>+</sup> ion as a function of  $\Gamma_n/\Gamma_i$  (Cl/Ar<sup>+</sup>). The etching yield increases rapidly for low  $\Gamma_n/\Gamma_i$  and saturates when the reaction becomes ion starved. Reproduced from Chang et al.[22] ..... 36
- Fig. 1.11 (a) Etch rate and (b) steady state polymer thickness ( $d_{CFx}$ ) as a function of self-bias voltage for several different materials. Reproduced from Standaert et al. [30] ..... 37

|  |     |
|--|-----|
| Fig. 1.12 Features with different critical dimensions etched simultaneously. Notice larger features etch faster than smaller ones. Reproduced from Bates et al.[37].....   | 38  |
| Fig. 1.13 Sources of wafer scale non-uniformity. Reproduced from Hwang and Kanarik.[37].   | 39  |
| Fig. 1.14 Schematic of incorporating the etch model into the mask design phase. Using the etch model in this way may enable the correction of etch imperfections which cannot otherwise be resolved. Reproduced from Zavyalova et al.[64] .....  | 40  |
| Fig. 2.1 Illustration of the simulation domain showing the origin and cardinal coordinates $\hat{e}_x$ , $\hat{e}_y$ , and $\hat{e}_z$ . An initial velocity vector, $\mathbf{v}_0$ , is shown along with the polar ( $\theta$ ) and azimuthal ( $\varphi$ ) angles. ....  | 77  |
| Fig. 2.2 Implant path of 60 argon ions with energy of 2000 eV impinging on silicon.....  | 78  |
| Fig. 2.3 The Morse potential used for the diffusion routine. The distance between cells $r$ is normalized to $r_0$ and the potential is normalized to $V_0$ . The $A_0$ used for this potential is 0.75.....   | 79  |
| Fig. 2.4 Illustration of possible diffusion locations for a physisorbed particle, shown in blue. The dotted cubes illustrate the allowable diffusion transitions. Nearest neighbor sites are shown in green, next-nearest neighbors in purple, and a next-next-nearest neighbor as hatched. The 4N site is not an allowable direct transition from the current site..... | 80  |
| Fig. 2.5 Angular dependence functions, $P(\theta)$ , for chemical and physical sputtering processes..  | 81  |
| Fig. 2.6 MCFPM algorithm flow chart. Code blocks colored orange are newly developed for this thesis. Darker blue blocks had substantial updates to enable new features. Light blue blocks are unchanged from the legacy 3D code. ....  | 82  |
| Fig. 2.7 Neutral transport simulation in MCFPM for cylindrical tubes with sticking coefficients $S_b$ on the bottom surface. Transmission ratio is the flux of particles at the bottom of the tube, divided by the flux of particles entering the feature. ....  | 83  |
| Fig. 2.8 MCFPM validation cases using He/Cl <sub>2</sub> plasma etching. Notice the close match of profile geometry in dense, semi-dense and end of array features at two different etch times.[84] .....  | 84  |
| Fig. 3.1 Schematic of the Si, Si <sub>3</sub> N <sub>4</sub> and SiO <sub>2</sub> etching mechanisms. The term M <sup>+</sup> denotes activation from any ion or hot neutrals. Straight lines through the polymer overlayer imply ion implantation, while wavy lines represent diffusion through the overlayer. ....   | 95  |
| Fig. 4.1 Reactor and plasma properties. (a) Reactor geometry with (left) total positive ion density and (right) electron density, shown on a log scale with a range of two decades. (b) Probability density of ions reaching the wafer surface as a function of ion energy and incident angle (IEAD), shown on a linear scale. ....                                      | 127 |
| Fig. 4.2 Mask pattern used for etching FinFET geometries. The simulation domain includes one sub-array of three fins with periodic boundary conditions. ....   | 128 |
| Fig. 4.3 Etched profiles for the FinFET geometry. (a) Color represents height of feature, showing the variation of etch depth in the longitudinal Y-direction between fins. The difference between the total etch depth between the fins and the open field is also visible.   |     |

- (b) Slice through the fins in the X-direction, taken at the center of the fin length. Each line is separated by a constant time interval. .... 129
- Fig. 4.4 Spatially resolved fluxes to the surface of the etch profile. (a) Power density delivered by ions and (b) chlorine radical flux. .... 130
- Fig. 4.5 Longitudinal slice (Y-direction) through the center of the trench in the 3-d FinFET, showing the etch front (solid lines) for three fin lengths: 200, 400 and 600 nm. (a) Perspective view with each color representing a different material. (b) Height at the bottom of the trench in the longitudinal (Y-direction) for different fin lengths. (The nominal fin lengths are shown as dotted lines for reference.) .... 131
- Fig. 4.6 Etch properties for trenches. (a) Simultaneously etched profiles showing ARDE for three trenches having different widths. Colors represent different solid materials. Black lines represent slices through the center of the trench at different times, taken at constant time intervals. (b) Normalized density of surface species at different locations along the 67 nm profile. The etch front measurement is taken on the horizontal surface being bombarded by ions. Side high, mid and low measurements are taken from the side wall just below the resist, halfway down the profile and just above the etch-front. All chlorination measurements were taken at the final time step. .... 132
- Fig. 4.7 Average surface chlorination (Cl atoms per silicon site) of the etch front as a function of etch depth for trenches having widths of 33, 50 and 67 nm. .... 133
- Fig. 4.8 Etch properties for different values of  $\Gamma_n/\Gamma_i$ . (a) Two dimensional slice through FinFET profile for several incoming neutral to ion flux ratios. The lines labeled  $D_1$  and  $D_2$  represent equal etch depths, and are taken at different etch times due to the different etch rates between cases. The slice is taken through the center of the length of the fin. (b) Normalized etch rates as a function of  $\Gamma_n/\Gamma_i$  for two different AR. Etch rates are normalized to the initial etch rate of each respective  $\Gamma_n/\Gamma_i$  to enable comparison. .... 134
- Fig. 4.9 Time evolution of silicon trench profile during Ar/Cl<sub>2</sub> etching for different neutral to ion ratios. The neutral to ion ratios are (a) 20, (b) 10 and (c) 5. Line spacing represents a constant time interval for all profiles. Numbered lines represent similar etch times in each profile. .... 135
- Fig. 4.10 Dependence of etch rate, chlorine flux and power density on aspect ratio and the  $\Gamma_n/\Gamma_i$  ratio. Lines are labeled with neutral to ion ratios  $\Gamma_n/\Gamma_i=5, 10, 20$  and  $30$ . (a) Etch rates normalized to the initial etch rate of each  $\Gamma_n/\Gamma_i$ . (b) Power densities (solid) and Cl flux (dotted) are measured in a small window centered in the etch front. Power density is normalized to the initial power density of each respective  $\Gamma_n/\Gamma_i$  ratio. .... 136
- Fig. 4.11 Two dimensional slice through fin profile for several surface recombination probabilities,  $S_r$ . The lines labeled  $t_1$  and  $t_2$  represent equal etch times. The slice is taken through the center of the length of the fin. .... 137
- Fig. 4.12 Time evolution of silicon trench profile during Ar/Cl<sub>2</sub> etching for different chlorine recombination probabilities,  $S_r$ . The recombination probabilities of atomic Cl on SiCl<sub>3</sub> shown are (a) 0.00, (b) 0.04 and (c) 0.16. Line spacing represents a constant time interval  $\Delta t$  for all profiles. Numbered lines represent similar etch times in each profile. .... 138

- Fig. 4.13 Dependence of (a) etch rate, and (b) chlorine flux and power density on aspect ratio and the probability of recombination of radical chlorine on the walls,  $S_r$ . (a) Etch rates are normalized to the etch rate in the open field for the base case ( $S_r = 0.08$ ). Power density and chlorine flux are measured at the etch front as it evolves. .... 139
- Fig. 4.14 Time evolution of silicon trench profile for different neutral angular distributions,  $\gamma_n$ . The normalized angular distribution scaling factors are (a) 0.25, (b) 0.50 and (c) 1.00. Line spacing represents a constant time interval  $\Delta t$  for all profiles. Numbered lines represent similar etch times in each profile. .... 140
- Fig. 4.15 Dependence of (a) etch rate, and (b) chlorine flux and power density on aspect ratio and the angular distribution of neutrals,  $\gamma_n$ . Etch rate is normalized to the etch rate in the open field for the base case ( $\gamma_n = 1.00$ ). Power density and chlorine flux are measured at the etch front as it evolves. Chlorine flux and power density are omitted above an AR of 10 for  $\gamma_n = 0.25$  due to the highly tapered profile interfering with the measurement technique. .... 141
- Fig. 4.16 Time evolution of silicon trench profile for different ion angular distributions,  $\gamma_i$ . The normalized angular distribution scaling factors shown are (a) 0.25, (b) 0.50, (c) 1.00, and (d) 1.50. Line spacing represents a constant time interval  $\Delta t$  for all profiles. Numbered lines represent similar etch times in each profile. .... 142
- Fig. 4.17 Dependence of (a) etch rate, and (b) chlorine flux and power density on aspect ratio and the angular distribution of ions,  $\gamma_i$ . Etch rates are normalized to the etch rate in the open field for the base case ( $\gamma_i = 1.00$ ). Power density and chlorine flux are taken at the etch front as it evolves. .... 143
- Fig. 4.18 Etch rate as a function of aspect ratio and trench width for two values of chlorine recombination rate,  $S_r$ . For the base case,  $S_r = 0.08$ , the etch rate depends only on aspect ratio and not trench width. For the case without chlorine recombination,  $S_r = 0.00$ , the peak in etch rate weakly depends on trench width, but at higher aspect ratios the ARDE trends are again independent of trench width. .... 144
- Fig. 5.1 Schematic of the ideal ALE process. (a) Schematic of the initial trench geometry used for ideal ALE simulations. (b) View of the etch front at multiple times, with different colors representing different materials. Time increases from top to bottom, but not with equal steps between images. .... 169
- Fig. 5.2 Etch front characteristics during ideal ALE etching. (a) Etch depth and surface roughness as a function of time for the second through fifth ALE pulses. The different sub-cycles (Cl = passivation,  $\text{Ar}^+$  = ion bombardment) are shown at the top for reference, with passivation phases being highlighted by grey bands in the figure. Four pulse periods are shown in total. (b) Surface coverage of Si, SiCl, SiCl<sub>2</sub>, SiCl<sub>3</sub> and average chlorine per site at the etch front as a function of time for the second pulse. .... 170
- Fig. 5.3 Surface coverage of Si and average chlorine per site at the etch front for ideal ALE as a function of time for the second ALE pulse for AR = 2 and 10 trenches. .... 171
- Fig. 5.4 Etch depth per cycle in the passivation and ion bombardment phase for values of  $\Gamma_i/\Gamma_n = 0.02, 0.01, 10^{-3}$  and  $10^{-4}$  in the passivation step, for both AR = 2 and 10 trenches. The dotted line represents ideal ALE, with an etch depth per cycle of 1 ML. .... 172

- Fig. 5.5 Surface roughness as a function of time. (a) First 25 pulses for  $\Gamma_i/\Gamma_n = 0.02, 0.01, 10^{-3}$  and  $10^{-4}$  in the passivation step, showing the transient roughening at early etch times. (b) Sub-cycle roughening behavior at steady-state (55<sup>th</sup> pulse) for  $\Gamma_i/\Gamma_n = 0.01$  in the passivation phase and 100 ppm  $\text{Cl}_2$  in the ion bombardment phase. ALE sub-cycles are listed at the top, with the passivation phase highlighted with grey in the figure. .... 173
- Fig. 5.6 Surface morphology of the trench bottom for  $\Gamma_i/\Gamma_n =$  (a)0.01, (b)  $10^{-3}$  and (c)  $10^{-4}$  in the passivation step after 25 pulses (87.5 s etch time). Color represents the profile height, with black being deeper etching, red representing the average etch depth and yellow/white being higher features. .... 174
- Fig. 5.7 Etch depth per cycle due to ideal (reactions which occur through ALE synergy) and non-ideal (continuous) etching for cases with 1, 10 and 100 ppm  $\text{Cl}_2$  in the ion bombardment step, for both AR = 2 and 10 trenches. The dotted line represents ideal ALE, with an etch depth per cycle of 1 ML. .... 175
- Fig. 5.8 Surface morphology of the trench bottom with 100 ppm  $\text{Cl}_2$  in the ion bombardment step after 25 pulses (32 s etch time). Color represents the profile height, with black being deeper etching, red representing the average etch depth and yellow/white being higher features. .... 176
- Fig. 5.9 Etch depth per cycle for physical and chemical sputtering processes for values of  $\varepsilon_m = 50, 55, 60$  and  $65$  in the ion bombard step, for both AR = 2 and 10 trenches. The dotted line represents ideal ALE, with an etch depth per cycle of 1 ML. .... 177
- Fig. 5.10 Reactor geometry and total ion densities in the (left) Cl passivation phase and (right)  $\text{Ar}^+$  ion bombardment phase. A log scale showing two decades is used. .... 178
- Fig. 5.11 Ion energy distribution for  $\text{Cl}^+, \text{Cl}_2^+$  and  $\text{Ar}^+$  in the (a) passivation and (b) ion bombardment phases. Each ion energy distribution is a probability density function for that ion, and is normalized such that integrating the function in energy results in a value of 1 regardless of the total flux of that ion. .... 179
- Fig. 5.12 Trend of etch depth per cycle (EPC) as a function of ion bombardment time ( $T_I$ ) and passivation time ( $T_P$ ). The solid line represents an EPC of 1, and the shaded region is the window from  $0.9 < \text{EPC} < 1.1$ . .... 180
- Fig. 5.13 Trends in the ALE synergy ( $\mathcal{S}_y$ ) as a function of pulse times for an AR of 4. (a)  $\mathcal{S}_y$  as a function of ion bombardment time ( $T_I$ ) for three values of passivation time ( $T_P$ ). (b)  $\mathcal{S}_y$  as a function of  $T_I$  and  $T_P$ . The solid black line represents EPC = 1 and the dotted lines bound the range  $0.9 < \text{EPC} < 1.1$ . .... 181
- Fig. 5.14 Initial geometry used for the gate etch case study. The crystalline silicon (c-Si) fin travels back into the page, as indicated by the dotted lines. The resist (red) masks the poly-silicon gate structure, which is pre-etched to a depth just above the top of the fins. .... 182
- Fig. 5.15 Profiles resulting from etching the gate structure with a (a-c) continuous etching process, and (d-f) the optimized ALE process. Time increases from left to right. Frames are taken at equal over-etch (as a percentage of the time required to expose the bottom  $\text{SiO}_2$ ), not at equal etch times. The etch times listed for the ALE process (d-f) are active

|  |     |
|--|-----|
| (plasma on) times, and ignore any purge or dwell times necessary for a functional ALE process.....   | 183 |
| Fig. 6.1 Reactor geometry and total ion density for three different antenna configurations. Antennas, from top to bottom are: (a) A1, (b) A2 and (c) A3. The ion densities are for the argon plasma used in ion bombardment during ALE – Ar/Cl <sub>2</sub> = 100/10 ppm, 10 mTorr. Powers were adjusted to provide the same ion flux to the center of the wafer.  | 197 |
| Fig. 6.2 Etch rate and ion flux to the wafer as a function radius for three antennas, A1, A2 and A3. (a) Continuous etching (Ar/Cl <sub>2</sub> = 90/10) with etch rate in nm/s. (b) Ion fluxes from argon plasma with 10 ppm Cl <sub>2</sub> contamination with ALE rate in ML/cycle. ....  | 198 |
| Fig. 6.3 Etch rate and ion flux normalized to their values at a radius of 1.5 cm for different ion bombardment times ( $T_i = 1.5, 3.0$ and $6.0$ s) for antenna A2. “CW” indicates the continuous etching rate. ....  | 199 |
| Fig. 6.4 Data points from three ion bombardment times $T_i$ are shown using different symbols (squares: $T_i = 1.5$ s; circles: $T_i = 3$ s; triangles: $T_i = 6$ s). For each $T_i$ , data from all three antenna configurations is shown without differentiation. (a) Etch rate. (b) ALE synergy $S_y$ . ....  | 200 |
| Fig. 6.5 Predicted etch profiles for using antenna A1 for (top) continuous etching and (bottom) ALE at radii of (left) 1.5 cm and (right) 13.5 cm. $T_i = 3$ s for ALE cases. The two radial positions are etched for the same time, representing the non-uniformity on the wafer just before clearing the feature at the wafer edge. ....   | 201 |
| Fig. 7.1 Plasma conditions used in continuous and ALE processing. (a) Ratios of fluxes of C <sub>4</sub> F <sub>8</sub> dissociation products incident onto the wafer for ICP powers of 300 W and 1200 W. (b) Ion energy distributions reaching the surface during the passivation (VRF = 0 V) and ion bombardment (VRF = 45 V) phases. ....   | 224 |
| Fig. 7.2 Continuous etching properties of Si, SiO <sub>2</sub> and Si <sub>3</sub> N <sub>4</sub> using the FC gas mixture as a function of RF bias voltage. (a) Etch rate where positive values represent continuous etching and negative values are the average polymer deposition rate for the first 200 s. (b) Steady-state polymer thickness. ....  | 225 |
| Fig. 7.3 Properties of SiO <sub>2</sub> ALE. (a) Change in total height (including polymer) as a function of time for polymerization times of $T_p = 7, 21, 23$ and $27$ s. All cases use $T_i = 30$ s. Height of individual material layers during the 5 <sup>th</sup> ALE pulse for (b) $T_p = 7$ s and (c) $T_p = 21$ s. The total ALE cycle time, $T_c$ , is in each frame. ....   | 226 |
| Fig. 7.4 Comparison of non-ideal and ideal SiO <sub>2</sub> ALE properties. (a) Pulse-periodic steady state etch per cycle (EPC) as a function of $T_p$ , for $T_i = 10, 20$ and $30$ s for ideal (dotted lines) and non-ideal (solid lines) reactive fluxes. (b) ALE synergy and steady state EPC for small values of $T_p$ with $T_i = 20$ s. Values are shown for ideal and non-ideal fluxes. ....  | 227 |
| Fig. 7.5 ALE of SiO <sub>2</sub> and Si <sub>3</sub> N <sub>4</sub> using non-ideal fluxes. (a) Change in total height (including polymer) as a function of time for SiO <sub>2</sub> and Si <sub>3</sub> N <sub>4</sub> . The shaded regions represent the overlayer thickness, comprised of both the selvedge and polymer layers. Height of individual material layers during the 5 <sup>th</sup> ALE pulse for (b) SiO <sub>2</sub> and (c) Si <sub>3</sub> N <sub>4</sub> . .... | 228 |
| Fig. 7.6 Thickness of each overlayer species as a function of time during three ALE pulses ( $t = 0$ is the start of the 5 <sup>th</sup> pulse) for (a) SiO <sub>2</sub> and (b) Si <sub>3</sub> N <sub>4</sub> . ....   | 229 |

Fig. 7.7 Total change in height ( $\Delta H$ ) of the surface of  $\text{SiO}_2$  or  $\text{Si}_3\text{N}_4$  (not including overlayer) after 15 ALE cycles as a function of passivation time ( $T_p$ ) for ion bombardment times ( $T_i$ ) of 10, 20 and 30 s.  $\text{SiO}_2$  ALE is shown as solid lines,  $\text{Si}_3\text{N}_4$  as dotted lines. .... 230

Fig. 7.8 Selectivity of ALE of  $\text{SiO}_2$  over  $\text{Si}_3\text{N}_4$ . (a) Selectivity after 15 cycles as a function of passivation time ( $T_p$ ) for ion bombardment times ( $T_i$ ) of 10, 20 and 30 s. (b) Selectivity as a function of  $T_p$  for three different etch durations (5, 10 and 15 cycles) using  $T_i = 20$  s. .... 231

Fig. 7.9 Self-aligned-contact etch profiles for continuous etching and ALE. (a) Initial profile. Continuous etch using the FC gas mixture with 1200 W ICP power for (b) VRF = 40 V and (c) VRF = 100 V. ALE profiles after 165 cycles using  $T_i = 20$  s and  $T_p =$  (d) 3.5 s, (e) 4.5 s and (f) 5.5 s. .... 232

Fig. 7.10 Shoulder loss and CD loss as a function of passivation time for the SAC feature with  $T_i = 20$  s. .... 233

## LIST OF TABLES

|   |    |
|---|----|
| Table 3.1 Chlorine surface reaction mechanism.....      | 96 |
| Table 3.2 Fluorocarbon surface reaction mechanism ..... | 98 |

## LIST OF ABBREVIATIONS

|                 |                                       |
|-----------------|---------------------------------------|
| ICP             | Inductively coupled plasma            |
| ALE             | Atomic layer etching                  |
| (I)EAD          | (Ion) energy and angular distribution |
| CD              | Critical dimension                    |
| ARDE            | Aspect ratio dependent etching        |
| $\Gamma_x$      | Flux of species $x$ to the surface    |
| HPEM            | Hybrid Plasma Equipment Model         |
| MCFPM           | Monte Carlo Feature Profile Model     |
| NN              | Nearest neighbor                      |
| NNN             | Next-nearest neighbor                 |
| 4N              | Next-next-nearest neighbor            |
| RF              | Radio frequency                       |
| ppm             | Parts per million                     |
| EPC             | Etch per cycle                        |
| $\mathcal{S}_y$ | ALE synergy                           |

## **ABSTRACT**

In this thesis, a nano-scale model of feature evolution is developed and used to illustrate several of the physical mechanisms at work during state-of-the-art plasma etching of semiconductor materials. A new model for plasma etching of silicon, silicon dioxide, and silicon nitride in fluorocarbon containing plasmas was developed. This new technique uses physically based models to take into account the transport of reactive species and ion energy through the finite thickness fluoropolymer overlayer which develops during etching to the etch interface beneath.

This etch model was used to explore the underlying physical mechanisms behind the aspect ratio dependence of etch rate in high aspect ratio etching, as well as the wafer scale uniformity of plasma etching. The results presented here indicate that, for a wide range of applications, diffusive neutral transport of reactive species is responsible for the aspect ratio dependence of etch rate. Etching silicon in a chlorine containing plasma was shown to have an etch rate which depends linearly on ion flux for a wide range of conditions. Because of this dependence, any non-uniformity of ion flux over the target wafer results in non-uniform etching.

Both of the issues described above can be addressed by introducing a technique referred to as atomic layer etching (ALE). This technique separates the reactive radical and ion fluxes in time, by dividing the etching reaction into two self-limited half step reactions. Only by cycling between the radical passivation phase and the ion etching phase is etching observed. The conditions under which this system is effective was explored using the ALE of silicon as a prototypical example. It was found that ideal ALE can provide total independence from aspect

ratio etch rates, and perfect wafer scale uniformity. By introducing non-ideal fluxes that are more representative of conditions found in a typical plasma etching reactor, both of these benefits were reduced, but not eliminated.

Applying the ALE technique to  $\text{SiO}_2$  is more difficult than bare silicon, as chlorine does not effectively passivate the surface. Instead a fluorocarbon containing plasma is employed. Unlike using a pure halogen gas, the inclusion of fluorocarbon species was found to result in non-self-limited passivation of the surface, with a fluoropolymer layer forming having a thickness that depends on the passivation time. Results indicate that this fluoropolymer layer functions as a fuel for continued etching during the ion bombardment phase, linking the etch per cycle to the passivation time. The selectivity of the ALE of  $\text{SiO}_2$  over  $\text{Si}_3\text{N}_4$  was also studied. It was found that very high selectivity can be obtained in the steady state, but a transient period exists at the beginning of etching during which the selectivity is low. The implications of this transient etching were explored using a self-aligned contact etch as an example application. It was found that thicker passivation in each cycle improved selectivity, but at the tradeoff of causing more tapered features, referred to as critical dimension loss.

## Chapter 1 INTRODUCTION

### 1.1. Plasma Etching in Semiconductor Processing

Low temperature plasmas have been used for etching in the semiconductor industry since the 1960's.[1,2] Before plasma etching became widely used, material removal and pattern transfer was accomplished using chemical etching in solution. The vast majority of solution based etching is isotropic, etching in all directions at the same rate. The few anisotropic solution based processes etch preferentially in one crystal direction over another [3], which is not useful for processing amorphous films or when etching directions must be arbitrarily imposed on the crystal for design considerations. Many chemical etching processes can have very high selectivity, meaning that a given etchant may etch one material much faster than another material.[4] This high selectivity made their use in early integrated circuit fabrication effective as long as the thickness of the film to be etched was much smaller than the size of the feature; that is, features which have a low *aspect ratio* (defined as etch depth divided by feature size) as shown in Fig. 1.1.

As the integrated circuit—and the microprocessor in particular—gained popularity in the 1970's, the trend became scaling features to smaller dimensions in order to produce more active components in a given area began.[5,6] As features shrank, the aspect ratio of the etch processes increased. Eventually the undercut (etching underneath the mask) of isotropic etching became too large to effectively pattern smaller features, requiring an anisotropic etch method, as depicted in Fig. 1.1. Plasma etching offered a method to achieve anisotropic etching by harnessing the energy of ions impinging on the surface to facilitate etching reactions that are otherwise

thermodynamically unfavorable. Because the impinging ions have a very anisotropic angular distribution with respect to the surface normal, with the majority of the ions having velocity aligned near the surface normal, the resulting etch is also very anisotropic.

Modern microprocessors rely on plasma etching for nearly all material removal and pattern transfer steps. Characteristic dimensions of features have continued to shrink, with the 10 nm node in full production and research and development in progress for 7 nm and 5 nm feature sizes. At these scales plasma technology is challenged to keep pace with increasingly demanding physical constraints. Atomic precision has gone from a theoretical notion [7] to a technological imperative [8]. While fundamental research into plasma etching mechanisms dates back to the 1960's, many limitations of the process are still not completely understood. New processes are continually being designed to meet the next challenge.

Several studies on the fundamental mechanisms of plasma etching, and new plasma etching processes, are presented in this thesis. A brief overview of the elements of plasma physics that relate to plasma etching will be given in Chapter 1.2. A description of the basic types of plasma surface interactions will be given in Chapter 1.3. Chapter 1.4 includes a description of some of the challenges which occur during plasma etching, and Chapter 1.5 provides a description of feature scale modeling, the main technique used in this thesis, and its role in the furthering of our understanding of plasma etching and process development.

## **1.2. Plasma Physics Overview**

The term plasma is typically used to describe an energetic gaseous state of matter that includes charged particles, typically electrons and ions. This definition is inclusive and the term plasma is used to refer to fully ionized gas in thermodynamic equilibrium (such as exists in the interior of stars), fully ionized non-equilibrium plasmas (such as occur in space) and partially

ionized non-equilibrium low-temperature plasmas (such as exist in commercial semiconductor etching reactors). In this thesis, only the last of these plasmas will be discussed. In this work, the term plasma implies a weakly ionized gas where the ionization fraction is small ( $< 1\%$ ), the electron temperature is relatively low (1-10 eV), and the system has at least three distinct temperatures (electrons, ions, and neutral gas).

The focus of this thesis is on the modeling of plasma surface interactions during semiconductor etching. As such, a full discussion of gas phase physics of non-equilibrium low-temperature plasmas is outside of the thesis' scope. Instead, a brief introduction is given to the elements of plasma physics which give rise to energetic interactions between the plasma and the surfaces it is in contact with. It is these energetic interactions, both in the form of kinetically accelerated ion bombardment of the surface and exposure to large fluxes of high enthalpy radical species, that differentiates plasma etching from gas phase thermal etching.

### 1.2.1. Quasi-Neutral Plasma

In a typical low temperature plasma studied here, the plasma is sustained in a neutral gas by accelerating electrons (usually using an electric field), and generating charged species by electron impact ionization, such as



In this scenario, it is reasonable to expect that the number of electrons,  $n_e$ , will be equal to the number of positive ions,  $N^+$ . This results in zero net space charge,  $\rho = q(N^+ - n_e)$ , in the isotropic plasma, referred to as the quasi-neutral assumption.

In a typical low temperature plasma for microelectronics fabrication, the electron temperature ( $T_e$ ) is on the order of 1-10 eV due to efficient heating by an applied radio frequency (RF) electric field, while ion temperatures ( $T_i$ ) are typically around 1000 K due to less efficient

heating by the field and more efficient cooling by momentum transfer with the background gas. This large difference in temperature, along with the large difference in mass, results in a large disparity in the average (RMS) thermal velocity of electrons and ions in the plasma,

$$\langle v_{th} \rangle = \sqrt{\frac{3k_b T_e}{m_e}} \quad \sqrt{\frac{3k_b T_i}{M_i}}, \quad (1.2)$$

where  $k_b$  is the Boltzmann constant,  $m_e$  is the electron mass and  $M_i$  is the ion mass. If ionization was localized to a small area in extended space, this difference in thermal velocity – in the absence of coulombic interaction – would allow electrons to quickly diffuse away leaving the slower ions behind. Since the species are oppositely charged, coulomb interactions prevent this behavior, establishing a correcting field any time a charge separation occurs in the plasma.

A quick examination of this self-restoring field gives significant insight into the characteristic time and length scales of the plasma. Imagine a one-dimensional plasma as a fixed region of positive charge (ions) and a mobile region of negative charge (electrons). An electric field will form between these two regions of charge according to Poisson's equation

$$\frac{dE}{dx} = \frac{\rho}{\epsilon_0}, \quad (1.3)$$

where  $\epsilon_0$  is the permittivity of free space,  $E$  is the electric field and  $\rho$  is the charge density. As the negative charge region moves in space this electric field will change as

$$\frac{dE}{dt} = \frac{dE}{dx} \frac{dx}{dt} = \frac{dE}{dx} v_e = \frac{v_e \rho}{\epsilon_0}. \quad (1.4)$$

where  $v_e$  is the velocity of the electron cloud. The largest  $dE/dt$  will occur when the charges are completely separated and  $\rho = -qn_e$ . The force exerted on the negative charge region changes the velocity as,

$$\frac{dv_e}{dt} = -\frac{qE}{m_e}. \quad (1.5)$$

This acceleration changes in time (at the point of complete charge separation) as,

$$\frac{d^2v_e}{dt^2} = -\frac{q}{m_e} \frac{dE}{dt} = \frac{v_e q^2 n_e}{\epsilon_0 m_e}. \quad (1.6)$$

The solution to this equation is a velocity which oscillates at the plasma frequency,  $\omega_p$ , given by

$$\omega_p = \sqrt{\frac{q^2 n_e}{\epsilon_0 m_e}}. \quad (1.7)$$

The average distance traveled during this oscillation is

$$\lambda_D = \sqrt{\frac{\epsilon_0 k_b T_e}{q^2 n_e}}. \quad (1.8)$$

This length,  $\lambda_D$ , is the Debye length, and represents the longest distance over which the plasma can be non-neutral. For distances larger than  $\lambda_D$ , the magnitude of the restoring field is such that the plasma will retain neutrality. For reference, this distance can range from tens to hundreds of microns in typical processing plasmas discussed here. This concept of establishing a self-restoring electric field, and the quasi-neutrality of the plasma are critical to behavior of the low temperature plasma.

### 1.2.2. Electron Impact Reactions

In order to sustain a plasma in a low pressure plasma etching reactor, the rate of ionization must be equal to the loss of charged species in the system. In a typical reactor used for plasma etching, the loss mechanism is often dominated by recombination on surfaces. Ionization is accomplished by electron impact reactions with the background gas. In order to achieve a steady state plasma, the electron temperature must be such that it satisfies the equation

$$\frac{\partial n_e}{\partial t} = n_e k_i(T_e) N - \frac{D_A(T_e) n_e}{\Lambda^2} = 0, \quad (1.9)$$

where  $k_i(T_e)$  is the ionization rate coefficient,  $N$  is the density of the background gas,  $\Lambda$  is the diffusion length (a parameter describing the average distance to the walls in a particular vessel) and  $D_A(T_e)$  is the ambipolar diffusion coefficient.

The ambipolar diffusion coefficient describes the diffusion behavior of the electrons (and ions) after taking into account the effect of the restoring field described in Chapter 1.2.1. The cumulative effect of the restoring field, referred to as the ambipolar field, is to increase the rate of diffusion of ions while dramatically reducing the rate of diffusion of electrons. In this way ions and electrons diffuse over long distances with the same diffusion constant, maintaining quasi-neutrality. The value of the ambipolar diffusion constant is approximately

$$D_A \approx D_i \left( 1 + \frac{T_e}{T_i} \right), \quad (1.10)$$

where  $D_i$  is the diffusion coefficient of the ion.

The rate of ionization depends on the ionization rate coefficient,  $k_i$ , which is

$$k_i = \int_{\varepsilon_{th}}^{\infty} f(\varepsilon) \sigma_i(\varepsilon) \left( \frac{2e}{m_e} \right)^{1/2} d\varepsilon, \quad (1.11)$$

where  $f(\varepsilon)$  is the electron energy distribution,  $\sigma_i(\varepsilon)$  is the cross section for ionization by electron impact and  $\varepsilon_{th}$  is the threshold energy for ionization. Below the ionization threshold the cross section is, by definition, zero. For the ionization rate to be significant there must be a population of electrons with enough kinetic energy to ionize the neutral gas. For most gasses of interest for plasma etching the ionization reaction requires 10-20 eV of electron energy, below this threshold energy the cross section is zero. From Eqn. 1.11, the electron energy distribution must have some overlap with the ionization cross section to produce a finite ionization rate coefficient. The

larger the overlap is (which increases with electron temperature), the higher the ionization rate coefficient becomes.

The end result of Eqns. 1.9, 1.10 and 1.11 is that the electron temperature in a plasma sustained in typical low pressure etching reactor will be between 2 to 10 eV. This is the temperature where the tail of the (approximately Maxwellian) electron energy distribution overlaps the ionization cross section in such a way as to produce enough ionization to balance the diffusion losses to the chamber walls. In such a population, the most likely energy for an individual electron (mode of the distribution) is between 1 and 2.5 eV, significantly less than the typical ionization potential. Therefore, a typical electron in the plasma will not have enough energy to ionize the background gas, but in the typical chemistries involved in plasma etching these electrons can participate in many important dissociation and excitation processes.

While  $T_e$  is determined primarily by the balance between ionization and losses, most technologically relevant plasma chemistries also include several lower threshold electron impact cross reactions. For instance, molecular chlorine has several process which occur at energies lower than ionization, including direct electron impact dissociation, vibrational excitation reactions and dissociative attachment, as shown in Fig. 1.2.[9] While processes such as direct dissociation and electronic excitation have lower threshold energies than ionization, their cross sections have a similar energy dependence. Vibrational excitation, on the other hand, has a very different cross section. This process is resonant in electron energy, having a large cross section for some energies (0.2 to 0.9 eV and 7.0 to 15 eV) and zero otherwise. Dissociative attachment, where the  $\text{Cl}_2$  molecule is decomposed into a Cl radical and a  $\text{Cl}^-$  ion, has an inverse electron energy dependence throughout much of the energy range.

The result of having a  $T_e$  large enough to produce significant ionization as well as several lower energy electron impact processes is to have significant power deposition in the neutral gas. Gases such as chlorine become significantly dissociated, generating large densities of highly reactive radical species. In gases of larger molecules, such as  $C_4F_8$ , the dissociation process has many more pathways, but the end result is always the breaking down of stable molecules into reactive fragments by energy transfer from electrons. The resulting reactive species then play an important role in the etching process, which is discussed in detail in Chapter 1.3.2.

### **1.2.3. Formation of the Plasma Sheath and Anisotropic Acceleration of Ions**

In close proximity to a surface the ambipolar field is unable to maintain charge neutrality. As discussed previously, for distances shorter than several  $\lambda_D$  the restoring field is unable to maintain charge neutrality. If a plasma is brought into contact with a surface, initially the flux of electrons to the surface will be much higher than the flux of ions due to the higher thermal velocity of electrons. This condition will negatively charge the surface, raising the potential of the bulk plasma above the boundary potential. This field will retard the flux of electrons to the surface. Eventually the negative charge buildup on the surface will balance the flux of electrons with the positive ion flux. The region where this electric field, and the resulting charge imbalance, exists is known as the plasma sheath. The development of the plasma sheath is extremely important to plasma etching because the potential which acts to retard the electron flux to the surface (referred to as the sheath potential,  $\Phi_0$ ) also acts to accelerate positive ions in the normal direction of flat surfaces. In this way, most ions reaching the surface will arrive aligned with the surface normal having kinetic energies much higher than their thermal velocity in the plasma.

At a point just outside of this sheath, the random flux of electrons directed toward the surface is

$$\Gamma_e = \frac{n_e v_{th}}{4}, \quad (1.12)$$

where  $v_{th}$  is the thermal velocity (mean of the magnitude of the velocity distribution) of the electron,

$$v_{th} = \sqrt{\frac{8k_b T_e}{\pi m_e}}. \quad (1.13)$$

At the sheath edge, the surface will collect all positive ions with a velocity oriented in the direction of the surface due to the attractive field. On the other hand, only the electrons with an energy larger than the sheath potential will be able to reach the surface. Assuming a Maxwellian distribution of electrons the fluxes can be balanced as

$$\frac{N^+}{4} \sqrt{\frac{8k_b T_i}{\rho m_i}} = \frac{n_e}{4} \sqrt{\frac{8k_b T_e}{\rho m_e}} \exp\left(\frac{q\Phi_0}{k_b T_e}\right), \quad (1.14)$$

where  $\Phi_0$  is the sheath potential. At the sheath edge, where  $\Phi_0$  is zero,  $N^+ = n_e$ , so that can be solved as

$$\Phi_0 = -\frac{k_b T_e}{2} \ln\left(\frac{T_e m_i}{T_i m_e}\right). \quad (1.15)$$

In a typical processing plasma, the magnitude of the negative sheath potential will be between 5 to 20 times  $k_b T_e/q$ , or about 10 to 30 V.

This potential is dropped over the span of a few  $\lambda_D$  moving into the plasma, as the charge density in the plasma masks the surface charge. This creates a strong electric field in the sheath region. In the presence of this field, all ions entering the sheath will be accelerated toward the surface. In the absence of collisions, the ions arrive at the wafer with an energy approximately

equal to  $q\Phi_0$ . The velocity imparted by the sheath is in the direction of the surface normal (perpendicular to the surface), and is much larger than the randomly directed thermal velocity of the ion before entering the sheath (tangential to the surface). Due to these relative speeds, ions reaching the surface have velocities that are closely aligned with the surface normal. The angle between the surface normal and the ion trajectory ( $\theta$ ) can be approximated as

$$\theta \sim \left( \frac{v_{th}}{v_{\perp}} \right)^{1/2} \quad (1.16)$$

where  $v_{\perp} \sim \Phi_0^{1/2}$ . This results in most ions being within  $5^\circ$  of the surface normal for typical plasma conditions. In a plasma reactor designed for plasma processing, this range can be smaller due to additional negative bias on the substrate, as described in the following section.

#### **1.2.4. Ion Energy Distributions and the Influence of RF Bias**

In addition to the acceleration provided to ions due to the floating sheath potential described by Eqn. 1.15, additional acceleration is often provided by the application of an RF bias on the electrode where etching is intended to occur. The influence of an applied RF bias on the sheath dynamics depends on many factors, including system pressure (collisional vs collisionless sheath), plasma density, reactor geometry, ion mass and RF frequency.[10] As such, a detailed analysis of the RF bias will not be included here. Instead a few important examples of how these factors affect the ion energy distribution to the wafer will be discussed qualitatively.

By applying an RF bias,  $V_{RF}$ , to the wafer it is possible to accelerate ions to a much higher energy than  $\Phi_0$ . For the positive half of the RF cycle the potential in the bulk plasma,  $V_p$ , must increase with  $V_{RF}$  in order to maintain a sheath potential of at least  $\Phi_0$ , as shown in Fig. 1.3(a). This is necessary as the positive potential would otherwise attract electrons and unbalance the flux of electrons and ions. During the negative half-cycle the plasma potential

remains at  $\Phi_0$ , requiring the sheath to drop a much larger voltage,  $\Phi_s$ , than without the RF bias. If we assume that ions transit the sheath quickly compared to the change in RF voltage, ions which enter the sheath during the negative cycle will gain  $V_{RF} + \Phi_0$  potential before they reach the wafer. While Fig. 1.3 shows a  $V_{RF} = 100$  V case, it is possible to create much larger sheath potentials, with ions being accelerated into the keV energy range.

In a typical plasma etching reactor there will also be a (usual negative) DC self-bias voltage on the powered electrode due to the reactor geometry, providing further acceleration to ions. This DC self-bias arises because the electrodes in a typical reactor design are asymmetric in size, with the powered wafer chuck being small compared to the remaining surface area in the reactor, which is typically grounded. The total current to these electrodes, including displacement current, must remain balanced in an AC system. If the powered electrode is interfaced to the power supply using a blocking capacitor, then the difference in current collecting area of the two electrodes results in the charging of this capacitor and a DC self-bias,  $V_{DC}$ , developing on the powered electrode. With this DC voltage imposed on the biased electrode, the sheath must drop  $V_{RF} + V_{DC} + \Phi_0$ , as shown in Fig. 1.3(b), and this potential can be transferred to ions before reaching the wafer.

While the potential dropped across the sheath can be as large as  $V_{DC} + V_{RF} + \Phi_0$ , it fluctuates throughout the RF period. Therefore, not all ions will reach the wafer with the same ion energy. The actual distribution of ion energies reaching the wafer depends strongly on  $\tau_{ion}/\tau_{rf}$ , where  $\tau_{ion}$  is the time required for the ion to transit the sheath, and  $\tau_{rf}$  is the RF period. If the ion transit time is large compared to the RF period then the ion motion through the sheath averages the RF potential over several cycles. In the absence of a DC bias, the average sheath potential becomes  $V_{RF} / 2$ , due to the rectification effect shown in Fig. 1.3. If the DC bias is large

compared to  $V_{RF}/2$ , then most ions gain about  $V_{DC} + \Phi_0$  energy before reaching the wafer. This results at a single narrow peak in the ion energy distribution. If  $\tau_{ion}$  is small compared to  $\tau_{rf}$  then the ion can gain an energy equal to the sheath potential at the instant the ion enters the sheath. As the sheath potential oscillates throughout the RF period, this results in a wide distribution of ion energies, with bi-modal peaks at  $\Phi_0$  and  $V_{DC} + V_{RF} + \Phi_0$ . For intermediate  $\tau_{ion}/\tau_{rf}$ , the distribution is bi-modal with peaks centered around  $V_{DC} + \Phi_0$ , but more narrowly spaced than the short  $\tau_{ion}$  limit, as shown in Fig. 1.4.[11]

The main factors which determine  $\tau_{ion}/\tau_{rf}$ , and therefore the ion energy distribution, are ion mass and RF frequency. Modifying the RF frequency changes  $\tau_{ion}/\tau_{rf}$  directly, with high frequencies resulting in narrower energy distributions and lower frequencies giving wider bi-modal distributions, as shown in Fig. 1.5.[10] The transit time depends primarily on ion mass, with larger ions resulting in longer transit times. Because of this scaling, lighter ions tend to have a wider, bi-modal energy distribution, while heavier ions tend to have a single peaked energy distribution, as shown in Fig. 1.6.[12]

### 1.3. Plasma Surface Interactions

All surfaces in contact with a plasma will undergo exposure to bombardment by high energy particles and reactive radical fluxes. These two main components, kinetic energy from ion bombardment and chemical potential from radical exposure, make plasma etching effective for many materials and applications. The balance of ion energy and radical exposure, and the possible synergy between these energy sources allows for etch mechanisms to be tailored for specific materials, providing selective etching of one material over another. Furthermore, the anisotropic nature of the ion energy deposition, and the isotropic flux of incoming reactive radicals provide a method to tune the directionality of the etch process which is not possible in

thermal etching (either wet or dry). The ability to control etch selectivity and directionality has made plasma etching essential in the semiconductor industry.

### 1.3.1. Physical Sputtering

Perhaps the simplest plasma surface interaction is the physical sputtering of surface atoms by energetic ions. The basic mechanism of physical sputtering is the transfer of kinetic energy from impinging ions to target atoms in the solid. If the energy transferred to the target atom is large enough to overcome the surface binding energy then the atom can be ejected from the solid material, referred to as sputtering.[13] For this energy transfer to result in sputtering, the target atom's final velocity must be directed back into the plasma. As the impinging ions arrive (on average) normal to the surface, this requires at least two collisions in order to eject target atoms, as shown in Fig. 1.7. In this figure, target atoms 2 and 4 are both ejected from the solid. In order to conserve momentum, both of these sputtered atoms required a collision cascade of at least two collisions before being ejected.

Due to the inherent complexity of the collision cascade, first-principals analytical models of the sputtering process are complex.[13] Phenomenological modeling and empirical fitting of experimental data has arrived at a general expression for sputtering yield at normal incidence of [14]

$$Y = \frac{A}{U} \frac{Z_t}{\left(Z_t^{2/3} + Z_i^{2/3}\right)^{3/4}} \left(\frac{Z_i}{Z_t + Z_i}\right)^B e_i^{1/2}, \quad (1.17)$$

where  $Z_t$  is the atomic number of the target,  $Z_i$  is the atomic number of the incoming ion (assuming single ionization),  $\varepsilon_i$  is the incident ion energy and  $U$  is the surface binding energy. The parameters  $A$  and  $B$  are essentially fitting parameters, and vary from one model to another, but are often given values of  $A = 5.2$  and  $B = 0.67$ .

This expression for sputtering yield presented in Eqn 1.17 results in several useful observations. First, the sputtering yield scales as the square root of the incoming ion energy. This trend remains consistent over a wide range of conditions and energies, even outside of the physical sputtering regime.[15] Second is that mass ratio  $Z_i/Z_t$  impacts the sputtering yield. This mass ratio dependency arises for the same reason as the mass ratio dependence in a simple binary elastic collision model, but in the case of sputtering a  $Z_i$  slightly larger than  $Z_t$  results in the most efficient sputtering (as opposed to elastic collisions, where  $Z_i=Z_t$  results in the largest energy transfer).

Due to the narrow range of mass ratios for different materials of interest, and the relatively low dependence on mass ratio, physical sputtering usually has little or no selectivity to different materials. It is therefore difficult to use for patterning purposes as any mask material will erode at a similar rate to the etch target. This lack of material selectivity can be beneficial for some purposes. Focused ion beam milling relies on physical sputtering by noble gas or metal ions, and is a critical metrology technique in the semiconductor industry.[16] Focused ion beam milling uses, as the name implies, electronic optics to generate a narrow beam of heavy ions. This beam can be used to etch patterns into arbitrary materials with very high spatial resolution. This technique is used extensively in the preparation of cross sectioned samples of semiconductor devices for scanning electron or transmission electron microscopy, as shown in Fig. 1.8.

### **1.3.2. Surface Passivation and Chemical Sputtering**

Reactive radical species generated in the plasma can also have a significant effect on the plasma etch process. Some of these species, particularly halogen radicals, can strongly bind with the surface of target materials.[17] The strong covalent bond between the halogen and the

surface atom can produce weaker binding between the surface atom and the underlying lattice.[18–20] This weakening of the bond with the underlying lattice effectively reduces the surface binding energy of the passivated surface site.

The reduced surface binding energy of passivated surface sites can significantly increase sputtering yield.[21] For example, in their seminal work Coburn and Winters studied the effect of combining XeF<sub>2</sub> exposure with Ar<sup>+</sup> ion bombardment. They found that neither XeF<sub>2</sub> nor Ar<sup>+</sup> exposure resulted in significant etch rates when used alone. When both fluxes are combined the etch rate increased to more than 10 times the background rate of XeF<sub>2</sub> etching, as shown in Fig. 1.9. This increase in etch rate can be directly attributed to the reduction of surface binding energy when the silicon becomes fluorinated by thermal decomposition of the XeF<sub>2</sub> on the surface. This synergistic effect of increased etch yield when a passivating radical is combined with ion bombardment has become referred to as chemically enhanced sputtering, or simply chemical sputtering.

In addition to the dramatic increase in sputtering yield associated with surface passivation, this process allows for the selective etching of one material over another due to differences in the reactivity with the passivating species. For instance, silicon can be chemically sputtered by exposing the surface to chlorine radical species.[22,23] Silicon dioxide, SiO<sub>2</sub>, on the other hand does not etch with the same increased yield in chlorine containing plasmas due to the lack of a strong oxygen chlorine bond.[24] This results in selective etching of silicon over SiO<sub>2</sub> in chlorine containing plasmas. This selectivity, enabled by carefully choosing the passivation chemistry, is fundamental to the success of plasma etching in the semiconductor fabrication industry.

One significant consequence of relying on passivation reactions to increase sputtering yield is the synergistic coupling of ion and radical fluxes. Chang et al. explored this coupling using molecular beam experiments and found that the etching yield depends strongly on the neutral to ion flux ratio,  $\Gamma_n/\Gamma_i$ , for low and moderate values of  $\Gamma_n/\Gamma_i$  ( $< 100$ ), as shown in Fig. 1.10.[22] The dependence saturates at larger values of  $\Gamma_n/\Gamma_i$  when the etching reaction becomes ion starved. In this ion starved regime the surface can be considered to be completely passivated, presenting each impinging ion with a similarly passivated surface and creating a constant etching yield. For lower values of  $\Gamma_n/\Gamma_i$  the surface is not fully passivated, and the coverage of passivated sites depends directly on ion flux, ion energy and radical flux.

The effects of neutral/ion synergy are compounded by the difference in transport methods between the two fluxes. At pressures and length scales typical of modern etching, neutral fluxes, including the reactive radicals which participate in surface passivation, must transport through the etch feature by molecular flow.[25] This implies that the radicals will ballistically travel from surface to surface inside the feature, with each interaction resulting in a re-emission from the surface with an isotropic Lambertian cosine law angular distribution. The properties of this transport method have been well studied in vacuum systems, where neutral conduction through high aspect ratio tubes has been of interest for decades.[26] The results of this transport method are that higher aspect ratio features will have significant reductions in neutral flux at the etch front (bottom of feature) than smaller aspect ratios. This is in contrast to the transport of ions, which occurs predominantly by ballistic transport aligned with the surface normal. Because of the anisotropic angular distribution, the ions tend to interact less with the walls, and reach the etch front with little dependence on aspect ratio. This difference in transport methods between neutrals and ions can create aspect ratio dependent etch rates (ARDE).

### 1.3.3. Fluorocarbon Etching

In some cases, particularly  $\text{SiO}_2$  and  $\text{Si}_3\text{N}_4$ , etching using halogen plasma does not provide effective surface passivation due to the lack of a strong bond between the halogen radical and the oxygen or nitrogen sites in these compounds.[27] In these cases it is typical to use a fluorocarbon gas plasma instead of a simple halogen. This allows for the removal of silicon as a volatile product containing fluorine, such as  $\text{SiF}_4$ , and for the removal of oxygen in the form of  $\text{CO}$ ,  $\text{CO}_2$  or  $\text{COF}_2$ . [28] Similarly, nitrogen removal from the  $\text{Si}_3\text{N}_4$  compound is aided by the availability of carbon, creating volatile gas phase products like  $\text{CNF}$ . [29]

While the addition of carbon containing radicals to the etch chemistry results in a chemically enhanced etching pathway for oxygen and nitrogen containing compounds, it also results in the formation of a steady state fluoropolymer layer on the etch surface. This fluorocarbon overlayer has been observed by Standaert et al. to play a critical role in plasma etching using fluorocarbon gases. [30] For a given plasma chemistry the steady state polymer thickness during continuous etching will depend on the ion energy and the material being etched, as shown in Fig. 1.11. This polymer thickness mediates the transport of reactive radical species and ion energy to the etch front. This results in an etch rate that depends on polymer thickness, and therefore offers selective etching of  $\text{SiO}_2$  over  $\text{Si}_3\text{N}_4$  or silicon. [29]

There are several factors which affect the steady state polymer thickness on dielectric materials etched in fluorocarbon gas plasmas. To achieve a steady state thickness, the polymer deposition rate must be balanced by polymer loss mechanisms. It is clear from experimental data that a fairly wide range of plasma conditions will produce steady state polymer thicknesses. [29] For this to be possible, either the deposition rate or loss term must depend on polymer thickness, such as

$$\frac{dp}{dt} = D - Sp = 0, \quad (1.18)$$

where  $p$  is the polymer thickness (cm),  $D$  is the polymer deposition rate (cm-s<sup>-1</sup>) and  $Sp$  is the polymer etch rate. In the steady state,  $p = D/S$ . In this simple model, the deposition rate is

$$D = \frac{a_p \phi_p}{\rho}, \quad (1.19)$$

$\phi_p$  is the incident flux of polymerizing species,  $a_p$  is the probability for depositing on the underlying polymer and  $\rho$  is the volumetric number density of the film. While the polymer etch rate in the physical system may not be linearly dependent on polymer thickness, as proposed in Eq. (1.18), there must be some dependency on polymer thickness or there would only be a single  $D/S$  ratio which would produce steady-state polymer thickness, which is not the experimental observation. The polymer etch rate,  $Sp$  (cm s<sup>-1</sup>) is conceptually given by

$$S = a_e \phi_e D, \quad (1.20)$$

$\phi_e$  is the incident flux of polymer removing (or etching) species,  $a_e$  is the probability for etching the polymer and  $D$  is the diffusivity of the etching species in the polymer film. This simple analysis implies that the deposition of polymer is a surface dominated process, depending on the exposed area of the feature, while polymer etching is a volumetric process, depending on the thickness of the polymer. This is a physically consistent picture of producing a steady state polymer thickness provided that the etching species is not significantly depleted in transporting through the polymer layer. In plasma etching of, for example, SiO<sub>2</sub> in fluorocarbon plasma, polymer deposition occurs dominantly by incorporation of radicals (e.g., CF, CF<sub>2</sub>, CF<sub>3</sub>) into the outermost surface of the polymer. Polymer etching, on the other hand, occurs predominantly due to thermal reactions with reactive radicals (e.g., F, O), which can diffuse through the bulk of the polymer, resulting in a volumetric process.[31]

These deposition and loss mechanisms depend only on plasma properties, and in principle should be identical on all materials exposed to the same plasma, provided the surface is covered by at least one monolayer of polymer. The difference between steady state polymer thickness on different materials is due to different rates of consumption of polymer at the etching interface between the polymer and the underlying material. These differences in polymer consumption result from the different stoichiometries of producing etch products for each material. When etching  $\text{SiO}_2$ , silicon sites are dominantly removed as  $\text{SiF}_{x(g)}$  species, while oxygen is removed from the surface mainly as CO or  $\text{COF}_2$ . [28] Therefore, for each Si atom removed, the etch process will consume two carbon atoms from the polymer overlayer. On bare silicon, this consumption of carbon by the formation of C-O bonds does not take place, resulting in a less polymer loss compared to  $\text{SiO}_2$ . This in turn results in a thicker polymer layer on silicon than on  $\text{SiO}_2$ . The interface reactions of polymer on  $\text{Si}_3\text{N}_4$  forming, for example, CNF, removes carbon at a rate that is intermediate between  $\text{SiO}_2$  and silicon, producing a polymer layer that is also intermediate in thickness. [29]

#### **1.4. Plasma Etching Challenges**

High fidelity pattern transfer into semiconductor, metal and dielectric materials is critical to the fabrication of microelectronics devices that now have characteristic feature sizes of < 10 nm. [32–34] Plasma etching has long been an essential tool that has enabled the economic scaling of pattern transfer as device scales continue to shrink. [35] Along with this aggressive scaling of transistor size comes significant challenges for plasma etching. [36]

As aspect ratios of features increase with scaling, and 3-dimensional (3d) features become more common, it is imperative that many etch processes are able to process features with different aspect ratios simultaneously. For this to be possible the etch rate of the process must be

independent of aspect ratio. Unfortunately, the difference in transport methods between reactive radical species and ions results in ARDE for many processes. This occurs due to the synergistic relationship between the neutral and ion fluxes, as discussed in Chapter 1.3.2. The most easily observable result of ARDE is that etching features with different width, or critical dimension (CD), simultaneously results in larger features etching faster than smaller ones, as shown in Fig. 1.12. [37] The reason for this trend is that for the same etch time the smaller etch features will reach a higher AR than the smaller ones, reducing the flux of reactive radical species to the etch front.

Obtaining uniform etch rates across the entire wafer is another issue which has challenged engineers throughout the history of plasma etching. This is particularly true as wafer sizes increase over time to reduce fabrication costs. As transistors are scaled down, some films which must be etched become very thin. In other applications, the aspect ratio is very high, and etch times are long. For both of these extremes it is very important that the etch process be very uniform across the wafer. There are several sources of non-uniform etching, some originating in the plasma, and some on the wafer itself, as depicted in Fig. 1.13.[38] Techniques to increase the uniformity of processes which originate in the plasma have been developed, but typically increase the complexity of the etching hardware or process.[39–41] Recently the self-limited process referred to as atomic layer etching (ALE) has been proposed as a method for increasing uniformity. This application will be discussed in detail in Chapter 6.

During plasma etching, exposing the wafer to high energy ions can result in damage to the underlying crystal lattice, often affecting device performance.[42,43] Minimizing this plasma damage is an important challenge. Minimizing ion energy can reduce plasma damage, as can increasing the neutral to ion ratio and avoiding reactive ions (eg.  $\text{Cl}^+$ ).[44] Atomic layer

etching can also possibly reduce the plasma damage in many applications, by reducing ion energy and eliminating (or minimizing) reactive ion fluxes. This will be discussed in detail in Chapter. 5.

### **1.5. Feature Scale Modeling**

Modeling of physical processes is important in many fields. Accurate modeling can provide insights into physical mechanisms which are difficult to isolate in experiment. Well validated models can be used in many cases to replace expensive experiments. Modeling of the plasma etching process, at different scales and levels of physical detail, has been used extensively over the history of plasma etching. In this thesis, a new model of the etching of SiO<sub>2</sub> in fluorocarbon gas plasmas will be introduced, so a review of previously published etch models will focus on that topic.

Several methods have been used previously to predict fluorocarbon plasma etching behavior. Atomistic simulations, including density functional theory[20], quantum chemical molecular dynamics[45,46] and classical molecular dynamics[47,48] have been used to explore reaction mechanisms and pathways. These atomistic techniques can incorporate very detailed physics, but they are challenged at resolving large enough simulation domains to predict feature scale etch evolution with current techniques and computing hardware.

Kinetic models of the SiO<sub>2</sub> etching process have been developed which can describe the polymer coverage and etch rates for various plasma conditions.[49,50] Such models allow for the etch yield, as well as source and loss terms for polymer deposition/etching, to depend on the polymer thickness, as has been seen experimentally. While kinetic models can accurately describe the etching mechanisms for a single set of plasma conditions, these conditions can vary within a typical etch feature, which in turn requires feature scale modeling to resolve.

To predict the evolution of an etch feature, a model should include transport of reactive species through the feature and position dependent etch rates. Current feature scale models typically rely on either the level-set technique or cell based methods. Level set methods are used to track the propagation of the etch or deposition front (that is, the top surface of the material) in the presence of a locally varying forcing function which represents the rate of material removal (etching) or addition (deposition).[51] In plasma etch modeling, the local rate of etch front propagation typically depends on the ratio of neutral to ion fluxes. This technique has been used to model the etching of silicon with a pulsed Bosch process using two simultaneously propagating level sets to track the passivation front separately from the underlying silicon.[52] Etching of SiO<sub>2</sub> in fluorocarbon plasma was modeled by Shimada et al. using a single level set to track the etch front propagation.[53] In this case, the polymer thickness was tracked separately for each point on the etch surface and etch rate depended on the local polymer thickness.

Cellular models divide the simulation domain into a computational grid where each cell or voxel represents the material of that region of space. Individual computational cells can represent a single material or be fractionally filled by different material species which aids in smoothing statistical noise.[54] Fractional filling of cells can also be used to resolve some of the kinetics of the mixing layer. The ratio and number of these species in a single cell then determine the reaction probability for incoming pseudoparticles representing the plasma produced fluxes. This technique was used by Guo et al. to study Cl<sub>2</sub> plasma etching of silicon and Ar/C<sub>4</sub>F<sub>8</sub> plasma etching of SiO<sub>2</sub>. [55,56] Cellular models have also been employed to study oxide etching in three dimensional features.[57]

Cellular models have also been used to represent ion implantation into the substrate. For example, Osano and Ono tracked the implantation of Cl<sup>+</sup> and O<sup>+</sup> ions into silicon using Monte-

Carlo techniques. [58–60] The distribution of implanted reactants was then used to obtain chemical sputtering probabilities which depended on the local density of implanted species. Takagi et al. used a more continuous approximation to study the effect of ion energy loss in a polymer layer while etching SiO<sub>2</sub>. [61,62] In this model, the polymer thickness was determined by local (position dependent) radical fluxes. The polymer thickness was then used to calculate a local etch rate based on an analytical slowing of ions in the polymer.

### **1.5.1. Goals for Feature Scale Modeling**

There are several possible goals for a model of the evolution of feature profiles during plasma etching. Depending on the specific goal being targeted, one model may be more advantageous than another. Possible goals for feature scale modeling include:

1. Process design and optimization.
2. Process control / feedback.
3. Access to operating conditions inaccessible to experiments.
4. Determine physical mechanisms responsible for observed behavior.

The first two goals, process design and control, are very important to the use of feature scale modeling in industry. Process control, in particular, is an interesting topic and worthy of future investigation. In the photolithography field, computational electrodynamics modeling is frequently used to simulate the lithography process. An inverse model is then employed to correct for imperfections in the final projected image by making changes the mask used. [63] Similar techniques may be possible using an etch model, incorporating corrections for etch imperfections in the original design, as depicted in Fig. 1.14. [64] In order to effectively meet these goals, the model must be well validated, requiring access to large amounts of experimental data. This access is difficult for academic purposes, as many of the processes being developed are trade secrets.

Being able to explore operating conditions inaccessible to experiments, and determining physical mechanism responsible for observed etching phenomenon require that the model incorporate a very complete set of physics. Reduced models (those incorporating less physics) often perform well within a well calibrated range, but may be less reliable outside of this range. On the other hand, a model constructed with every effort to capture a complete picture of the physics involved can be more successful at predicting behavior outside of its calibrated range. The models described here have been designed with this latter goal in mind. Every effort has been made to incorporate all relevant physical processes into the model, with the goal of creating a model which is useful for the study of physical mechanisms in technologically relevant etching processes.

## **1.6. Summary**

Plasma etching is critical to the semiconductor industry, and feature scale modeling can play an important role in expanding our understanding of this process. The interactions between the plasma and the etching surface are complex, with strongly coupled effects from reactive neutral species and energetic ions. Modeling this process requires a detailed representation of the physics inside the gas phase plasma, reactions on the surface and transport of reactive species through the feature. In this thesis, a model will be developed describing these processes. This model is then used to better understand several physical mechanisms affecting the plasma etching of modern semiconductor devices.

In Chapter 2 a detailed description of the model will be given. A brief review of the model used here to predict gas phase plasma behavior, the Hybrid Plasma Equipment Model (HPEM) will be given. A complete description of the Monte Carlo Feature Profile Model will then be given, including details on the newly developed models for ion implantation, neutral

diffusion through solids and the surface diffusion of physisorbed species. An overview of the code structure and parallelism techniques is presented, as well as an overview of recent validation efforts.

Chapter 3 describes the surface reaction mechanisms developed for use with the MCFPM. A previously reported model for Ar/Cl<sub>2</sub> etching of silicon was expanded to include physical sputtering pathways for passivated species at higher energy. A fluorocarbon etch mechanism for SiO<sub>2</sub>, Si<sub>3</sub>N<sub>4</sub> and silicon is also presented. This reaction mechanism utilizes the new implant and diffusion capabilities of the MCFPM to simulate the effect of ions and radicals transporting through the polymer overlayer.

The physical mechanisms involved in aspect ratio dependent etching are discussed in Chapter 4. Particularly, the effect of neutral transport is discussed in detail. The results of this study indicate that the onset of ARDE can be postponed to higher aspect ratios if the neutral flux is high enough to saturate the passivation. Doing so also results in more tapered features and a propensity to form micro-trenches. The implications of ARDE on 3d structures are also discussed. The results indicate that 3d features complicate the concept of an aspect ratio, as no single critical dimension can be defined. Instead, 3d features must be thought of as having a range of effective aspect ratios, depending on position in the feature.

The atomic layer etching (ALE) technique is introduced and discussed in Chapter 5. This chapter focuses on the ALE of silicon using a chlorine containing plasma for passivation. An ideal ALE mechanism is developed and compared to typical non-ideal fluxes originating from an inductively coupled plasma reactor. The results indicate that the presence of non-ideal fluxes that introduce continuous etching during either etching phase, re-introduces ARDE and causes surface roughening. These issues were not observed in the ideal model. The ALE model was

also used to demonstrate the ability to clear high aspect ratio gate etch features with reduced over-etch when compared to continuous etching.

The use of ALE to improve wafer scale uniformity of plasma processing is discussed in Chapter 6. It was found that fully saturated ALE reactions can dramatically reduce the dependence of etch rate on the local ion flux, improving wafer scale uniformity. Without over-saturation of the ALE surface reactions, the improvement in etch uniformity is reduced. This over-saturation is only achieved by exposing the etch feature to a much larger total fluence of ions than a comparable continuous etch, which may cause undesirable effects in some applications.

The use of fluorocarbon containing plasma for the passivation phase of ALE of  $\text{SiO}_2$  is discussed in Chapter 7. The selectivity of the etch mechanism to  $\text{SiO}_2$  over  $\text{Si}_3\text{N}_4$  is discussed. The results indicate that the polymer overlayer thickness is critical to the selectivity of the etch process. This polymer deposition process is continuous, so when used for ALE this introduces non-self-limited behavior. The etch per cycle was found to depend on the polymer thickness, coupling the passivation time to the etch rate, which is undesirable in an ALE process. The use of ALE does provide a window where infinite selectivity to  $\text{SiO}_2$  over  $\text{Si}_3\text{N}_4$  is achievable in the steady state. Because this selectivity depends on the polymer overlayer, and the polymer overlay must develop over several cycles, there is a transient period at the beginning of etching where the selectivity is less than the steady state value. The use of this fluorocarbon ALE is applied to the application of etching self-aligned contacts. The results indicate that careful tuning of the ALE process is required to balance the loss of  $\text{Si}_3\text{N}_4$  mask material with the CD loss during etching.

A final summary of this work, a description of possible future works and concluding remarks are given in Chapter 8.

## 1.7. Figures

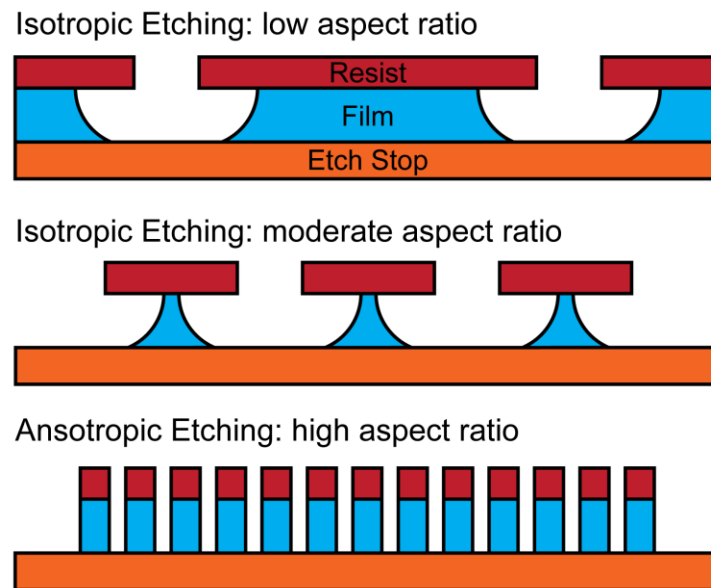


Fig. 1.1 Comparison of isotropic and anisotropic etching. Low aspect ratio features can be etched adequately by isotropic etching, while high aspect ratio features require an anisotropic etch profile.

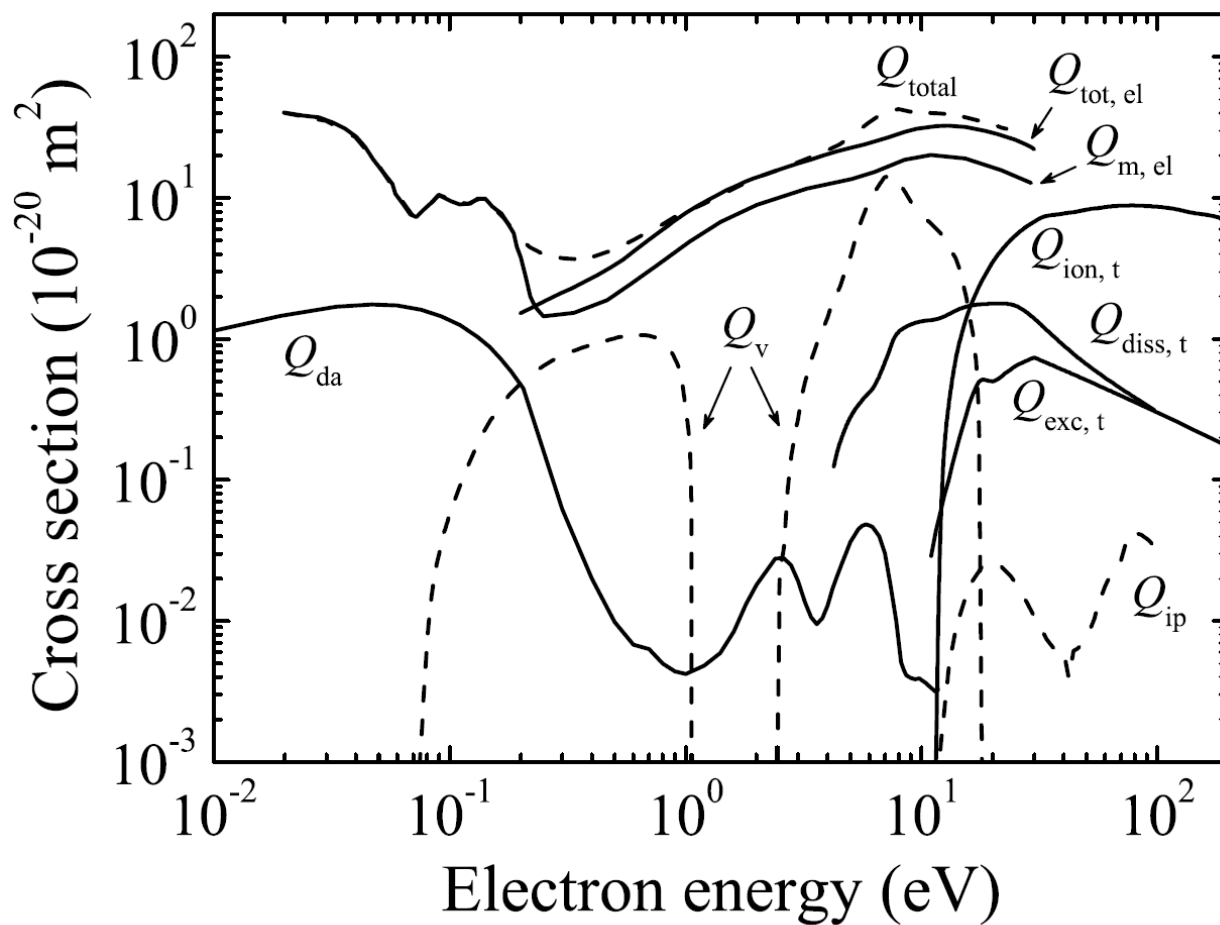


Fig. 1.2 Electron – Cl<sub>2</sub> collision cross section set. Cross sections for dissociative attachment ( $Q_{da}$ ), vibrational excitation ( $Q_v$ ), ion pair formation ( $Q_{ip}$ ), electronic excitation ( $Q_{exc}$ ), direct dissociation ( $Q_{diss}$ ), ionization ( $Q_{ion}$ ) and momentum transfer ( $Q_m$ ). Reproduced from Gregório et al..[9]

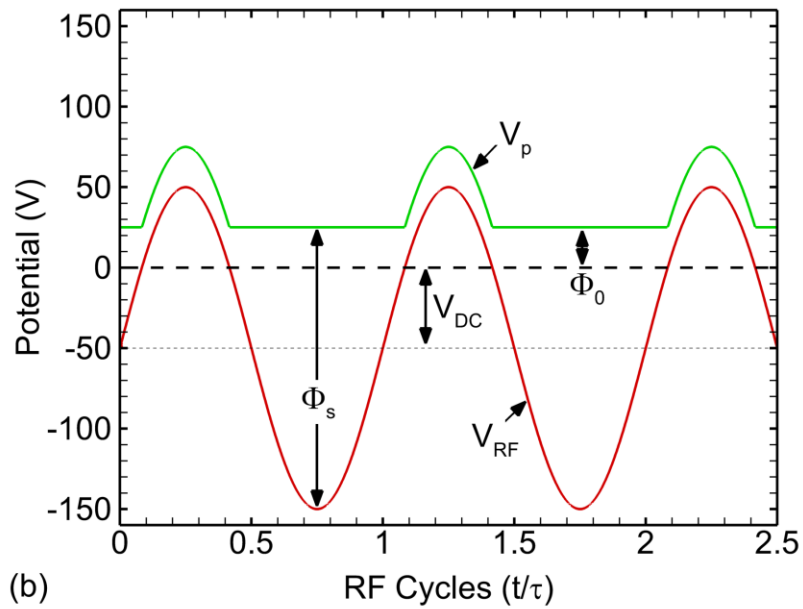
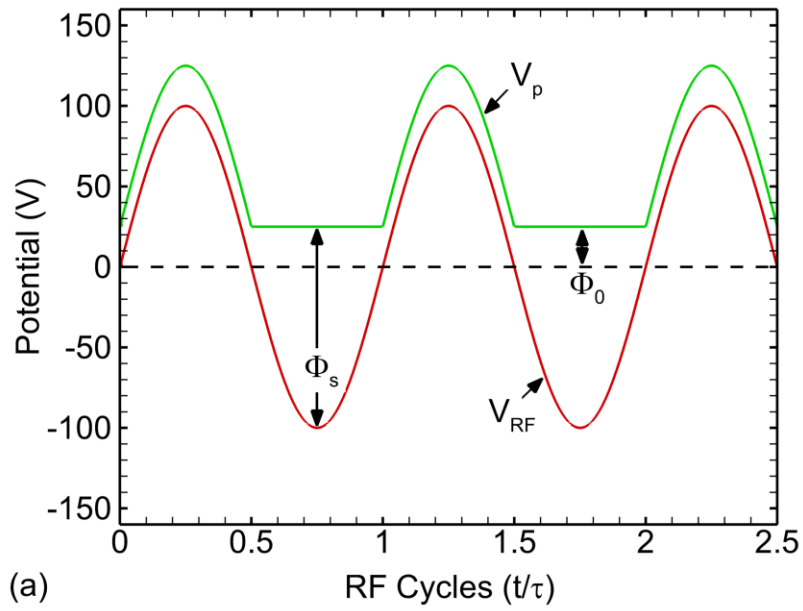


Fig. 1.3 Schematic example of the effect of applying a RF bias to a wafer in a (a) symmetric and (b) asymmetric reactors.

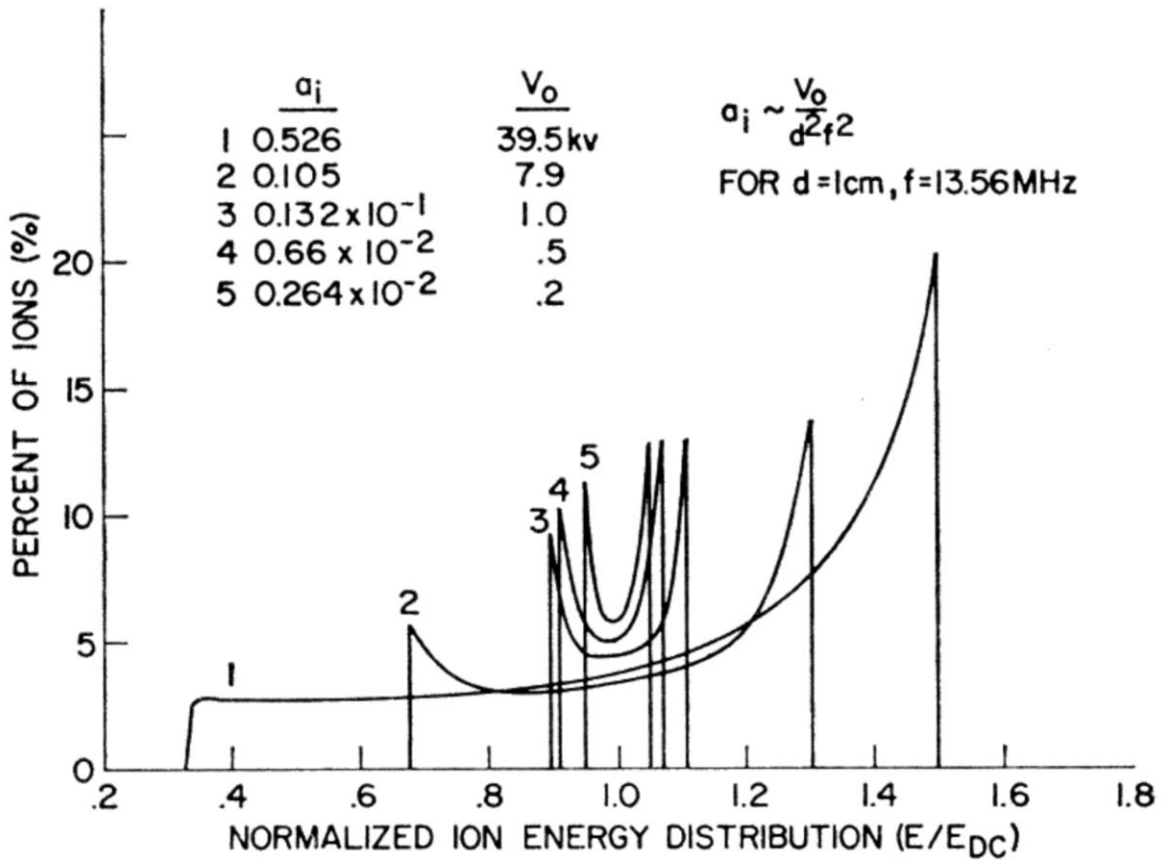


Fig. 1.4 Ion energy distributions for different values of  $\tau_{ion}/\tau_{rf}$ . The curve marked 1 is the lowest  $\tau_{ion}/\tau_{rf}$  and 5 is the highest. The lack of a low frequency peak is due to an assumption that the sheath width is constant, and is not typical of experiment. Reproduced from Tsui.[11]

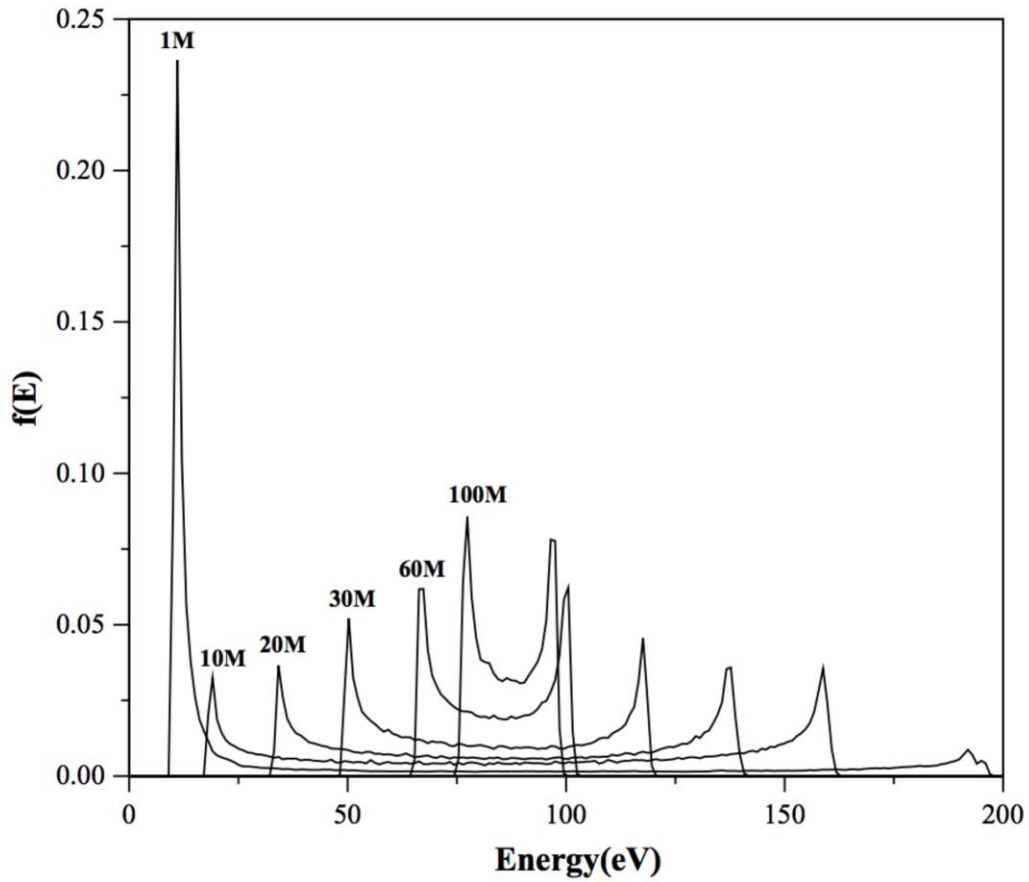


Fig. 1.5 Ion energy distribution function for several values of RF frequency. Lower frequency results in wider bi-modal distributions, while higher frequencies converge on a single peak distribution. Reproduced from Kawamura et al.[10]

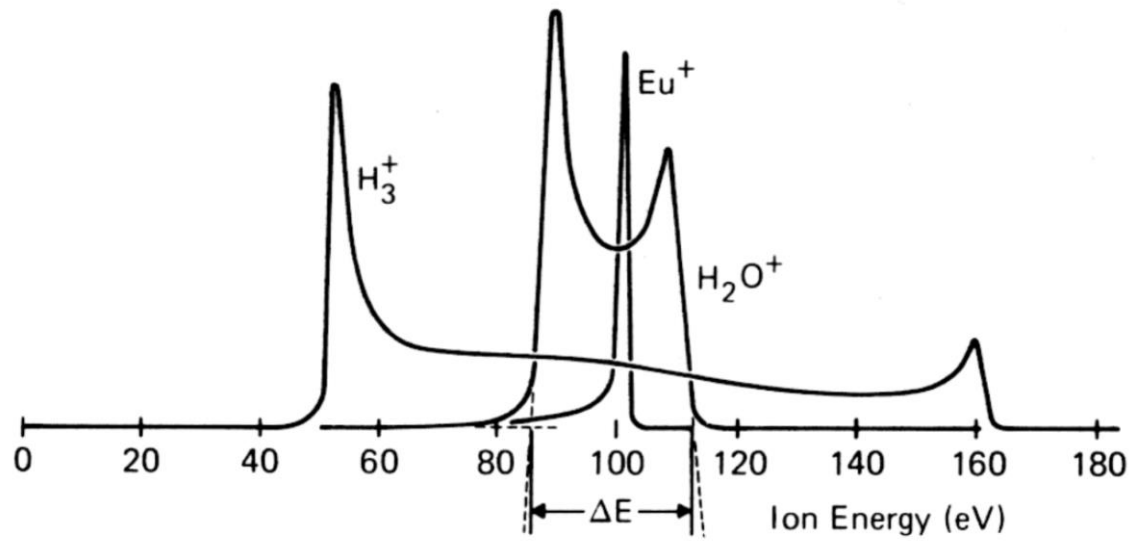


Fig. 1.6 Ion energy distribution for several ions with different masses. Reproduced from Coburn and Kay.[12]

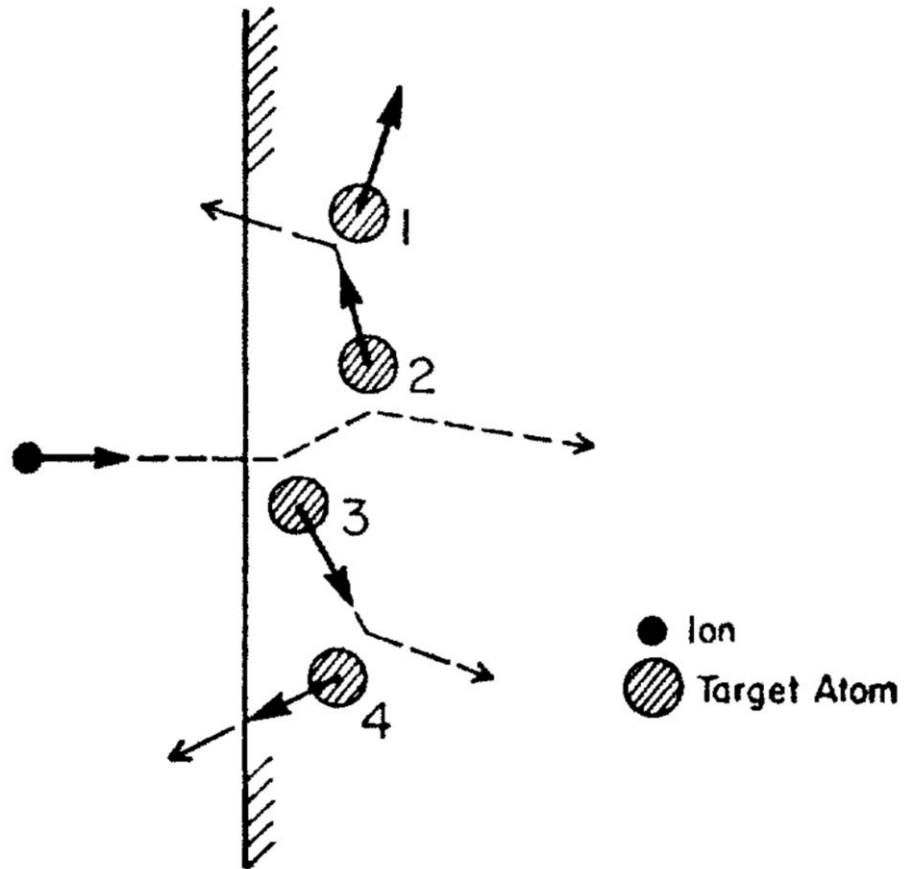


Fig. 1.7 Two different three body collision cascades which result in sputtering. Target atom 2 undergoes a collision with the incoming ion, then a second collision with target atom 1 before being ejected from the solid. Target atom 3 undergoes a collision with the incoming ion, then transfers (some of) the kinetic energy from the ion collision to atom 4, which is ejected from the solid. Reproduced from Sigmund.[13]

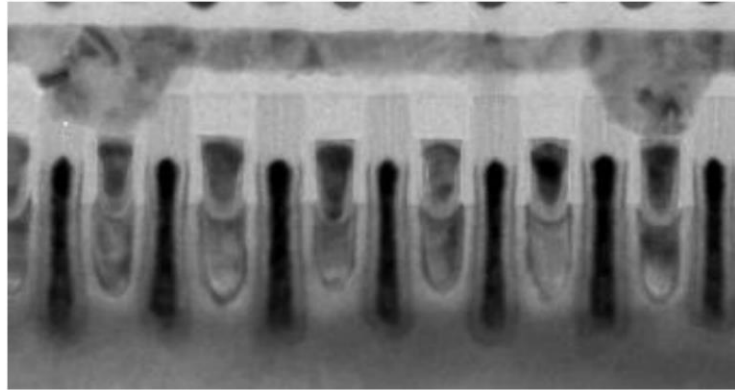
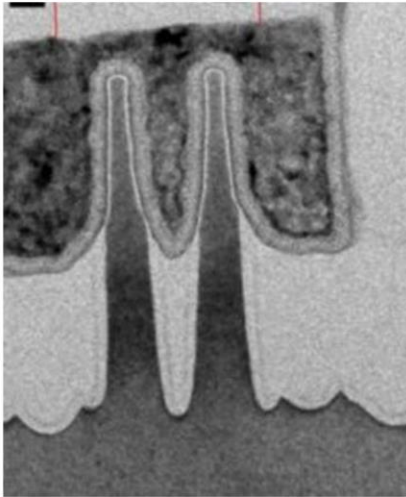


Fig. 1.8 Two cross sectional scanning electron microscope images of the gate structure in Intel's 10 nm process. In order to take these images, the transistors were cut using focused ion beam milling to expose the cross-sectional view. Reproduced from Auth et al..[65]

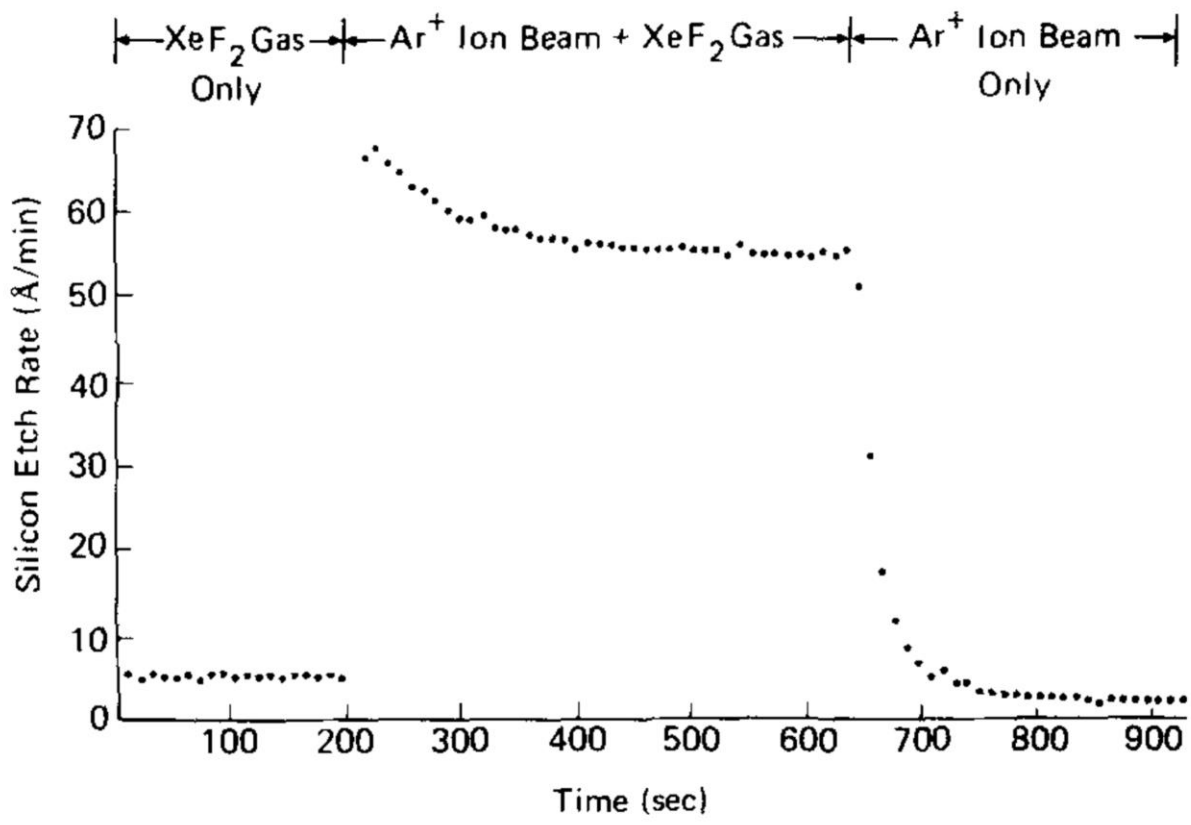


Fig. 1.9 Etch rate of silicon exposed to XeF<sub>2</sub> only, XeF<sub>2</sub>/Ar<sup>+</sup> and Ar<sup>+</sup> only. The dramatic increase in etch rate when XeF<sub>2</sub> is combined with Ar<sup>+</sup> exposure is due to the reduced surface binding energy of fluorinated silicon. Reproduced from Coburn and Winters.[21]

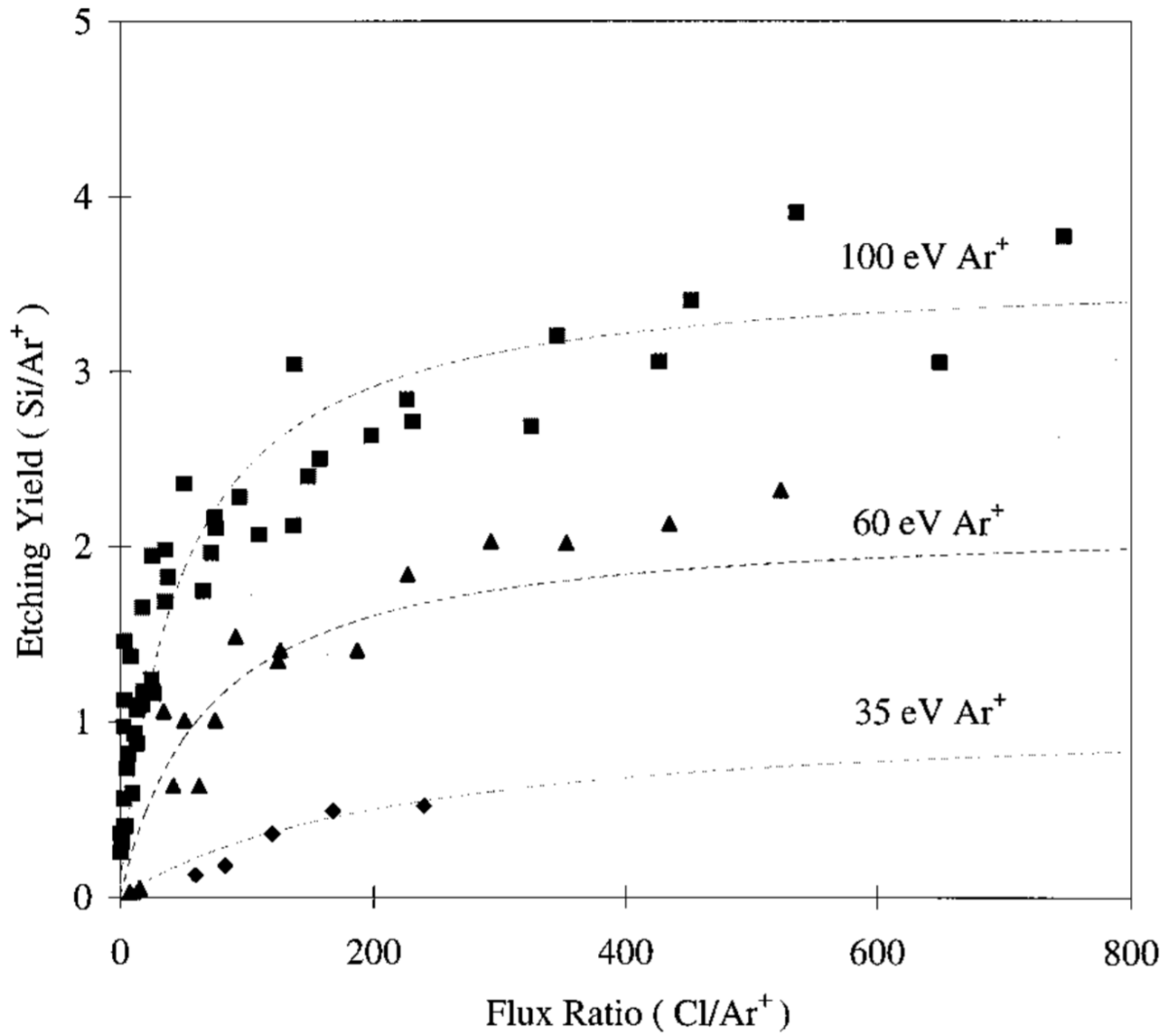


Fig. 1.10 Etch yield per Ar<sup>+</sup> ion as a function of  $\Gamma_n/\Gamma_i$  (Cl/Ar<sup>+</sup>). The etching yield increases rapidly for low  $\Gamma_n/\Gamma_i$  and saturates when the reaction becomes ion starved. Reproduced from Chang et al.[22]

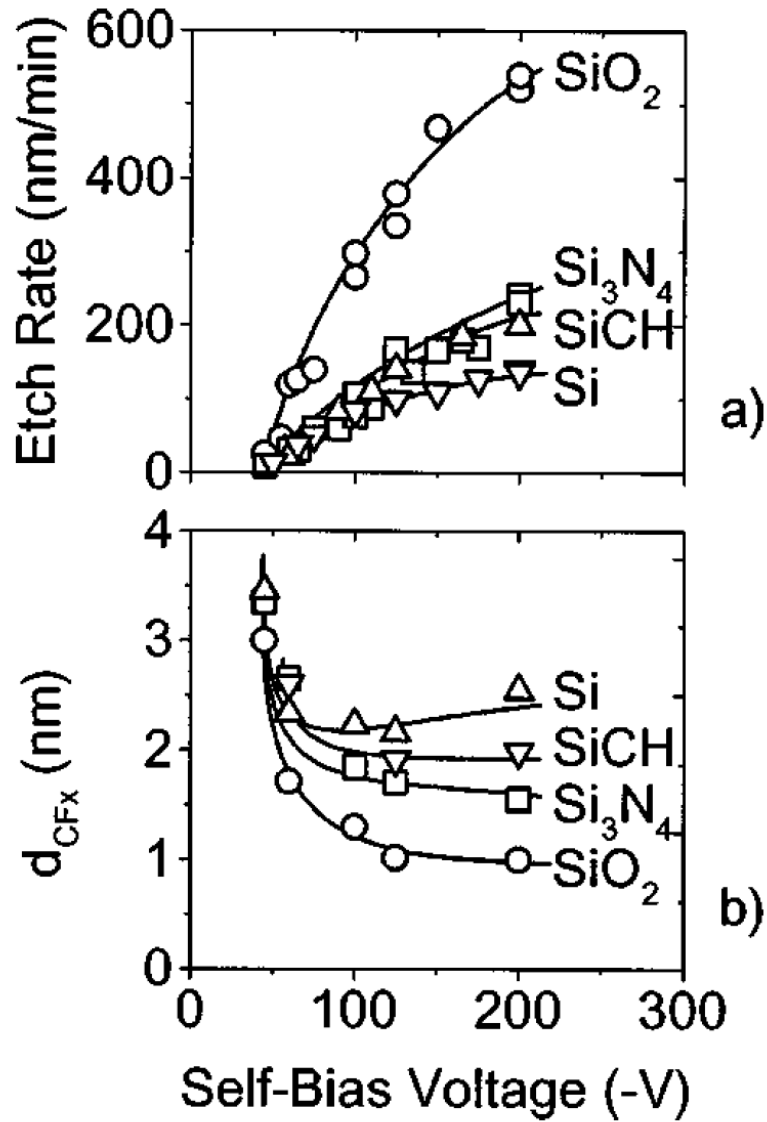


Fig. 1.11 (a) Etch rate and (b) steady state polymer thickness ( $d_{\text{CFx}}$ ) as a function of self-bias voltage for several different materials. Reproduced from Standaert et al. [30]

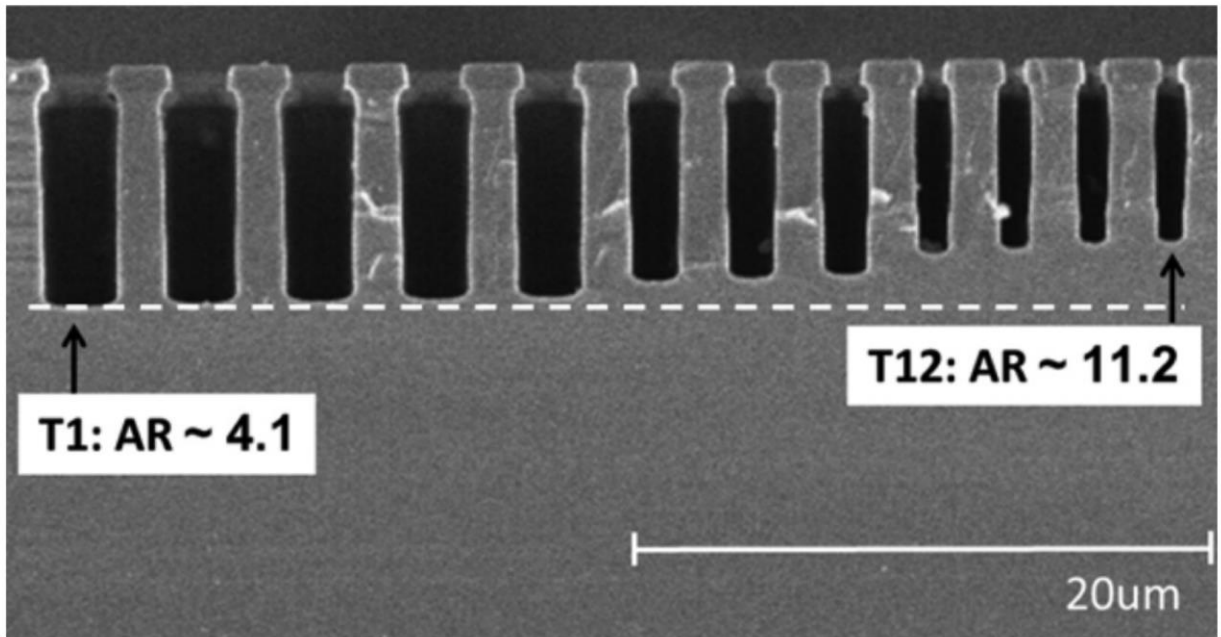


Fig. 1.12 Features with different critical dimensions etched simultaneously. Notice larger features etch faster than smaller ones. Reproduced from Bates et al.[37]

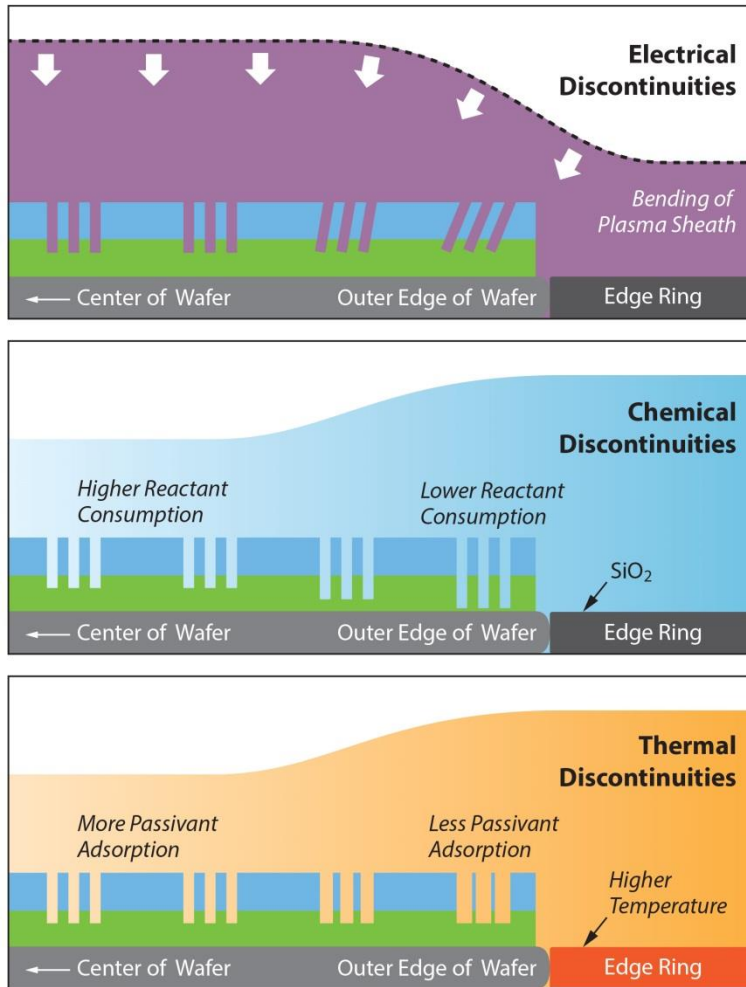


Fig. 1.13 Sources of wafer scale non-uniformity. Reproduced from Hwang and Kanarik.[37]

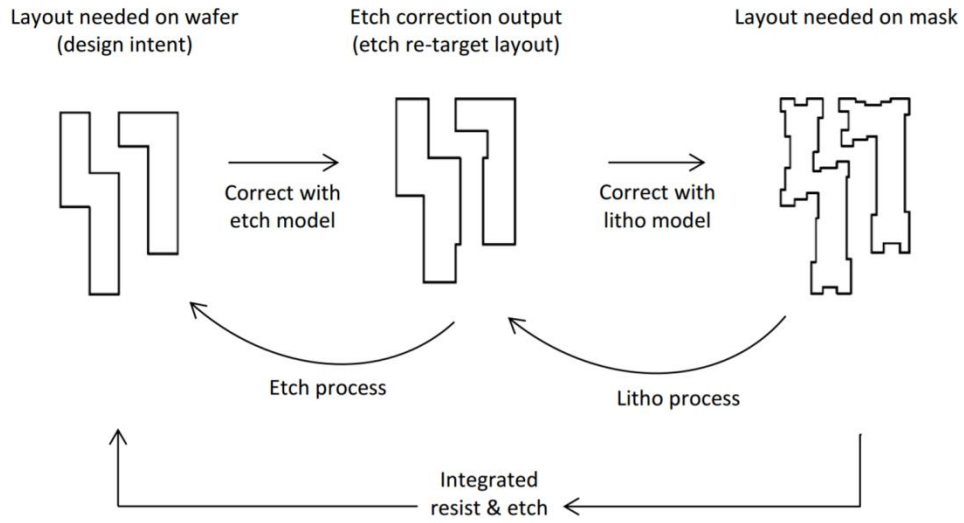


Fig. 1.14 Schematic of incorporating the etch model into the mask design phase. Using the etch model in this way may enable the correction of etch imperfections which cannot otherwise be resolved. Reproduced from Zavyalova et al.[64]

## **Chapter 2 DESCRIPTION OF MODELS**

### **2.1. Overview of Monte Carlo Feature Profile Model (MCFPM)**

The MCFPM uses statistical methods to simulate the progression of etch features when exposed to plasma conditions. The model uses a cubic mesh of computational cells, each representing either a solid material or gas, to represent the etch feature. This mesh can be initialized in an arbitrary initial condition, which may include multiple materials and features within the etch domain. This allows the simulation of complex steps in the fabrication process, such as the gate etch during finFET fabrication. This etch step, discussed in detail in Chapter 4, must etch poly-silicon masked by a photoresist (or hard-mask), from around and in-between existing fin structures. The ability to simulate specific, industry-relevant etch processes with accurate physical models is of great interest as etch processes begin to be limiting steps in yield optimization.

The basic MCFPM algorithm, launches pseudo-particles at the initial material mesh and tracks the interactions of these particles with the mesh using Monte-Carlo techniques. The statistics of the incoming fluxes of pseudo-particles are often derived from a reactor scale plasma model, such as the HPEM described in Chapter 2.2, but they may also be user defined to represent arbitrary conditions. This allows the MCFPM to be used to explore the coupling of plasma reactor parameters with the etch result, or to be used for studies of more fundamental questions regarding the etch process by decoupling the incoming flux statistics from a physical plasma model. This versatility makes the MCFPM a strong tool for process development and optimization, as well as general scientific exploration of the physics of plasma etching.

In this chapter, all of the models used for the work presented in this thesis will be discussed. The HPEM, which is used as a reactor scale plasma model for many of the studies presented here, is described in Chapter 2.2. The remaining sections are devoted to describing the MCFPM. A description of the 3-d mesh used in the MCFPM, and the derivation of simulation time is provided in Chapters 2.3 and 2.4. The behavior of gas phase pseudo-particles is described in Chapter 2.5. The types and probabilities of surface reactions are described in Chapter 2.6, and the layout of the code is presented in Chapter 2.8. Finally, two different validation efforts are presented in Chapter 2.8.

## **2.2. Reactor Scale Modeling**

All reactor scale modeling presented in this thesis was done using the Hybrid Plasma Equipment Model (HPEM). The HPEM is thus named because it uses a hybrid time slicing technique to solve all relevant plasma equations, in 2-dimensions, self-consistently by addressing each physical process on a different timescale relevant to that process.[66] This model has been discussed in detail before,[67] and will only be introduced here in the context of generating self-consistent realistic etching conditions for use in the MCFPM.

The HPEM uses several computational modules, each of which address a different aspect of the plasma physics at its own relevant timescale. The electromagnetic module (EMM) solves Maxwell's equations for the time varying fields in the plasma reactor due to RF current in the inductively coupled antenna. The fluid kinetics module (FKM) solve continuity, momentum and energy equations for ions and neutral species separately using a multi-fluid approach. The FKM also solves the Poisson equation for the potential due to the position dependent charge density in the gas phase and on surfaces. Using the electromagnetic and electrostatic fields calculated in the EMM and FKM, the electron energy transport module (EETM) solves the Boltzmann

equation for electron transport and energy kinetically using Monte-Carlo techniques. Electron impact reaction rates are calculated by integrating the self-consistently solved electron energy distribution with a database of electron impact reaction cross-sections for all species in the gas phase chemistry. The resulting electron impact source functions are used by the FKM as source and loss terms. This loop is iterated until a self-consistent answer is achieved. The resulting 2-d profiles of species densities, potentials, fields and temperatures represent a self-consistent picture of the plasma physics in the reactor.

As part of this self-consistent calculation, the HPEM must address fluxes to the reactor walls and the composition of the species returning to the plasma. This can be done with different levels of detail within the HPEM. The simplest approach is to assign fixed reactive sticking coefficients for each gas species on each surface material. This allows for simple surface reactions, such as neutralization of ions or recombination of radical O to form O<sub>2</sub> molecules, but only with fixed probabilities that are uniform throughout the reactor. In a real system, many sticking coefficients will be dependent on the local plasma properties, which vary throughout the reactor. When these effects become important the HPEM can address the non-uniform surface reactions using the Surface Kinetics Model (SKM). In this model, a simple reaction mechanism, similar to that used by the MCFPM, is evaluated using a surface-site-balance kinetic model at each surface mesh point.[68,69] This allows the plasma to change the reactor surface conditions over longer timescales, with the reactive sticking coefficients of each species changing with position in the reactor and simulation time. Both of these techniques result in a position dependent measurement of the flux of each gas phase species to the wafer, which is output from the HPEM for use in the MCFPM.

In order to accurately simulate the plasma surface interactions using the MCFPM, we need both the flux of each reactive species, as well as the energy and angular distributions of energetic species. The fluxes of each reactive species are a direct product of the FKM, but the energy distribution is solved separately using the Plasma Chemistry Monte Carlo Module (PCMCM). This module initializes ion pseudo-particles based on electron impact sources functions derived from the EETM and FKM, and propagates them through time using the phase resolved fields and species densities from the EMM and FKM. All collisions accounted for in the plasma chemistry reaction mechanism are included in the Monte Carlo simulation. Some of these particles will make it to the wafer, after being accelerated through the sheath region. The energy and angle of incidence of these particles are recorded, and a statistical distribution is accumulated. This energy and angular distribution (EAD) is output from the HPEM for use in the MCFPM.

With the position dependent fluxes of reactive species from the FKM and the energetic particle distributions from the PCMCM, the plasma conditions relevant to etching can be fully described. The MCFPM accepts these conditions as user input. The EAD output file from the HPEM is read directly by the MCFPM. The values in the EAD file are organized into energy and angle bins, and have units of  $\text{cm}^{-2} \text{s}^{-1} \text{steradian}^{-1} \text{eV}^{-1}$ . Therefore, if integrated for all angles and energies, the resulting value is the average flux of that species on the wafer in units of  $\text{cm}^{-2} \text{s}^{-1}$ . This average value may be accurate if the plasma conditions are very uniform across the wafer, but in many systems the non-uniformity is large enough significantly affect the etch process, as discussed in detail in Chapter 6. In this case the average value of the fluxes does not well represent any specific point on the wafer. Because of this the standard practice is to use values of fluxes measured from the output of the FKM, not the values embedded in the EAD file.

### 2.3. 3D Mesh

The MCFPM discretizes 3D space into a cubic lattice of computational cells. The size of the computational cell determines many aspects of the model behavior. Because the only supported lattice is cubic, the size of each cell is identical in all three dimensions,

$$\Delta x = \Delta y = \Delta z, \quad (2.1)$$

where  $\Delta x$  is the size of the cell in the  $x$  dimension. The choice of  $\Delta x$  has several implications on the model behavior. Most obvious is model resolution; the MCFPM cannot resolve features smaller than several times  $\Delta x$ . Another consideration is computational overhead. Assuming a given feature size must be simulated, choosing a smaller  $\Delta x$  results in an increase in memory and computational runtime requirements as approximately  $O(n^3)$ , where  $n$  is the number of cells per side in the simulation domain (assuming a cubic domain). The choice of  $\Delta x$  also affects the time weighting of each pseudo-particle, as described in Chapter 2.4.

Each cell in the mesh is assigned a material property. The materials used within the MCFPM are user defined, and can be elements or compounds (i.e. Si, SiCl, SiCl<sub>2</sub>, etc.). For most etching reactions, it is important to respect stoichiometry, and most materials are defined as elements or compounds to facilitate this, but there is no inherent limitation on the material properties in the MCFPM. Because of this, arbitrary materials can be adopted which usually model a material which is difficult to treat stoichiometrically. An example of an arbitrary material definition is “Resist”, which is used to represent polymers photo-resists used for patterning. These resists can have varying material properties and chemistries, and it is not always possible or necessary to capture their stoichiometry accurately.

By default, the MCFPM assigns a single material to each cell. Each solid cell in the mesh is assumed to have the same atomic density,  $\rho \text{ cm}^{-3}$ , which is a user input. This density is used to calculate number of atoms per cell

$$N_s = D x^3 r. \quad (2.2)$$

Typical values of  $\rho$  range from  $5.0 \times 10^{22} \text{ cm}^{-3}$  for silicon to  $2.3 \times 10^{22} \text{ cm}^{-3}$  for  $\text{SiO}_2$ . Because all cells contain a single (usually stoichiometric) material, but are represented as having the same volume and density, it is important to remember that all materials in the MCFPM represent average behaviors of their respective compounds. Despite being able to address atomic scale meshes, there is no attempt to calculate inter-atomic potentials, which precludes modeling effects like surface reconstruction or steric repulsion.

#### 2.4. Simulation Time / Pulsing

An important aspect of accurate simulation of profile evolution, particularly for pulsed systems such as ALE, is the rigorous representation of physical time in the simulation. In the MCFPM this is performed by assigning each incoming pseudo-particle a time weight of

$$\Delta t = \frac{N_s}{\Gamma_t A}, \quad (2.3)$$

where  $N_s$  is the number of atoms per solid computational cell (Eqn. 2.2),  $\Gamma_t$  is the total flux of all gas phase species entering the feature ( $\text{cm}^{-2} \text{ s}^{-1}$ ) and  $A$  is the area through which the flux is launched into the computational domain. Scaling the time weighting of each pseudo-particle by  $N_s$  in Eqn. (2.3) is required to enable gas phase particles to react stoichiometrically with solid cells having non-unity numbers of atoms per cell.

The concept of assigning each pseudo-particle an equal time is necessary to ensure that the number of particles delivered per square centimeter per second of simulation time is exactly

the user defined flux,  $\Gamma_f$ . This is similar to the *N-fold way* (NFW) used in Kinetic Monte Carlo (KMC) simulations[70], with **two additional assumptions**:

- A1. A particle entering the feature is a *rare event*. This implies that all of the effects each particle has on the feature are instantaneous compared to the time between incoming particles.
- A2. The number of total particles (not pseudo-particles) entering the feature per square centimeter per second of simulation time is **exactly**  $\Gamma_f$ .

These assumptions allow us to construct a KMC simulation where there is only one possible event; the release of a pseudo-particle. In this construct, the time between each event becomes uniform and is given exactly by Eqn. 2.3. This allows the model to treat each pseudo-particle, and its effects on the profile mesh, as independent and non-interacting. When a particle generates multiple changes to the profile mesh (for instance an ion sputters a material from the bottom of the feature, and the sputtered etch product subsequently sticks to the wall before escaping the feature) the entire cascade of mesh changes can be handled without updating the simulation time. Only the release of new particles results in an update of the simulation clock.

To support the validity of these assumptions, we will look at worst case scenarios which may occur during typical simulations. For assumption A1 to be valid, the time a particle spends interacting with a feature must be small when compared with  $\Delta t$ . A worst-case example may occur when a neutral particle impinges on a high aspect ratio feature. In this case, the particle may interact with the walls many times before finally reacting or being released back into the bulk gas. Take, as a specific example, a circular via with a depth of 3  $\mu\text{m}$  and a radius of 30 nm (aspect ratio of 50), represented as a 3000 $\times$ 120 $\times$ 120 cell mesh ( $\Delta x = 1$  nm). Assuming a neutral particle might travel a total distance of 5 times the depth of the feature, at a thermal speed of 350 m/s (approximately that of  $\text{CF}_2$ ), the particle will spend  $< 5 \times 10^{-8}$  s in the feature. If we assume a

total flux of  $5 \times 10^{18} \text{ cm}^{-2} \text{ s}^{-1}$ , and  $\rho = 2.3 \times 10^{22} \text{ cm}^{-3}$  we have a  $\Delta t > 4 \times 10^{-7} \text{ s}$ , almost ten times longer than the particle residence time.

The  $\Delta t$  calculated for the example above is based on the pseudo-particle atomic weighting,  $N_s$ , from Eqn. 2.3. In the limit where  $N_s$  goes to 1 (each pseudo-particle represents one atom), the  $\Delta t$  shrinks to  $2 \times 10^{-8} \text{ s}$ , for the same example. This implies that, on average, between two and three atoms may be in the feature at any given time. While this means that multiple particles can be interacting with the feature at the same time, as long as they are dilute enough that the particles do not interact with each other directly (through collisions) or indirectly (by changing a mesh cell which a simultaneous particle then interacts with) then the result will be the same. This implies that A1 can be relaxed to assuming that the particles do not interact with each other, only the mesh. Given that the example feature has a volume of  $8 \times 10^6 \text{ nm}^3$  and relevant radicals have van der waals radii in the neighborhood of 0.2 nm, the assumption of non-interacting particles seems to be appropriate, even in this worst-case scenario.

In the physical etching system, we would expect the time between particles to be Poisson distributed. The choice to use a fixed  $\Delta t$  is made possible by assumption A2, assuming the particles per unit time is exactly the user defined total flux. Because the etch system is probed as a function of time, not number of particles, the only error which could come from this assumption would be if a different number of particles impinged on the system in a Poisson distributed model than in the fixed  $\Delta t$  model. The standard deviation of the number of particles per unit time goes as  $n^{1/2}$ , where  $n$  is the mean number of particles in that period of time. If, for example, we have a 5 s etch time (very small) using a total flux of  $1 \times 10^{18} \text{ cm}^{-2} \text{ s}^{-2}$  and a simulation area of  $100 \times 100 \text{ nm}$ , the total number of particles in the fixed  $\Delta t$  model would be  $5 \times 10^8$ . In the Poisson distributed model, the number of particles in this same time would be

$5.0 \times 10^8 \pm 2.2 \times 10^4$  particles. The difference between the two is less than one in 20,000. This source of error is not expected to have any impact on the simulation.

While the  $\Delta t$  is fixed in any given simulation, the time interval between launching a particle of a particular species, whose total number of particles may be a small fraction of the total, is purely statistical and Poisson distributed. In complex gas mixtures, there may be ten or more different radical and ion species whose fluxes may differ by factors of 100 or more. For the species with low fluxes, there may be a statistically different number of particles of that species launched into the computational domain during each pulsed cycle.

In addition to simulating continuous etching using a single set of plasma conditions, the MCFPM is also capable of simulating pulsed plasma systems. In the continuous etching mode, the MCFPM measures time by the number of particles released, with a fixed  $\Delta t$  as described above. In a pulsed plasma simulation, the MCFPM uses the total fluxes of each sub-cycle ( $m$ ) to calculate the time per particle for that particular sub-cycle,  $\Delta t_m$ . The length of the sub-cycles is defined by the user in seconds. The code converts the user defined sub-cycle time into a number of particles using the  $\Delta t_m$  of that sub-cycle. This results in each sub-cycle having the same number of particles per sub-cycle from period to period, invalidating assumption A2 for very short sub-cycles. The shortest sub-cycle used in the simulations discussed here use  $2 \times 10^4$  particles, giving a deviation of less than 1% in the number of particles in each sub-cycle from pulse to pulse when using Poisson statistics. This pulse-to-pulse variation is not expected to contribute to the results, and the constant  $\Delta t$  for each particle can be assumed. Species having low fluxes are chosen at random by Monte Carlo techniques (described shortly). In this way, the number of a given low flux species released in a given cycle will be Poisson distributed, despite the total number of particles in that cycle being fixed.

## 2.5. Pseudo-particle Behavior

The trajectories of the incoming pseudo-particles are advanced in 3-dimensions through continuous space until they impact a solid mesh cell. When a pseudo-particle strikes a solid surface, a reaction is chosen from a user defined reaction mechanism. This mechanism can include reactions with both energy and angular dependencies. Based on this reaction mechanism, particle collisions can result in a reflection of the incoming particle without changing the material cell properties. After a particle collides with a surface, any resulting particles emitted into the gas phase – including etch products and/or the original particle – are tracked in a similar manner as the initially launched particle until the next collision with a surface. This process is repeated for each particle until that particle (and the gas phase particles it generates) are removed by reacting with a surface, or the particle leaves the computational domain by scattering out of the top of the domain.

### 2.5.1. Pseudo-Particle Initialization

Pseudo-particles are initialized such that their fluxes, as well as energy and angle distributions, statistically match the input obtained from reactor scale modeling. This is done using a typical Monte-Carlo technique, by choosing a random number  $u \in [0,1]$  and selecting the corresponding species,  $i$ , where

$$\frac{\sum_{j=1}^i \Gamma_j}{\Gamma_t} \leq u < \frac{\sum_{j=1}^{i+1} \Gamma_j}{\Gamma_t}. \quad (2.4)$$

If the chosen species is an ion (or an energetic neutral with a user defined IEAD) the energy and initial polar angle of the particle are chosen from a cumulative distribution function  $f_i(\varepsilon, \theta)$  using the same Monte-Carlo selection technique. The IEADs are provided to the MCFPM (calculated from the HPEM) in a probability density function,  $F(\varepsilon, \theta)$ , normalized to the flux of

that species. The input IEAD is discretized into  $n_\varepsilon$  energy bins and  $n_\theta$  angle bins. This input format is converted by the MCFPM into a cumulative distribution function as

$$f_i(\varepsilon_j, \theta_k) = \frac{\sum_{\varepsilon}^j \sum_{\theta}^k F(\varepsilon, \theta)}{\sum_{\varepsilon}^{n_\varepsilon} \sum_{\theta}^{n_\theta} F(\varepsilon, \theta)}. \quad (2.5)$$

The energy and initial (polar) angle is chosen from  $f_i$  by choosing three random numbers,  $u_1$ ,  $u_2$  and  $u_3$ . The random number  $u_1$  is used to find the energy and angle bin in  $f_i$  using

$$f_i(\varepsilon_j, \theta_k) \leq u_1 < f_i(\varepsilon_{j+1}, \theta_{k+1}). \quad (2.6)$$

Once the energy and angle bin has been selected from  $f_i$ , the exact energy (angle) is linearly interpolated between  $\varepsilon_i$  and  $\varepsilon_{i+1}$  ( $\theta_i$  and  $\theta_{i+1}$ ) at a point  $u_2$  ( $u_3$ ) of the distance between the values. If the chosen species is a thermal neutral particle the energy is chosen from a Maxwellian energy distribution with a user defined temperature corresponding to the gas temperature of the plasma. The initial polar angle of thermal neutrals is chosen from a uniform distribution from 0 to  $\pi$  (only downward trajectories).

To fully describe the initial position and velocity the MCFPM must have an initial position,  $\mathbf{r}_0$ , as well as two angles; a polar angle and an azimuthal angle. The value of  $\mathbf{r}_0$  is chosen from a uniform distribution of all positions in the  $\hat{e}_x, \hat{e}_y$  plane at the top of the simulation domain. The polar angle,  $\theta$ , which is chosen from the IEAD as described above, is the angle between the  $-\hat{e}_z$  axis and the initial velocity vector,  $\mathbf{v}_0$ , as shown in Fig. 2.1. The azimuthal angle,  $\varphi$ , between  $-\hat{e}_y$  and  $\mathbf{v}_0$  in the  $\hat{e}_x, \hat{e}_y$  plane is also need. Due to the 2D nature of the HPEM, the IEAD data only includes the single polar angle. This polar angle is in the range of  $-\pi/2$  to  $\pi/2$ , with negative angles representing initial velocities in the  $-\hat{e}_x$  direction (left moving), and positive angles resulting in initial velocities in the  $\hat{e}_z$  direction (right moving). Therefore,

because the MCFPM is a 3D code, for  $\theta > 0$  an azimuthal angle is chosen from a uniform distribution from 0 and  $\pi$ . For  $\theta < 0$ ,  $\varphi$  is chosen in the range from 0 and  $-\pi$ .

### 2.5.2. Particle Trajectories

Particles are advanced in time through 3D continuous space according to a first order explicit discretization of Newton's equations,

$$\mathbf{v}_\tau = \mathbf{v}_{\tau-1} + \frac{q\mathbf{E}}{m}\Delta\tau \text{ and} \quad (2.7)$$

$$\mathbf{r}_\tau = \mathbf{r}_{\tau-1} + \mathbf{v}_\tau\Delta\tau, \quad (2.8)$$

where  $\mathbf{v}_\tau$  is the velocity at particle time  $\tau$ ,  $\mathbf{r}_\tau$  is the position,  $q$  is the particle charge,  $m$  is the particle mass and  $\mathbf{E}$  is the electric field. In this study, electric potentials due to charging will not be calculated, so that the electric field is zero everywhere. The variable  $\tau$  is used to denote particle time to emphasize the difference between the particle time step  $\Delta\tau$ , and the simulation time step  $\Delta t$ , which was discussed in Chapter 2.4. As previously discussed,  $\Delta t$  is the period (in simulation time) between particles impinging on the simulation domain. For most simulations  $\Delta\tau$  is chosen to be the time required to cross at most a fraction of a computational cell, and so depends on the speed of the particle. This choice of  $\Delta\tau$  is used to avoid the particle trajectory passing through any solid materials without detecting a collision. In some cases (particularly in the fluorocarbon cases presented in Chapter 7, where a slightly porous polymer overlayer develops on all surfaces)  $\Delta\tau$  can be chosen to be between one and two computational cells. This would be done to allow particles to occasionally pass through very small obstructions in the particle trajectory, providing a type of real-time smoothing of the surface roughness. When ion trajectories are being affected by electric fields, it is possible that  $\Delta\tau$  may need to be significantly smaller than otherwise. For this reason, it is possible to set  $\Delta\tau$  differently for neutral and charged

species. The largest allowable  $\Delta\tau$  in a charging scenario is typically found through a convergence study. The behavior of each of those particles is considered instantaneous in simulation time. Therefore, particle time,  $\tau$ , is only used to accurately track particles, and its value is never used to influence the simulation clock.

As the particle is tracked through continuous space, it must be mapped onto the computational mesh of materials using

$$i = \lfloor r_x \Delta x \rfloor + 1, \quad (2.9)$$

$$j = \lfloor r_y \Delta y \rfloor + 1, \quad (2.10)$$

$$k = \lfloor r_z \Delta z \rfloor + 1, \quad (2.11)$$

where  $\lfloor x \rfloor$  is the floor function of  $x$ , and  $r_x$  is the component of the current position vector  $\mathbf{r}$  in the  $\hat{e}_x$  direction. The particle is thus mapped onto cell  $\mathbf{M}_{i,j,k}$  of the 3D matrix,  $\mathbf{M}$ , which represents the material of that region of space. The material matrix,  $\mathbf{M}$ , is indexed from one in each dimension, such that the domain origin is at the front-most lower left corner of cell  $\mathbf{M}_{1,1,1}$  if viewing from the same view as Fig. 2.1. The use of the floor function in this mapping guarantees that the lower boundary and upper boundary of each index are handled symmetrically.

At each step in particle time the MCFPM must check the material matrix,  $\mathbf{M}$ , to detect when the particle enters a solid material. The particle is assumed to have a finite (user defined) size,  $\Delta x_p$ , occupying a cubic volume  $\pm\Delta x_p$  around the current position  $\mathbf{r}$  in each dimension. A collision with the material matrix is considered fully resolved only when a single point in the seven-point molecule formed by the current position and points located  $\pm\Delta x_p$  in each cardinal direction from the current position, maps to a mesh cell which is occupied by a solid material. If more than one point in this set maps to a cell which is occupied by a solid material, the particle is

returned to its previous position and the propagation time step,  $\Delta\tau$ , cut in half. This process is repeated until only a single point maps to an occupied cell, at which time that cell is considered to be the impact location.

There are two different ways of handling boundaries in the MCFPM; reflective boundary conditions and periodic boundaries. When a particle encounters a reflective boundary, it is reflected back as by a mirror. That is, if the particle position is mapped onto the mesh, and the calculated  $i$  index is outside the bounds of  $\mathbf{M}$  ( $i < 1$ , or  $i > n_x$ , where  $n_x$  is the number of cells in the  $x$  dimension), its position and velocity are re-calculated as:

$$\text{Reflective Boundary: } \begin{cases} i = \begin{cases} -i + 1 & \text{if } i < 1 \\ 2n_x - i & \text{if } i > n_x \\ i & \text{otherwise} \end{cases} \\ r_x = \begin{cases} -r_x & \text{if } i < 1 \\ 2x_{\max} - r_x & \text{if } i > n_x \\ r_x & \text{otherwise} \end{cases} \\ v_x = \begin{cases} -v_x & \text{if } i < 1 \\ -v_x & \text{if } i > n_x \\ v_x & \text{otherwise} \end{cases} \end{cases} \quad (2.12)$$

This reflective boundary condition is good for reducing the simulation size for geometries which have a line of reflective symmetry. Of course, if a simulation domain is constructed that only includes half of a geometry, split at a line of mirror symmetry, there is no way for the MCFPM to predict asymmetries.

The periodic boundary condition allows right moving particles to pass from the right-hand boundary of the simulation domain to the left boundary, without altering the velocity. This accurately models the effects of translational symmetry. While, many geometries are able to be represented by both periodic and reflective boundaries, in these cases, periodic is often

preferable. When a particle interacts with the left or right boundaries with periodic boundary conditions, the position and is remapped as:

$$\text{Periodic Boundary:} \quad \begin{cases} i = \begin{cases} n_x - i & \text{if } i < 1 \\ i - n_x & \text{if } i > n_x \\ i & \text{otherwise} \end{cases} \\ r_x = \begin{cases} x_{\max} + r_x & \text{if } i < 1 \\ r_x - x_{\max} & \text{if } i > n_x \\ r_x & \text{otherwise} \end{cases} \end{cases} \quad (2.13)$$

Recall that with periodic boundaries, there is no need to modify the velocity.

### 2.5.3. Surface Normal Calculation

When a particle collides with the solid material, the MCFPM must calculate the surface normal of the profile at the collision point. Because the mesh is cubic the normal of the face where the particle impacted is not useful, since it will always be in one of the six cardinal directions ( $\hat{e}_x, \hat{e}_y, \hat{e}_z, -\hat{e}_x, -\hat{e}_y, -\hat{e}_z$ ). Instead the MCFPM fits a plane to nearby surface sites, and uses the normal of this plane as the surface normal. The process begins by finding all surface sites within a user defined search distance. This distance is typically  $\pm 4\Delta x$  in this work. As the surface is approximated with a linear function, increasing this search distance works to average local fluctuations and smooth the surface. The size of the search radius also affects the maximum local curvature, and therefore the resolution of the feature. Because of this, large values of search radius maintain smoother surfaces, but compromise the smallest features which can be represented with the same mesh. Surface sites are defined as any computational cell with one or more faces exposed to the plasma. Once all surface sites are found then a plane, defined as  $Ax+By+Cz=D$ , is fit to the points by finding A, B, C and D such that they minimize the sum of the squared error,

$$Q = \sum_{i=1}^m (Ax_i + By_i + Cz_i - D)^2, \quad (2.14)$$

where  $m$  is the number of surface points within the search region, and  $x_i$ ,  $y_i$  and  $z_i$  are the  $x$ ,  $y$ ,  $z$  locations of the centers of the  $i^{\text{th}}$  surface point in that set.

The derivative of  $Q$  with respect to each coefficient has two points where it reaches zero, the best and worst fits. To find the best fit we solve by setting the each derivative to zero,[71]

$$\begin{aligned} \frac{dQ}{dA} &= \sum_{i=1}^m 2x_i (Ax_i + By_i + Cz_i - D) = 0 \\ \frac{dQ}{dB} &= \sum_{i=1}^m 2y_i (Ax_i + By_i + Cz_i - D) = 0. \\ \frac{dQ}{dC} &= \sum_{i=1}^m 2z_i (Ax_i + By_i + Cz_i - D) = 0 \end{aligned} \quad (2.15)$$

The value of  $D$  can be found as the center of mass of the surface points,

$$D = \frac{A}{m} \sum_{i=1}^m x_i + \frac{B}{m} \sum_{i=1}^m y_i + \frac{C}{m} \sum_{i=1}^m z_i = A\bar{x} + B\bar{y} + C\bar{z}. \quad (2.16)$$

Substituting Eqn. 2.16 back into Eqn. 2.15 results in the system of equations:

$$\begin{bmatrix} \sum_{i=1}^m (x_i - \bar{x})^2 & \sum_{i=1}^m (x_i - \bar{x})(y_i - \bar{y}) & \sum_{i=1}^m (x_i - \bar{x})(z_i - \bar{z}) \\ \sum_{i=1}^m (x_i - \bar{x})(y_i - \bar{y}) & \sum_{i=1}^m (y_i - \bar{y})^2 & \sum_{i=1}^m (y_i - \bar{y})(z_i - \bar{z}) \\ \sum_{i=1}^m (x_i - \bar{x})(z_i - \bar{z}) & \sum_{i=1}^m (y_i - \bar{y})(z_i - \bar{z}) & \sum_{i=1}^m (z_i - \bar{z})^2 \end{bmatrix} \begin{bmatrix} A \\ B \\ C \end{bmatrix} = \begin{bmatrix} 0 \\ 0 \\ 0 \end{bmatrix}. \quad (2.17)$$

This system of equations can be solved as an eigenvalue problem by assuming  $A^2 + B^2 + C^2 = 1$  (to avoid the trivial solution) and using the Jacobi algorithm.[72] This algorithm returns three eigenvectors and three eigenvalues. The eigenvector corresponding to the smallest eigenvalue is parallel to the unit normal of the profile at the impact site.

Since the algorithm described above only has information about the surface, and not the state of the surrounding solid or gas cells, it is possible that the unit vector returned will be pointing into the solid. To select a normal vector of the surface pointing into the plasma, three points along the given vector are polled in the positive and negative directions. If the point maps to a cell which is occupied by a solid material, it casts a vote against that direction being the surface normal. If the cell is un-occupied (gas) the point casts a vote in favor of that direction being the surface normal. If one direction has more votes for it than the other, it is selected as the surface normal. If the vote is tied, then the sign of the surface normal is selected at random.

#### **2.5.4. Reflections: Specular and Diffusive**

When gas particles interact with the solid material the resulting reflected or re-emitted particles must have the correct velocity distributions. If the particle is energetic, meaning that it has  $> 1$  eV translational energy, it has a tendency to reflect from a surface specularly. In the MCFPM, all ions (positive and negative) neutralize when striking surfaces, retaining an energy and angular dependent fraction of their incident energy as a *hot neutral* particle, dispersed in specular and diffusive modes, as described below. All processes involving energetic particles apply equally to energetic ions and hot neutrals.

In a specular reflection, the angle between the incoming particle velocity  $\mathbf{v}_i$  and the surface normal vector  $\mathbf{n}$  is the same as the angle between the final velocity  $\mathbf{v}_f$  and  $\mathbf{n}$ . The component of the velocity which is tangential to the surface normal does not change during specular reflection. The resulting velocity is computed using the vector expression,[73]

$$\hat{\mathbf{v}}_f = 2(\hat{\mathbf{n}} \times \hat{\mathbf{v}}_i) \hat{\mathbf{n}} - \hat{\mathbf{v}}_i \quad (2.18)$$

where hatted vectors are the unit direction vectors.

Particles lose energy during the reflection as a function of initial energy and incident angle. Both of these processes scale the reflected energy as

$$\varepsilon_f = \gamma_0 f(\theta) f(\varepsilon_i) \varepsilon_i, \quad (2.19)$$

where  $\varepsilon_i$  is the initial energy,  $\varepsilon_f$  is the final energy,  $\gamma_0$  is a user defined maximum fraction for the reflected energy and  $\theta$  is the angle between the surface and the incoming velocity. Energy dependent energy loss favors retaining a larger proportion of the initial velocity for more energetic particles. The energy scaling factor,  $f(\varepsilon_i)$ , is zero for initial energies less than  $\varepsilon_0$ , unity for initial energies greater than  $\varepsilon_s$  and scales linearly between the two user defined energies, such as

$$f(\varepsilon) = \begin{cases} 0 & \text{if } \varepsilon < \varepsilon_0 \\ \frac{\varepsilon - \varepsilon_0}{\varepsilon_s - \varepsilon_0} & \text{if } \varepsilon_0 \leq \varepsilon \leq \varepsilon_s \\ 1 & \text{if } \varepsilon > \varepsilon_s \end{cases}.$$

The angle dependent energy loss term,  $f(\theta)$ , is unity for  $\theta = 0^\circ$  (grazing incidence) and decreases linearly to zero at a user defined  $\theta_0$ , as

$$f(\theta) = \begin{cases} \frac{\theta_0 - \theta}{\theta_0} & \text{if } \theta < \theta_0 \\ 0 & \text{if } \theta > \theta_0 \end{cases}.$$

In this study the values of  $\gamma_0 = 0.85$ ,  $\varepsilon_0 = 0$  eV,  $\varepsilon_s = 50$  eV and  $\theta_0 = 30^\circ$  were used for all simulations. The magnitude of the final velocity is then calculated as

$$\mathbf{v}_f = \sqrt{\frac{2\varepsilon_f}{m}} \hat{\mathbf{v}}_f. \quad (2.20)$$

Ions are assumed to be neutralized when striking a surface, and – in the absence of an electric field – are not distinguished from the hot-neutrals which result from reflections of ions

from the surface.[74] For simplicity, we use the term *ion* to denote a hot, non-thermal, particle – the initial ion before striking a surface or the hot-neutral after striking a surface. Ions whose energy drops below 1 eV by energy lost through reflections will be converted to their thermal neutral counterparts, and are then indistinguishable from the incoming neutral flux of that species.

Neutral particles with thermal, or near thermal ( $< 1$  eV) energies reflect or re-emit from surfaces diffusively following a cosine angular distribution.[26,75] This occurs because each particle is in thermal equilibrium with the surface, allowing them to briefly physisorb to the surface, before being re-emitted into the gas by vibrational processes in the solid, such as phonon scattering. This scattering is done in the MCFPM by assuming the re-emitted particle is traveling in the direction of the surface normal  $\mathbf{n}$ , in a local coordinate system  $(\hat{e}_x', \hat{e}_y', \hat{e}_z')$  where the  $\hat{e}_z'$  axis is aligned with  $\mathbf{n}$ . Two rotations are then applied, first  $\mathbf{R}_1(\theta, \varphi)$  applies a rotation in the local coordinates with polar angle  $\theta$  and azimuthal angle  $\varphi$ . Next  $\mathbf{R}_2(\alpha, \beta)$  rotates the local coordinate system back to the global  $(\hat{e}_x, \hat{e}_y, \hat{e}_z)$  coordinates, using the Euler angles  $\alpha$  and  $\beta$ . The  $\alpha$  and  $\beta$  angles are calculated as

$$\begin{aligned} a &= \arccos\left(\frac{n_x}{\sqrt{n_x^2 + n_y^2}}\right) \\ b &= \arccos\left(\frac{n_z}{\sqrt{n_x^2 + n_y^2 + n_z^2}}\right), \end{aligned} \tag{2.21}$$

where  $n_x$  is the component of the surface normal in the global  $\hat{e}_x$  direction. The angle  $\alpha$  rotates the  $\mathbf{n}$  vector about the  $\hat{e}_z$  axis to bring it into the  $\hat{e}_x, \hat{e}_y$  plane. The angle  $\beta$  rotates the  $\mathbf{n}$  vector again, this time about the  $\hat{e}_y$  axis to bring it into alignment with the  $\hat{e}_z$  axis. The combined rotation matrix is  $\mathbf{R}(\alpha, \beta, \theta, \varphi) = \mathbf{R}_2(\alpha, \beta)\mathbf{R}_1(\theta, \varphi)$ . Since the initial velocity is in the  $\hat{e}_z'$

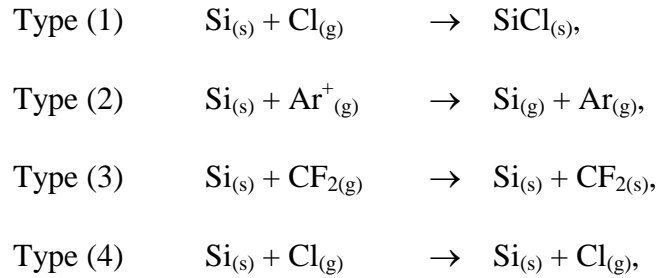
direction by construction, the rotation can be applied as,

$$\begin{aligned} v_x &= v_{th} \left( \cos(b)\cos(a)\sin(q)\cos(j) + \cos(b)\sin(a)\cos(q) - \sin(b)\sin(q)\sin(j) \right) \\ v_y &= v_{th} \left( \sin(b)\cos(a)\sin(q)\cos(j) + \sin(b)\sin(a)\cos(q) + \cos(b)\sin(q)\sin(j) \right), (2.22) \\ v_z &= v_{th} \left( -\sin(a)\sin(q)\cos(j) + \cos(a)\cos(q) \right) \end{aligned}$$

where  $v_{th}$  is the thermal velocity chosen from a Maxwellian energy distribution with a user defined temperature, representing the temperature of the substrate.

### 2.5.5. Surface Reactions

Surface reactions occur when a gas phase pseudo-particle interacts with any solid cell in the mesh. These reactions can be (1) chemical reactions that change the material identity, (2) sputtering reactions that convert the cell from a solid material into a gas cell and (3) deposition reactions that deposit a new solid cell on top of the reaction cell. Each of these reactions are described in a universal reaction format in the MCFPM reaction mechanism. For example



The reactions can be defined with fixed probabilities, or with energy and angle dependent probabilities. Typically Type (1) and Type (3) reactions are defined with fixed probabilities, while Type (2) reactions usually have energy and angle dependent reaction probabilities. Type (4) reactions are simply reflections without reaction – the equivalent of an elastic scattering event in the gas phase.

Gas-solid reactions involving thermal reactions are modeled in the MCFPM as having fixed probabilities, which includes most reactions of Type (1) and Type (3). These thermal reactions, in a real etching system would be functions of gas and substrate temperatures. In the MCFPM both gas and substrate temperatures are assumed to be constant, resulting in fixed probabilities for all thermal reactions.

Ion activated reactions usually have an energy dependence proportional to  $\varepsilon^{1/2}$ , where  $\varepsilon$  is the energy of the impinging particle.[76] This dependence is implemented in the MCFPM using the form

$$P(\varepsilon) = p_0 \left( \frac{\varepsilon - \varepsilon_{th}}{\varepsilon_0 - \varepsilon_{th}} \right)^n, \quad (2.23)$$

$P(\varepsilon)$  is the energy dependent yield, having threshold energy  $\varepsilon_{th}$ ,  $\varepsilon_0$  is a reference energy,  $p_0$  is the sputtering yield at the reference energy and  $n$  is the energy dependency exponent (typically  $1/2$ ).

In addition to an energy dependence, most ion-activated reactions also have a dependence on the angle of incidence of the impinging particle. This can be significantly different for physical sputtering and chemically enhanced sputtering processes.[24] To distinguish these processes, the MCFPM includes two angular dependent probability functions,  $P(\theta)$ . One angular dependency typically has a maximum near a  $60^\circ$  angle of incidence, is less than unity at normal incidence, and drops to zero at grazing incidence, characteristics of physical sputtering. The second angular dependency function is unity at normal incidence, gradually dropping after  $45^\circ$  until reaching zero at grazing incidence, characteristic of chemical sputtering. Therefore, the total yield of a sputtering reaction is given by

$$P(e, q) = P(e)P(q). \quad (2.24)$$

When gas particle intersects with a surface, the probability of reaction is, by definition, unity. The process of choosing a particular reaction for a gas-solid pair requires a series of renormalizations. Since  $P(\varepsilon, \theta)$  can both exceed one, and there may be several energy dependent reactions between any gas/solid pair, the probability of the  $i^{\text{th}}$  reaction must be re-normalized so as to not exceed one,

$$P_i(e, q) = \frac{P_i(e)P_i(q)}{\sum_{j=1}^N P_j(e)P_j(q)}, \quad (2.25)$$

where  $N$  is the number of reactions between this gas/solid pair. If the sum of the un-normalized probabilities is less than one, then the probability of the elastic Type (4) reaction is increased to so the sum is unity. If the sum of the un-normalized probabilities is greater than one, then the probability of thermal reactions are scaled down so that the probability is unity. The normalized probabilities are converted to a cumulative probability distribution in the same manner as for choosing the initial velocity of a particle. Choice of a random number then determines which reaction occurs.

### 2.5.6. Radical Diffusion Through Bulk Solids

Atomic radical species, such as fluorine atoms, can diffuse through a steady-state polymer capping layer and play an important role in etching processes.[77] Since the MCFPM utilizes pseudo-particles, an atomistic approach was adopted in which a random walk through the computational lattice represented the diffusion of individual pseudo-particles through the polymer layer. Diffusion occurs with a user defined, fixed probability whenever a diffusible gas species strikes a surface of a permeable material, such as the polymer. If the such a particle interacts with a permeable surface but does not enter the material to diffuse, it diffusively reflects.

Diffusion of a particle through the permeable material takes place on the computational mesh, not in continuous space as particle propagating in the gas phase or during implantation. When the particle begins to diffuse through the solid, the position of the particle projected onto the mesh as described by Eqns. (2.9)-(2.11). The particle propagates through the mesh by randomly choosing its next location from the current set of six nearest neighbors. If the new chosen position is a gas phase cell, as would occur if the particle diffused back to the surface, the particle is re-emitted from the solid at that point with a Lambertian distribution, similar to a thermal particle reflecting from the surface at that point. If the new position is not also a permeable material, the interaction with that cell is treated in the same way as a gas phase particle interacting with a new site. For instance, if a F atom diffuses through a polymer overlayer and encounters a Si material site beneath the surface, there is a possibility a reaction will occur forming SiF, consuming the F radical. If such a reaction does not occur with the non-permeable, a different nearest neighbor is chosen, and the particle continues propagating by random-walk through the polymer layer.

To ensure that during the random walk the particle visits each nearest neighbor only once, the next position in the random walk is chosen from a shuffled list of possible transitions. First, a list of integers from 1 to 6 representing the nearest neighbors is generated. This list is then shuffled using the Fisher-Yates algorithm.[78] The first integer from the shuffled list is selected and mapped to a nearest neighbor transition from a static lookup table. If this neighbor does not result in an allowable transition (the new site is not polymer) or produces a reaction which consumes the diffusing particle, the next integer in the list is selected.

The species which are tracked in the MCFPM diffusion routine are often highly reactive. Some atomic species may only react with the underlying material, but most (F and O in

particular) will also react with the polymer itself. Such thermal reactions are assigned a fixed probability, and this probability is evaluated at each step in the random walk. A cumulative probability array for reactions with the solid is constructed, and choice of a random number determines whether the diffusing radical reacts with the polymer. As a result of these reactions, highly reactive species will have a smaller average depth of penetration (sampling a smaller volume surrounding the point of entering the solid) than less reactive particles, despite using the same mean free path.

### **2.5.7. Ion Implantation**

Modeling of ion implantation phenomenon is necessary for capturing the physics of the fluorocarbon etching mechanism. Several physical processes, including energy transport to the etch front, mixing and energy activated sub-surface chemical reactions should be addressed. The MCFPM enables user defined energetic species to penetrate into solids and continue to propagate until a stochastically determined implant range is reached. The average implant range for each ion (hot neutral) for each solid material in the mechanism is calculated using SRIM[79], then added into the MCFPM database.

The actual implant range for a specific ion and solid is randomly chosen from a Gaussian distribution with the mean range provided by the SRIM data with a standard deviation equal to half of the mean. For most ions of interest (e.g.,  $\text{Cl}^+$ ,  $\text{F}^+$ ,  $\text{O}^+$ ,  $\text{Ar}^+$ ) this process produces a close match to the longitudinal straggle predicted by SRIM. During implantation, the particle is tracked through continuous 3D space, with a scattering event occurring each time the particle enters a new computational cell, resulting in an average mean-free-path of approximately  $\Delta x = 0.3$  nm. At each scattering event, polar and azimuthal scattering angles are chosen using Monte Carlo techniques. The polar angle is selected from an exponential distribution with a user

defined mean ( $7^\circ$  was used for all results presented here). This mean polar scattering angle was adjusted to closely match the SRIM results for lateral straggle for typical ions ( $\text{Ar}^+$  and  $\text{F}^+$ ). The exponential distribution of polar angles results in mostly small-angle scattering, with the occasional high angle scattering event. The azimuthal angle is chosen from a uniform distribution from  $[0, 2\pi]$ . Scattering is implemented using the same Euler angle rotations described in Eqns. (2.21) and (2.22), substituting the current velocity vector for the surface normal vector.

There are several benefits to modeling the scattering of ions during implant as a series of discrete scattering events compared to a simpler line-of-sight technique. First, distributions of implanted ions more accurately reflect the true distribution, as shown in Fig. 2.2, produced by SRIM calculations. Second, including discrete sub-surface scattering of ions enables the modeling of the reflection of quasi-grazing ion impacts. (That is, an ion that penetrates a surface, scatters beneath the surface and exits the solid back into the gas phase.) All ions striking a solid surface with an incident angle greater than  $1^\circ$  are assumed to implant. For ions with small angles (quasi-grazing), scattering within the material results in a large fraction of implanting ions re-emerging from the solid. Such particles continue to travel in the gas phase with the velocity and energy which they had when emerging from the implant path. The energy of the particle is calculated as,

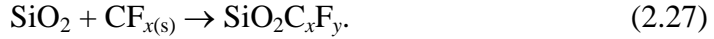
$$\varepsilon = \varepsilon_i \left( 1 - \exp \left[ \alpha \left( \frac{l}{\Lambda} - 1 \right) \right] \right), \quad (2.26)$$

where  $\varepsilon_i$  is the ion's initial energy,  $\Lambda$  is the implant range,  $l$  is the path length traveled and  $\alpha$  is a user defined parameter. A value of  $\alpha = 8.0$  was used for all simulations presented here. The result is the reflection of quasi-grazing ions with a distribution of scattering angles and energies

which are related to the implant properties of the particles. Similar distributions of scattering angle and energy have been observed experimentally and using molecular dynamics simulations.[48,80]

The collision cascade initiated by ion implantation deposits energy into the solid, not only near the implant site, but also along the implant path due to electronic stopping forces and stochastic nuclear stopping.[79] To model this cascade, *ion induced mixing* was implemented whereby energy deposition is represented as the exchange of the material properties of two adjacent computational cells. This ion induced mixing occurs at each cell along the implant path with a probability defined by the user – 100% is used for all simulations presented here. When a mixing even occurs, the material identity of the cell currently containing the ion is swapped with the material identity of a randomly chosen nearest neighbor. In the bulk of a material this mixing goes unnoticed, but near interfaces the results of ion mixing are critical.

When two solid materials are brought into contact due to ion induced mixing, there is a probability that a *solid-solid reaction* will occur. In the MCFPM, a solid-solid reaction represents the reaction of two chemical compounds in the solid phase that forms a new material. Since ion mixing represents energy deposition these reactions are effectively ion activated mixing processes at the scale of the computational cell. For example, our solid phase model of the SiO<sub>2</sub> etching reaction involves three materials: SiO<sub>2</sub>, CF<sub>x</sub> polymer and a selvedge layer SiO<sub>2</sub>C<sub>x</sub>F<sub>y</sub>. This SiO<sub>2</sub>C<sub>x</sub>F<sub>y</sub> material represents the thin layer where C-O and Si-F bonds exist.[46] During etching it is common for an ion implantation event to bring a CF<sub>x</sub> polymer cell in direct contact with a SiO<sub>2</sub> cell. In this case, a solid-solid reaction can occur which converts the CF<sub>x</sub> polymer cell and the SiO<sub>2</sub> cell into a SiO<sub>2</sub>C<sub>x</sub>F<sub>y</sub> cell due to the ion energy deposited in the lattice, such as,



Since the reaction between  $\text{SiO}_2$  and  $\text{CF}_{x(s)}$  in Eqn (2.27) results in two solid material cells reacting to form one new solid cell, a vacancy is generated at the interface between the polymer and  $\text{SiO}_2$ . This vacant cell must be addressed in the model, or the polymer surface would become porous eventually become artificially separated from the  $\text{SiO}_2$  surface. (The polymer is assumed to remain dense during this reaction.) To prevent this artificial porosity, the resulting vacancy diffuses out of the polymer, using an algorithm identical to the process of neutral diffusion described previously where the reaction probability is zero. The vacancy diffusion proceeds by a random walk through the polymer overlayer until the particle reaches a gas cell, at which point it is released to the gas phase. This diffusion of the vacancy was necessary due to the inability to a priori specify the direction in which a polymer overlayer would be “compressed” to eliminate an in-situ vacancy.

In order to speed the rejection of vacancies, materials that are non-permeable to vacancies can be specified. For example, if there is an underlying etch-stop layer which is known to always be at the bottom of the feature, this material can be denoted as non-permeable. The vacancy will then be reflected from that non-permeable material in a direction more likely to find the solid-gas boundary.

In addition to solid-solid reactions which occur due to the energy transfer from the implanting ion to the solid, it is also possible for the ion to undergo reactions at sub-surface interfaces. Selection of these reactions is performed in the same manner as for reactions at the gas/solid interface – construction of a cumulative probability array and choice of a random number. The ion energy that produces the reaction at the sub-surface site will have been appropriately scaled by Eqn. (2.26) due to energy loss during implantation. Such reactions can,

for example, result in sputtering which generates a vacancy in the solid. Such vacancies diffuse to the gas surface in the same manner as for vacancies generated by solid-solid reactions. Sub-surface reactions can also produce a gas phase, volatile product such as SiF<sub>4</sub> or CO. If the product is non-reactive, it is not tracked in the simulation, assuming that it will eventually diffuse out of the feature without having reacted. If the gas phase product is a radical, (F, CF<sub>2</sub>, SiF) then the particle is diffused out of the feature using the neutral diffusion technique as previously described. This procedure results in some probability of the product reacting with the polymer layer before emerging into the gas phase.

When an ion reaches the end of its implant path, there are several possible outcomes. It is possible that the implanting ion will generate interstitial defects. Depending on the size of the ion, this type of defect can be modeled in different ways in the MCFPM. For large non-reactive atoms [e.g., heavy ions (Ar, Xe)] a new cell can be generated in the lattice, displacing a (randomly chosen) nearest neighbor cell. This displaced cell will then displace one of its neighboring cells, continuing in a random-walk until one of the displaced cells reaches a surface by displacing a gas cell. The algorithm is similar to the diffusion of radical species discussed previously, with the exception that the material identity of each cell in the random walk path will be replaced with the material of the previous cell. The end result is that each atom along the random walk path is pushed one cell in the direction of the displaced particle. This random walk behavior is intended to model the secondary collision cascade(s) which occur due to atoms displaced by primary “knock-on” ion impacts.[81] For smaller non-reactive ions (e.g., He, Ne) the interstitial defect may be neglected, resulting in no change to the lattice at the end of the implant range. For more reactive ions, such as F<sup>+</sup>, Cl<sup>+</sup> or O<sup>+</sup>, substitutional defects may form,

effectively acting as sub-surface chemical reactions. For instance,  $\text{Cl}^+$  implanting into silicon can generate a SiCl cell at the implant site.

### 2.5.8. Surface Diffusion of Adsorbed Particles

The MCFPM can address the diffusion of adsorbed particles on surfaces. This type of diffusion is particularly important in depositing chemistries, such as PECVD or polymerizing fluorocarbon plasmas to prevent dendritic growth. In the simulations presented here, the polymer species,  $\text{CF}_{x(s)}$ , deposited by the sticking of  $\text{CF}_{x(g)}$  species are allowed to diffuse along the surface to ensure conformal polymer film formation. In this process, species are designated as being physisorbed species or chemisorbed. When, for example, a  $\text{CF}_{x(g)}$  radical deposits onto the surface as a physisorbed species, the particle is propagated that along the surface using a Metropolis like algorithm to minimize the Hamiltonian function,

$$\hat{H} = U^M + U^H + U^G. \quad (2.28)$$

The three terms in this Hamiltonian represent the contributions of neighboring solid cells through the Morse binding potential ( $U^M$ ), the energy penalty for hopping to next-nearest-neighbor sites ( $U^H$ ) and a phenomenological potential which attracts the deposited material toward a ‘base’ material ( $U^G$ ).

The Morse potential is the dominant term in most systems. This term represents the potential between two solid cells as

$$U_{ij}^M = V_M \left[ \exp\left(-\frac{2(r_{ij} - r_0)}{A_0}\right) - 2 \exp\left(-\frac{r_{ij} - r_0}{A_0}\right) \right], \quad (2.29)$$

where  $r_{ij} = \|\mathbf{r}_i - \mathbf{r}_j\|$  is the distance between cells  $i$  and  $j$ . The variables  $V_M$ ,  $r_0$  and  $A_0$  have user defined values that scale the potential ( $V_M$ ), define the distance of strongest binding ( $r_0$ ) and define the width of the binding well ( $A_0$ ), respectively. The shape of the potential as a function

of  $r_{ij}$  is shown in Fig. 2.3. A typical value of  $V_M = 5$  meV was used for this work. The general assumption of using this potential is that having more close neighbors produces more binding energy than fewer neighbors. To achieve this end  $r_0 = \Delta x$ , so that nearest neighbors (NN) contribute the largest (most negative) binding energies. (In this cubic lattice nearest neighbors are cells that share a face with the cell in question, next-nearest neighbors share an edge and next-next-nearest neighbors share a corner point) The width of the binding region,  $A_0$ , can be adjusted to provide larger or smaller contributions from next-nearest-neighbors (NNN) and next-next-nearest-neighbors (4N). The value of  $A_0$  used for this study was 1 Å. Contributions from cells beyond 4N are not considered regardless of the value of  $A_0$ .

The hopping potential represents an energy penalty for hopping to a NNN site instead of a NN site. It is evaluated as

$$U_{ij}^H = \begin{cases} 0 & \text{NN} \\ V_H & \text{NNN} \\ \infty & \text{otherwise} \end{cases}, \quad (2.30)$$

where  $V_H$  is the user defined energy penalty in eV ( $V_H = 5$  meV was used in this study). Hopping to 4N or further in a single step is not allowed. Allowing for NNN hopping is required to diffuse across steps in the cubic lattice. Otherwise, diffusion would be limited to only smooth surfaces only, as shown in Fig. 2.4.

The gravity potential is provided to enable smooth and conformal coatings when diffusion with only Morse and hopping potentials does not suffice. The gravity potential offers an empirical method to force the polymer deposition to favor smooth and conformal films matching experimental results. The gravity potential is calculated as

$$U_{ij}^G = V_G (D_j - D_i), \quad (2.31)$$

where  $V_G$  is the strength of the gravity potential in  $\text{eV}/\Delta x$ , and  $D_i$  is the distance from cell  $i$  to the nearest *base material* in units of  $\Delta x$ . A value of  $V_G = 50 \text{ meV}$  was used for all simulations presented here. This method enables a set of base materials which attract the depositing species, as by gravity. To quickly calculate  $D_i$ , the MCFPM periodically calculates the distance from each gas cell in the mesh to the nearest base material. This distance is stored as a scalar field, which can be quickly evaluated during the diffusion process. As long as this distance field is updated frequently enough this technique offers a way to empirically tune the smoothness of the deposited film.

The distance field is calculated using a rapid but approximate method. The simplest method which gives an exact result would involve looping through the entire mesh for each point on the mesh to look for the nearest base material. This method would be  $O(n^2)$  where  $n$  is the number of cells in the mesh. Instead an iterative method is employed, looping through the mesh several times to build the solution. On the first pass through the mesh, cells which have a base material nearest neighbor are assigned a distance value of 1, cells which are next nearest neighbors with a base material are assigned a value of  $\sqrt{2}$  and  $4N$  cells are assigned  $2\sqrt{2}$ . On subsequent passes, cells that have neighbors with distance values are assigned the value of the neighbor cell with the smallest distance value plus 1 for nearest neighbors,  $\sqrt{2}$  for NNN and  $2\sqrt{2}$  for  $4N$ . In this way, the distance field can be calculated by looping through the mesh a number of times,  $D$ , that can be dramatically less than the number of cells in the mesh, resulting in  $O(n)$  algorithm scaling. If  $D$  is equal to the number of cells in the largest side of the computational domain, the entire distance mesh will be calculated. If  $D$  is smaller, cells which are not given a distance value by the algorithm are assumed to be infinitely far from the base material. This allows for values of  $D$  which address typical film thicknesses without needing to calculate the

entire mesh. In the work presented here, the algorithm uses  $D = 40$  iterative loops, while  $n$  is typically  $10^6$ - $10^7$ .

The diffusion of physisorbed particles proceeds as discrete hopping events which are chosen with a similar technique to the Metropolis-Hastings algorithm.[82] In this algorithm, if the particle is currently at position  $i$ , a new proposed position,  $j$ , is chosen randomly from a list of all NN and NNN sites. The potential difference between these sites,  $\Delta E_{ij}$  in eV, is calculated as

$$\Delta E_{ij} = \left( \sum_n^{N_i} U_{in}^M - \sum_n^{N_j} U_{jn}^M \right) + U_{ij}^H + U_{ij}^G, \quad (2.32)$$

where  $N_i$  is the set of all NN, NNN and 4N of site  $i$ . The proposed transition is accepted with probability

$$P_{i \rightarrow j} = \begin{cases} 1 & \text{if } \Delta E_{ij} < 0 \\ \exp\left(-\frac{\Delta E_{ij}}{k_B T}\right) & \text{if } \Delta E_{ij} \geq 0 \end{cases}, \quad (2.33)$$

where  $k_B$  is Boltzmann's constant and  $T$  is the substrate temperature ( $T = 313$  K in this study). Regardless if the transition is accepted or rejected, the particle will undergo another diffusion step with probability  $P_d$ , which is a user defined parameter ( $P_d = 0.99$  here) to regulate the amount of diffusion to be allowed. Notice that, even if very high values of  $P_d$  are chosen, if the diffusing particle finds a potential well where  $\Delta E_{ij} \gg k_B T$  for all possible transitions then it will likely remain trapped there. This process continues, choosing a new random number each step, until a number is chosen which is greater than  $P_d$ . This process allows some reasonable large jumps to, for example, escape from a potential well. When diffusion is completing the physisorbed species is converted to the corresponding chemisorbed species.

## 2.6. Code Layout / Parallelism

The MCFPM is divided into three main functional units: serial processes, parallel processes and output processes. Each of these processes are split into different files, each containing many sub-functions. The main parallel section of the code is the particle propagation routine. Serial processes are those which must be run on the entire system at one time. These include operations which only occur once, such as reading input files and initialization of the simulation. Other serial processes are run periodically, modifying or using the entire mesh simultaneously, thus requiring serial execution. The output processes are a large sub-group of the serial processes, requiring the entire mesh to be output by a single thread. The MCFPM is written in FORTRAN.

The MCFPM algorithm, shown in Fig. 2.6, mirrors this parallel, serial division. There are two main loops in the algorithm: the *iteration* loop, where serial processes occur, and the particle loop, where the parallel particle propagation algorithm occurs. By construction the parallel particle loop exists inside of the iteration loop. Therefore the iteration loop executes after every  $N$  particles have been processed in the particle loop. The value of  $N$  is set by the user, and represents a period of time as defined in Eqn. 2.3. Therefore, serial processes, including outputting the profile, are run periodically every  $N \times \Delta t$  s.

The main parallel particle propagation routine is parallelized over particles using a shared memory model. Meaning that, during parallel execution, each parallel thread is tracking a different particle, and their effects are synchronized by utilizing a material mesh which is stored in shared memory. To accomplish parallelism in FORTRAN, openMP directives were added to the code to guide an openMP compiler (Intel ifort) in parallel compilation. This parallel

programming model is effective at allowing the algorithm to scale to utilize a significant portion of the resources of a modern multi-core CPU architecture.

The MCFPM usually obtains scaling benefits from 6-8 core operation, with reduced scaling efficiency after that. The main obstacle to obtaining better scaling performance in the MCFPM algorithm is the existence of a parallel race condition in the basic algorithm which occurs stochastically, and must be addressed specifically. This condition occurs when two parallel threads, each tracking a different particle, attempt to modify the same cell in the material mesh at the same time. Due to the internal memory handling techniques of openMP this condition results in non-deterministic effects and often errors. This race condition is resolved through the use of the openMP *critical* statement. This parallel construct demands that only one thread can be operating during the execution of a critical section of the code, and before parallel operation is resumed all threads must be fully synchronized. All changes to the main mesh matrix are contained in these openMP critical statements, forcing other threads to wait while the mesh is modified and synchronized across threads. This resolves the issue, but as more and more threads are added to the same problem, it introduces more and more pauses into the parallel execution, limiting strong scaling.

## **2.7. MCFPM Validation**

The recent 3d-MCFPM code has been validated in two different studies at different levels of model complexity. To validate the neutral transport aspects of our model, simple test problems were simulated and compared to results of analytical models by Clausing [83] of neutral transport in the molecular flow regime. The transmission of neutral fluxes through a circular tube was computed with the MCFPM and transmission probabilities were derived as function of AR and the reactive sticking probability,  $S_b$ , of the bottom surface of the feature.

(Transmission probability is the ratio of the flux of neutral particles on the bottom surface of the tube divided by the flux of particles entering the tube.) The walls of the tube are assumed re-emit all incident particles with cosine law angular distributions, as discussed in Chapter 2.5.4. The computed transmission probabilities agreed with theory with an error of  $< 6\%$  over the range of AR studied, as shown in Fig. 2.7. The error was found to be directly related to the discretization of a circular tube by a rectilinear mesh and not due to any issue with the neutral transport model itself.

Validation of a more complex plasma etching reaction were done in collaboration with Lam Research by comparing simulated profiles with experiments for features etched in a He/Cl<sub>2</sub> plasma.[84] The He/Cl<sub>2</sub> mechanism is not discussed in detail in this thesis, but is discussed by Zhang et al. in Ref [84], and is very similar to the Ar/Cl<sub>2</sub> mechanism discussed in Chapter 3.1. By tuning the reaction probabilities of the basic reactions, a very good match to experiment was obtained for etch rate, profile shape and feature density dependency, as shown in Fig. 2.8. While the etch mechanism includes many fitted parameters, the ability of the model to match well for all of these features at two different etch times indicates that the model includes much of the important physics involved in this etching reaction. It is reasonable to expect such a model, which has been calibrated in such a way to be quantitatively predictive over a range of process parameters significantly larger than the training set. Furthermore, it is also reasonable to expect a similar physical mechanism to be qualitatively predictive over an even larger range of process parameters, even if it has not been calibrated to produce an exact match of experimental results, provided it also incorporates the important physics of the process being modeled. This assumption, that a MCFPM mechanism which incorporates the important physics of a given etch process will provide qualitative predictions for trends of etch metrics with changes in process

parameters, is fundamental to this work.

## 2.8. Figures

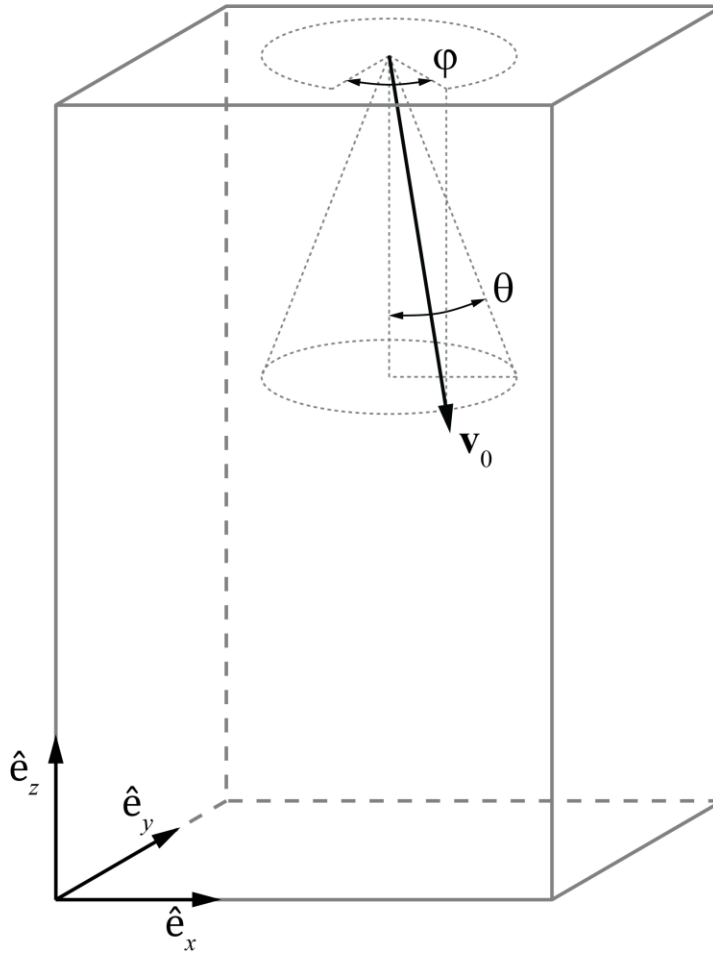


Fig. 2.1 Illustration of the simulation domain showing the origin and cardinal coordinates  $\hat{e}_x$ ,  $\hat{e}_y$ , and  $\hat{e}_z$ . An initial velocity vector,  $\mathbf{v}_0$ , is shown along with the polar ( $\theta$ ) and azimuthal ( $\phi$ ) angles.

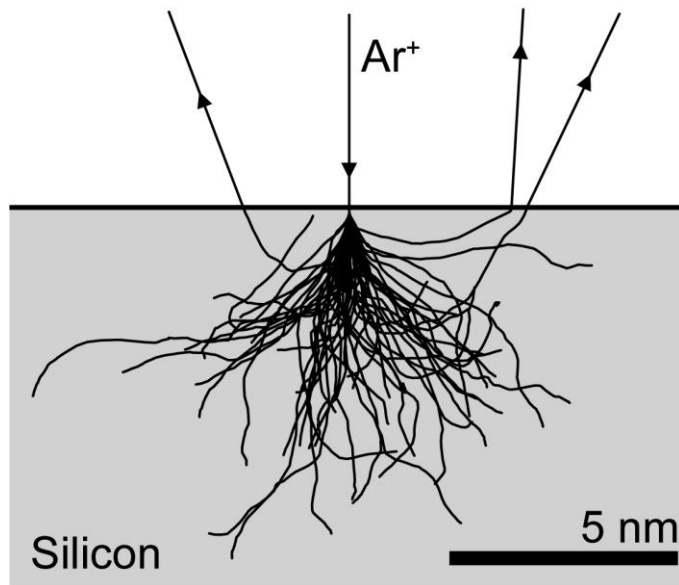


Fig. 2.2 Implant path of 60 argon ions with energy of 2000 eV impinging on silicon.

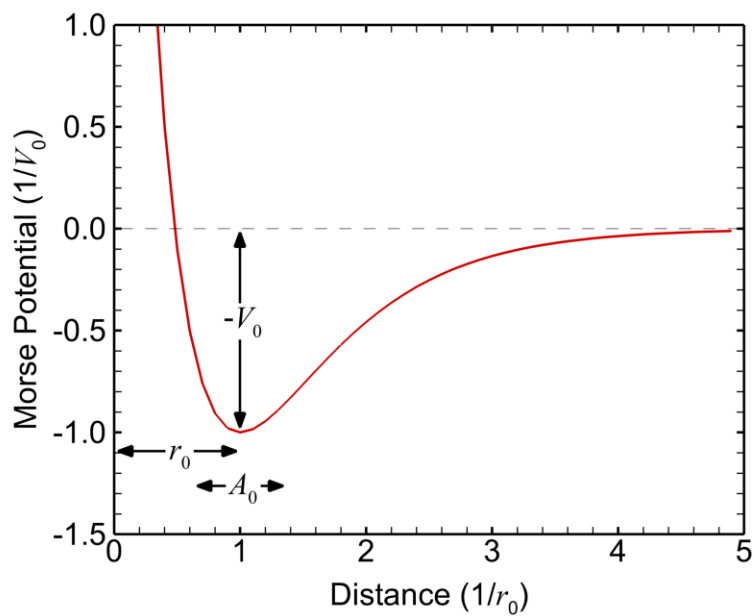


Fig. 2.3 The Morse potential used for the diffusion routine. The distance between cells  $r$  is normalized to  $r_0$  and the potential is normalized to  $V_0$ . The  $A_0$  used for this potential is 0.75.

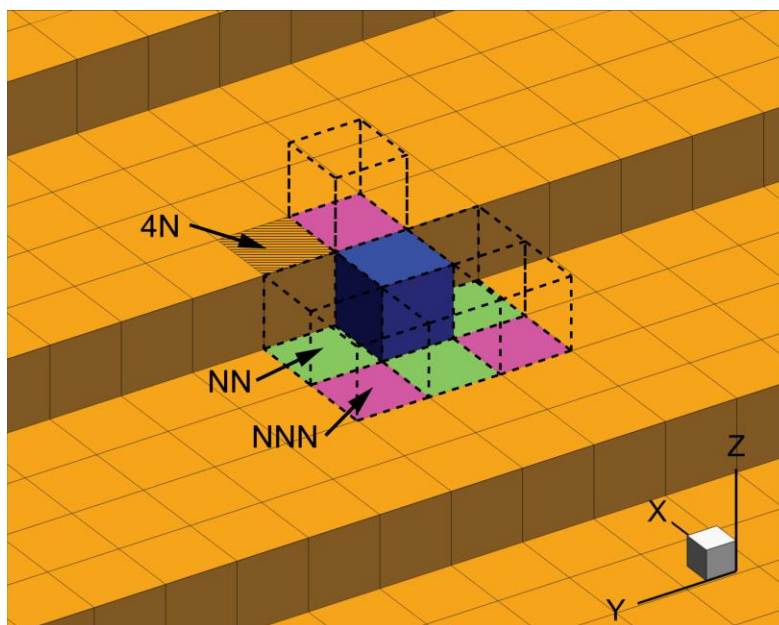


Fig. 2.4 Illustration of possible diffusion locations for a physisorbed particle, shown in blue. The dotted cubes illustrate the allowable diffusion transitions. Nearest neighbor sites are shown in green, next-nearest neighbors in purple, and a next-next-nearest neighbor as hatched. The 4N site is not an allowable direct transition from the current site.

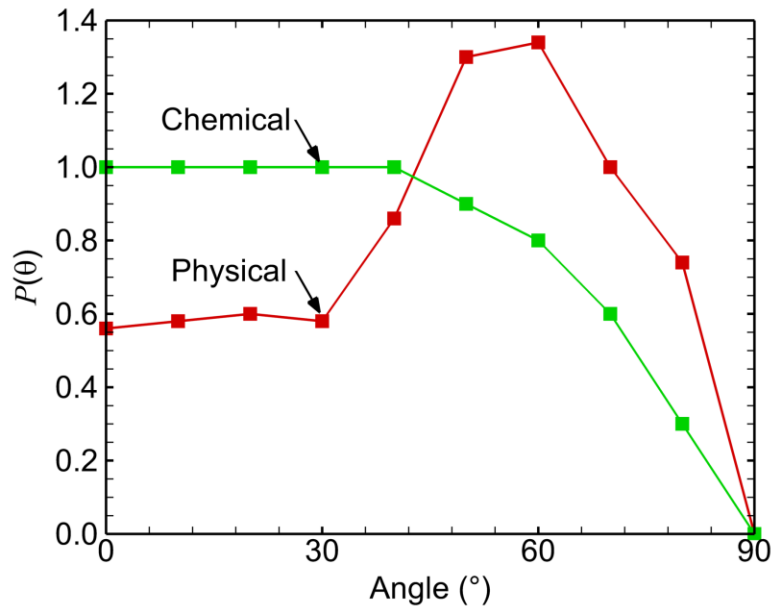


Fig. 2.5 Angular dependence functions,  $P(\theta)$ , for chemical and physical sputtering processes.

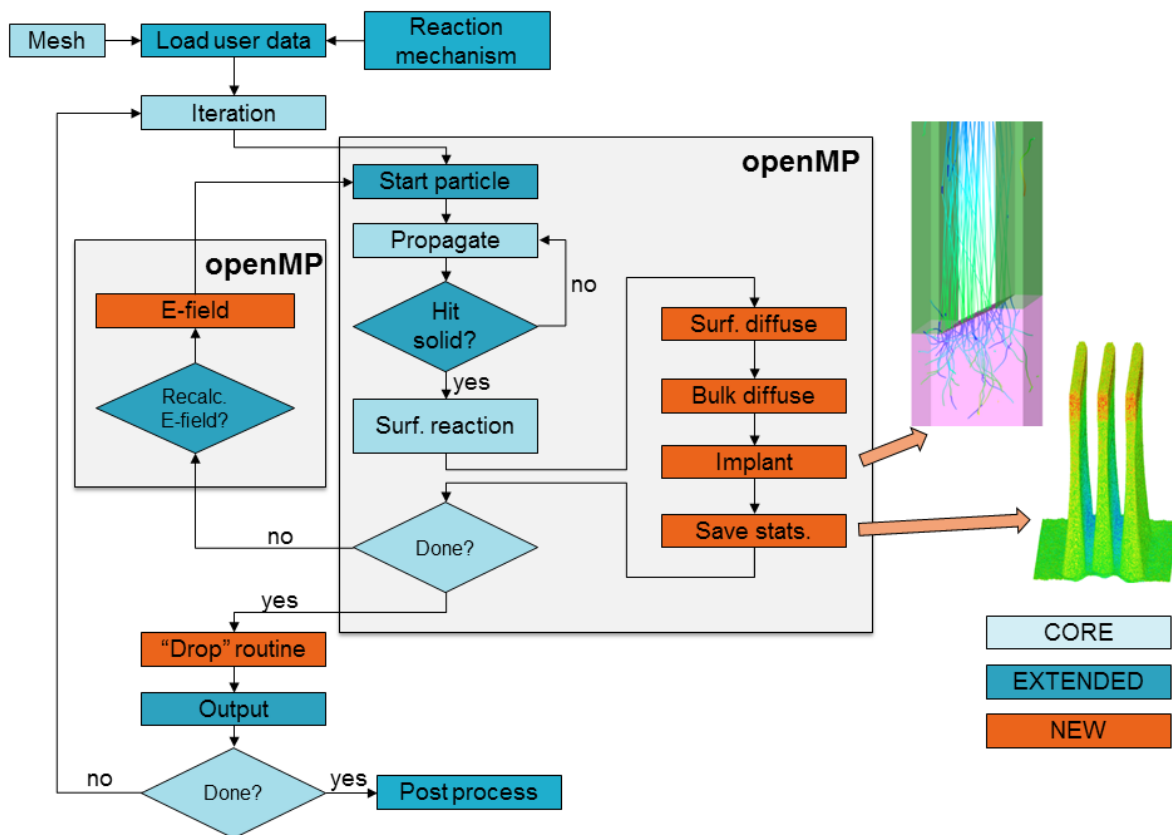


Fig. 2.6 MCFPM algorithm flow chart. Code blocks colored orange are newly developed for this thesis. Darker blue blocks had substantial updates to enable new features. Light blue blocks are unchanged from the legacy 3D code.

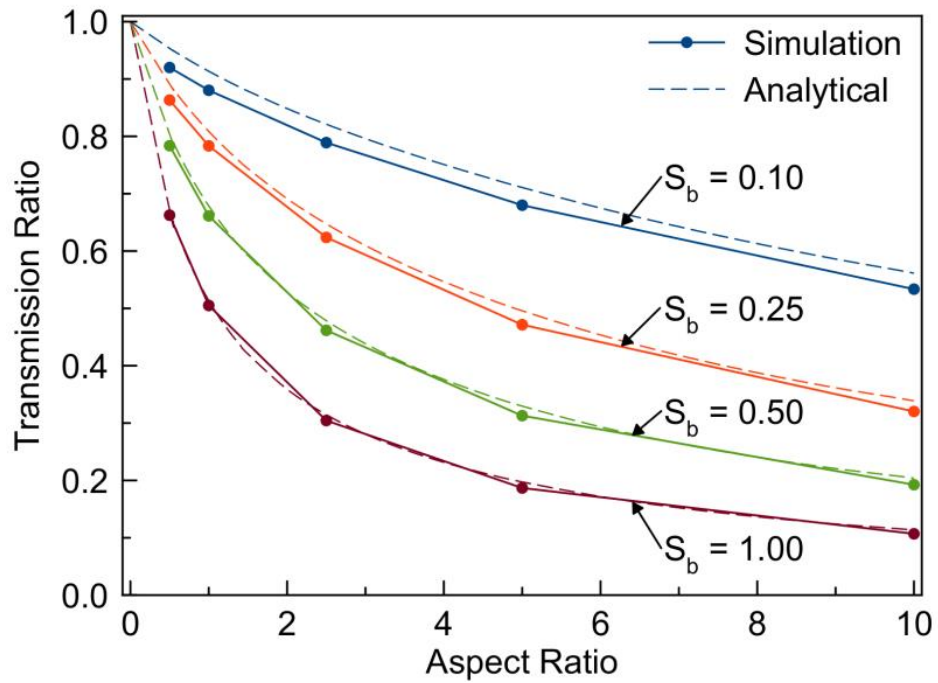


Fig. 2.7 Neutral transport simulation in MCFPM for cylindrical tubes with sticking coefficients  $S_b$  on the bottom surface. Transmission ratio is the flux of particles at the bottom of the tube, divided by the flux of particles entering the feature.

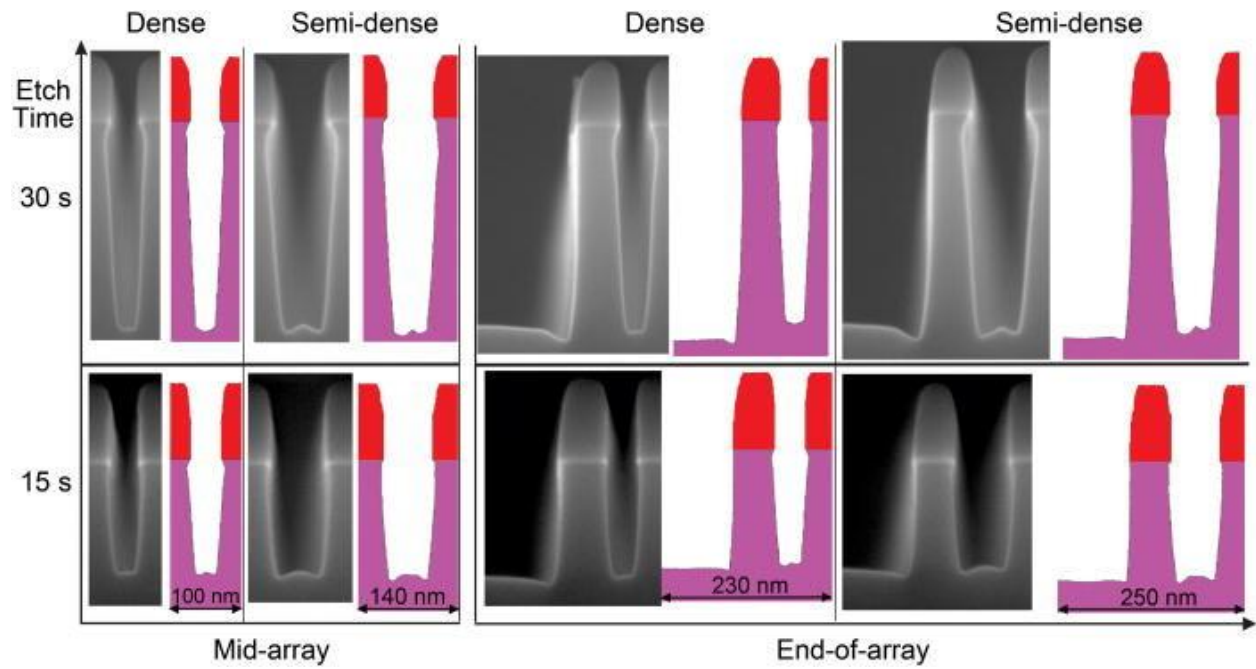


Fig. 2.8 MCFPM validation cases using He/Cl<sub>2</sub> plasma etching. Notice the close match of profile geometry in dense, semi-dense and end of array features at two different etch times.[84]

## Chapter 3 SURFACE REACTION MECHANISMS

### 3.1. Introduction

In addition to the computational framework provided by the MCFPM, as described in Chapter 2, a user defined reaction mechanism is required to represent the chemical reaction pathways possible in a given plasma surface interaction. For this mechanism to be consistent with the goals discussed in Chapter 1.5.1, it must include all relevant reactions between each gas phase species and every solid species in the mechanism. These reactions are listed in a text format, which is included as an input to the MCFPM. The types of reactions which can be described are discussed in Chapter 2.5.5.

In this thesis two different etching chemistries were used,  $\text{Cl}_2$  and  $\text{C}_4\text{F}_8$ . Both of these feedstock gases were typically diluted in argon, though some simulations of pure chlorine discharges were also used. These two gases generate very different chemistry, and require different physics to represent the plasma/surface interactions. The chlorine mechanism uses only surface reactions, described in Chapter 2.5.5. The fluorocarbon gas mechanism requires the use of the implant and diffusion models to accurately capture the physics of delivering reactive species and ion energy through a finite thickness polymer overlayer. Therefore, this reaction mechanism requires additional reactions, such as implant reactions and solid-solid reactions (described in Chapter 2.5.7), in addition to the typical surface reactions, in order to provide a complete physical picture of the plasma surface interaction.

In this chapter detailed descriptions are given of two different reaction mechanisms. In Chapter 3.2 a description is given of how the physics of chlorine/silicon etching are modeled in

the MCFPM. In Chapter 3.3, the model of the fluorocarbon surface interactions is given. This section is intended to describe the reaction mechanisms used in the work presented here, and to provide justification for the mechanisms included and reaction rates (probabilities) used. These reaction mechanisms are an integral part of the model.

### 3.2. Halogen Plasma Surface Reaction Mechanism

The etching of silicon by Ar/Cl<sub>2</sub> plasmas proceeds by first passivating the surface with chlorine. The process begins with a reaction of a Cl radical with the bare silicon surface to form SiCl<sub>(s)</sub>. Subsequent reactions with chlorine further chlorinate the SiCl<sub>(s)</sub> surface to form SiCl<sub>x(s)</sub>, where  $x < 4$ . [19,20,85] The surface reaction mechanism used in this investigation is outlined in Table 3.1. In our model, this process is represented by having a series of materials which represent different chlorination levels: Si<sub>(s)</sub>, SiCl<sub>(s)</sub>, SiCl<sub>2(s)</sub> and SiCl<sub>3(s)</sub>. Each of these materials with  $x < 3$  can undergo additional chlorination reactions, with successively lower probabilities, to increase the chlorination level to SiCl<sub>x+1(s)</sub>. The probabilities of passivation are 99%, 40% and 30% for  $x = 0, 1$  and  $2$ . As these materials are applied to entire computational cells, which can represent several atoms, they are not meant to exactly represent the chlorination state of every silicon atom in the cell, but rather they represent an increasing average surface chlorination level. At pressures above a few mTorr this chlorination process is carried out mostly by Cl radicals, however Cl<sub>2</sub><sup>+</sup> and Cl<sup>+</sup> species are also capable of chlorinating surface sites in this mechanism. Thermal etching is included, with a small probability, by the chlorination of a SiCl<sub>3(s)</sub> site by a Cl radical to form volatile SiCl<sub>4</sub> – that is, the surface site is converted to a gas phase SiCl<sub>4</sub> particle, which is emitted from the feature leaving behind a vacated surface cell.

The recombination of atomic Cl on surfaces is incorporated into the reaction mechanism as an Eley-Rideal (ER) type reaction. In this reaction, chlorine radicals impinging on SiCl<sub>x(s)</sub> ( $x$

= 2,3) sites can abstract one of the chlorine atoms from the solid surface and return to the gas phase as  $\text{Cl}_2$ , leaving  $\text{SiCl}_{x-1(\text{s})}$  on the surface. Reactions (4) and (6) in Table 3.1 show the recombination reactions and probabilities as included in the base case. We assumed that  $\text{SiCl}_{(\text{s})}$  represents a strongly chemisorbed state which does not allow recombination reactions. The reaction probabilities in the basic mechanism (Table 3.1) result in a chlorine recombination coefficient of 0.07 on a steady-state passivated surface. Due to the disordered nature of the amorphized silicon layer resulting from plasma exposure, the recombination coefficient was chosen to be between the measured values for pristine crystalline silicon ( $< 0.01$ ) and polysilicon ( $\approx 0.14$ ) in a neutral beam experiment.[86] This value is also similar to the recombination coefficient of 0.03 on a plasma exposed silicon oxy-chloride surface, as measured by Khare et al. using the spinning wall technique.[87] Cunge et al. have measured lower recombination coefficients of 0.005-0.007 on the  $\text{SiOCl}$  surfaces formed in  $\text{Cl}_2/\text{O}_2$  plasmas.[88] Although there is always some likelihood for oxygen contamination from sputtering of alumina or quartz in contact with the plasma, we expect that the proportion of  $\text{SiOCl}$  sites to be smaller than in a plasma with  $\text{O}_2$  as a feedstock gas. While the experimental data can be fit well with a Langmuir-Hinshelwood (LH) model [86,87], most of the recombination for our conditions occurs on the fully saturated sidewalls. For these saturated conditions the ER and LH models are expected to converge.

The chlorinated passivation layer has an increased sputtering yield when compared to the bulk silicon, as discussed in detail in Chapter 1.3.2. The reduction in surface binding energy increases with increased chlorination. Chemical sputtering reactions of all  $\text{SiCl}_{x(\text{s})}$  surface sites have a threshold energy of 10 eV, and values of  $p_0$  which increase with chlorine coordination. For  $\varepsilon_0 = 100$  eV,  $p_0 = 0.20, 0.50$  and  $0.50$  for  $\text{SiCl}_{1(\text{s})}, \text{SiCl}_{2(\text{s})}$  and  $\text{SiCl}_{3(\text{s})}$ . Direct sputtering of

unpassivated silicon sites was included with a threshold energy of 25 eV ( $\varepsilon_0 = 100$  eV,  $p_0 = 0.05$ ). In this model, each gas pseudoparticle can only react with a single solid cell, including sputtering reactions. This limitation poses a problem for process conditions where there are high ion energies and high neutral-to-ion flux ratios. For these conditions, experiments show that the etch yield per ion can exceed one.[23] Our sputter yield parameters were chosen to best represent experimental trends over a wide range of etching conditions while acknowledging that our etch yields will be low when operating with high ion energies and high neutral-to-ion flux ratios.

In addition to a dependence on ion energy, sputtering reactions also have a dependence on the angle of incidence of the impinging particle with respect to the local surface normal. This angular dependence for chemically enhanced sputtering involving a passivating species is typically different than for direct physical sputtering.[22,54] There is evidence that both physical and chemical sputtering mechanisms can be simultaneously active, with chemical sputtering dominating at low ion energy and physical sputtering becoming more important as ion energy increases.[89–91] Different processes, each with a different threshold energy ( $\varepsilon_{th}$ ) and reaction probability ( $p_0$ ), are used to represent these two reactions. Physical sputtering reactions have a peak in the probability for angles of incidence around  $60^\circ$ , with reduced probability at normal incidence and zero probability at grazing incidence. These reactions were given higher threshold energies than chemically enhanced processes, and lower etch probabilities for more chlorinated species. Chemically enhanced sputtering reactions have unity probability for normal incidence and angles up to  $45^\circ$ , with a monotonic roll-off above this value to zero probability at grazing incidence.

Gas species generated deep in the feature, such as etch or recombination products, must

diffuse out of the feature by molecular flow before returning to the bulk plasma. The etch products are typically neutral, often are radicals, and generally have approximately thermal energy. Radical etch products ( $\text{SiCl}_x$ ,  $x < 4$ ) have a finite probability of re-depositing within the feature each time they strike the surface. The sticking coefficients for SiCl on SiOCl coated reactor walls has been measured to be near unity, while  $\text{SiCl}_2$  has lower sticking probability of 0.05.[88] In our mechanism, a sticking coefficient of 0.02 was chosen for all  $\text{SiCl}_x$  ( $x < 4$ ) etch products on all other solid surfaces. While fluxes of  $\text{SiCl}_x$  and  $\text{SiCl}_x^+$  returning to the feature from the bulk gas have been shown to be important in industrial plasmas [92,93] their contributions have been neglected here for simplicity.

The probabilities of the reactions used for this study were chosen, wherever possible, to match available experimental data. Chemical sputtering probabilities, and their energy and angular dependence, were chosen to match experimental trends for etch yield for low ion energy.[23] Recombination probabilities are set such that a steady-state passivated surface produces a recombination coefficient of 0.07, which is between the measured values for pristine crystalline silicon and that of poly-silicon in a neutral beam experiment.[86] Passivation reactions between Cl radicals and silicon surface sites were chosen to qualitatively reproduce surface species coverage results from XPS data of  $\text{Cl}_2$  plasma etching.[94]

### **3.3. Fluorocarbon Plasma Surface Reaction Mechanism**

A new reaction mechanism was developed for the interaction between reactive species produced in an  $\text{Ar}/\text{C}_4\text{F}_8$  plasma and  $\text{SiO}_2$ ,  $\text{Si}_3\text{N}_4$  and Si. This mechanism heavily relies on the transport of reactive and energetic species through the polymer overlayer. This mechanism

should be applicable to majority of fluorocarbon plasmas that produce similar varieties of radicals.

The lowest energy etching reaction pathway involves five steps:

1. Passivation of the surface by  $CF_{x(g)}$  radicals, forming a selvedge layer where C-O (or C-N) and Si-F bonds exist.
2. Deposition of a finite thickness polymer layer on top of the selvedge layer.
3. Anion (O or N) removal from the solid by chemical sputtering, leaving  $SiF_{x(s)}$ , activated by ions penetrating through the polymer layer.
4. Etching of  $SiF_{x(s)}$  by chemical sputtering (by implanting ions) or thermal reactions with radical fluorine diffusing through the polymer.
5. Re-passivation of the underlying surface by ion mixing of surface sites with the polymer overlayer. (Repeat steps 2-5)

In addition to the reactions which make up the minimum energy etching pathway, many other reactions are possible and necessary for a complete description of the fluorocarbon etching mechanism. In this section, a description is given of the reactions involved, with a complete list of possible reactions included in this mechanism given in Table 3.2.

The mechanism relies on the formation of two distinct material regions in the overlayer which forms on the substrate; the selvedge layer, and the polymer layer. The selvedge layer is the thin region where covalent bonds exist between the fluoropolymer overlayer and the underlying material. For  $SiO_2$  this region is modeled using the species  $SiO_2C_xF_{y(s)}$ ,  $SiOC_xF_{y(s)}$  and  $SiF_{x(s)}$ . For  $Si_3N_4$  the selvedge layer is composed of  $SiNC_xF_y$  and  $SiF_{x(s)}$  species. On top of the selvedge layer a fluoropolymer (denoted  $CF_{x(s)}$ ) layer forms which is unaffected by the substrate material being etched. Taken together the selvedge and polymer layers will be referred to as the *overlayer*.

The selvedge species in the  $SiO_2$  system,  $SiO_2C_xF_y$ ,  $SiOC_xF_y$  and  $SiF_{x(s)}$ , represent different phases in the etching process. The  $SiO_2C_xF_y$  species represents a site where a  $CF_{x(g)}$

molecule has chemisorbed to a SiO<sub>2</sub> site, either by the formation of a C-O or Si-F bond. The SiOC<sub>x</sub>F<sub>y</sub> material is a site which has undergone de-oxygenation due to an ion impact reaction, such as



This reaction converts the initial SiO<sub>2</sub>C<sub>x</sub>F<sub>y</sub> cell to SiOC<sub>x</sub>F<sub>y</sub>, releasing a CO etch product. Because of the strong C-O bond, this reaction is considered a chemically enhanced sputtering reaction in this mechanism, with a low energy threshold ( $\epsilon_{th}$ ) of 10 eV. The SiOC<sub>x</sub>F<sub>y</sub> can then be de-oxygenated again by ion impact, resulting in a SiF<sub>x(s)</sub> site. Finally, the SiF<sub>x(s)</sub> site can be sputtered by low energy ions due to the strength of the Si-F bond weakening the strength of the bonding with the underlying lattice, or it can be thermally etched by radical fluorine. This process is schematically shown in Fig. 3.1. These materials are not intended to represent individual molecules, but rather the average behavior of the materials in the computational cell in question. Due to this average behavior, the exact stoichiometry of each reaction is not necessarily conserved. The etching of Si<sub>3</sub>N<sub>4</sub> proceeds through a similar pathway, but with only two seldge materials; SiNC<sub>x</sub>F<sub>y</sub> and SiF<sub>x(s)</sub>. For each silicon atom removed from the lattice, this results in the removal of only one carbon atom, as opposed to two carbon atoms in the case of SiO<sub>2</sub>C<sub>x</sub>F<sub>y</sub> etching channel. As a result, less polymer is consumed during the etching of Si<sub>3</sub>N<sub>4</sub> than SiO<sub>2</sub>.

Each of the seldge species has a reduced surface binding energy compared to the underlying lattice, meaning that it is also possible to directly chemically sputter SiO<sub>2</sub>C<sub>x</sub>F<sub>y</sub> or SiOC<sub>x</sub>F<sub>y</sub>, instead of following the pathway described above. Direct chemical sputtering of each of these materials is included in the model, but with higher energy thresholds (14 - 30 eV) and lower probability than the lowest energy pathway described above. As a result, with

predominantly low energy ions (as used for ALE) the multi-step process described above dominates. With higher ion energy ( $> 100$  eV) direct sputtering of  $\text{SiO}_2\text{C}_x\text{F}_{y(s)}$ ,  $\text{SiOC}_x\text{F}_y$  and  $\text{SiNC}_x\text{F}_y$  becomes the dominant etching pathway. Higher energy ions can also participate in physical sputtering reactions, directly removing  $\text{SiO}_2$  or  $\text{Si}_3\text{N}_4$ . Physical sputtering reactions for these materials are given a higher threshold energy (70 eV) and lower probability than chemical sputtering reactions.

The formation of a steady-state polymer overlayer is critical to the fluorocarbon plasma etching mechanism, as described in Chapter 1.3.3. In this mechanism, the steady-state behavior is achieved by allowing for chemisorption of CF and  $\text{CF}_2$  radicals on the surface of the polymer, sputtering of polymer and etching of the polymer by fluorine radicals which diffuse through the polymer volume. This process results in a deposition term in Eqn. (1.18) which is proportional to the surface area, and a loss term that has components proportional to the polymer volume. The model only includes deposition from CF and  $\text{CF}_2$  radicals due to their higher number of radical sites making them more reactive in general, though including deposition of  $\text{CF}_3$  (or  $\text{C}_n\text{F}_x$ ,  $n > 1$ ) can be incorporated by the appropriate entries into the data file representing the reaction mechanism.

The  $\text{CF}_2$  species in particular is in high abundance in the gas phase chemistries used here, and has been experimentally shown to play an important role in polymerization.[95] The sum of the polymerizing species, CF and  $\text{CF}_2$ , will be referred to as  $\text{CF}_{(2)}$  for brevity. The main polymer loss term is etching by radical fluorine, as has been seen experimentally.[30,77] Polymer etching by fluorine is a thermally driven process, given a fixed probability of 0.008 in our model. This probability is the likelihood of the F atom etching the polymer at any step during the diffusion of the F radical through the polymer. The average chance of an etching event occurring per

$F_{(g)}/CF_{x(s)}$  interaction is much higher than this value due to the multiple interactions. The exact value of this rate was adjusted to result in steady-state polymer thicknesses similar to experimental results during continuous etching.[30] In addition to polymer etching by radical fluorine, ion sputtering of the polymer surface is also included in the model with a threshold of 30 eV. Despite the relatively low threshold, the sputtering reaction is given a low probability to conform with experimental observation that sputtering plays a minimal roll in polymer loss in this system.[31]

This model also includes a polymer activation channel, whereby low energy ions can create activated polymer sites which have a larger sticking coefficient for  $CF_{(2)}$  radicals. This polymer activation mechanism models the breaking of bonds within the polymer layer, exposing a larger dangling bond density on the surface. This mechanism has been proposed to explain the higher polymer deposition rate in etch features with direct exposure to low energy ions, compared to neutral deposition of  $CF_{(2)}$  radicals without such exposure.[96,97] The ion activation process is given a negative energy dependence to model the balance between ion activation at low energies and sputtering of polymer at higher ion energies. This results in the polymer deposition term, and therefore steady-state polymer overlayer thickness, that depends on the ion energy reaching the surface.[30] The sticking coefficients for  $CF_{(2)}$  on  $SiO_2$ , un-activated polymer and activated polymer are 0.20, 0.01, and 0.03, respectively. These sticking coefficients are similar to those obtained recently by Kaler et al. in cyclic plasma beam exposure experiments.[98]

The transfer of ion energy through the polymer overlayer to the etch front is critical to this etch mechanism. Which energetic particles carry the activation energy to the etch front is difficult to analyze. In this mechanism,  $Ar^+$  is allowed to penetrate the polymer overlayer and

react sub-surface, a flux that is important during the ion bombardment phase of ALE where it is the dominant flux. During continuous etching in  $C_4F_8/Ar$  plasmas, though, the dominant ions are  $C_3F_5^+$  and  $C_2F_4^+$ . Even at the relatively low ion energies used in this study, the total kinetic energy of the arriving ion exceeds the bond energy of the molecule, implying that fragmentation of these larger ions is to be expected. Fragmentation of such ions for energies of tens to hundreds of eV has been investigated using first principals.[99] To account for fragmentation, large ions are allowed to dissociate into two fragments in the model,  $F^+$  and  $CF^*$ . The  $F^+$  particle carries the majority of the ion energy through the film to deliver the energy to the etch front. Fluorine was chosen to be the ion energy carrier because once it has cooled it will act as a source of radical fluorine, as has been previously proposed as a result of large fluorocarbon fragmentation.[77] The  $CF^*$  particle is a model construct which allows the  $CF_{x(g)}$ -like remains of the larger molecule to imbed in the polymer matrix forming a new polymer site. This process couples the polymer deposition rate to the  $C_xF_y^+$  flux, as has been seen experimentally.[100]

### 3.4. Figures

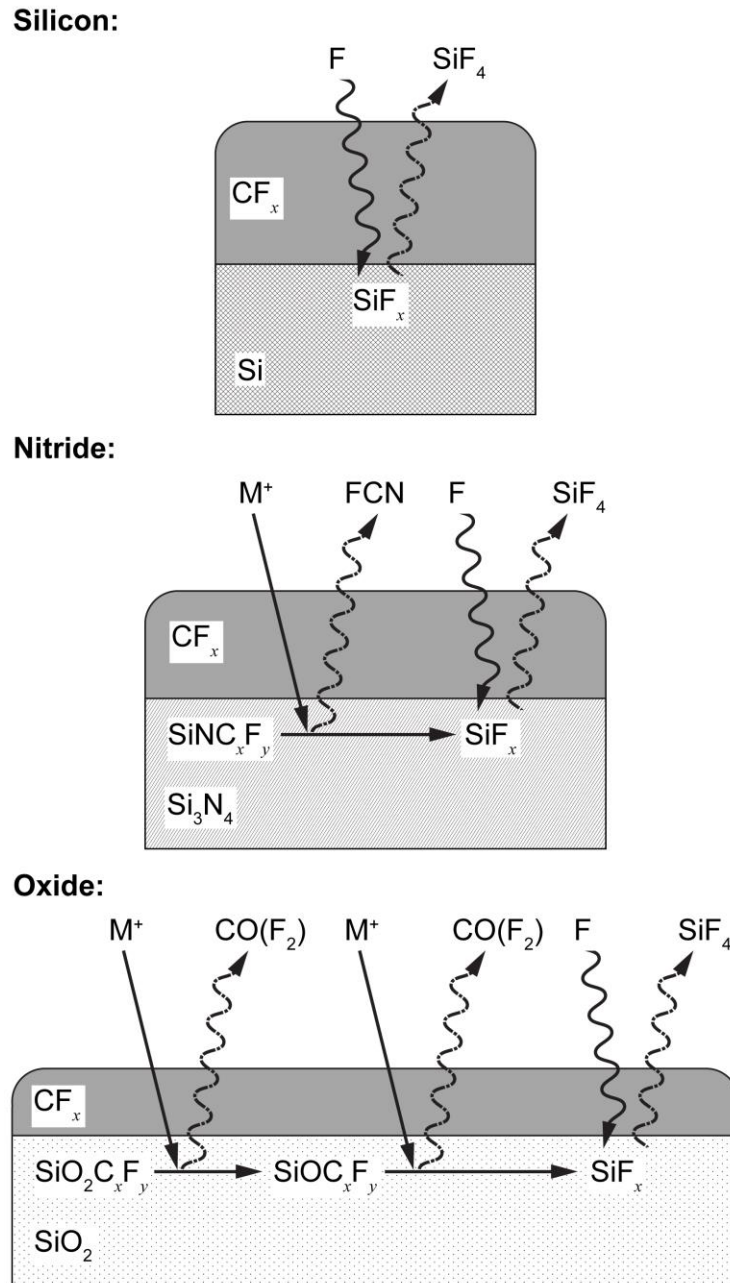


Fig. 3.1 Schematic of the Si, Si<sub>3</sub>N<sub>4</sub> and SiO<sub>2</sub> etching mechanisms. The term M<sup>+</sup> denotes activation from any ion or hot neutrals. Straight lines through the polymer overlayer imply ion implantation, while wavy lines represent diffusion through the overlayer.

### 3.5. Reaction Mechanism Tables

**Table 3.1: Chlorine Surface Reaction Mechanism**

|      | <u>Reaction</u>  | <u>Probability</u> <sup>(a)</sup> | <u><math>\epsilon_{th}</math> (eV)</u> <sup>(a)</sup> | <u><math>p_0</math></u> <sup>(a)</sup> | <u>Angle</u> <sup>(b)</sup> | <u>Notes</u> |
|------|--|-----------------------------------|---|--|-----------------------------|--------------|
|      | <i>Cl Radical Reactions</i>  |                                   |   |  |                             |              |
| (1)  | $\text{Si}_{(s)} + \text{Cl} \rightarrow \text{SiCl}_{(s)}$                      | 0.99                              |   |  |                             |              |
| (2)  | $\text{SiCl}_{(s)} + \text{Cl} \rightarrow \text{SiCl}_{2(s)}$                   | 0.40                              |   |  |                             |              |
| (3)  | $\text{SiCl}_{2(s)} + \text{Cl} \rightarrow \text{SiCl}_{3(s)}$                  | 0.30                              |   |  |                             |              |
| (4)  | $\text{SiCl}_{2(s)} + \text{Cl} \rightarrow \text{SiCl}_{(s)} + \text{Cl}_2$     | 0.02                              |   |  |                             |              |
| (5)  | $\text{SiCl}_{3(s)} + \text{Cl} \rightarrow \text{SiCl}_4$                       | 0.0001                            |   |  |                             |              |
| (6)  | $\text{SiCl}_{3(s)} + \text{Cl} \rightarrow \text{SiCl}_{2(s)} + \text{Cl}_2$    | 0.08                              |   |  |                             |              |
| (7)  | $\text{R}_{(s)} + \text{Cl} \rightarrow \text{R}_{(s)} + \text{Cl}$              | 1.00                              |   |  |                             | c            |
|      | <i>Redeposition</i>  |                                   |   |  |                             |              |
| (8)  | $\text{M}_{(s)} + \text{SiCl}_x \rightarrow \text{M}_{(s)} + \text{SiCl}_{x(s)}$ | 0.02                              |   |  |                             | d            |
|      | <i>Ion Reactions</i>   |                                   |   |  |                             |              |
| (9)  | $\text{Si}_{(s)} + \text{Cl}^+ \rightarrow \text{Si} + \text{Cl}^*$              |                                   | 25  | 0.05                                   | P                           | e,f          |
| (10) | $\text{SiCl}_{(s)} + \text{Cl}^+ \rightarrow \text{SiCl}_2$                      |                                   | 35  | 0.10                                   | P                           | e            |
| (11) | $\text{SiCl}_{(s)} + \text{Cl}^+ \rightarrow \text{SiCl}_2$                      |                                   | 10  | 0.20                                   | C                           | e            |
| (12) | $\text{SiCl}_{2(s)} + \text{Cl}^+ \rightarrow \text{SiCl}_2 + \text{Cl}^*$       |                                   | 10  | 0.50                                   | C                           | e,f,g        |
| (13) | $\text{SiCl}_{3(s)} + \text{Cl}^+ \rightarrow \text{SiCl}_3 + \text{Cl}^*$       |                                   | 10  | 0.50                                   | C                           | e,f,g        |
| (14) | $\text{R}_{(s)} + \text{Cl}^+ \rightarrow \text{R} + \text{Cl}^*$                |                                   | 15  | 0.01                                   | P                           | c,e,f        |
| (15) | $\text{Si}_{(s)} + \text{Cl}_2^+ \rightarrow \text{Si} + \text{Cl}_2^*$          |                                   | 25  | 0.02                                   | P                           | e,f          |
| (16) | $\text{SiCl}_{(s)} + \text{Cl}_2^+ \rightarrow \text{SiCl}_2 + \text{Cl}^*$      |                                   | 10  | 0.20                                   | C                           | e,f,g        |
| (17) | $\text{SiCl}_{2(s)} + \text{Cl}_2^+ \rightarrow \text{SiCl}_2 + \text{Cl}_2^*$   |                                   | 10  | 0.25                                   | C                           | e,f,g        |
| (18) | $\text{SiCl}_{2(s)} + \text{Cl}_2^+ \rightarrow \text{SiCl}_3 + \text{Cl}^*$     |                                   | 10  | 0.25                                   | C                           | e,f,g        |
| (19) | $\text{SiCl}_{3(s)} + \text{Cl}_2^+ \rightarrow \text{SiCl}_3 + \text{Cl}_2^*$   |                                   | 10  | 0.25                                   | C                           | e,f,g        |
| (20) | $\text{SiCl}_{3(s)} + \text{Cl}_2^+ \rightarrow \text{SiCl}_4 + \text{Cl}^*$     |                                   | 10  | 0.25                                   | C                           | e,f,g        |
| (21) | $\text{R}_{(s)} + \text{Cl}_2^+ \rightarrow \text{R} + \text{Cl}_2^*$            |                                   | 15  | 0.01                                   | P                           | c,e,f        |
| (22) | $\text{Si}_{(s)} + \text{Ar}^+ \rightarrow \text{Si} + \text{Ar}^*$              |                                   | 25  | 0.05                                   | P                           | e,f          |
| (23) | $\text{SiCl}_{(s)} + \text{Ar}^+ \rightarrow \text{SiCl} + \text{Ar}^*$          |                                   | 10  | 0.20                                   | C                           | e,f,g        |
| (24) | $\text{SiCl}_{2(s)} + \text{Ar}^+ \rightarrow \text{SiCl}_2 + \text{Ar}^*$       |                                   | 10  | 0.50                                   | C                           | e,f,g        |
| (25) | $\text{SiCl}_{3(s)} + \text{Ar}^+ \rightarrow \text{SiCl}_3 + \text{Ar}^*$       |                                   | 10  | 0.50                                   | C                           | e,f,g        |
| (26) | $\text{R}_{(s)} + \text{Ar}^+ \rightarrow \text{R} + \text{Ar}^*$                |                                   | 15  | 0.01                                   | P                           | c,e,g        |

**Notes:**

- (a) If  $\epsilon_{th}$  and  $p_0$  are blank the reaction has no energy dependency, and the reaction probability is constant.
- (b) Angular dependence of the reaction. P = physical sputtering, C = chemical sputtering, blank for reactions with no angular dependency.
- (c)  $\text{R}_{(s)}$  is the solid photoresist. The gas phase etch product, R, is assumed to be volatile and does not re-deposit on feature surfaces.

- (d) Re-deposition reaction.  $M_{(s)}$  denotes any solid surface.  $SiCl_x$  ( $x = 1,2,3$ ).
- (e) Energy dependent reaction with probability defined by Eq. (2.23). Probability is renormalized as necessary, as described in the text. When probability of reaction is less than unity, remaining probability is allocated to non-reactive reflection (other than neutralization of ions).
- (f) Asterisk superscript (i.e.  $Cl^*$ ) indicates a hot neutral. Hot neutrals have identical reactions and probabilities as the corresponding ion.
- (g) A reaction with the same reactants and products is also included, but with physical sputtering angular dependence,  $\epsilon_{th} = 35$  eV and  $p_0 = p_{0(c)} / 2$ , where  $p_{0(c)}$  is the  $p_0$  of the (listed) chemical sputtering reaction. Reactions (10) and (11) show this relationship explicitly.

**Table 3.2: Fluorocarbon Surface Reaction Mechanism**

|      | <b>Reaction</b>  | <b>Prob.<sup>(a)</sup></b> | <b><math>\epsilon_{fl}</math><sup>(a)</sup></b> | <b><math>p_0</math><sup>(a)</sup></b> | <b>ref<sup>(a)</sup></b> | <b>Ang<sup>(b)</sup></b> | <b>Notes</b> |
|------|--|----------------------------|---|---------------------------------------|--------------------------|--------------------------|--------------|
|      | <i>Polymer Deposition Reactions</i>  |                            |   |                                       |                          |                          |              |
| (1)  | $\text{Si}_{(s)} + \text{CF}_{(2)(g)} \rightarrow \text{Si}_{(s)} + \text{CF}_{x(s)}$  | 0.20                       |   |                                       |                          |                          | c            |
| (2)  | $\text{SiO}_{2(s)} + \text{CF}_{(2)(g)} \rightarrow \text{SiO}_2\text{C}_x\text{F}_{y(s)}$   | 0.20                       |   |                                       |                          |                          | c            |
| (3)  | $\text{Si}_3\text{N}_{4(s)} + \text{CF}_{(2)(g)} \rightarrow \text{SiNC}_x\text{F}_{y(s)}$   | 0.20                       |   |                                       |                          |                          | c            |
| (4)  | $\text{SiO}_2\text{C}_x\text{F}_{y(s)} + \text{CF}_{(2)(g)} \rightarrow \text{SiO}_2\text{C}_x\text{F}_{y(s)} + \text{CF}_{x(s)}$          | 0.20                       |   |                                       |                          |                          | c            |
| (5)  | $\text{SiOC}_x\text{F}_{y(s)} + \text{CF}_{(2)(g)} \rightarrow \text{SiOC}_x\text{F}_{y(s)} + \text{CF}_{x(s)}$                            | 0.20                       |   |                                       |                          |                          | c            |
| (6)  | $\text{SiNC}_x\text{F}_{y(s)} + \text{CF}_{(2)(g)} \rightarrow \text{SiNC}_x\text{F}_{y(s)} + \text{CF}_{x(s)}$                            | 0.20                       |   |                                       |                          |                          | c            |
| (7)  | $\text{CF}_{x(s)} + \text{CF}_{(2)(g)} \rightarrow \text{CF}_{x(s)} + \text{CF}_{x(s)}$  | 0.01                       |   |                                       |                          |                          | c            |
| (8)  | $\text{CF}_x^*(s) + \text{CF}_{(2)(g)} \rightarrow \text{CF}_{x(s)} + \text{CF}_{x(s)}$  | 0.03                       |   |                                       |                          |                          | c,d          |
| (9)  | $\text{CF}_{x(s)} + \text{CF}^*(\text{implant}) \rightarrow \text{CF}_{x(s)} + \text{CF}_{x(s)}$   | 1.00                       |   |                                       |                          |                          | e            |
|      | <i>Polymer Loss Reactions</i>  |                            |   |                                       |                          |                          |              |
| (10) | $\text{CF}_{x(s)} + \text{F}_{(g)} \rightarrow \text{CF}_{4(g)}$   | 0.008                      |   |                                       |                          |                          |              |
| (11) | $\text{CF}_x^*(s) + \text{F}_{(g)} \rightarrow \text{CF}_{4(g)}$   | 0.004                      |   |                                       |                          |                          | d            |
| (12) | $\text{CF}_{x(s)} + \text{Ar}^+(g) \rightarrow \text{CF}_{x(g)} + \text{Ar}$   |                            | 30  | 0.030                                 | 100                      | P                        |              |
| (13) | $\text{CF}_{x(s)} + \text{C}_x\text{F}_y^+(g) \rightarrow \text{CF}_{x(g)} + \text{CF}_{(2)(g)}$   |                            | 30  | 0.003                                 | 500                      | P                        | c            |
| (14) | $\text{SiO}_{2(s)} + \text{CF}_{x(s)} + \text{M}^+ \rightarrow \text{SiO}_2\text{C}_x\text{F}_{y(s)}$                                      | 1.00                       |   |                                       |                          |                          | f            |
| (15) | $\text{Si}_3\text{N}_{4(s)} + \text{CF}_{x(s)} + \text{M}^+ \rightarrow \text{SiNC}_x\text{F}_{y(s)} + \text{CF}_{x(s)}$                   | 1.00                       |   |                                       |                          |                          | f            |
|      | <i>Polymer Activation</i>  |                            |   |                                       |                          |                          |              |
| (16) | $\text{CF}_{x(s)} + \text{Ar}^+(g) \rightarrow \text{CF}_x^*(s) + \text{Ar}_{(g)}$   |                            | 150 <sup>(g)</sup>                              | 0.03 <sup>(g)</sup>                   |                          | C                        | d            |
| (17) | $\text{CF}_{x(s)} + \text{C}_x\text{F}_y^+(g) \rightarrow \text{CF}_x^*(s) + \text{F}^+(\text{implant}) + \text{C}_x\text{F}_{y(g)}$       |                            | 60 <sup>(g)</sup>                               | 0.30 <sup>(g)</sup>                   |                          | C                        | d            |
| (18) | $\text{CF}_{x(s)} + \text{C}_x\text{F}_y^+(g) \rightarrow \text{CF}_x^*(s) + \text{CF}^*(\text{implant}) + \text{F}^+(\text{implant})$     |                            | 30 <sup>(g)</sup>                               | 0.10 <sup>(g)</sup>                   |                          | C                        | d            |
| (19) | $\text{CF}_{x(s)} + \text{C}_x\text{F}_y^+(g) \rightarrow \text{CF}_{x(s)} + \text{F}^+(\text{implant}) + \text{C}_x\text{F}_{y(g)}$       | 0.95                       |   |                                       |                          |                          |              |
| (20) | $\text{CF}_{x(s)} + \text{C}_x\text{F}_y^+(g) \rightarrow \text{CF}_{x(s)} + \text{F}^+(\text{implant}) + \text{CF}_{(2)(g)}$              | 0.05                       |   |                                       |                          |                          | c            |
|      | <i>Silicon Reactions</i>   |                            |   |                                       |                          |                          |              |
| (21) | $\text{Si}_{(s)} + \text{F}_{(g)} \rightarrow \text{SiF}_{(s)}$  | 0.90                       |   |                                       |                          |                          |              |
| (22) | $\text{SiF}_{(s)} + \text{F}_{(g)} \rightarrow \text{SiF}_{2(s)}$  | 0.50                       |   |                                       |                          |                          |              |
| (23) | $\text{SiF}_{2(s)} + \text{F}_{(g)} \rightarrow \text{SiF}_{3(s)}$   | 0.50                       |   |                                       |                          |                          |              |
| (24) | $\text{SiF}_{3(s)} + \text{F}_{(g)} \rightarrow \text{SiF}_{2(s)} + \text{F}_{2(g)}$   | 0.01                       |   |                                       |                          |                          |              |
| (25) | $\text{SiF}_{3(s)} + \text{F}_{(g)} \rightarrow \text{SiF}_{4(g)}$   | 0.10                       |   |                                       |                          |                          |              |
| (26) | $\text{X}_{\text{SiF}(s)} + \text{F}_{(g)} \rightarrow \text{SiF}_{4(g)}$  | 0.90                       |   |                                       |                          |                          |              |
| (27) | $\text{Si}_{(s)} + \text{M}^+(g) \rightarrow \text{Si}_{(g)} + \text{M}_{(g)}$   |                            | 50  | 0.010                                 | 200                      | P                        |              |
| (28) | $\text{SiF}_{x(s)} + \text{M}^+(g) \rightarrow \text{SiF}_{x(g)} + \text{M}_{(g)}$   |                            | 10  | 0.010                                 | 200                      | C                        |              |
| (29) | $\text{SiF}_{x(s)} + \text{M}^+(g) \rightarrow \text{SiF}_{x(g)} + \text{M}_{(g)}$   |                            | 150   | 0.010                                 | 200                      | P                        |              |
|      | <i>Oxide Reactions</i>   |                            |   |                                       |                          |                          |              |
| (30) | $\text{SiO}_{2(s)} + \text{M}^+(g) \rightarrow \text{SiO}_{2(g)} + \text{M}_{(g)}$   |                            | 70  | 0.010                                 | 140                      | P                        |              |
| (31) | $\text{SiO}_{2(s)} + \text{C}_x\text{F}_y^+(g) \rightarrow \text{SiO}_{2(s)} + \text{CF}_{(2)(g)}$   | 0.05                       |   |                                       |                          |                          | c            |
| (32) | $\text{SiO}_{2(s)} + \text{C}_x\text{F}_y^+(g) \rightarrow \text{SiO}_2\text{C}_x\text{F}_{y(s)}$  | 0.80                       |   |                                       |                          |                          |              |
| (33) | $\text{SiO}_2\text{C}_x\text{F}_{y(s)} + \text{F}_{(g)} \rightarrow \text{SiO}_2\text{C}_x\text{F}_{y(s)} + \text{F}_{2(g)}$               | 0.01                       |   |                                       |                          |                          |              |
| (34) | $\text{SiO}_2\text{C}_x\text{F}_{y(s)} + \text{C}_x\text{F}_y^+(g) \rightarrow \text{SiO}_2\text{C}_x\text{F}_{y(s)} + \text{CF}_{(2)(g)}$ | 0.05                       |   |                                       |                          |                          | c            |
| (35) | $\text{SiO}_2\text{C}_x\text{F}_{y(s)} + \text{C}_x\text{F}_y^+(g) \rightarrow \text{SiO}_2\text{C}_x\text{F}_{y(s)} + \text{CF}_{x(s)}$   | 0.80                       |   |                                       |                          |                          |              |

|      |  |      |     |       |     |   |   |
|------|--|------|-----|-------|-----|---|---|
| (36) | $\text{SiO}_2\text{C}_x\text{F}_y(\text{s}) + \text{M}^+(\text{g}) \rightarrow \text{SiOC}_x\text{F}_y(\text{s}) + \text{CO}(\text{F}_2)_{(\text{g})} + \text{M}_{(\text{g})}$ |      | 10  | 0.800 | 75  | C |   |
| (37) | $\text{SiO}_2\text{C}_x\text{F}_y(\text{s}) + \text{M}^+(\text{g}) \rightarrow \text{SiF}_{4(\text{g})} + \text{CO}(\text{F}_2)_{(\text{g})} + \text{M}_{(\text{g})}$          |      | 50  | 0.800 | 100 | C |   |
| (38) | $\text{SiO}_2\text{C}_x\text{F}_y(\text{s}) + \text{M}^+(\text{g}) \rightarrow \text{SiF}_{4(\text{g})} + \text{CO}(\text{F}_2)_{(\text{g})} + \text{M}_{(\text{g})}$          |      | 100 | 0.800 | 125 | P |   |
| (39) | $\text{SiOC}_x\text{F}_y(\text{s}) + \text{C}_x\text{F}_y^+(\text{g}) \rightarrow \text{SiOC}_x\text{F}_y(\text{s}) + \text{CF}_{2(\text{g})}$                                 | 0.05 |     |       |     |   | c |
| (40) | $\text{SiOC}_x\text{F}_y(\text{s}) + \text{C}_x\text{F}_y^+(\text{g}) \rightarrow \text{SiOC}_x\text{F}_y(\text{s}) + \text{CF}_{x(\text{s})}$                                 | 0.80 |     |       |     |   |   |
| (41) | $\text{SiOC}_x\text{F}_y(\text{s}) + \text{M}^+(\text{g}) \rightarrow \text{X}_{\text{SiF}(\text{s})} + \text{CO}(\text{F}_2)_{(\text{g})} + \text{M}_{(\text{g})}$            |      | 10  | 0.800 | 75  | C |   |
| (42) | $\text{SiOC}_x\text{F}_y(\text{s}) + \text{M}^+(\text{g}) \rightarrow \text{SiF}_{4(\text{g})} + \text{CO}(\text{F}_2)_{(\text{g})} + \text{M}_{(\text{g})}$                   |      | 50  | 0.800 | 100 | C |   |
| (43) | $\text{SiOC}_x\text{F}_y(\text{s}) + \text{M}^+(\text{g}) \rightarrow \text{SiF}_{4(\text{g})} + \text{CO}(\text{F}_2)_{(\text{g})} + \text{M}_{(\text{g})}$                   |      | 100 | 0.800 | 125 | P |   |
|      | <i>Nitride Reactions</i>   |      |     |       |     |   |   |
| (44) | $\text{Si}_3\text{N}_{4(\text{s})} + \text{M}^+(\text{g}) \rightarrow \text{Si}_3\text{N}_{4(\text{g})} + \text{M}_{(\text{g})}$   |      | 70  | 0.010 | 140 | P |   |
| (45) | $\text{Si}_3\text{N}_{4(\text{s})} + \text{C}_x\text{F}_y^+(\text{g}) \rightarrow \text{Si}_3\text{N}_{4(\text{s})} + \text{CF}_{2(\text{g})}$                                 | 0.05 |     |       |     |   | c |
| (46) | $\text{Si}_3\text{N}_{4(\text{s})} + \text{C}_x\text{F}_y^+(\text{g}) \rightarrow \text{SiNC}_x\text{F}_y(\text{s})$   | 0.80 |     |       |     |   |   |
| (47) | $\text{SiNC}_x\text{F}_y(\text{s}) + \text{F}_{(\text{g})} \rightarrow \text{SiNC}_x\text{F}_y(\text{s}) + \text{F}_{2(\text{g})}$   | 0.01 |     |       |     |   |   |
| (48) | $\text{SiNC}_x\text{F}_y(\text{s}) + \text{C}_x\text{F}_y^+(\text{g}) \rightarrow \text{SiNC}_x\text{F}_y(\text{s}) + \text{CF}_{2(\text{g})}$                                 | 0.05 |     |       |     |   | c |
| (49) | $\text{SiNC}_x\text{F}_y(\text{s}) + \text{C}_x\text{F}_y^+(\text{g}) \rightarrow \text{SiNC}_x\text{F}_y(\text{s}) + \text{CF}_{x(\text{s})}$                                 | 0.80 |     |       |     |   |   |
| (50) | $\text{SiNC}_x\text{F}_y(\text{s}) + \text{M}^+(\text{g}) \rightarrow \text{X}_{\text{SiF}(\text{s})} + \text{CNF}_{(\text{g})}$   |      | 30  | 0.20  | 75  | C |   |
| (51) | $\text{SiNC}_x\text{F}_y(\text{s}) + \text{M}^+(\text{g}) \rightarrow \text{SiF}_{4(\text{g})} + \text{CNF}_{(\text{g})}$  |      | 50  | 0.20  | 100 | C |   |
| (52) | $\text{SiNC}_x\text{F}_y(\text{s}) + \text{M}^+(\text{g}) \rightarrow \text{SiF}_{4(\text{g})} + \text{CNF}_{(\text{g})}$  |      | 100 | 0.20  | 125 | P |   |

**Notes:**

- (a) If  $\epsilon_{th}$  and  $p_0$  are blank the reaction has no energy dependency, and the reaction probability is constant.
- (b) Angular dependence of the reaction. P = physical sputtering, C = chemical sputtering, blank for reactions with no angular dependency.
- (c)  $\text{CF}_{2(\text{s})}$  represents the sum of CF and  $\text{CF}_2$  flux.
- (d)  $\text{CF}_{x(\text{s})}$  represents the ion activated polymer, discussed in Chapter 3.3.
- (e) Reaction at end of implant path. Described in Chapter 2.5.7.
- (f) Solid-solid reaction. Occurs due to ion activation energy supplied by  $\text{M}^+$ .
- (g) Activation reaction. Probability drops linearly from  $p_0$  at 5 eV to zero at  $\epsilon_{th}$ .

## Chapter 4 ASPECT RATIO DEPENDENCE OF PLASMA ETCHING

### 4.1. Introduction

As feature sizes continue to decrease with each technology node the problem of aspect ratio dependent etching (ARDE) in plasma processing continues to challenge process development, as discussed in Chapter 1.4. Of particular interest is the role neutral transport plays in the aspect ratio dependence of etch rates, and how 3-d feature geometries affect this process. The sources of, and remedies for, ARDE are significant to several plasma etching processes, and remain a field of active research.[8,37,101]

Any etching process that relies on fluxes of reactive neutral species that arrive at the wafer with isotropic angular distributions will be subject to the effects of neutral conductance in the transport through the feature of these species from the bulk plasma to the etch front.[102] Ion fluxes are less sensitive to conductance during their transport through the feature since their angular distributions are usually anisotropic. Due to the pressures and feature length scales typically involved in plasma semiconductor processing, transport within the feature is in the molecular flow regime, meaning that the mean free path between gas phase collisions greatly exceeds the feature size.[103] In the molecular flow regime, low energy neutral species travel ballistically from surface to surface inside the feature, while typically reflecting (or being re-emitted after adsorption) from the surface with a Lambertian cosine angular distribution.[75] This process has been studied in the context of vacuum gas transport since early in the development of fluid mechanics,[26] and has also come to be understood as a major contributing factor to ARDE.[102]

Analytical models incorporating neutral transport [102,104] and computer simulations [54,59,91,105,106] have been used to investigate ARDE during plasma etching with different assumptions and levels of detail. While all robust numerical models of plasma etching of features incorporate the effects of neutral transport, the consequences of neutral conductance are sometimes difficult to discern due to the complexity of the model. Analytical models, on the other hand, can focus more directly on the topic of conductance and neutral transport, but then require simpler representations of the actual etch process. Coburn and Winters, for example, determined that if the etch front consumes incident radicals with a reactive sticking coefficient,  $S_n$ , well known vacuum conductance concepts can be used to provide insights to ARDE. They proposed that the ratio of neutral flux arriving at the etch front,  $\Gamma_f$ , compared to the incoming flux from the bulk plasma,  $\Gamma_{in}$ , could be approximated as [102]

$$\frac{\Gamma_f}{\Gamma_{in}} = \frac{K}{K + S_n - KS_n}, \quad (4.1)$$

where  $K$  is the aspect ratio dependent probability that a randomly directed neutral particle incident on the feature opening will reach the etch front. The parameter  $K$  is analogous to Clausing's transmission probability for vacuum systems if the etch front is likened to an opening to a second chamber with zero pressure.[83] The value of  $K$  can be calculated analytically for simple shapes (e.g., circular via or 2-dimensional trench), or numerically for more complicated shapes. As  $K$  decreases with increasing aspect ratio (AR), this model predicts a reduction of neutral flux to the etch front, which results in an aspect ratio dependent etch rate. The assumptions required for this expression to be valid are that the side walls do not consume neutrals, and that the reactive sticking coefficient on the etch front,  $S_n$ , is constant in time and aspect ratio.

Gottscho *et al.* expanded on the model proposed by Coburn and Winters by introducing

the concept of neutral-ion synergy.[104] The basic premise of this model is that  $S_n$  is not constant, but rather simultaneously depends on the neutral and ion fluxes at the etch front. In this model, each surface site can only be passivated once, and will then require an ion impact event before the underlying site can accept a new passivating radical. Therefore, high neutral fluxes will progressively produce smaller values of  $S_n$  since the available sites may already be occupied by reaction with earlier fluxes. Neutral starved regimes (that is, a low neutral radical flux relative to the ion flux) will have larger values of  $S_n$  since there is higher likelihood that sites will be empty. Since the neutral flux reaching the etch front depends on AR, then  $S_n$  also depends on AR. Gottscho et al. developed analytical expressions for two extreme cases – perfectly diffusive walls (molecular flow), and perfectly absorbing walls (neutral shadowing). Most actual etching processes fall between these two extremes. The model has provided valuable insights for understanding the implications of the neutral-ion synergy and has been used to fit to experimental studies.[107]

There are at least two complicating factors when applying analytical models of neutral transport to predicting etch properties for even basic features – neutral consumption by the side walls and varying conductance with profile evolution. Neutral species can be consumed on the side wall through several processes, including recombination of radicals on the surface to form non-reactive molecules [86] and passivation of exposed silicon sites where off-axis ions have eroded the passivation layer. In addition to changing with aspect ratio, neutral conductance can also significantly change with the shape of the profile. For instance, a tapered feature will have a different conductance than a feature with parallel sides. This issue is further complicated by a profile transitioning from a flat-bottomed cylinder or a trench with parallel sides, to a tapered profile as a function of aspect ratio. These changes in profile also have significant effects on the

area of the feature that receives high energy particles (ions and hot neutrals following ion neutralization on side walls) which then defines the etch front. These dependencies can lead to significant changes in the effective value of  $S_n$ , again impacting the transport of neutral radicals.

When etching simple geometries, such as infinite trenches or circular vias, it is straight forward to establish an aspect ratio – usually height divided by width. This AR can then function as a scaling parameter to describe neutral transport. The ability to so simply specify an AR does not necessary translate to 3-d structures. Since the molecular flow of neutral species through a 3-d feature takes place through many adsorption and re-emission events which sample different portions of the 3-d feature, it is difficult to a priori estimate the conductance between the bulk plasma and any given point on the profile. These issues complicate the extrapolation of our understanding of conductance effects on etching from 1-d (e.g., circular vias) or 2-d (e.g., infinite trenches) structures to 3-d features. The use of numerical models is necessary to accurately evaluate the scaling of neutral transport in features with difficult to define aspect ratios.

To investigate the role of neutral transport on ARDE, and particularly in 3-d etching processes, the MCFPM was used to simulate the etching process in a variety of ARDE producing conditions. A feature which resembles the shallow trench isolation (STI) etch that defines the silicon fins in a FinFET fabrication process has been used for this study. The model system is an inductively coupled plasma sustained in an Ar/Cl<sub>2</sub> mixture etching silicon. Several experimental parameters such as the incoming neutral to ion flux ratio and recombination probability of radical Cl atoms on the side walls were varied to determine their effect on ARDE when simultaneously etching several features having different critical dimensions (CD). In order to gain additional insights to the causes of ARDE for these conditions, the etch depth dependent fluxes of neutrals and ions to the etch front in a 2-d trench were also investigated. We found that for the conditions

investigated in this chapter, the dominant cause of ARDE is the depletion of neutral species reaching the etch front relative to ions as the AR increases due to neutral transport issues. We also found that increasing the neutral flux reaching the etch front relative to the ion flux can alleviate ARDE for small to moderate AR ( $< 8$ ), but at the expense of producing more tapered features and sometimes increasing ARDE at larger AR.

The scaling of ARDE (Chapter 4.2) is discussed as a function of the ratio of neutral-to-ion fluxes (Chapter 4.3), recombination of chlorine radicals (Chapter 4.4), neutral angular distributions (Chapter 4.5), ion angular distributions (Chapter 4.6) and width of the feature (Chapter 4.7). The dominant factors affecting ARDE are discussed in Chapter 4.8. A summary of the results, and concluding remarks are given in Chapter 4.9.

## **4.2. Scaling of ARDE**

The reactor used in this study is an inductively coupled plasma etch chamber. The reactor geometry is 22.5 cm in diameter and is shown in Fig. 4.1(a). For all simulations 150 W of power was delivered to the plasma through a 3-turn antenna (powered at 10 MHz) located above a quartz window 10 cm from the wafer surface. The wafer (15 cm diameter) was mounted on a metallic chuck with an applied radio frequency (rf) bias having an amplitude of 150 V at 10 MHz. The gas mixture was  $\text{Ar}/\text{Cl}_2 = 80/20$  with an incoming flowrate of 200 sccm. The chamber was maintained at 20 mTorr pressure by adjusting the outflow pumping rate, as in a feedback controlled gate valve. The resulting maximum positive ion density, shown in Fig. 4.1(a), is  $3.4 \times 10^{11} \text{ cm}^{-3}$  and the electron density is  $1 \times 10^{11} \text{ cm}^{-3}$ , indicating an electronegativity of about 2.5. The resulting dc bias on the substrate is  $-113 \text{ V}$ , which generates IEADs to the substrate that are bimodal with peaks around 125 eV and 325 eV and average angular distributions of  $\pm 2.22^\circ$  (half-width-half-max), as shown in Fig. 4.1(b). These IEADs were used

for all cases discussed here, unless specified otherwise. The fluxes to the substrate used in the simulations (unless specified otherwise) are  $\text{Cl} = 2.2 \times 10^{17} \text{ cm}^{-2} \text{ s}^{-1}$ ,  $\text{Cl}^+ = 1.0 \times 10^{16} \text{ cm}^{-2} \text{ s}^{-1}$ ,  $\text{Cl}_2^+ = 8.3 \times 10^{15} \text{ cm}^{-2} \text{ s}^{-1}$  and  $\text{Ar}^+ = 6.1 \times 10^{14} \text{ cm}^{-2} \text{ s}^{-1}$ , which were adjusted from the HPEM results to give a smaller neutral to ion ratio reaching the wafer.

With the goal of understanding the consequences of neutral transport on ARDE when etching 3-d features having different effective aspect ratios, a model geometry similar to the shallow trench isolation etch used to define the fins in a FinFET process was used. The feature consists of 30 nm wide fins with a pitch of 80 nm and a finite length of 400 nm, as shown in Fig. 4.2. The fins are arranged in a sub-array of 3 fins separated from other sub-arrays by a 200 nm gap in the transverse (X) direction, and 100 nm in the longitudinal (Y) direction. The actual simulation domain consisted of one sub-array of 3 fins, with periodic boundary conditions, having the effect of simulating a larger array of identical structures. The region having a lower aspect ratio in the area between the sub-arrays is referred to as the *open field*.

The resulting 3-d etch profile is shown in Fig. 4.3. In the 50 nm wide trenches between the fins, the total etch depth is significantly smaller than in the open field between the sub-arrays, as shown in Fig. 4.3(b). These trends indicate that there is an ARDE effect in the base etching mechanism. In addition to lower etch rates in the high AR trenches, etch depth is also a function of position along the finite trench, visible in Fig. 4.3(a) and discussed below, resulting in a significantly deeper trench at the ends of the finite length fins than in the middle of the feature.

The origins of the differences in total etch depth between the 50 nm wide trenches and the open field in the transverse X-section; and along the longitudinal length of the trenches (Y-direction), lie with the relative values of power density and neutral flux to these surfaces, as shown in Fig. 4.4. The power density delivered to the horizontal surfaces by energetic ions,

shown in Fig. 4.4(a), is nearly uniform along the length of the trenches, as well as in the open field. This lack of sensitivity to AR results from the ion angular distribution being sufficiently anisotropic (that is, a narrow angular distribution about the wafer surface normal), and the side wall scattering being sufficiently specular, that the view-angle to the plasma of sites on all horizontal surfaces subtends the majority of the ion fluxes.

On the other hand, the flux of chlorine radicals incident onto surfaces, shown in Fig. 4.4(b), decreases from the top of the feature to the bottom, as well as decreasing longitudinally from the open field at the ends of the trench to the center of the trench. This strong dependence of neutral radical fluxes on the vertical position within the trench implies an aspect ratio dependence. This dependence on AR results from the flux of chlorine radicals incident onto the etch feature being essentially isotropic in the direction towards the wafer, and relying on diffusive neutral transport to reach the etch front. The relative insensitivity of power density to the etch front as a function of AR, compared to the strong dependence of neutral flux, indicates that neutral transport likely dominates the ARDE process for this mechanism. The longitudinal dependence of the chlorine flux and etch rate along the trench indicates a significant 3-d component to neutral transport. There is an *effective aspect ratio* which depends on etch depth and proximity to the open field at the ends of the trench. The effective aspect ratio is larger in the center of the trench and smaller near the ends.

The lower effective aspect ratio near the ends of the trenches is partly due to an increase in the view-angle to the plasma at the ends of the trench relative to the view-angle to the plasma in the center of the trench. This larger view-angle intercepts more of the isotropic flux of Cl atoms than at the center of the trench. There is also a contribution of diffusively scattered Cl atoms from the surface of the open field adjacent to the trench. These diffusively reflected Cl

atoms enter the trench from the end, often near the bottom of the feature. This proximity to the etch front, combined with the stochastic nature of the molecular flow of neutral species in the feature, results in these Cl atoms having a much larger probability of reaching the etch front compared to Cl atoms entering the feature from the top. These conditions can be interpreted as a reduction in the effective aspect ratio at the longitudinal ends of the finite length fins due to the proximity to the open field.

Etching of the same FinFET layout having different fin lengths – 200, 400 and 600 nm – was simulated to estimate the range of feature dimensions susceptible to these 3-d transport issues. The results are shown in Fig. 4.5. At the center of the 600 nm fin there is a region of nearly uniform etch depth with an aspect ratio of  $\approx 10$ , based on the width of the trench and etch depth of the feature at that point. At the ends of the fin, the trench is the nearly the same depth as the open field (ignoring microtrenching), which has an aspect ratio of  $\approx 3.5$ . There is a 200 nm long region, starting at the ends of the 600 nm fin and progressing toward the center, where the etch front transitions from the etch depth of the open field to the shallower etch depth at the center of the fin. This region of varying etch depth is sensitive to the 3-d transport of neutral radicals entering from the ends of the fin in addition to those radicals entering from the top of the feature. At shallower total etch depths (not shown), there are smaller differences in etch depth between the center of the trench and the open field. However, the length along the trench that is sensitive to 3-d transport is approximately the same.

The etch depth for the 200 nm fin is a function of position along its entire length, indicating that 3-d transport of Cl radicals is important throughout the feature. The etch depth for the 600 nm fin is constant for the center half of the trench, a region that is not overly sensitive to 3-d transport. The 400 nm fin lies somewhere between these two extremes, having a short

length in the center of the trench which is not sensitive to 3-d transport of Cl radicals. These trends indicate that it may be useful to consider an effective *horizontal aspect ratio*. This metric is the ratio of horizontal distance from a site to the open field divided by the width of the feature (50 nm in this case). This feature and reaction mechanism has a local etch rate which depends on horizontal aspect ratio up to  $\approx 4$ , above which 3-d transport issues no longer dominate.

To investigate the effects of ARDE without the complications of 3-d transport resulting from end effects, simulations were performed of etching effectively 2-d trenches having different widths – 33 nm, 50 nm and 67 nm. These profiles were modeled in 3-d while using periodic boundary conditions at the open ends of the features, which has the result of making the trench appear to be infinitely long. The three features were etched during the same simulation to minimize the stochastic effects that might result from separate simulations. The resulting etch profiles, shown in Fig. 4.6(a), have a dependence of final etch depth on feature size, with smaller features etching slower than larger ones. (The lines in each of the features show intermediate profiles at the same times.) In the time required to etch the 67 nm (left-most) trench to a depth of 600 nm, the 50 nm (center) trench has only etched to a depth of 540 nm and the 33 nm (right-most) trench has only reached a depth of 450 nm. The differences in etch depth increase with increasing etch time.

The yield for chemically enhanced sputtering in our mechanism increases for increasingly chlorinated silicon sites. The chlorination state of the site is therefore an important metric when evaluating etch results. The normalized surface concentrations of  $\text{SiCl}_x(\text{s})$  at four points along the profile of the 67 nm trench are shown in Fig. 4.6(b). The upper portion of the trench under the resist is heavily chlorinated, with an average of 2.8 chlorine atoms per silicon surface site. The concentrations at the middle of the side wall (labeled 2 in Fig. 4.6) are similar

to that higher in the trench (labeled 1). The concentrations 10 nm above the bottom of the features (labeled 3) have significantly more SiCl and bare silicon sites, with a proportional decrease in the SiCl<sub>3</sub> coverage, having an average of 2.2 Cl atoms per surface site. This lowering of the chlorination is dominantly due to primary ions impacting the mildly sloped side walls and etching these sites. Primary ion impacts with the side walls, even at this side wall slope, are at grazing angles and mostly reflect off the surface becoming hot neutrals. Nonetheless, a significant number of SiCl<sub>3</sub> sites are being etched at this location in the profile. These heavily chlorinated Si sites are consistent with XPS measurements of Petit-Etienne et al. who observed that nearly half of the SiCl<sub>x</sub> sites in similar Cl<sub>2</sub> plasmas are composed of SiCl<sub>3</sub>. [94]

The chlorination density of the horizontal etch front at the bottom of the feature provides insights to the origins of ARDE. Ion starved processes (etch rate limited by the flux of ions) have a high chlorination density at the etch front. Neutral starved processes (etch rate limited by the flux of Cl atoms) have lower chlorination and bare Si sites. At the bottom of the 67 nm wide trench with an etch depth corresponding to an aspect ratio of 3.25, the surface sites are 14% bare Si, 29% SiCl, 26% SiCl<sub>2</sub> and 30% SiCl<sub>3</sub>, resulting in an average of  $\approx 1.7$  chlorine atoms per surface site. After etching to an aspect ratio of 10.4 the surface sites are 34% bare Si, 43% SiCl, 16% SiCl<sub>2</sub> and 7% SiCl<sub>3</sub>, with  $\approx 0.95$  chlorine atoms per surface site, as shown in Fig. 4.6(b). The changing composition of chlorination as a function of depth and aspect ratio contributes to ARDE.

The surface chlorination as a function of etch depth is shown in Fig. 4.7 for each of the three feature widths. Each feature has two distinct regimes to the surface chlorination. The surface chlorination decreases as etch depth increases with a slope inversely proportional to feature width for small etch depths. At larger etch depths the surface chlorination is nearly

independent of etch depth, though lower for narrower features. The etch depth at which the chlorination becomes constant depends on the width of the feature – shallower depths for narrower features – however the depth corresponds to an AR of 7 for each feature. The fluxes of the initially isotropic Cl atoms that reach the bottom of the feature decrease with etch depth. The fact that the chlorination eventually becomes independent of etch depth for all feature widths implies the chlorination is not solely a function of the transport of radicals from the bulk plasma through the trench. At these etch depths a significant fraction of the Cl atoms producing surface passivation is delivered by ions having anisotropic trajectories. These Cl atoms are delivered either directly to the surface or following neutralizing, grazing collisions on the side walls. This decrease in chlorine passivation on the surface of the etch front with increasing aspect ratio significantly effects the etch rate, and directly contributes to ARDE.

The consequences of transport of energetic particles (ions and hot neutrals) also play a role in the profile evolution and ARDE. Two such consequences are micro-trenching and ion funneling. Micro-trenches are the small features of localized deeper etching at the foot of vertical, or nearly vertical, side walls. These micro-trenches occur at the base of the side walls adjacent to the open field of our 3-d test structure, as shown in Fig. 4.3. Micro-trenches are the result of the specular reflection of grazing incidence ions (or hot neutrals) from the side walls, effectively increasing the power density delivered to the corners of the trench.[108,109] In the 67 nm trench shown in Fig. 4.6(a), and to a lesser extent the 50 nm trench, micro-trenches appear at aspect ratios of about 3-6. As the etch progresses, the slight taper of the profile begins to draw the micro-trenches together until they merge. After the micro-trenches have merged, ions reflected by grazing collisions with the tapered side walls impinge on the entire etch-front as opposed to the isolated corners. When combined with the primary anisotropic ions from the

plasma, the additional contributions of the reflected ions can increase the etch rate in the feature as a whole. This effect will be referred to here as *ion funneling*. After the onset of ion funneling, the etch continues with a relatively flat etch front. The width of the etch front after the micro-trenches have merged remains fairly constant and is proportional to the CD of the respective feature, which is the width of the photoresist opening in these cases.

### 4.3. Neutral to Ion Flux Ratios

If neutral starvation in the areas of a 3-d feature having high AR is a dominant cause of ARDE, then increasing the ratio of neutral fluxes to ion fluxes is potentially a means to reduce ARDE. While these two fluxes are usually linked through the properties of the plasma producing the fluxes, artificially adjusting the fluxes provides insights to the causes of ARDE. In this regard, the magnitude of the incident ion flux ( $\Gamma_i$ ) was varied while keeping the shape of the IEAD and the incident neutral flux ( $\Gamma_n$ ) constant. Simulated profiles for etching the FinFET structure with  $\Gamma_n/\Gamma_i = 5, 10$  and  $20$  (the base case has  $\Gamma_n/\Gamma_i = 11.6$ , for reference) are shown in Fig. 4.8(a). The etch rate in the open field is highly dependent on the  $\Gamma_n/\Gamma_i$  ratio, which complicates making comparisons at equal etch times. For example, the initial etch rates for the first 6 s in the 50 nm trench are 1.66, 1.04, 0.58 and 0.41 times that of the base case for  $\Gamma_n/\Gamma_i = 5, 10, 20$  and  $30$ . This trend indicates that the etch rate in the open field is dominantly ion starved – there is sufficient Cl radical flux to nearly fully passivate sites and so the etch rate increases nearly linearly with increasing ion flux. As discussed previously, for a given ion flux ARDE depends on the arrival of neutral flux at the etch site. As a result, ARDE behaves as though the process is neutral starved, higher ratios of  $\Gamma_n/\Gamma_i$  reduce the dependence of etch rate on etch depth. Lower or higher absolute etch rates do not necessarily correspond to more or less sensitivity to ARDE.

To minimize the consequences of absolute etch rates and so emphasize ARDE, the profiles marked  $D_1$  and  $D_2$  in Fig. 4.8(a) are shown at equal etch depths in the open field instead of equal etch times. Larger  $\Gamma_n/\Gamma_i$  results in more tapered features in the trenches, while lower  $\Gamma_n/\Gamma_i$  (higher ion flux) produces a more ideal, flat bottomed profile. No micro-trenching is evident inside the trenches because the widths of the expected micro-trenches are commensurate with the width of the feature. However, the tapered side walls indicate that ion funneling may be important. On the other hand, there is micro-trenching at the base of the side wall facing the open field, and the degree of micro-trenching is sensitive to  $\Gamma_n/\Gamma_i$ . Larger values of  $\Gamma_n/\Gamma_i$  produce more micro-trenching.

The ratio  $\Gamma_n/\Gamma_i$  also affects ARDE. As a reference, the etch depth in the open field suffers from little, if any ARDE. At the intermediate level,  $D_1$ , the etch depth in the trenches for  $\Gamma_n/\Gamma_i = 20$  is nearly the same as that in the open field, whereas the etch depths for the lower values of  $\Gamma_n/\Gamma_i$  lag behind the open field. At the deeper level,  $D_2$ , the etch depth for  $\Gamma_n/\Gamma_i = 20$  begins to lag behind that of the open field, indicating the onset of ARDE, an effect that is more pronounced with decreasing  $\Gamma_n/\Gamma_i$ .

The dependence of ARDE on  $\Gamma_n/\Gamma_i$  also changes with aspect ratio. Normalized etch rates as a function of  $\Gamma_n/\Gamma_i$  are shown in Fig. 4.8(b) for two values of AR. Note that each  $\Gamma_n/\Gamma_i$  is normalized to its own initial etch rate. If the results were normalized to a single etch rate in the open field – say, that of the base case – the line labeled “Open Field” would be sloped. The etch rates for each AR are obtained at different times for different values of  $\Gamma_n/\Gamma_i$  which is due to the difference in absolute etch rates. For AR=10, the normalized etch rate monotonically increases by 46%, from 0.50 to 0.73, for  $\Gamma_n/\Gamma_i$  increasing from 5 to 30. At AR = 6 (which corresponds approximately to when ion funneling begins) the dependence of normalized etch rate on  $\Gamma_n/\Gamma_i$  is

stronger. The normalized etch rate increases by 66%, from 0.70 to 1.16 times the etch rate in the open field, for  $\Gamma_n/\Gamma_i$  increasing from 5 to 30. For  $\Gamma_n/\Gamma_i > 20$ , the taper of the feature is severe enough that ion funneling increases the etch rate above that of the open field. Etch rates in the trench that are higher than the open field occur, in this model, only over a small range of AR, as discussed below.

To more quantitatively investigate the consequences of  $\Gamma_n/\Gamma_i$  on ARDE, etching of 2-d trenches with a width of 50 nm were simulated for  $\Gamma_n/\Gamma_i = 5$  to 30. The resulting profiles are shown in Fig. 4.9 for  $\Gamma_n/\Gamma_i = 5, 10$  and 20. Lower values of  $\Gamma_n/\Gamma_i$  etch faster for the entire duration of the etch while larger values of  $\Gamma_n/\Gamma_i$  produce more tapered profiles, similar trends as in the 3-d structures. The large difference in etch rate when varying  $\Gamma_n/\Gamma_i$  makes it difficult to directly assess ARDE from the raw profiles, requiring us to employ the computational metrics described previously, along with normalization.

The instantaneous etch rates of the 2-d trenches as a function of aspect ratio are shown in Fig. 4.10(a). The etch rates for each value of  $\Gamma_n/\Gamma_i$  are individually normalized to their own initial etch rate. In general, the etch rates decrease with increasing AR for all values of  $\Gamma_n/\Gamma_i$ . The etch rates for  $\Gamma_n/\Gamma_i \geq 20$ , though, are peaked at  $AR \approx 6$ , which produces a range of AR that is relatively free of ARDE. ARDE then begins at  $AR \approx 6$  and by  $AR = 10-12$  the etch rate as a function of AR for  $\Gamma_n/\Gamma_i \geq 20$  is similar to the smaller values of  $\Gamma_n/\Gamma_i$ . Lower values of  $\Gamma_n/\Gamma_i$  have normalized etch rates that decrease with increasing AR over the entire range studied.

Power densities, normalized to their initial values, and Cl fluxes to the etch front are shown in Fig. 4.10(b) as a function of AR for different values of  $\Gamma_n/\Gamma_i$ . Since the shape of the IEAD is kept constant, the average ion energies incident into the feature are also constant. Doubling the relative number of incoming ions (by halving  $\Gamma_n/\Gamma_i$ ) therefore also doubles the

power density at the etch front, resulting in initial power densities of 0.80, 0.39, 0.19 and 0.12 W/cm<sup>2</sup> for  $\Gamma_n/\Gamma_i = 5, 10, 20$  and 30. For  $\Gamma_n/\Gamma_i = 20$  and 30, cases which exhibit peaked normalized etch rates at  $AR \approx 6$ , the power density has a peak beginning at  $AR = 6$ . This peak in power density is due to ion funneling.

The incoming flux of chlorine atoms was held constant. The differences between chlorine fluxes to the etch front at high aspect ratios for different values of  $\Gamma_n/\Gamma_i$  are likely due to the contributions from Cl atoms that were generated by ion impact with the etch front or from the side walls. These contributions result from neutralization and subsequent thermalization of  $Cl^+$  or the disassociation of  $Cl_2^+$  upon impact. Since any ion incident onto the etch front will eventually thermalize (if the ion does not react), the majority of the flux of  $Cl^+$  and a fraction of the  $Cl_2^+$  flux will produce a source of chlorine radicals deep within the feature. These radicals can then diffuse up the feature and into the bulk gas. However, they will do so with a fairly low probability due to the low conductance of the feature at these large aspect ratios. It is more likely that the neutralized and thermalized ions will first strike the etch front before diffusing out the feature and so be included in the measurement of Cl flux. The Cl atoms originating from ions thereby appear as an additional source of Cl flux to passivate the surface. The ion flux for  $\Gamma_n/\Gamma_i = 5$  is larger and so there is a larger flux of Cl atoms at high AR. The same argument can be applied to the peak in the chlorine flux occurring at  $AR \approx 6$  for the  $\Gamma_n/\Gamma_i \geq 20$  cases. In this case, the small increase in the flux of Cl atoms is due to ions that reflect from the tapered walls and are directed into the etch front window.

The range of  $\Gamma_n/\Gamma_i$  studied here, from 5 to 30, is not inclusive of all  $Cl_2$  etch processes. Due to the high disassociation fraction of  $Cl_2$  at high power,  $\Gamma_n/\Gamma_i$  can be as large as several hundred.[110] To verify that the trends observed at lower  $\Gamma_n/\Gamma_i$  persist to a higher flux ratios,

simulations were also performed at  $\Gamma_n/\Gamma_i = 100$ . The results indicate that the observed trends continue into this regime. The etch rate, Cl flux and power density all appear qualitatively similar to the case of  $\Gamma_n/\Gamma_i = 30$ , but with more exaggerated peaking around an AR of 6. The trend of increased tapering also continues with increasing  $\Gamma_n/\Gamma_i$ , which complicates the use of our computational diagnostics. These measurement techniques are most reliable for features having relatively flat bottoms, and so do not provide consistent results as features begin to significantly taper. For the remainder of the parameters investigated here, etch conditions were limited to those which produce a relatively flat etch front up to an AR of at least 10 where neutral transport issues are expected to be most influential.

#### **4.4. Chlorine Recombination**

The recombination of atomic Cl on surfaces to become non-reactive  $\text{Cl}_2$  can also significantly contribute to ARDE. The initial flux of Cl atoms entering the feature is essentially isotropic, and so the view-angle to the plasma from points deep inside the feature only subtends a small fraction of the incoming neutral flux. Therefore, the vast majority of Cl atoms that reach the etch front at high aspect ratio have reflected from the inner side walls or have been emitted by the walls due to chemical reactions. There may be many such reflections prior to a Cl atom reaching the etch front. The availability of Cl atoms at the etch front is therefore a function of the rate of surface recombination on side walls, and so ARDE will be sensitive to the recombination coefficient,  $S_r$ , of Cl atoms on the side walls. Etching of the 3-d FinFET feature was simulated using values of  $S_r$  from 0.00 to 0.16; representing the range from the low recombination rate on pristine crystalline silicon to values close to that of poly-Si at room temperature.[86] The resulting profiles are shown in Fig. 4.11 for  $S_r = 0.00, 0.04$  and  $0.16$ , and suggest that radical recombination on side walls does indeed have a significant effect on

ARDE for these conditions. Profiles are shown at two etch times,  $t_1$ , approximately half-way through the etch, and  $t_2$ , at the end of the etch. The profile having  $S_r = 0$  has little difference in etch depth between inside the trenches and the open field, indicating there being little ARDE. However, profiles having  $S_r$  as small as 0.04 already show some evidence of ARDE at  $t_1$ . By time  $t_2$  significant differences in etch depth between the open field and the trenches are evident for both  $S_r = 0.04$  and 0.16. The etch rate of an unpatterned wafer is not expected to have a dependence on  $S_r$ . Without patterning, none of the impinging Cl atoms will have interacted with surfaces prior to striking the etch front. Therefore, the differences in etch depth at  $t_2$  as a function of  $S_r$  in the quasi-open field (200 nm gap) between the arrays of fins indicates that ARDE occurs even for the modest AR ( $\approx 3.5$ ) in this region. Other than the aspect ratio dependence of the etch rates, the resulting profiles are similar for different values of  $S_r$ .

To better quantify the consequences of radical recombination on neutral transport and separate these effects from 3-d transport issues, profiles were simulated for infinite trenches having a width of 50 nm for the same range of recombination probabilities. The resulting profiles are shown in Fig. 4.12. The profiles show that smaller recombination probabilities produce more tapered features at the same aspect ratio while having a higher etch rate. These trends result, in part, from the etching in high AR features being neutral starved, and so any process that increases the flux of Cl atoms to the etch front will increase the rate of etching.

The instantaneous normalized etch rates for these features are shown in Fig. 4.13(a) as a function of aspect ratio. Etch rates for different values of  $S_r$  are all normalized to the open-field etch rate of the base case ( $S_r = 0.08$ ). These etch rates have significantly different responses to varying  $S_r$  at low and high aspect ratios. At low aspect ratios ( $AR < 7$ ) there is a direct correlation between recombination rate and ARDE – larger recombination probabilities

produce an etch rate which is more strongly dependent on aspect ratio than lower recombination probabilities. For the limiting case of  $S_r = 0.0$ , which is likely unphysical on any real material, there is an increase in the etch rate above the open field rate between  $AR = 5-7$ . This increase in etch rates correlates to the onset of ion funneling, and so is probably more related to geometry, the particular slopes of the side wall and our method of measuring etch rate, rather than an actual inverse ARDE. However, there is a clear trend that low probabilities of recombination are less sensitive to ARDE. At high aspect ratios ( $AR > 10$ ) all etch rates show a similar dependence on aspect ratio, despite having different absolute values.

The Cl atom fluxes and power densities onto the etch front as a function of AR are shown in Fig. 4.13(b) for different values of  $S_r$ . There is a strong correlation between the chlorine flux and ARDE – higher values of Cl fluxes (lower values of  $S_r$ ) at lower AR correspond to higher etch rates. The power flux remains nearly constant throughout the etch, with the exception of a small peak between  $AR = 8-9$ . This peak is related to ion funneling as the features begin to taper. Similar to the etch rate, for small aspect ratios ( $AR < 7$ ) larger recombination probabilities have lower chlorine fluxes to the etch front. Perhaps more important, the change in chlorine flux with aspect ratio is also greater for larger recombination probabilities, leading directly to ARDE. At higher aspect ratios, larger recombination probabilities still reduce the chlorine flux to the etch front, but the dependence on aspect ratio is similar between the different recombination rates, indicating that some other physical process is influencing neutral transport at these ARs.

(The Cl flux and power density for  $S_r = 0$  and  $AR > 12$  are omitted from Fig. 4.13(b). This omission is due to our measurement technique becoming susceptible to statistical variation when features become highly tapered. This issue only affects the measurement of fluxes but does not significantly affect measurements of the etch rate.)

#### 4.5. Neutral Angular Distribution

One possible method to decouple neutral transport issues from aspect ratio is to produce neutral reactant fluxes having an anisotropic angular distribution. As Coburn and Winters suggested, if the incoming neutral flux was perfectly anisotropic then the neutral flux on the etch front would actually increase with increasing aspect ratio.[102] This scaling results from all incoming neutrals striking the bottom of the feature while the etch front only consumes a fraction of those based on there being a small reactive sticking coefficient,  $S_n$ . The Cl atoms that do not react with the etch front must diffuse back up the feature to return to the bulk gas. As the aspect ratio increases the conductance of the tube decreases, resulting in an increased probability that the Cl atoms reflecting from the etch front will also be reflected off the side walls back down to the etch front. While a perfectly anisotropic neutral flux would be difficult to produce, some degree of anisotropy in the neutral flux can be produced by techniques such as neutral beam etching where neutrals are produced by grazing angle collision of anisotropic ions.[111–113].

To assess the consequences of anisotropic neutral fluxes on ARDE, the initial angle with respect to the vertical of each neutral pseudoparticle was linearly scaled by the factor  $\gamma_n$ . The naturally occurring isotropic angular distribution has  $\gamma_n = 1$ , while values smaller than one represent a narrowed neutral angular distribution. The resulting profiles for the 2-d trenches for  $\gamma_n = 1, 0.5$  and  $0.25$  are shown in Fig. 4.14. Smaller values of  $\gamma_n$  produce higher etch rates due to the increased neutral flux to the etch front, but the profiles also have significantly more tapering. The side wall chlorination just above the etch-front for  $\gamma_n = 0.25$  is 2.1 Cl atoms/site. This value is only slightly lower than for the base case (2.2 Cl atoms/site). One might expect a significantly lower Cl passivation on the side walls for the anisotropic Cl flux as there would be fewer collisions on the side wall. The higher than expected chlorination results from Cl isotropically

reflecting from other surfaces, tempered by the larger number of primary ions striking on the more tapered side walls.

The normalized etch rate, chlorine flux and power density at the etch front as a function of AR for different values of  $\gamma_n$  are shown in Fig. 4.15. While there is significantly more chlorine reaching the etch front with narrower neutral angular distributions, the neutral flux retains a significant dependence on aspect ratio. The resulting normalized etch rate for  $\gamma_n = 0.25$  has a peak at an aspect ratio of  $\approx 6$ . The etch rate for  $\gamma_n = 0.50$  appears to have a mild peak in the same range of AR, producing a process window having quasi ARDE-free behavior. Power density is essentially constant compared to the Cl flux over the range of aspect ratios investigated. (Note that, power density and chlorine fluxes are omitted for  $\gamma_n = 0.25$  with AR > 10 due to the highly tapered profile, as discussed previously.)

#### **4.6. Ion Angular Distribution**

While previous cases more directly address details of the neutral transport, it is also possible that ion shadowing can contribute to ARDE, and even have a second order effect on neutral transport through, for example, removing Cl atoms from the side walls. By artificially varying the angular distribution of ions in the simulation, the contribution of ion shadowing to ARDE can be assessed. Changing process conditions, such as bias voltage, to narrow (or broaden) the IEAD unfortunately also produces changes in the magnitudes of fluxes of both neutral and ions. Instead, a linear scaling factor,  $\gamma_i$ , was used similarly to the neutral fluxes, to narrow or broaden the angular distribution of ions obtained from the base case of the reactor scale model.

Etch profiles for  $\gamma_i = 0.25$  to 1.5, with  $\gamma_i = 1$  representing the base case, are shown in Fig. 4.16. Values of  $\gamma_i < 1$  are narrower distributions than the base case and values of  $\gamma_i > 1$  are

wider. The average ion angular distribution of the base case is  $\pm 2.2^\circ$ , therefore  $\gamma_i = 0.25$  results in an average ion angle distribution of  $\pm 0.55^\circ$  and  $\gamma_i = 1.5$  yields an angular spread of  $\pm 3.3^\circ$ . The resulting etch profiles have differences in side wall slope, extending to bowing, but fairly similar integrated etch rates. Narrower angular distributions produce more tapered side wall profiles than the base case (18% reduction in width at half etch height for  $\gamma_i = 0.25$  compared to the base case). At the other extreme, the profile resulting from  $\gamma_i = 1.5$  has increased side wall bowing (30% increase in width at half etch height compared to the base case). The broader ion angular distributions enable sites having off normal view-angles to the plasma to intercept a larger fraction of the incoming ion flux, the first consequence being bowing under the mask. Once this initial bowing occurs, ions specularly reflecting from the bowed surface are more likely to strike the side wall deeper in the trench. Therefore, maximal bowing occurs at deeper locations in the trench, in areas that do not have large view-angles to the plasma.

In spite of the differences in side wall slope and bowing, there is little difference in etch rate until an aspect ratio of 6-7, at which time larger values of  $\gamma_i$  have smaller etch rates. These trends are shown more quantitatively in Fig. 4.17 where normalized etch rates, Cl fluxes and power densities are shown as a function of aspect ratio for different values of  $\gamma_i$ . The ion angular distributions for all  $\gamma_i$  have similar sensitivity to ARDE, a predominantly (negative) linear dependence of etch rate on aspect ratio over the entire range studied, but slightly steeper slopes (more sensitive to ARDE) for the wider angular distributions. While the overall trends in etch rate are similar for different values of  $\gamma_i$ , the small differences in etch rate, when integrated over a large range of aspect ratio, produces significant differences in etch depth. These trends indicate that ion shadowing does affect ARDE, but its contributions are relatively small compared to the consequences of neutral transport.

The chlorine flux incident onto the etch front is essentially insensitive to the angular distribution of the ions. Power density, however, monotonically decreases for broader distributions (larger values of  $\gamma_i$ ) and particularly so for larger values of AR. These trends indicate that the average sticking coefficient of neutrals on the etch front,  $S_n$ , is not significantly changed by modulation in the power density for these process conditions, as is implied by the synergy model.[104]

#### **4.7. Dependence on Feature Width**

One of the defining characteristics of ARDE is that the etch rate depends only on aspect ratio and not necessary on the absolute critical dimension (CD) of the etched feature, generally the width of the feature. Other profile parameters, such as the loss of CD due to tapering, have been shown to be dependent on view angle to the plasma.[114] While the two-dimensional view angle to the plasma is related to AR, the correlation of loss of CD to view angle suggests a sensitivity to reactive fluxes that directly arrive at a surface site. To determine if the etch rate of simple structures using this reaction mechanism is related to AR, CD or view angle, etch profiles were simulated for three trench widths of 33 nm, 50 nm and 67 nm. The resulting normalized etch rates for two values of chlorine recombination probabilities ( $S_r$ ) are shown in Fig. 4.18. With  $S_r = 0.08$ , the base case, the etch rate depends only on aspect ratio with only small differences between the different trench widths that are likely statistical in nature. The etch rate in the absence of recombination of chlorine on the walls,  $S_r = 0$ , is nearly the same for all trench widths for small AR ( $< 4$ ) and large AR ( $> 9$ ). At intermediate values of AR (4-9) the etch rate is sensitive to the width of the feature.

These results imply that the local peaking in etch rates observed in many of these parameterizations are likely related to fine details of the evolution of the feature that may depend

on critical dimension. The technique used here to measure the etch rate, described in Sec. II.D, is based on the change in height of the profile within a small area at the center of the feature. This technique may somewhat exaggerate the severity of the peaks in etch rate which are driven by geometry dependent ion funneling. The total number of silicon atoms removed per second, for instance, shows a similar decrease with aspect ratio, but does not exhibit the peaking as observed in the calculated etch rate.

#### **4.8. Parameters affecting ARDE**

The results of this computational investigation suggest that a dominant cause of ARDE is the decrease in neutral radical flux reaching the etch front with increasing AR, provided the process is not already in a neutral saturated regime. By increasing the neutral radical flux relative to the ions, the surface at etch front becomes more passivated, and so the etch rate is less sensitive to modest changes to the neutral flux that may occur with aspect ratio. These trends have been experimentally observed.[22,91] The available experimental data indicating that large values of neutral-to-ion flux ratio produces a saturation in etch rate were predominantly obtained from measurements in the open field (non-patterned wafers). Although these data have provided extremely important insights, the data do not address the possible coupling of neutral and ion fluxes that may occur within features. In this study, changes in system parameters that increased the neutral flux to the etch front relative to the ion flux (e.g., reducing the recombination of radicals on the feature walls, increasing the neutral to ion ratio in the incoming fluxes, or employing an anisotropic flux of neutral radicals) all reduced ARDE but also produced more tapered features.

The onset of tapering of the feature at an AR of 6-8 is correlated with a decrease in chlorine radical flux to the etch front as well as with the etch rate. This correlation between

tapered features and reduced neutral transport could be due to several different mechanisms. The first is the reduction in conductance of neutral particles due to the angle of the surface normal in the tapered region. Since the solid-angle normalized probability of emission or reflection for a Lambertian angular distribution is maximum along the surface normal, neutral species which diffuse down to the tapered region of the feature are preferentially directed back up the feature as the angle of the taper increases.

Another factor which contributes to the decrease in neutral flux at the etch front in tapered features is the erosion of side wall passivation and the subsequent re-passivation of the exposed silicon site. Due to the flux of ions being anisotropic, the tapered side walls are exposed to higher fluxes of ions than strictly vertical side walls. While our reaction mechanism includes an angular dependence to the sputter reactions, which goes to zero at grazing angles, there is still a finite probability on the tapered walls. The effect of this side wall scattering is shown in the results of Fig. 4.6, where the number of chlorine atoms per Si site decreases from 2.8 to 2.2 as the tapering becomes more severe. This erosion of the side wall exposes bare silicon sites which will consume incoming Cl flux through passivation, which in turn reduces the neutral flux in the etch front of a tapered feature.

The synergy model of Gottscho et al. predicts that there is a coupling between the ion and neutral fluxes such that changing the incoming ion flux can change the neutral flux to surfaces deep in the feature with no change in the neutral flux entering the feature.[104] This process occurs due to the ion flux changing the steady state surface chlorine coverage on the etch front, which changes  $S_n$ . The change in  $S_n$  then impacts the neutral flux through Eq. 4.1. Since the tapering of the side walls affects the ion flux at the etch front through ion funneling, it is possible that the synergy coupling may also modulate neutral flux to the etch front as a function of side

wall taper. Our results do not indicate that this effect is strongly influencing the neutral flux or etch rate for this reaction mechanism. The power densities and chlorine fluxes, shown in Fig. 4.17(b) for a range of  $\gamma_i$ , display a doubling of power density from  $\gamma_i = 1.5$  to  $\gamma_i = 0.25$ , but no discernable decrease in measured Cl flux at the etch front.

While increasing the neutral radical flux to the etch front does not eliminate ARDE over all ARs investigated here, it is possible to postpone the onset of ARDE. For example, when varying the recombination probability of Cl atoms on the side walls [see Fig. 4.13(a)], there were ranges of AR where ARDE was not significant. For these ranges of AR, the feature has not yet formed any significant taper, and so is able to benefit from the higher neutral flux as predicted by analytical models. A similar trend occurs when narrowing the angular distribution of the neutrals. For example, etch rates with  $\Gamma_n/\Gamma_i = 20$  [Fig. 4.10(a)] and  $\gamma_n = 0.5$  [Fig. 4.15(a)] are not sensitive to ARDE for AR as large as 8.

The results of our investigation indicate that issues related to the transport of radicals from the bulk gas into the feature dominate ARDE for the conditions studied here. That is, there are surface reactions that are rate limited by the availability of neutral radical fluxes and reactions that are rate limited by ion fluxes. Differences in substrate temperature, operating pressure or ion energies may affect ARDE behavior by their influence on reactions initiated by neutral or radical fluxes. However, in general, for the etch rate to depend on AR, either the neutral or ion flux reaching the etch front must also depend on AR. For the reaction mechanism used here, the strongest AR dependence originates from the change of the neutral conduction with AR. For other reaction mechanisms or operating conditions, the transport of neutral etch products out of the feature may dominate ARDE due to re-deposition. However, in both scenarios, it is the dependence of neutral transport on AR which result in ARDE.

#### 4.9. Concluding Remarks

Aspect ratio dependent etching remains a challenge to optimizing feature profiles during plasma etching, a situation that has become more critical with the introduction of 3-d structures such as FinFETs. In this investigation of etching of Si in Ar/Cl<sub>2</sub> gas mixtures, the majority of ARDE arises from issues related to neutral transport. Several factors were varied that affect neutral transport, including surface recombination of radicals, neutral-to-ion flux ratios, critical dimension, 3-d geometry and neutral angular distribution. A general conclusion of this chapter is that any reaction that relies on a flux of neutral species from the bulk gas will, to some degree, suffer from ARDE. However, some trade-offs can be made to change the dependence on aspect ratio. Increasing neutral flux to the etch front may produce a quasi-aspect ratio independent regime of etching for low and moderate aspect ratios. Doing so may involve a trade-off with a greater propensity for tapered features, and increased ARDE outside of this aspect ratio independent window.

The details of the results presented in this chapter depend on the details of the reaction mechanism, which is described in Chapter 3.3. Etching of dielectrics, such as SiO<sub>2</sub> and Si<sub>3</sub>N<sub>4</sub>, etch according to the more complex reaction mechanism, discussed in detail in Chapter 3.4, based on the use of fluorocarbon containing gas mixtures.[28,115,116] In dielectric etching, the etch rate is sensitive to the thickness of the fluorocarbon polymer layer on the etch front and the etch process requires multiple steps. (That is, a Si<sub>3</sub>N<sub>4</sub> unit is not necessarily removed with a single strike of an ion.) The end result is that the dependence of etch rate on the ratio of passivating neutral and ion fluxes, and their angular distributions, is more complex. For example, in the Si etch mechanism described here, increasing Cl fluxes to the etch front typically reduces ARDE. In the dielectric etch mechanism, increasing fluorocarbon fluxes to the etch

front can increase etch rates over a limited range of  $\Gamma_n/\Gamma_i$  beyond which etch rates may decrease (or terminate – an etch stop) due to thickening of the passivation layer. With those caveats, based on results from preliminary numerical investigations of ARDE in fluorocarbon containing plasmas, the same general trends discussed here appear to be valid.

#### 4.10. Figures

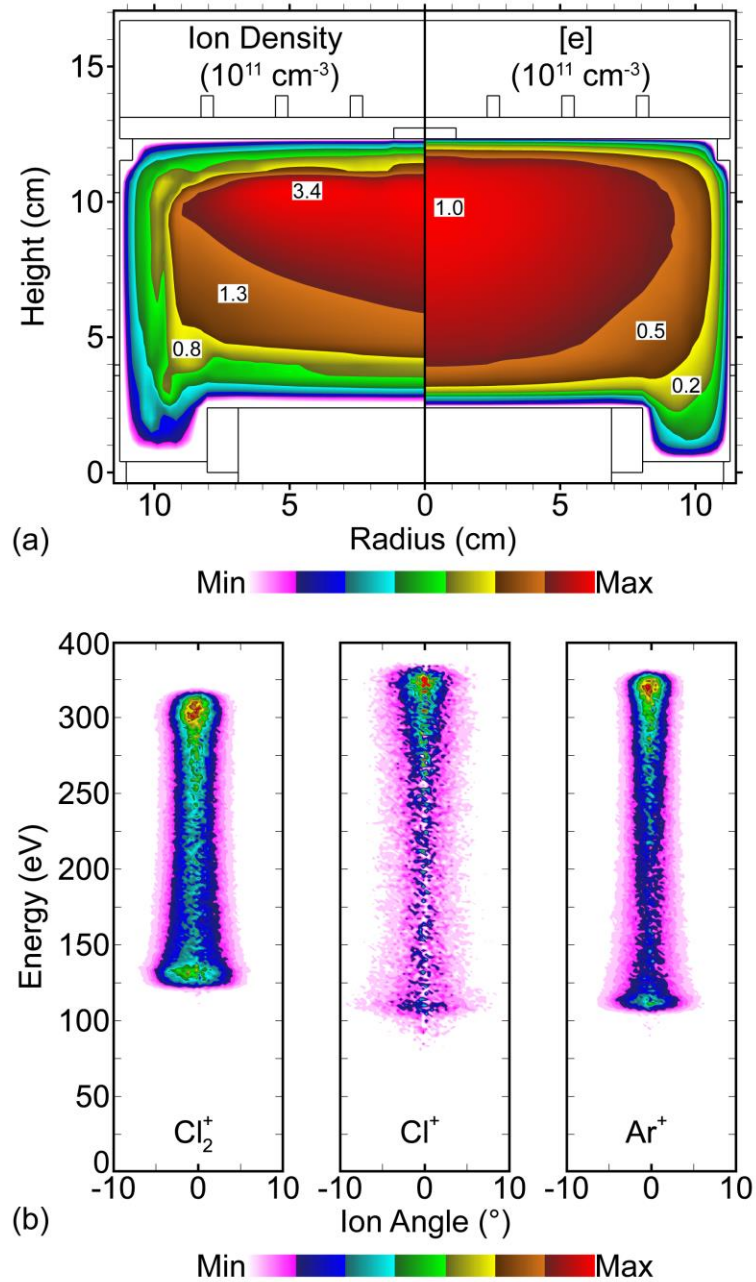


Fig. 4.1 Reactor and plasma properties. (a) Reactor geometry with (left) total positive ion density and (right) electron density, shown on a log scale with a range of two decades. (b) Probability density of ions reaching the wafer surface as a function of ion energy and incident angle (IEAD), shown on a linear scale.

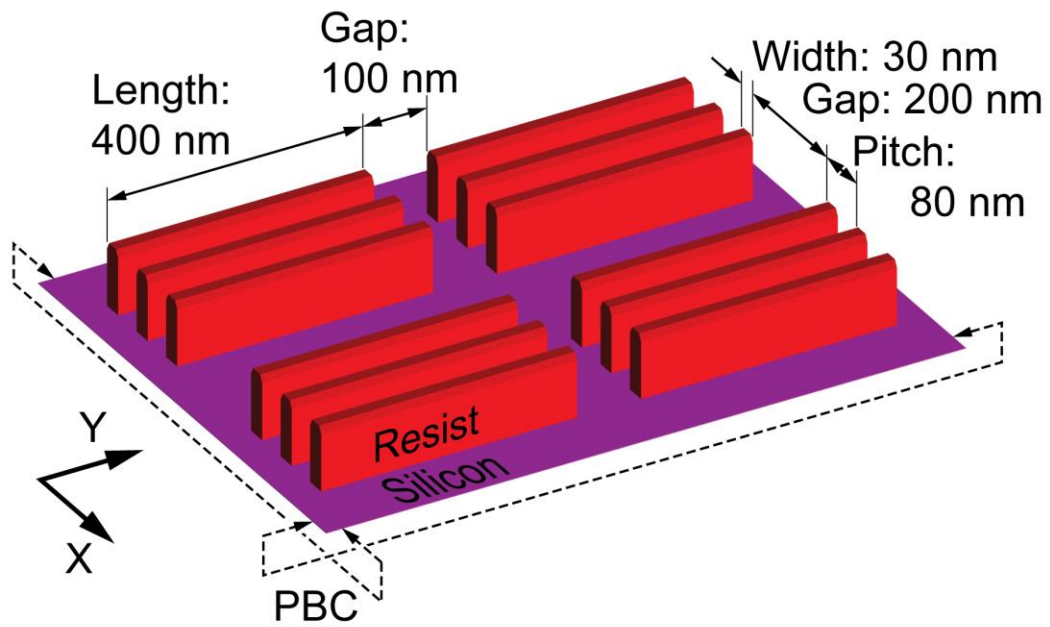


Fig. 4.2 Mask pattern used for etching FinFET geometries. The simulation domain includes one sub-array of three fins with periodic boundary conditions.

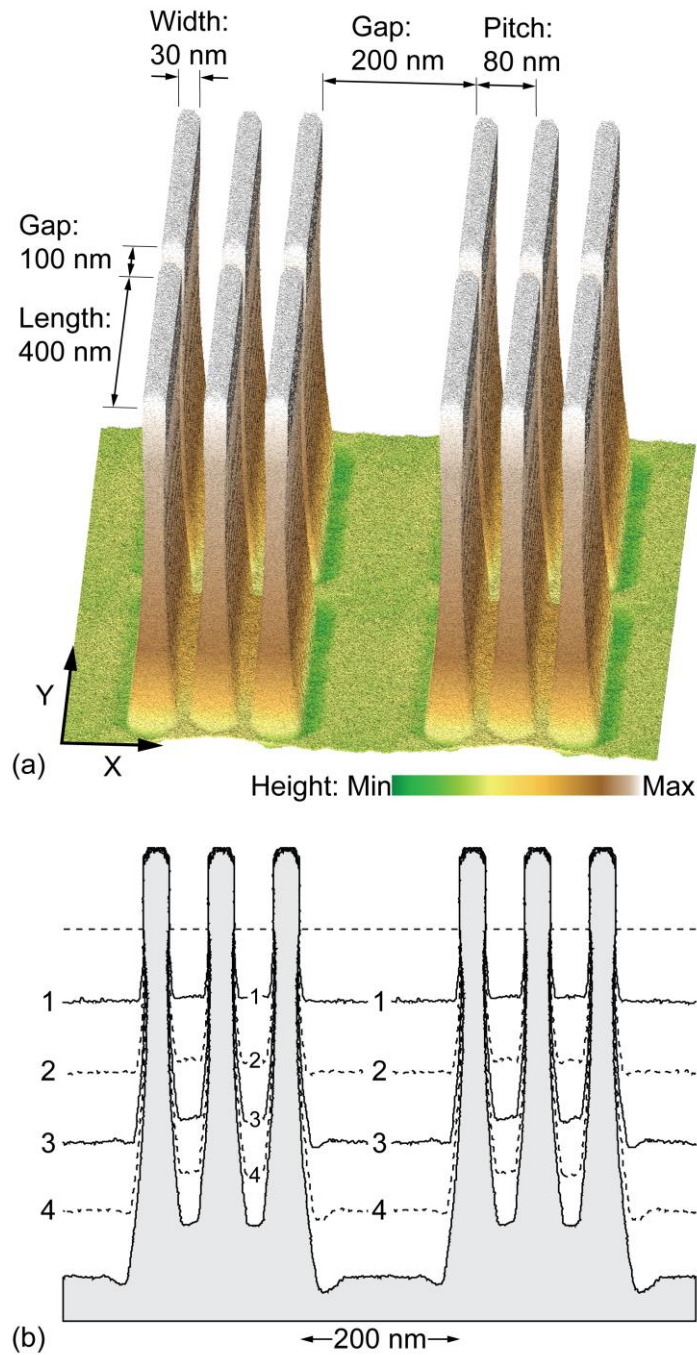


Fig. 4.3 Etched profiles for the FinFET geometry. (a) Color represents height of feature, showing the variation of etch depth in the longitudinal Y-direction between fins. The difference between the total etch depth between the fins and the open field is also visible. (b) Slice through the fins in the X-direction, taken at the center of the fin length. Each line is separated by a constant time interval.

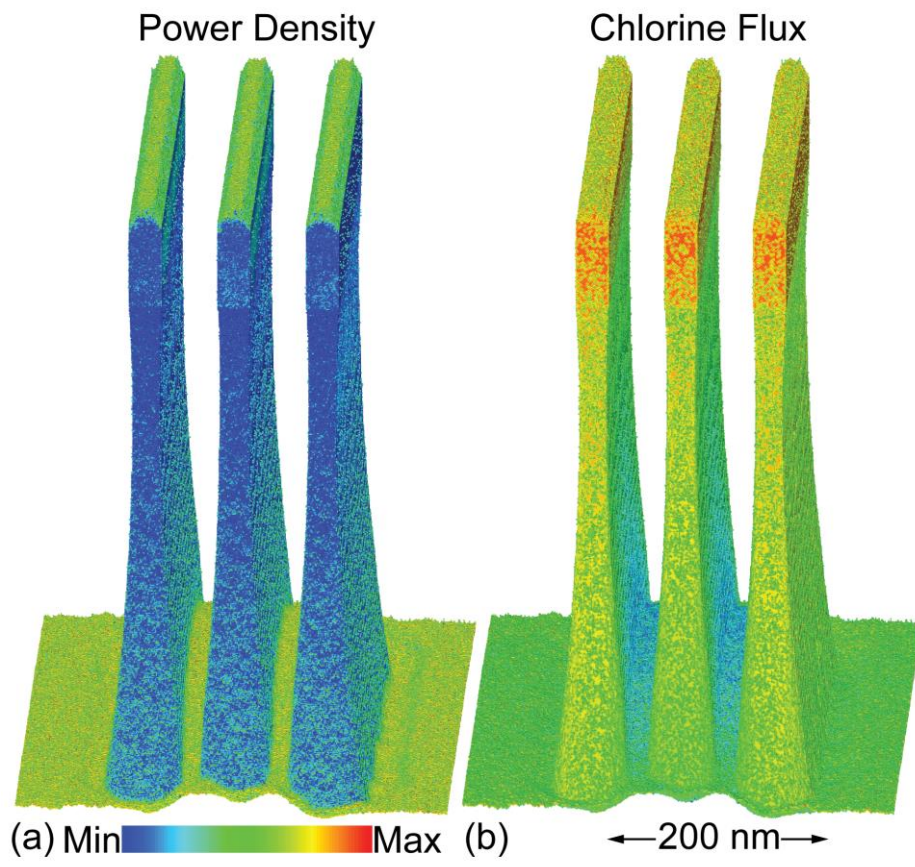


Fig. 4.4 Spatially resolved fluxes to the surface of the etch profile. (a) Power density delivered by ions and (b) chlorine radical flux.

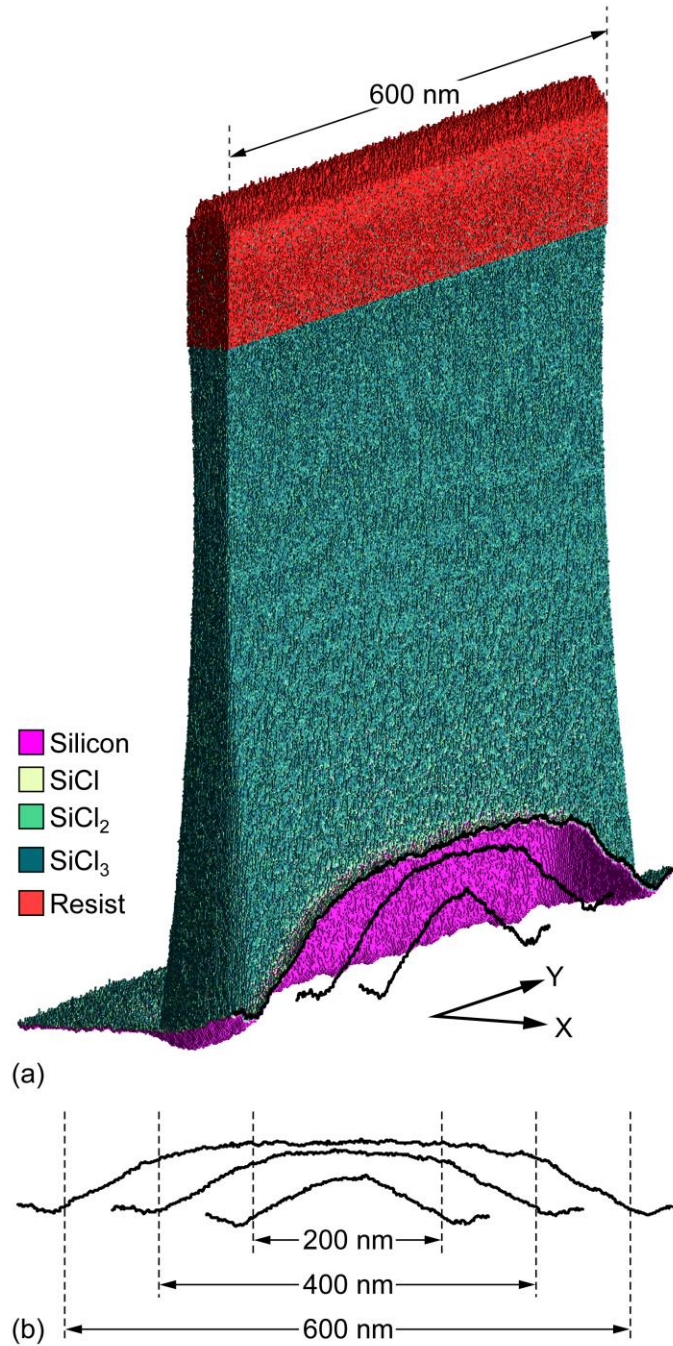


Fig. 4.5 Longitudinal slice (Y-direction) through the center of the trench in the 3-d FinFET, showing the etch front (solid lines) for three fin lengths: 200, 400 and 600 nm. (a) Perspective view with each color representing a different material. (b) Height at the bottom of the trench in the longitudinal (Y-direction) for different fin lengths. (The nominal fin lengths are shown as dotted lines for reference.)

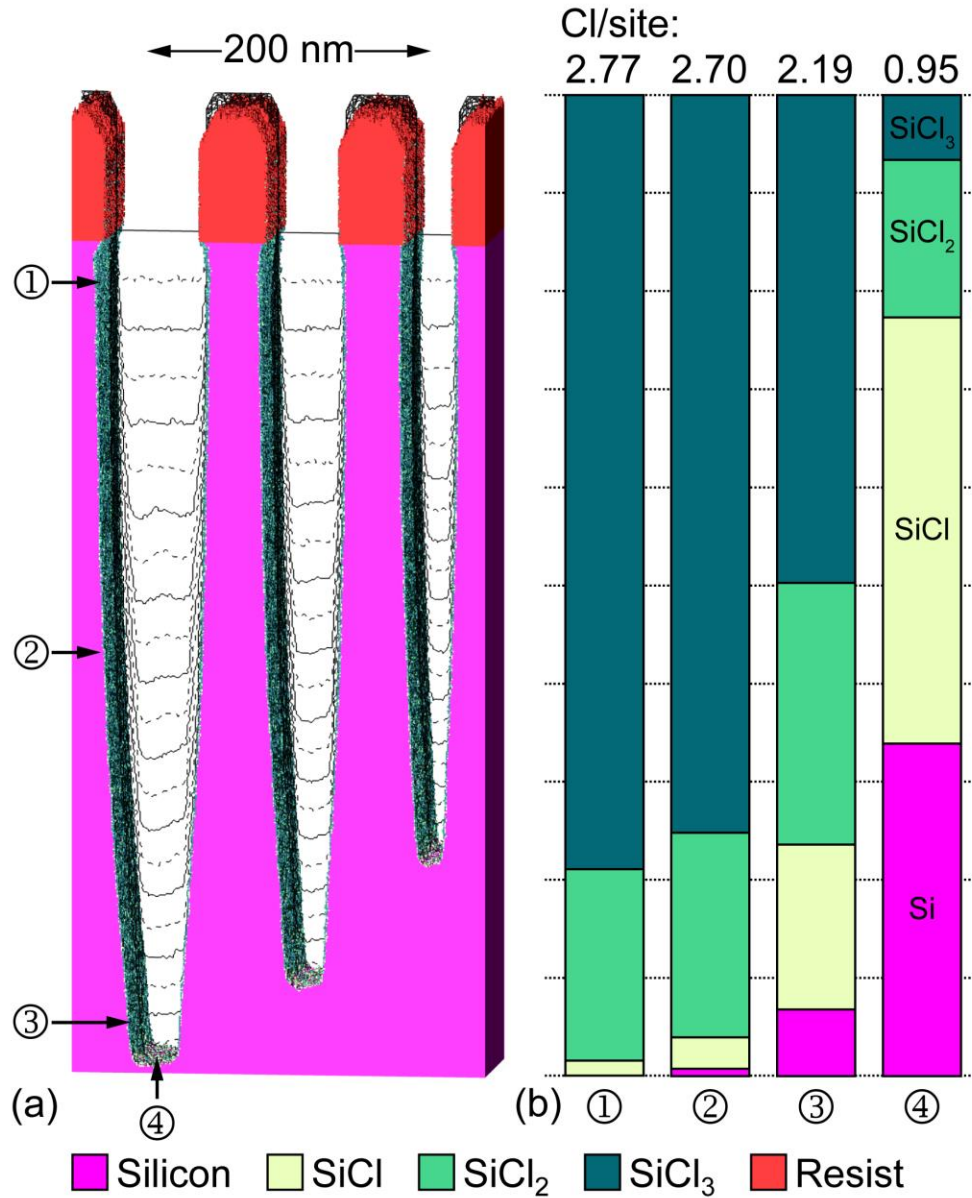


Fig. 4.6 Etch properties for trenches. (a) Simultaneously etched profiles showing ARDE for three trenches having different widths. Colors represent different solid materials. Black lines represent slices through the center of the trench at different times, taken at constant time intervals. (b) Normalized density of surface species at different locations along the 67 nm profile. The etch front measurement is taken on the horizontal surface being bombarded by ions. Side high, mid and low measurements are taken from the side wall just below the resist, halfway down the profile and just above the etch-front. All chlorination measurements were taken at the final time step.

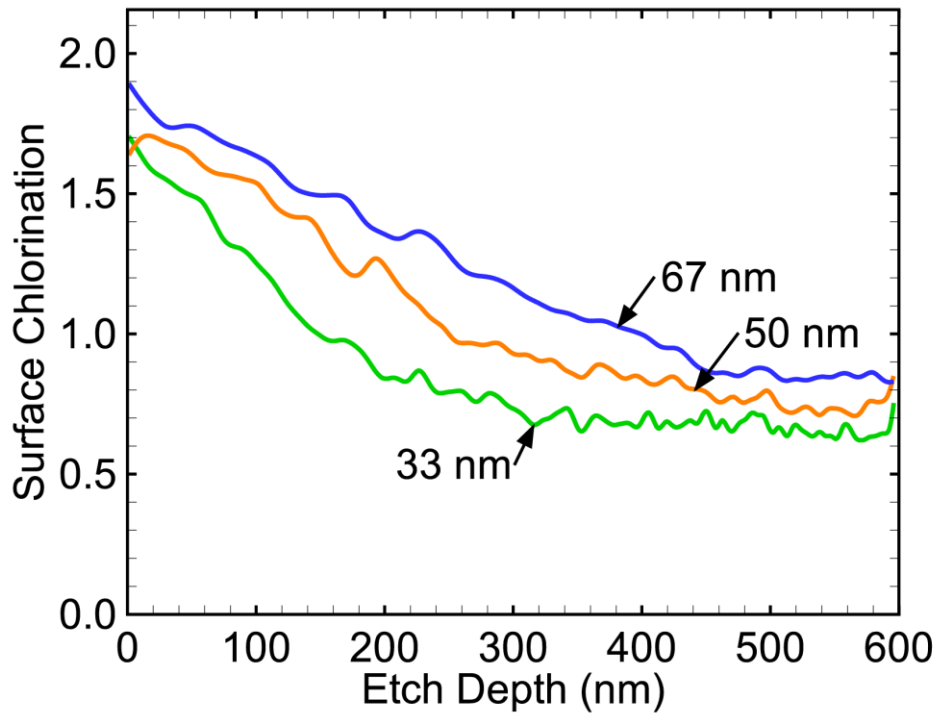


Fig. 4.7 Average surface chlorination (Cl atoms per silicon site) of the etch front as a function of etch depth for trenches having widths of 33, 50 and 67 nm.

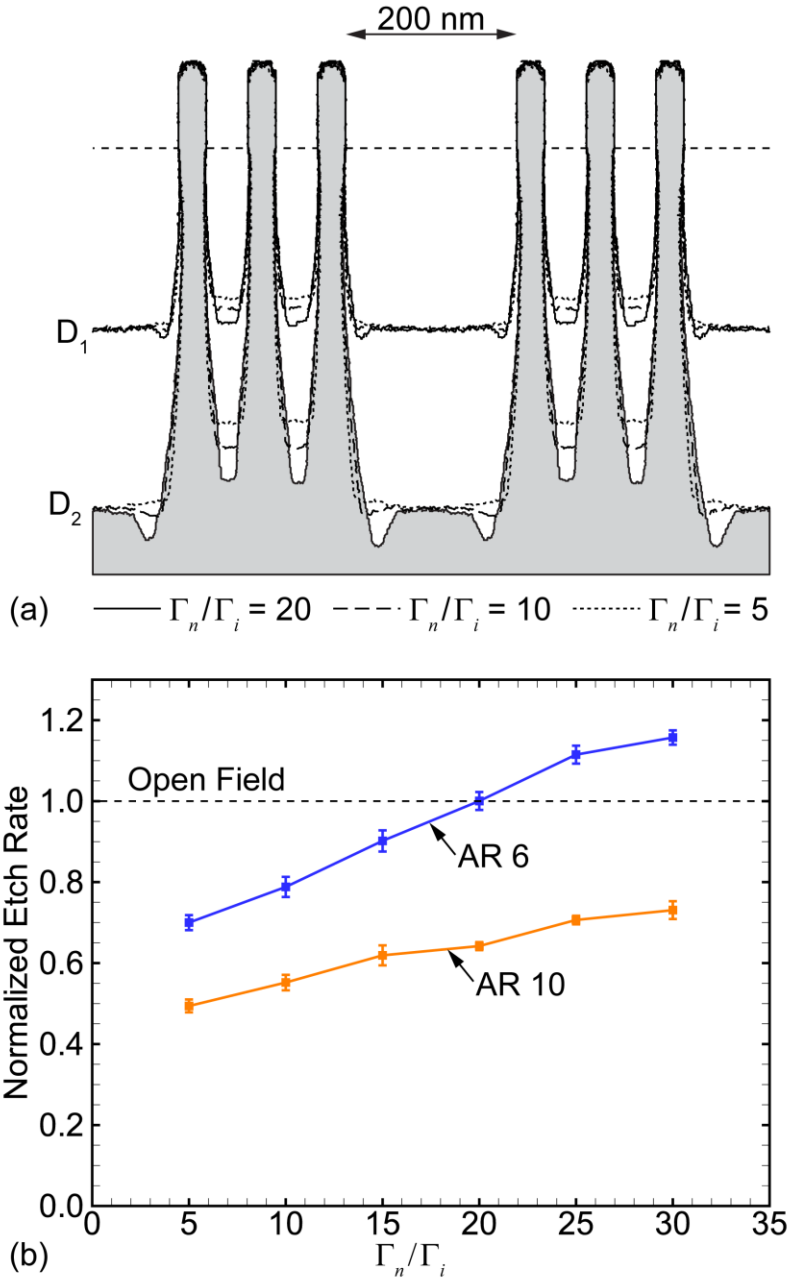


Fig. 4.8 Etch properties for different values of  $\Gamma_n/\Gamma_i$ . (a) Two dimensional slice through FinFET profile for several incoming neutral to ion flux ratios. The lines labeled  $D_1$  and  $D_2$  represent equal etch depths, and are taken at different etch times due to the different etch rates between cases. The slice is taken through the center of the length of the fin. (b) Normalized etch rates as a function of  $\Gamma_n/\Gamma_i$  for two different AR. Etch rates are normalized to the initial etch rate of each respective  $\Gamma_n/\Gamma_i$  to enable comparison.

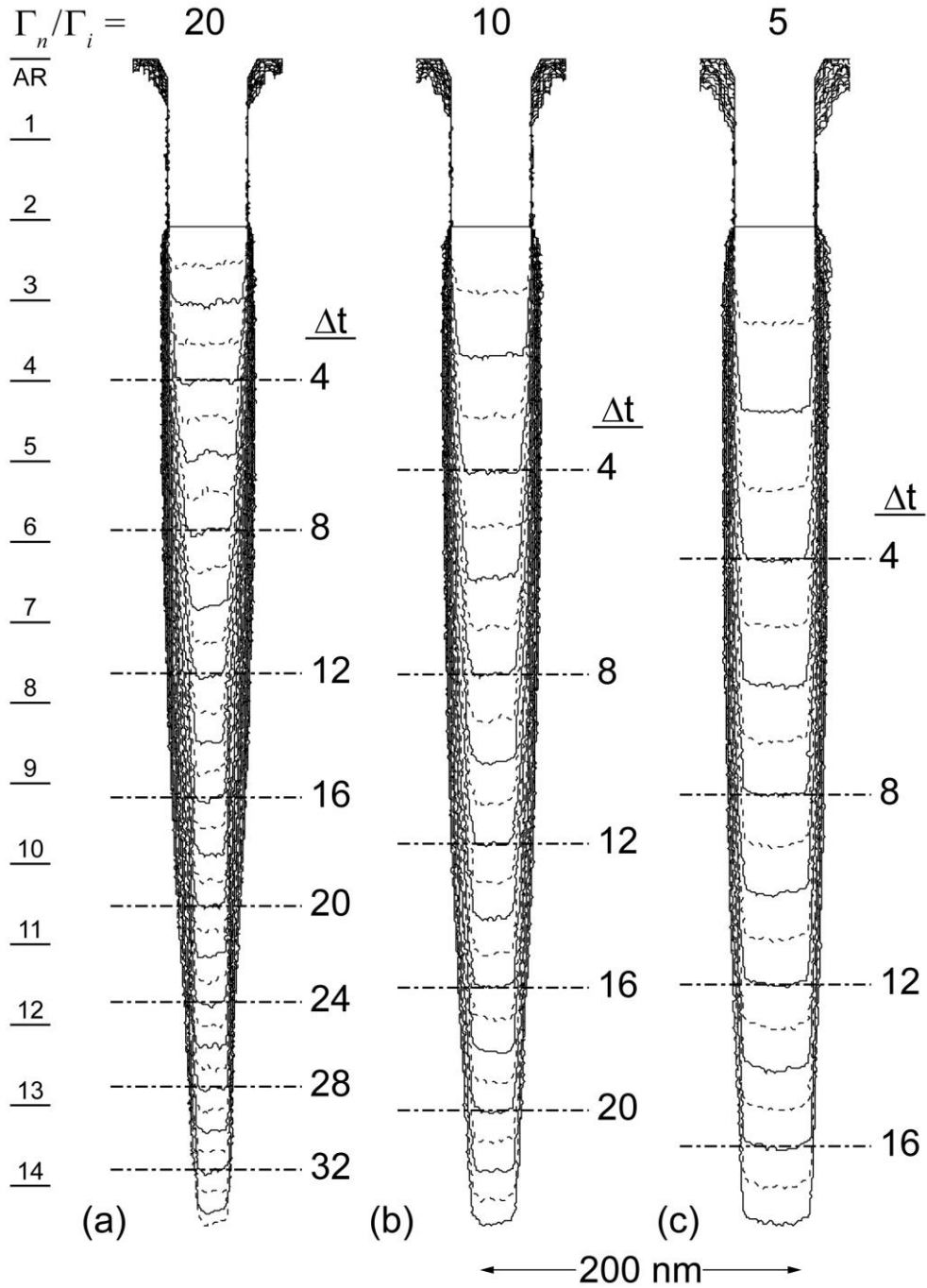


Fig. 4.9 Time evolution of silicon trench profile during Ar/Cl<sub>2</sub> etching for different neutral to ion ratios. The neutral to ion ratios are (a) 20, (b) 10 and (c) 5. Line spacing represents a constant time interval for all profiles. Numbered lines represent similar etch times in each profile.

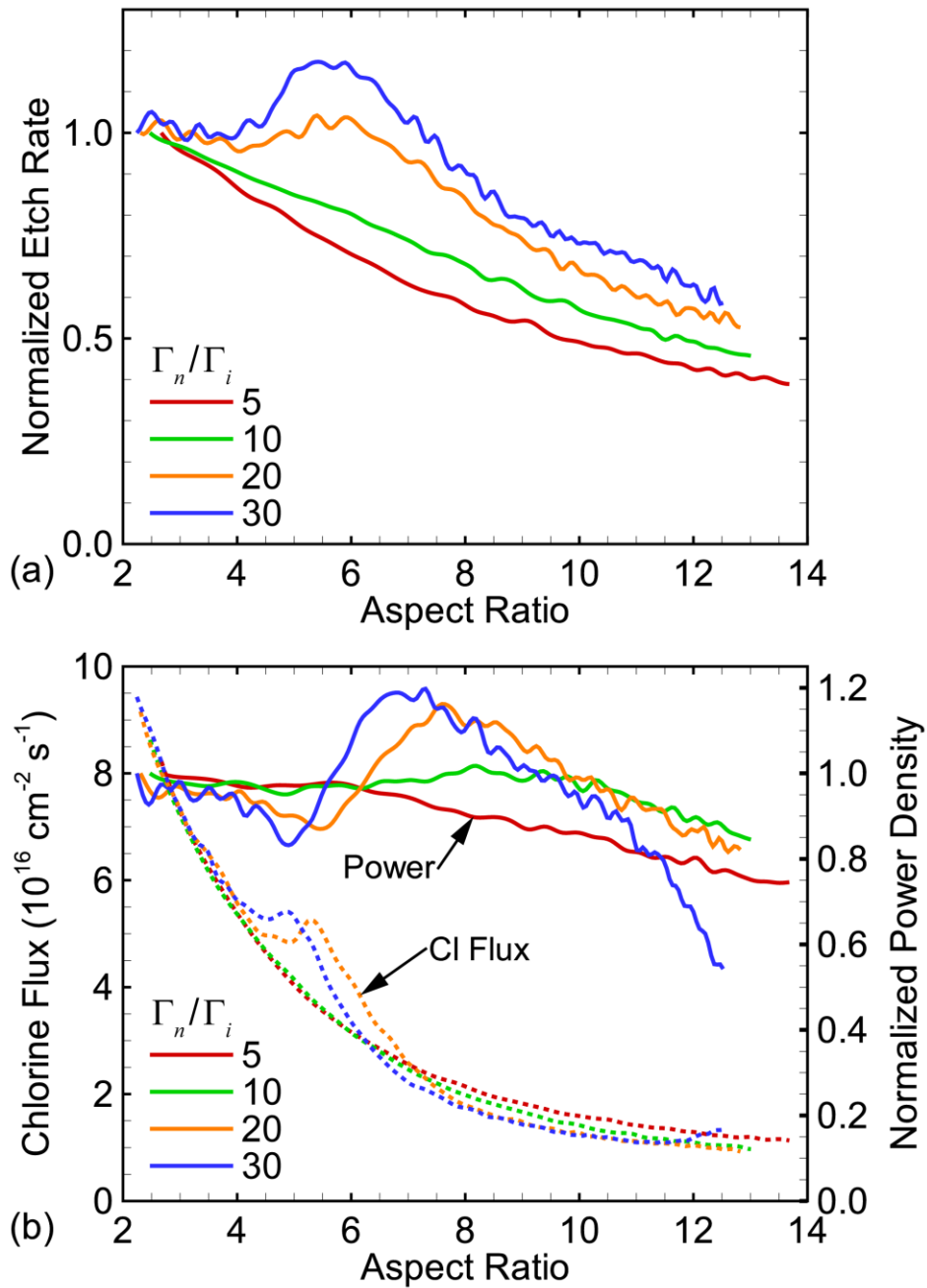


Fig. 4.10 Dependence of etch rate, chlorine flux and power density on aspect ratio and the  $\Gamma_n/\Gamma_i$  ratio. Lines are labeled with neutral to ion ratios  $\Gamma_n/\Gamma_i=5, 10, 20$  and  $30$ . (a) Etch rates normalized to the initial etch rate of each  $\Gamma_n/\Gamma_i$ . (b) Power densities (solid) and Cl flux (dotted) are measured in a small window centered in the etch front. Power density is normalized to the initial power density of each respective  $\Gamma_n/\Gamma_i$  ratio.

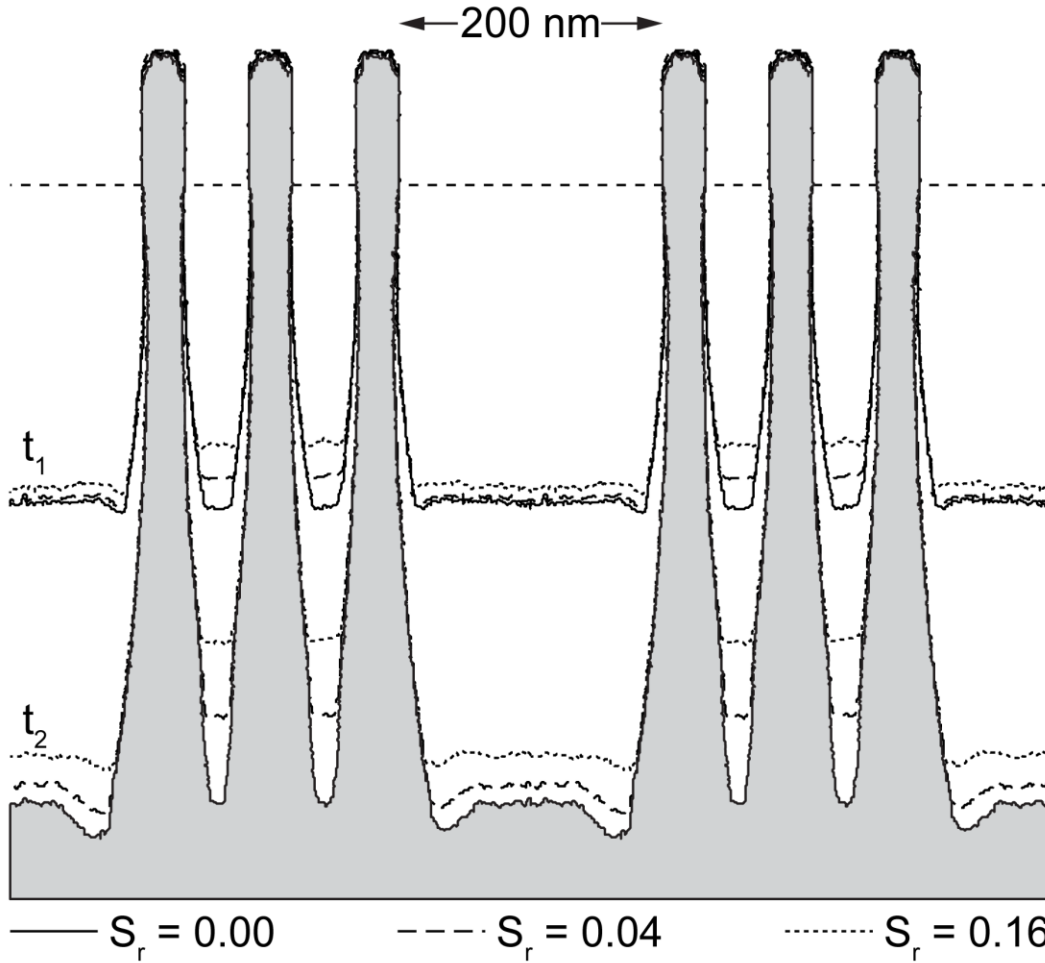


Fig. 4.11 Two dimensional slice through fin profile for several surface recombination probabilities,  $S_r$ . The lines labeled  $t_1$  and  $t_2$  represent equal etch times. The slice is taken through the center of the length of the fin.

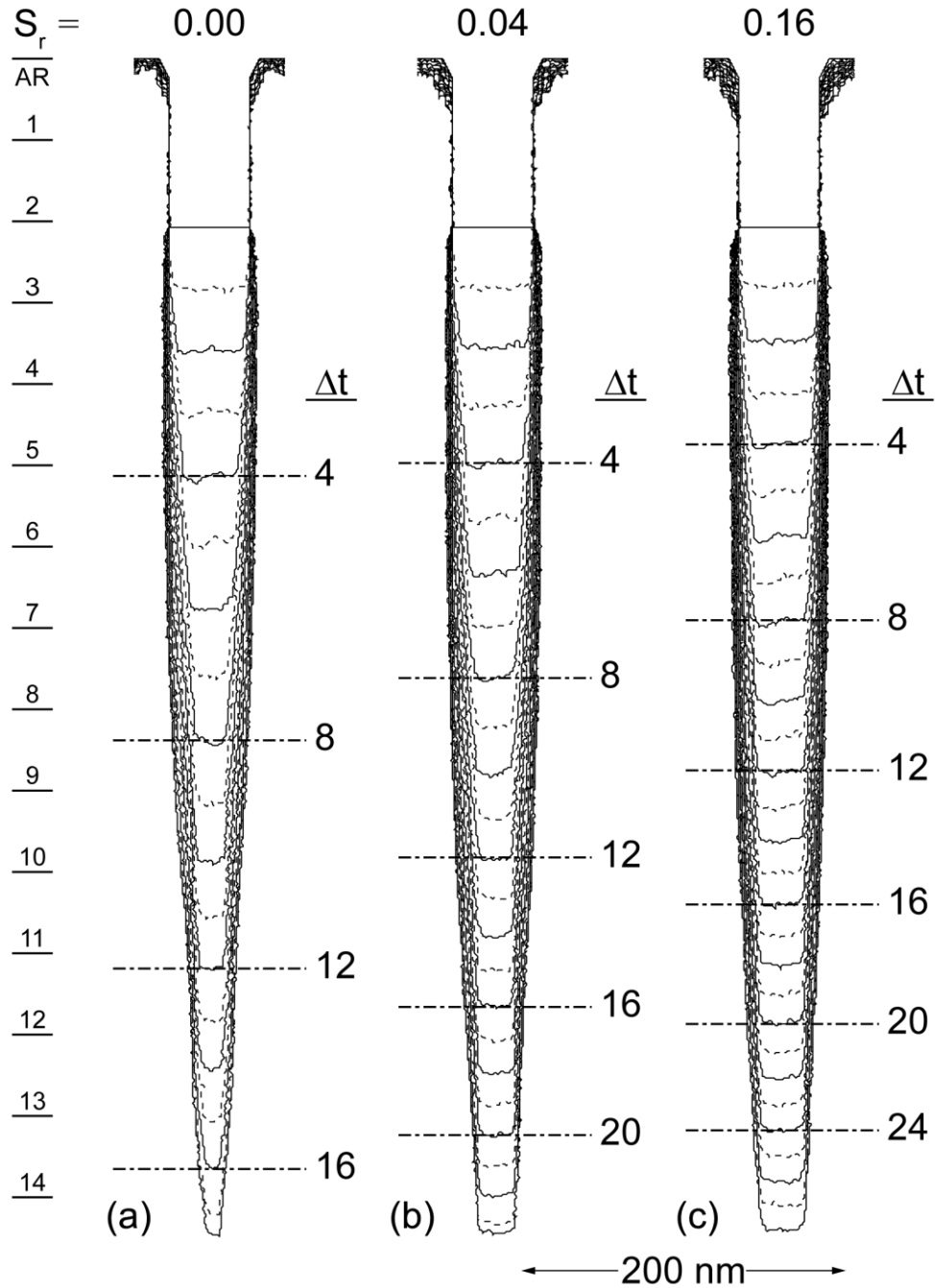


Fig. 4.12 Time evolution of silicon trench profile during  $\text{Ar}/\text{Cl}_2$  etching for different chlorine recombination probabilities,  $S_r$ . The recombination probabilities of atomic Cl on  $\text{SiCl}_3$  shown are (a) 0.00, (b) 0.04 and (c) 0.16. Line spacing represents a constant time interval  $\Delta t$  for all profiles. Numbered lines represent similar etch times in each profile.

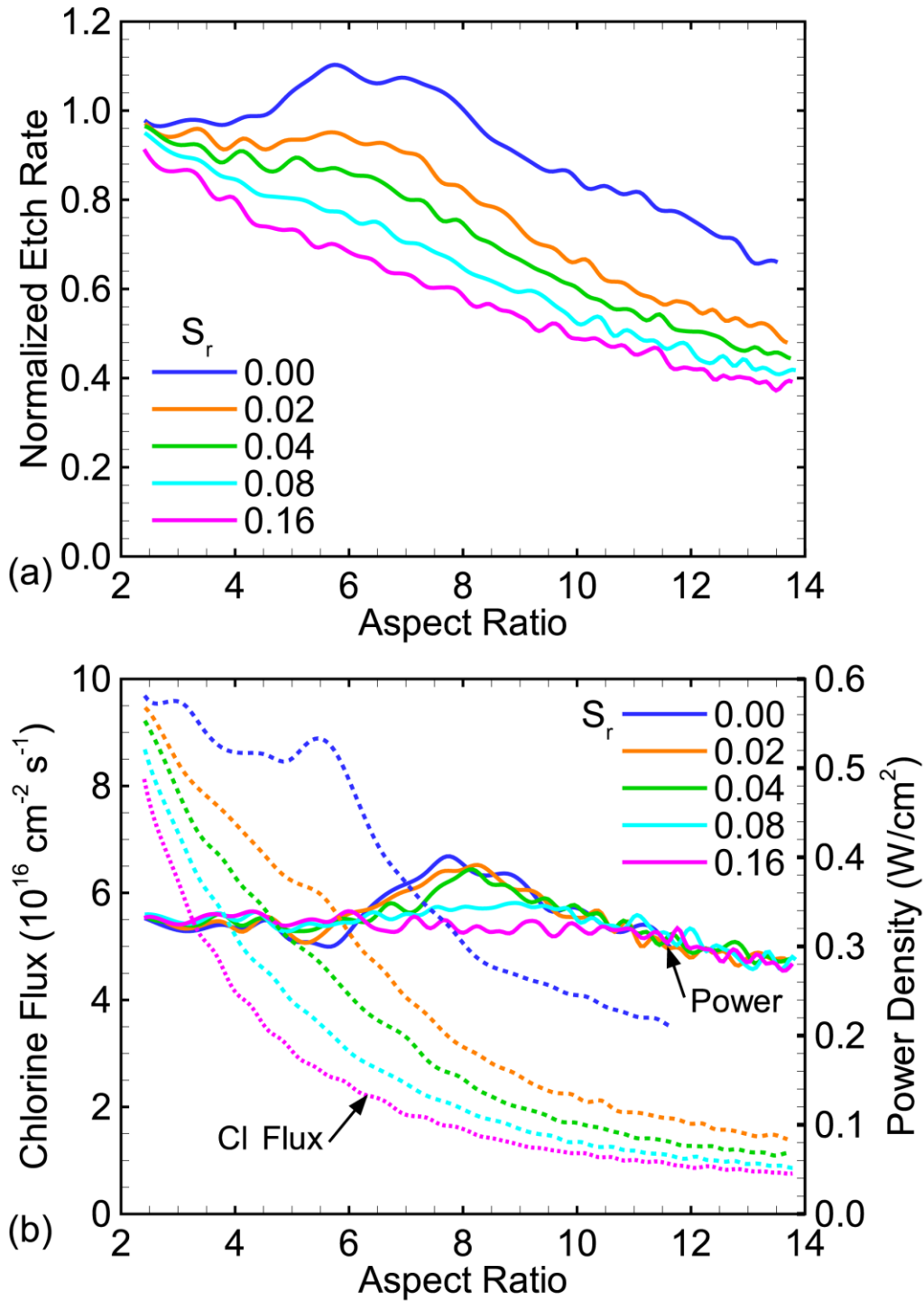


Fig. 4.13 Dependence of (a) etch rate, and (b) chlorine flux and power density on aspect ratio and the probability of recombination of radical chlorine on the walls,  $S_r$ . (a) Etch rates are normalized to the etch rate in the open field for the base case ( $S_r = 0.08$ ). Power density and chlorine flux are measured at the etch front as it evolves.

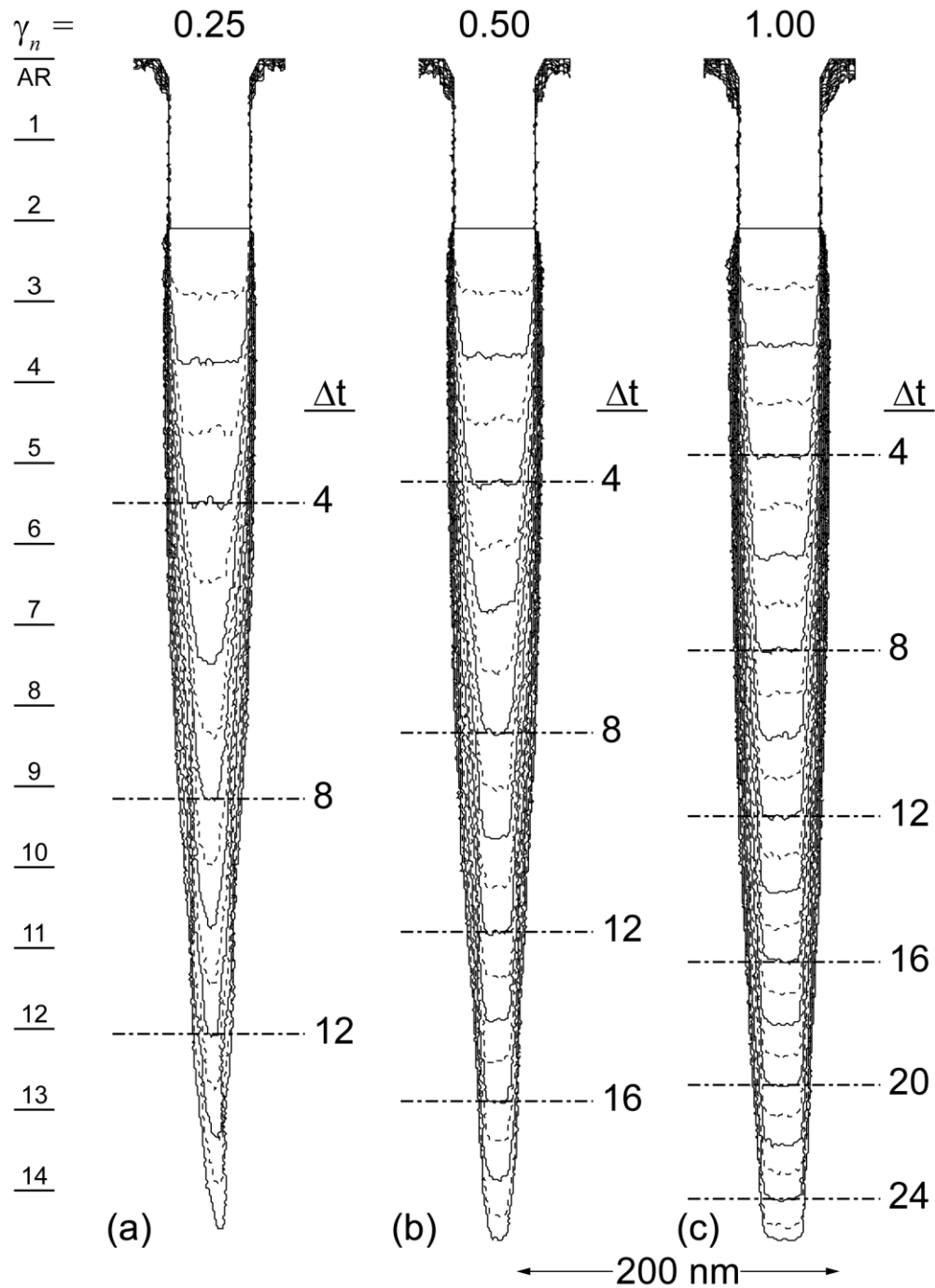


Fig. 4.14 Time evolution of silicon trench profile for different neutral angular distributions,  $\gamma_n$ . The normalized angular distribution scaling factors are (a) 0.25, (b) 0.50 and (c) 1.00. Line spacing represents a constant time interval  $\Delta t$  for all profiles. Numbered lines represent similar etch times in each profile.

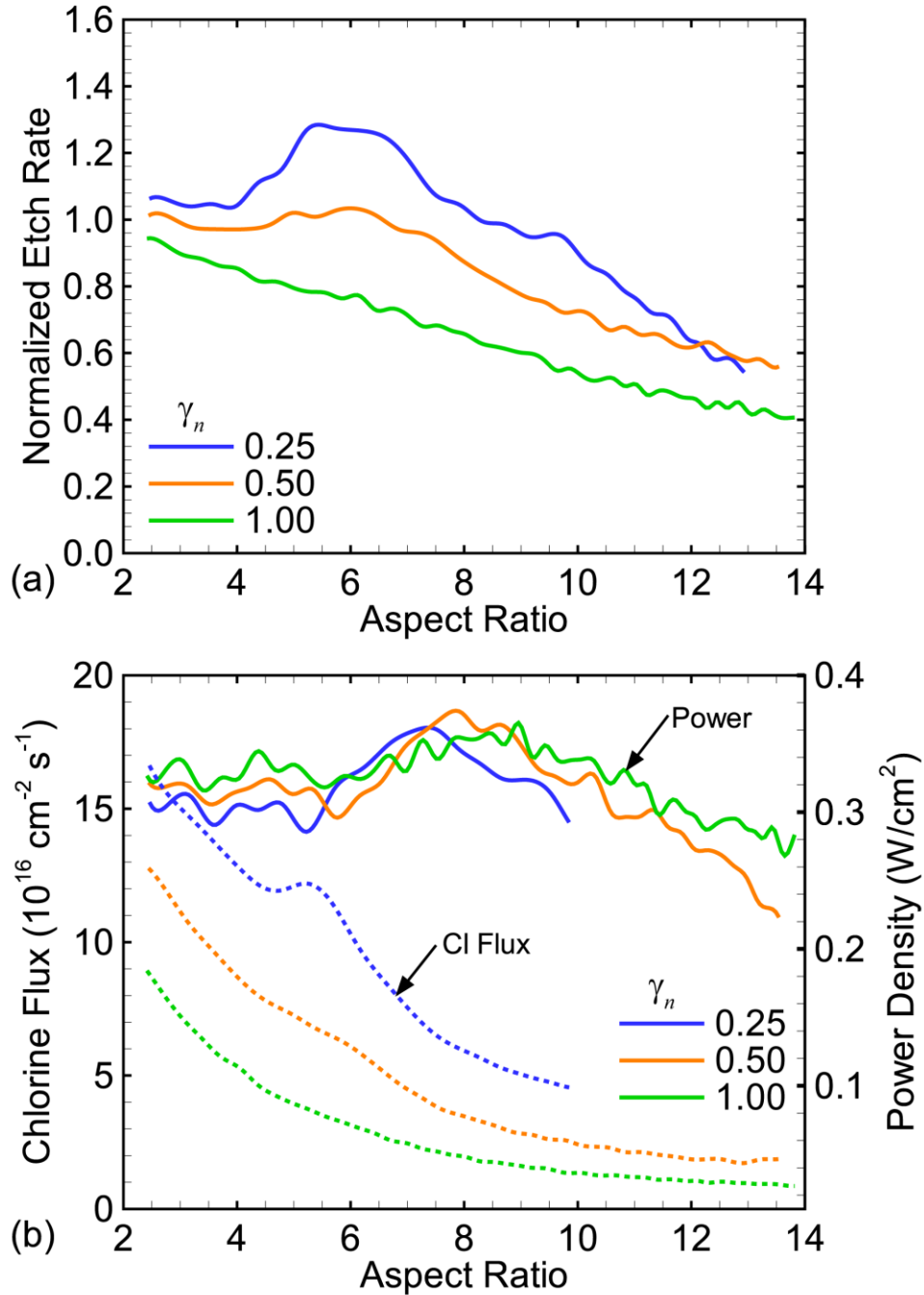


Fig. 4.15 Dependence of (a) etch rate, and (b) chlorine flux and power density on aspect ratio and the angular distribution of neutrals,  $\gamma_n$ . Etch rate is normalized to the etch rate in the open field for the base case ( $\gamma_n = 1.00$ ). Power density and chlorine flux are measured at the etch front as it evolves. Chlorine flux and power density are omitted above an AR of 10 for  $\gamma_n = 0.25$  due to the highly tapered profile interfering with the measurement technique.

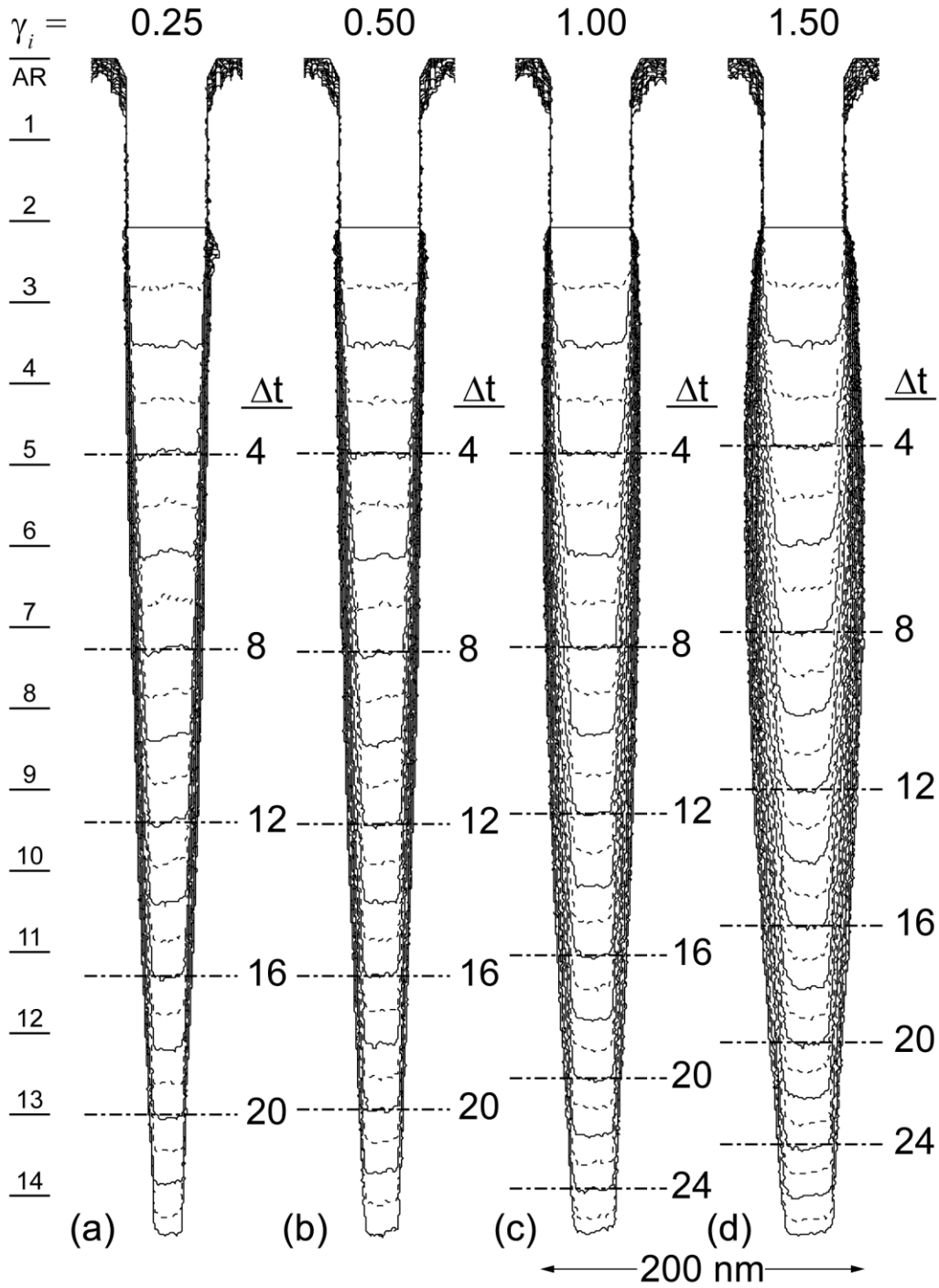


Fig. 4.16 Time evolution of silicon trench profile for different ion angular distributions,  $\gamma_i$ . The normalized angular distribution scaling factors shown are (a) 0.25, (b) 0.50, (c) 1.00, and (d) 1.50. Line spacing represents a constant time interval  $\Delta t$  for all profiles. Numbered lines represent similar etch times in each profile.

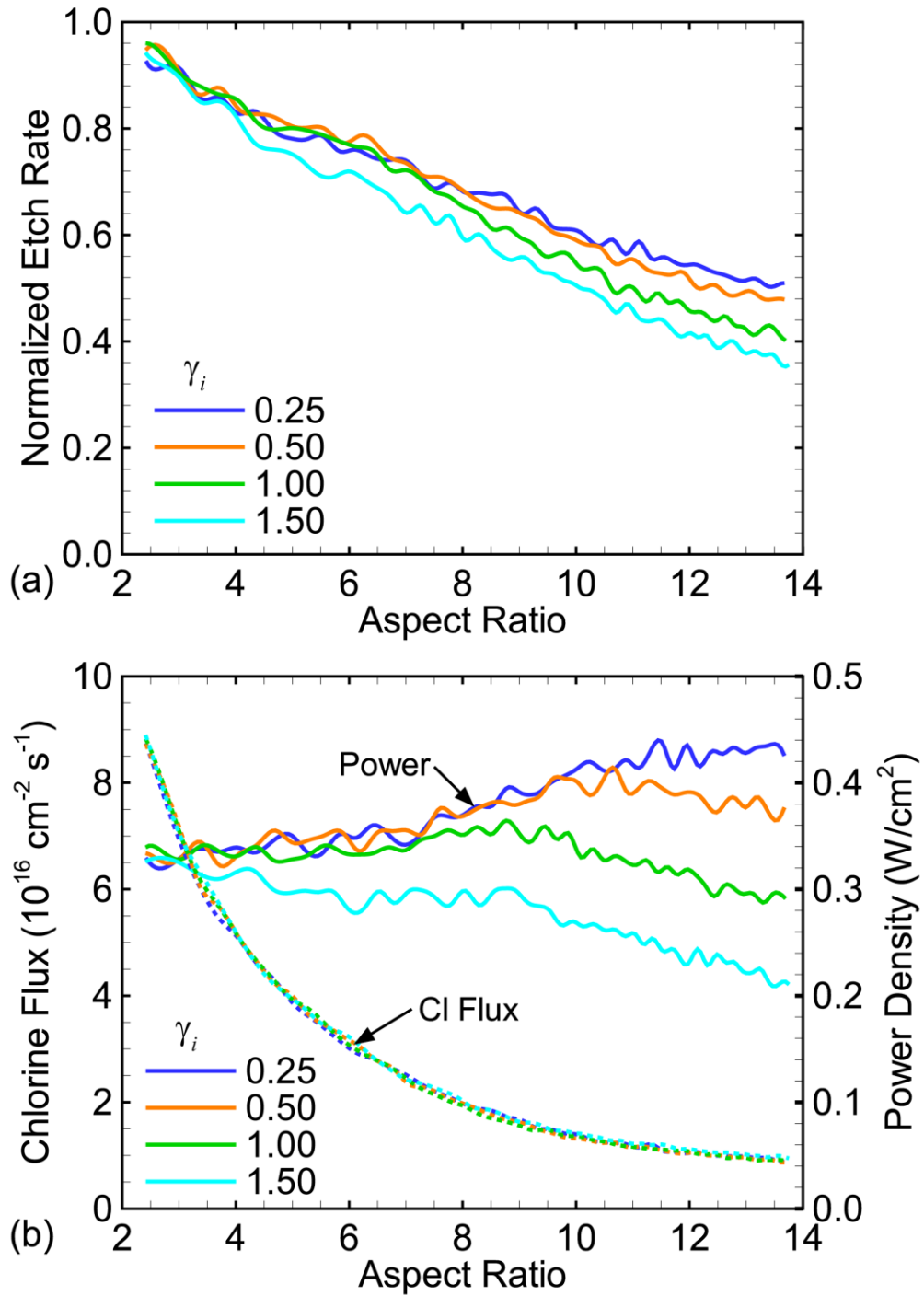


Fig. 4.17 Dependence of (a) etch rate, and (b) chlorine flux and power density on aspect ratio and the angular distribution of ions,  $\gamma_i$ . Etch rates are normalized to the etch rate in the open field for the base case ( $\gamma_i = 1.00$ ). Power density and chlorine flux are taken at the etch front as it evolves.

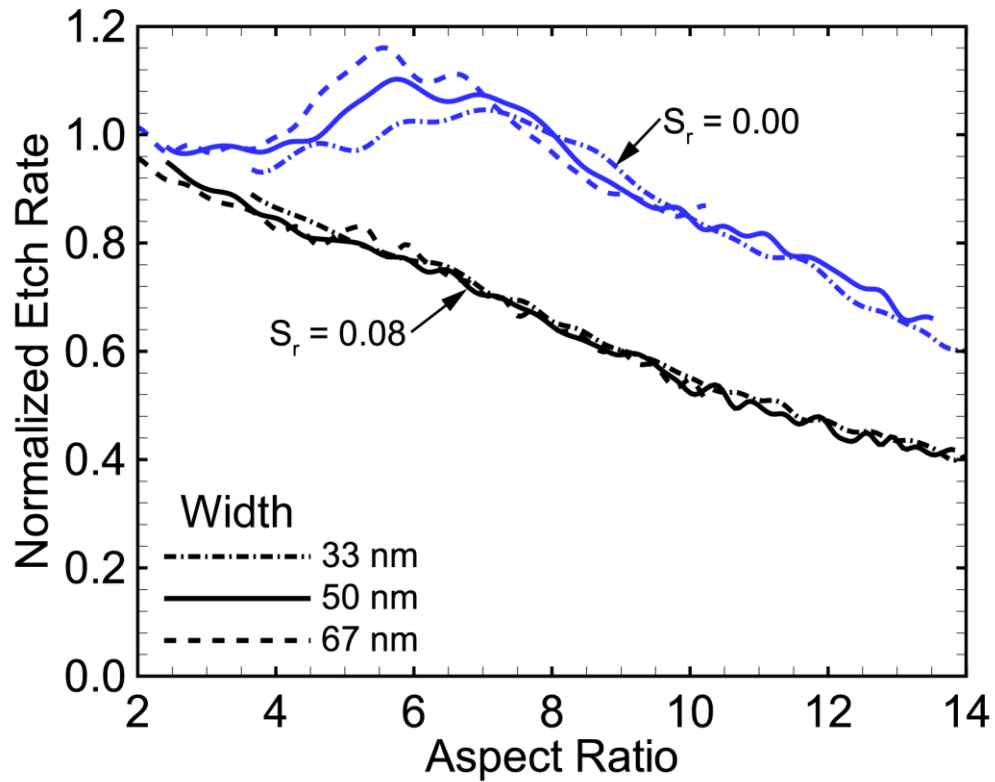


Fig. 4.18 Etch rate as a function of aspect ratio and trench width for two values of chlorine recombination rate,  $S_r$ . For the base case,  $S_r = 0.08$ , the etch rate depends only on aspect ratio and not trench width. For the case without chlorine recombination,  $S_r = 0.00$ , the peak in etch rate weakly depends on trench width, but at higher aspect ratios the ARDE trends are again independent of trench width.

## Chapter 5 ATOMIC LAYER ETCHING USING HALOGEN GASES

### 5.1. Introduction

As the critical dimension (CD) of devices approach atomic scales, the demands placed on plasma etching techniques have become difficult to meet using traditional continuous or pulsed etching processes.[8,117] The use of self-limited surface reactions to remove a well-defined layer of material in a controlled fashion, atomic layer etching (ALE), has been proposed as a method to overcome some of the limitations in current etching techniques.[117–119] A typical ALE cycle consists of a minimum of two steps. The first step passivates the top layer of material in a self-limited manner. That is, the passivation ceases when the exposed surface is fully passivated. An example is the passivation of a Si surface by Cl atoms – the process ends when the surface is fully occupied by  $\text{SiCl}_x$ . The second step preferentially removes the passivated layer. For example, low energy ion bombardment removes the  $\text{SiCl}_x$  but not the underlying Si.[120]

By using self-limited surface reactions in both steps, ALE decouples the formation of a preferentially etched passivation layer on the surface from the actual etching step.[121] The passivation step is usually accomplished by chemical reactions between radical species and the surface. These radical species diffusively transport through the feature by molecular flow, which is highly dependent on the aspect ratio and geometry of the feature, as discussed in Chapter 4. Even though the transport of radicals through the feature depends on aspect ratio, if the passivation is self-limiting then features will eventually fully passivate regardless of the aspect ratio. Etching, on the other hand, often occurs by ion bombardment. Most ions reach the etch

front ballistically from the plasma by line-of-sight due to the anisotropic angular distribution of ions. This anisotropic transport mechanism enables the ion flux reaching the etch surface to be essentially independent of aspect ratio. During continuous processing, the etch rate depends on the ratio of neutral to ion species incident onto the etch front, and so the difference in transport mechanisms between radicals and ions gives rise to an aspect ratio dependent etch rate (ARDE) in many systems, as discussed in Chapter 1.4 and in detail in Chapter 4. Decoupling the fluxes of passivating radicals and etch stimulating ions through time multiplexing enables their contributions to the etch process to be definitively controlled for all aspect ratios, despite their different transport mechanisms.

Decoupling passivation and etching phases can alleviate several of the problems discussed in Chapter 1.4, including reducing aspect ratio independent etching, increasing selectivity and reducing plasma induced damage.[118] The reduction of ARDE is accomplished directly by being able to control the ratio of the passivating and etching fluxes independent of aspect ratio. The remaining advantages, high selectivity and low plasma induced damage, are related to the use of low ion energies during the ALE cycle.

In many etching systems, it is difficult to achieve fully self-limited reactions during both phases of the ALE cycle in order to obtain ideal results. To achieve fully self-limiting passivation requires that no ion activated processes take place during the passivation step. This requirement implies that either there are no ions present in the incident passivating fluxes, or that the ion energies are strictly below the threshold for chemical sputtering of the passivated layer. Both of these requirements can be difficult to meet as practical etching processes demand a reasonably large flux of radicals to rapidly passivate the surface – and this usually requires an active plasma source.[122,123]

During the ion etching step, control of the incident ion energies is required such that the surface is exposed to ions with energies greater than the sputtering threshold of the passivated layer, but below the sputtering threshold of the bare underlying material. This energy window is often small, perhaps a few tens of eV in silicon, when compared to the ion energy range in many conventional plasma etching processes.[22] Control of ion energies to this level has been shown with conventional plasma sources, indicating that this requirement may be strict but manageable in ALE processes.[124,125] In addition to the ion energy requirement, no passivating radical should reach the wafer during the etch step, as these fluxes would enable a continuous etching process. This requirement implies using an inert gas for the ion etching phase along with a long purge time to remove reactive species that may remain in the reactor from the passivation step. This is a particularly challenging requirement for systems that rely on radicals that can adsorb on the surfaces of the reactor or reactive etch products that may deposit on the reactor walls. Either scenario may release passivating radicals back into the plasma during the etching phase.

While the requirements for ideal ALE are strict, it remains unclear how much continuous, non-ideal etching can occur during the ALE cycle while still retaining the benefits of ALE. To design effective ALE processes, one should understand how close to ideal an ALE process must be in order to maintain the desired CDs. For example, the gate etch in a finFET process requires that 3-dimensional (3-d) corners be accurately resolved to maintain a uniform metallurgical gate length along the height of the fin. Producing this accuracy may require significant etching after clearing the majority of the feature in order to remove residual poly-silicon from 3-d corners, a condition termed *over-etch*. Plasma damage during over-etch can be detrimental to device performance [126], and so the reduction in over-etch time enabled by ALE is an attractive feature. In this particular application, clearing 3-d corners, the roughness of the etch front and

the exact etch depth per cycle are not as critical as the ability of ALE to be resistant to ARDE. While other applications will have different requirements, not all applications require ideal ALE for the process to favorably compare to continuous etching.

In this chapter, results are discussed from a computational investigation of ALE when either or both of the process steps are not fully self-limited – that is, non-ideal ALE. As a base case, we investigated the ALE of Si. This ALE mechanism ideally consists of two self-limited reactions: a Cl passivation step, which utilizes an Ar/Cl<sub>2</sub> plasma to generate a flux of Cl radicals resulting in a single layer of SiCl<sub>x</sub> passivation, and an Ar<sup>+</sup> ion bombardment step, using a pure Ar plasma to generate fluxes of ions to remove the single layer of passivated Si. This system is capable of producing ALE behavior in experiments, and previous modeling efforts.[123,127–129] Starting from an idealized process, where only completely self-limited reactions occur, individual non-idealities are introduced to examine their effect on ALE performance. Once these dependencies are established, realistic non-idealities are introduced by coupling the feature scale model to a reactor scale model of an inductively coupled plasma (ICP). A procedure for optimizing the pulse times in an ALE process with non-self-limited conditions is discussed. Finally, the etching of a poly-silicon gate in a finFET-like structure is used as a case study to demonstrate the benefits of ALE etching even in the presence of non-idealities.

The results of these studies indicate that an ideal ALE mechanism is capable of etching essentially uniform and consistent depths per cycle, with little surface roughening or ARDE. The introduction of continuous etching processes to an otherwise self-limited ALE mechanism produces surface roughening and ARDE. Continuous etching reactions which rely on a neutral – ion synergy (e.g., chemical etching of SiCl<sub>x</sub>) generate both roughening and ARDE, whereas processes initiated only by ions (e.g., ions with energies above the physical sputtering threshold

of Si) generate roughness but not ARDE. By reducing pulse times, the consequences of non-ideal process conditions can be partially mitigated, at the expense of reintroducing some components of ARDE. A case study of a finFET gate etching indicates that ALE with non-ideal fluxes is capable of significantly reducing the over-etch time required to clear 3-d corners, provided that the pulse times are properly optimized.

To enable the sequence of two self-limited sets of reactions, as required for ALE, pulsing of input gas and plasma properties is often used, involving two different plasma chemistries. Modeling this process is accomplished by running the HPEM to a steady state for each of the two plasma conditions using different reaction mechanisms, which then produces two separate sets of fluxes and IEADs/NEADs. Repetitive pulsing is addressed in the MCFPM by selecting pseudo-particles from one set fluxes and IEADs/NEADs until the number of particles released is equal to the sub-cycle duration divided by  $\Delta t$ . The process is then repeated for the other sub-cycle, recognizing that  $\Delta t$  will usually be different between sub-cycles due to the difference in fluxes. In this study, the largest  $\Delta t$  is about 0.5  $\mu\text{s}$ , and pulse times range from tens of milliseconds to several seconds, making the discretization error small. Pulsing using the MCFPM is discussed in more detail in Chapter 2.4. The surface reaction mechanism used for this study is described in Chapter 3.2, and is the same as was used in Chapter 4, except where changes are explicitly described to enable ideal ALE.

## **5.2. Characteristics of Ideal ALE**

Before investigating the impact of non-idealities on ALE processes, a baseline was established using an idealized reaction mechanism. In this baseline, fluxes and energy distributions from the HPEM were not used. Instead, conditions which allow for ideally self-limited surface reactions were chosen. The passivation sub-cycle included only an isotropic flux

of Cl radicals of  $7.0 \times 10^{17} \text{ cm}^{-2} \text{ s}^{-1}$  with zero ion flux. The ion bombardment sub-cycle had an ion flux of  $2.3 \times 10^{16} \text{ cm}^{-2} \text{ s}^{-1}$ , composed entirely of  $\text{Ar}^+$  with zero flux of  $\text{Cl}^+$ ,  $\text{Cl}_2^+$  or Cl. The ions were given a perfectly anisotropic angular distribution and were mono-energetic at 24 eV. This energy, in our mechanism, is above the threshold for chemically-enhanced sputtering of  $\text{SiCl}_x$  and below the threshold for physical sputtering of Si. The normal angular distribution eliminates ions interacting with vertical sidewalls and minimizes interactions with sloped walls. With the initial ion energy, strictly between the threshold energies of the passivated  $\text{SiCl}_x$  and that of bare Si, there is no physical sputtering of Si.

These idealized etching conditions were used to simulate the etching of a 30 nm wide trench in silicon using pulse times of 0.5 s for the passivation step and 3.0 s for the ion bombardment phase. The geometry used in the study is shown in Fig. 5.1(a), and includes a shallow feature with an AR of 2 and a deeper feature with an AR of 10. The aspect ratios were established by pre-etched ideal trenches of different depths in the bulk silicon. Etching of the top surface is prevented by a thin hard mask to avoid complications caused by mask erosion and energetic particles reflecting from the mask. The composition of the surface is qualitatively shown in Fig. 5.1(b) at several times throughout a single ALE cycle. Note that the surface coverages in Fig. 5.1(b) are not shown with a constant time interval between images. The images are intended to show the progress of the chlorination and etching during the ALE period. During the passivation phase the surface concentration of Cl quickly increases to a steady state coverage. Once  $\text{Ar}^+$  bombardment begins, the passivated surface is eroded to leave an ideally smooth silicon surface.

The ideal ALE etching behavior is shown more quantitatively in Fig. 5.2. The etch depth as a function of time for the AR=2 feature shows exactly one ML of material being removed in

each ALE cycle in Fig. 5.2(a), from the second cycle after starting the etch, to the fifth cycle. The roughness increases at the beginning of each ion bombardment step as the passivated layer is partially and statistically eroded. The roughness returns to zero as the smooth Si under-layer is exposed. This smooth under-layer of silicon cannot be physical sputtered by the low energy  $\text{Ar}^+$ , resulting in the process being self-limiting. The surface coverages of  $\text{SiCl}_x$  plotted as a function of time for one ALE cycle in Fig. 5.2(b), indicate that there is a short ( $\approx 50$  ms) transient period at the beginning of the Cl passivation step where  $\text{SiCl}_x$   $x < 3$  species dominate. After the initial transient, the surface quickly establishes a steady state coverage of 1%  $\text{SiCl}$ , 21%  $\text{SiCl}_2$  and 78%  $\text{SiCl}_3$ , making an average chlorination per surface site,  $\langle \text{Cl} \rangle$ , of 2.77. The predicted time to saturation for both the chlorination and ion bombardment phases are similar to those observed by Ranjan et al. [20], as well as Goodyear and Cooke.[34]

The same etching conditions were used on the  $\text{AR} = 10$  feature as for the  $\text{AR} = 2$  feature. The etch results also produce an ideal ALE as expected, with an identical etch sequence and roughness values as for the  $\text{AR} = 2$  case. This result implies that the ideally self-limited nature of the reactions allow for the process to decouple etching from the transport of neutral species, thereby negating ARDE over this range of aspect ratio. The only significant difference between the ideal ALE of features having  $\text{AR} = 2$  and  $\text{AR} = 10$  is the time required to achieve the steady state value of  $\langle \text{Cl} \rangle$ , as shown in Fig. 5.3. A longer time is required to fully passivate the  $\text{AR} = 10$  feature compared to  $\text{AR} = 2$ . As the AR increases, the neutral conductance through the feature decreases, and a larger portion of the incoming neutral flux is reflected back into the plasma by collisions with the sidewalls before the flux can passivate the etch front at the bottom of the feature. The lower conductance of the  $\text{AR} = 10$  feature requires a larger fluence of Cl radicals, and therefore a longer passivation time, to achieve the same  $\langle \text{Cl} \rangle$  as the  $\text{AR} = 2$  feature. Since

the passivation step is perfectly self-limiting, the passivation time used here is chosen to be long enough for both the AR = 2 and AR = 10 features to reach a steady state surface passivation with there being no ill effects for the AR = 2 feature.

For ion fluxes that have highly anisotropic angular distributions, such as those used here, there should be little dependence of Cl surface coverage on AR during the ion bombardment step. If the ions had a larger angular spread there would be a weak dependence on AR due the loss of ions striking the sidewalls at larger AR (ion shadowing). A longer etch time would be required to remove the single layer passivation, as the view-angle of any given point on the etch front would subtend less of the incoming flux. However, the final etch surface would be independent of AR, provided the ion bombardment time was long enough. However, if the angular distribution is broad enough to desorb Cl atoms from the side walls, then additional etching at the bottom of the feature could occur by recycling the Cl atoms into passivation of the etch front.

With fluxes and a reaction mechanism that produce self-limiting passivation and etching, perfect ALE can be achieved independent of AR. Due to the ideally self-limited nature of the ALE reactions described here, ideal ALE behavior can always be achieved by using sufficiently long pulse times.

### **5.3. ALE with Non-Ideal Reactant Fluxes**

#### **5.3.1. Non-ideal Radical or Ion Fluxes**

In this section, small deviations from the fluxes that produce ideal ALE will be investigated. In this regard, the ratios of ion to neutral radical fluxes ( $\Gamma_i/\Gamma_n$ ) during the passivation step, and neutral Cl radical to ion fluxes ( $\Gamma_n/\Gamma_i$ ) in the ion bombardment step of the ALE cycle were varied. Having a nonzero value of  $\Gamma_i/\Gamma_n$  during the passivation step introduces

ions while the surface is being chlorinated or is fully chlorinated, enabling the possibility of continuous etching, which is detrimental to ALE. Similarly, having a neutral flux during the ion bombardment phase (by having a non-zero  $\Gamma_n/\Gamma_i$ ) also enables the possibility of continuous etching by allowing the surface to re-chlorinate while under ion bombardment. Both of these sources of continuous etching proceed by the chemical sputtering of  $\text{SiCl}_x$  species, making them dependent on ion/neutral synergy. A third non-ideal aspect investigated is having ion fluxes with energies greater than the physical sputtering threshold for Si.

Introducing a small flux of ions into the passivation phase demonstrates the sensitivity of the ALE mechanism to this non-ideality. The outcomes of having nonzero  $\Gamma_i/\Gamma_n$ ,  $10^{-4}$  to 0.02, are shown in Fig. 5.4 where EPC,  $\mathcal{S}_y$  and the proportion of etching occurring during passivation and ion bombardment are shown for aspect ratios of  $\text{AR} = 2$  and 10. The pulse times used were the same as the ideal case, 0.5 s for the passivation phase and 3.0 s for the ion bombardment step. The exact amount of non-ideal etching reactions which take place will depend directly on the passivation phase time, as will be discussed in more detail later. For these pulse times, ideal behavior for both low and high AR is retained for  $\Gamma_i/\Gamma_n = 10^{-4}$ . However, etching with  $\Gamma_i/\Gamma_n$  as low as  $10^{-3}$  shows significant non-ideality. For  $\text{AR} = 2$ , the EPC increases to 1.1 ML while  $\mathcal{S}_y$  decreases to 96%. With  $\Gamma_i/\Gamma_n = 0.01$  and 0.02, values that would be typical if an ICP was used to generate the Cl flux, the results indicate far from ideal behavior.  $\mathcal{S}_y$  decreases to 76% for  $\Gamma_i/\Gamma_n = 0.01$  and to 63% for  $\Gamma_i/\Gamma_n = 0.02$ . These results imply that for  $\Gamma_i/\Gamma_n = 0.02$ , over one third of the etching occurs during the passivation phase through continuous etch processes.

The results shown in Fig. 5.4 also indicate an unexpected trend – not all of the etching in excess of 1 ML occurs during the passivation phase. For  $\Gamma_i/\Gamma_n \geq 10^{-3}$ , etching during the ion bombardment phase results in removal of more than 1 ML. The conditions of the ion

bombardment phase are the same as for the ideal case, so in principle the ion-bombardment phase is intrinsically self-limited. The extra etching producing  $>1$  ML per cycle results from roughness produced by the non-ideal passivation phase. Since this etching mechanism is self-limited, it cannot lower  $\mathcal{S}_y$  during the ion bombardment phase. In fact, extending the ion bombardment phase will not introduce more etching per cycle. The excess material ( $>1$  ML) removed during the ion bombardment phase is only a function of the surface roughness introduced during the passivation phase. More than 1 ML of material is removed because roughness enables more Si atoms to be exposed to the plasma and so be chlorinated. This correlation between surface roughness and increased material removed per cycle does not *necessarily* introduce non-ideality since the self-limited nature of the etch process is retained. However, this coupling of surface roughness and  $\mathcal{S}_y$  could jeopardize etch uniformity and aspect ratio independence if the surface roughness depends on etch time or aspect ratio.

A motivation for implementing ALE processing is to reduce or eliminate the propensity for ARDE that occurs in continuous processing due to in-feature transport phenomena. The etch characteristics shown in Fig. 5.4 indicate that for  $\Gamma_i/\Gamma_n > 0$  the EPC is different for the AR = 2 and AR = 10 features. Ion fluxes during the passivation phase reintroduce an ARDE which was absent in the ideal case. ALE synergy,  $\mathcal{S}_y$ , does not have the same dependence on AR, being nearly constant for both ARs over the entire range of  $\Gamma_i/\Gamma_n$  studied. Etching the AR = 10 feature resulted in a lower EPC than the AR = 2 feature in spite of having the same  $\mathcal{S}_y$ . These results indicate that the amount of etching during the passivation phase is less for AR = 10 than for AR = 2, in spite of having the same ion fluence. The larger AR, with its lower conductance of Cl radicals from the plasma, results in a lower rate of re-passivation of etched sites at the bottom of the feature. This lower rate of re-passivation then slows the rate of non-ideal etching. Any

conductance dependent process will have a strong dependence on aspect ratio. The fact that  $\mathcal{S}_y$  remains nearly constant over this range of AR could be coincidental. However, it may also imply that there is a correlation between the amount of material removed by the non-ideal etching during the passivation phase and the increase in the self-limited etching during the ion bombardment phase. This coupling between the etching mechanisms of the passivation and ion bombardment phases occurs due to increase in surface roughness due to the non-ideal etching.

The just-discussed correlation emphasizes the importance of surface roughness in producing ideal-ALE. Smooth surfaces are important not only because smooth features are usually preferred to rough surfaces, but also due to the coupling between surface roughness and material removed per cycle. The surface roughness as a function of time is shown in Fig. 5.5(a) for  $\Gamma_i/\Gamma_n = 10^{-4}$ ,  $10^{-3}$  and 0.01. The case having  $\Gamma_i/\Gamma_n = 10^{-4}$  during the passivation phase produces  $\mathcal{S}_y \approx 100\%$ , but still suffers from a steadily increasing cycle averaged roughness over the pulses shown. This roughness will eventually saturate at a value of 0.9, significantly higher than the ideal case despite the nearly ideal  $\mathcal{S}_y$ . The cycle averaged steady state roughness is 1.8, 1.6, 1.4 and 0.9 for  $\Gamma_i/\Gamma_n = 0.02$ , 0.01,  $10^{-3}$  and  $10^{-4}$ . There is also a characteristic time scale before the system reaches a steady state roughness. Larger  $\Gamma_i/\Gamma_n$ , produce more roughness but reach it quasi-steady state value sooner. The details of the roughening depend on etch time and etch depth. However, the roughening is similar when compared on the basis of the fluence of ions during the passivation phase. This similarity suggests that each ion impinging on the etch front during the passivation phase is responsible for some stochastic roughening of the surface. This trend was also recently observed experimentally for very low ion to neutral flux ratios generated in pulsed  $\text{Cl}_2$  plasmas.[131] A ion fluence of  $\approx 4 \times 10^{15} \text{ cm}^{-2}$  is required to reach the steady state roughness, after which no further dependence on fluence is observed. These factors

indicate that there is a competition between a roughening process, produced by stochastic ion impacts during the passivation phase, and a smoothing process during the otherwise ideal ALE cycle.

The surfaces at the bottom of the trench are shown in Fig. 5.6 for  $\Gamma_i/\Gamma_n = 0.01$ ,  $10^{-3}$  and  $10^{-4}$  after 25 ALE pulses (87.5 s) for the AR = 2 feature. The overall roughness increases as the ion to neutral flux ratio increases. The surface for  $\Gamma_i/\Gamma_n = 10^{-4}$  has a scattering of small divots caused by individual ion strikes and larger divots where several ion strikes stochastically occurred in close proximity during the same passivation step. The surface for  $\Gamma_i/\Gamma_n = 10^{-3}$  has a similar pattern of larger divots, but with significantly more uniform roughening as well. The surface for  $\Gamma_i/\Gamma_n = 0.01$  has few large divots with the surface being dominated by random roughness, however the divots which persist are larger and deeper.

In addition to non-idealities caused by ions during the passivation phase, non-idealities can also occur by chlorine fluxes onto the wafer during the ion bombardment phase, a condition that can also result in continuous etching. While long purge times can be used to eliminate most of the gas phase Cl remaining in the chamber from the passivation phase, etch products released from the wafer during the ion bombardment phase are themselves chlorine containing. These etch products can be dissociated by electron impact in the plasma, or they can deposit on the chamber walls which can then act as a source of Cl radicals under ion bombardment. Cl may also be adsorbed onto any surface in contact with the plasma during the passivation phase, and desorb during the etching phase. While the actual source of Cl radicals during the ion bombardment phase is likely not Cl<sub>2</sub> gas in the feedstock gases, it is convenient to quantify the level of Cl contamination by parts-per-million (ppm) of Cl<sub>2</sub> in the gas phase. In this case, the HPEM was used to calculate the Cl flux to the surface of the wafer when the feedstock Ar gas

contained 1, 10 and 100 ppm of  $\text{Cl}_2$ . These levels of contamination resulted in Cl fluxes of  $2.3 \times 10^{13}$ ,  $1.1 \times 10^{14}$  and  $7.9 \times 10^{14} \text{ cm}^{-2}\text{s}^{-1}$  to the wafer. The argon ion flux was kept constant at  $2.3 \times 10^{16} \text{ cm}^{-2} \text{ s}^{-1}$ . The simulation of profiles was then performed with these fluxes during the ion bombardment phase using the idealized etch mechanism.

EPC and  $\mathcal{S}_y$  for AR = 2 and 10 with these small levels of  $\text{Cl}_2$  contamination are shown in Fig. 5.7. These results indicate that increasing concentrations of  $\text{Cl}_2$  result in increased EPC and decreased  $\mathcal{S}_y$  due to the continuous etching enabled by even these small Cl fluxes. Only 1 ppm of  $\text{Cl}_2$  in the reactor can generate enough Cl flux to the wafer to decrease  $\mathcal{S}_y$  from 100% in the ideal case to 98% for the AR = 2 feature. For 10 ppm  $\text{Cl}_2$   $\mathcal{S}_y$  decreases to 94% and with 100 ppm  $\text{Cl}_2$  there is a further reduction of  $\mathcal{S}_y$  to 71%. In order to evaluate  $\mathcal{S}_y$  in these cases the Cl labeling technique described in Sec. II was used to determine the ratio of etch products which were passivated in the ion bombardment phase to those passivated during the passivation phase.

Since the chlorine flux transports through the feature by molecular flow, the high aspect ratio feature is less sensitive to increasing Cl fluxes due to its lower neutral conductance. In the AR = 10 feature the reduction of  $\mathcal{S}_y$  is smaller than statistical errors ( $\approx 100\%$ ) with 1 ppm  $\text{Cl}_2$ , decreasing to 99% and 92% for 10 and 100 ppm  $\text{Cl}_2$ . There is a strong aspect ratio dependence in both the etch rate and in  $\mathcal{S}_y$ . These trends contrast with adding ions to the passivation phase, where EPC depended on AR but  $\mathcal{S}_y$  did not. With the introduction of radicals into the ion bombardment phase, the etching due to the self-limited chlorination during the passivation phase increases slightly with  $\text{Cl}_2$  concentration – again, due to surface roughening. However, this increase is not a function of AR. The larger dependence on AR of continuous etching by radicals in the ion bombardment is due to neutral transport through the feature. This process is particularly sensitive to AR due to the dependence of conductance on AR. As the AR increases

and the neutral conductance decreases, a significant fraction of the non-ideal flux of radicals during the ion bombardment phase will be reflected back into the plasma by the feature without ever having interacted with the etch front.

Having a passivating radical flux during the ion bombardment phase also results in a roughening of the surface compared to the ideal case. The average roughening again increases over several pulses at the beginning of the etch before reaching a steady state. The cycle averaged steady state roughness increases with larger concentrations  $\text{Cl}_2$ , reaching 1.1, 1.2 and 1.4 for 1, 10 and 100 ppm of  $\text{Cl}_2$ . The sub-cycle resolved pattern of roughness, shown in Fig. 5.5(b) for 100 ppm of  $\text{Cl}_2$ , indicates that the majority of the roughening occurs during the latter part of the ion bombardment phase when the continuous etching occurs. In the prior case of adding an ion flux during the passivation step, roughening occurred dominantly during the passivation step while the surface was smoothed during the ion bombardment step; enabling the system to achieve a steady state. With a Cl flux during the ion bombardment step, smoothing and roughening both occur during the ion bombardment step. The two mechanisms compete to enable the system to reach a steady state roughness after an initial transient.

The surface morphology generated by having a Cl flux during the ion bombardment phase differs slightly from that when having an ion flux during the passivation phase. The height of the etched surface at the bottom of the  $\text{AR} = 2$  trench after 25 ALE pulses (32 s) is shown in Fig. 5.8 for the 100 ppm  $\text{Cl}_2$  case. The surface has the characteristic divots, but the surface is also slightly concave due to a higher etch rate in the center of the feature. This higher etch rate is due to a higher flux of Cl atoms incident onto the center of the feature. The concavity becomes more pronounced with longer etch times (more pulses).

Another non-ideality is having ions with energies greater than  $\varepsilon_{th}$  for physical sputtering during the ion bombardment phase. To investigate this non-ideality, the IEADs consisted of a continuous distribution from 25 eV to the maximum ion energy  $\varepsilon_m$ , where  $\varepsilon_m$  was 50, 55, 60 and 65 eV. The resulting etch characteristics are shown in Fig. 5.9. With  $\varepsilon_m = 50$  eV, there is little difference compared to the ideal case. Although the IEAD is not mono-energetic, it also does not include any ions with energies greater than  $\varepsilon_{th} = 50$  eV. Other than the increased rate of chemical sputtering of  $\text{SiCl}_x$  species, the etch should be ideal. With  $\varepsilon_m > 50$  eV, the distribution contains ions with energies high enough to sputter bare silicon, introducing a continuous etching mechanism due to physical sputtering. Even having a small fraction of the ions with energies greater than the Si sputtering regime produce significant non-ideality with these pulse times, with  $S_y$  decreasing to 71% for  $\varepsilon_m = 65$  eV in the AR = 10 feature. However, this non-ideality does not result in significant ARDE. The physical sputtering of bare silicon is a purely ion driven process, while the other two non-idealities discussed are based on a chemically enhanced sputtering mechanism. Chemical sputtering inherently requires a neutral/ion synergy which relies on conductance through the feature and will therefore be susceptible to ARDE. The extra etching is due to physical sputtering by anisotropic ion fluxes and not due to a synergistic process reliant on conductance limited Cl fluxes. If the ion angular distribution is narrow enough, the rate of physical sputtering will be independent of AR. The pattern of roughness resulting from physical sputtering of silicon is similar in character to having ions in the passivation phase.

### **5.3.2. Controlling EPC and ALE synergy with pulse times**

Introducing a single non-ideality into the ALE process provides insights into the requirements for designing an optimized process. In the practical implementation of ALE, it is

possible that all of the non-idealities discussed here may occur at the same time, and so their effects must be simultaneously mitigated. If the fluxes and ion energies have been tailored to be as ideal as possible for a given plasma reactor, the last process parameter that can be used to tune the ideality of the ALE process is the pulse times of the two ALE process steps – passivation time ( $T_P$ ) and ion bombardment time ( $T_I$ ). Tuning the pulse times also incurs some trade-offs. For instance, if ions fluxes are significant during the passivation step and producing continuous etching,  $T_P$  can be decreased to a point where the entire surface is chlorinated, but perhaps not to the fully saturated state of  $\text{SiCl}_3$ . Such a condition will enable the ALE process to proceed, as all  $\text{SiCl}_x$  species have a reduced threshold compared to bare silicon, but will require longer  $T_I$  to be removed. If there are any non-idealities in the ion bombardment phase, they will be exacerbated by the longer  $T_I$  required to reduce the continuous etching during the passivation phase.

In practice, if the radical Cl and ion bombardment fluxes onto the wafer are being directly produced by a plasma in contact with the wafer, it is difficult to obtain perfectly self-limited ALE reactions. Using a plasma in the vicinity of the wafer to generate a high radical flux during the passivation phase will inevitably also result in some ion flux. With the expected electron temperatures in typical inductively coupled plasmas of 2-5 eV, the sheath produced by the floating potential may have a large enough potential drop to produce ions above  $\varepsilon_{th}$ . During the ion bombardment phase, the plasma must be sustained in pure Ar to avoid there being chlorine radical and ion fluxes to the wafer. Reducing the chlorine concentration in the reactor to zero is difficult due to the chlorine containing etch products which are released from the wafer during this step and Cl containing passivation on the sidewalls.

In this section, we discuss the consequences and possible remedies of using fully non-ideal reactant fluxes and IEADs during ALE. These non-ideal fluxes were obtained from reactor

scale modeling of an ICP. The reactor, shown in Fig. 5.10, has a 3-turn flat antenna delivering 300 W at 10 MHz to the plasma. The coil is located above a quartz window 10 cm from the wafer, in a reactor 22.5 cm in diameter. The resulting plasma densities are also shown in Fig. 5.10 for both the ion bombardment and passivation phases. For the passivation phase a gas mixture of Ar/Cl<sub>2</sub> = 70/30 at 200 sccm was used with a regulation system maintaining the chamber pressure at 20 mTorr. No bias was applied to the wafer during the passivation phase, however a plasma potential of 25 V provided acceleration to ions reaching the wafer surface. The resulting fluxes to the wafer are  $7.0 \times 10^{17}$ ,  $1.1 \times 10^{16}$ ,  $1.6 \times 10^{15}$  and  $4.9 \times 10^{14}$  cm<sup>-2</sup> s<sup>-1</sup>, for Cl, Cl<sub>2</sub><sup>+</sup>, Cl<sup>+</sup> and Ar<sup>+</sup>, with ion energies peaked around 24 V, as shown in Fig. 5.11(a). During the ion bombardment phase Ar gas with 100 ppm Cl<sub>2</sub> was used to simulate chlorine contamination of the process due to incomplete purging, etch products or desorption from the walls. The total gas flow was 200 sccm at a pressure of 20 mTorr. A bias of 30 V at 10 MHz was applied to the wafer, resulting in a DC bias of -8.4 V and a plasma potential oscillating between 35 V and 49 V. The resulting fluxes to the wafer are  $7.8 \times 10^{14}$ ,  $3.9 \times 10^{12}$ ,  $9.2 \times 10^{13}$  and  $2.3 \times 10^{16}$  cm<sup>-2</sup> s<sup>-1</sup>, for Cl, Cl<sub>2</sub><sup>+</sup>, Cl<sup>+</sup> and Ar<sup>+</sup>, with ion energies distributed from 33 eV to 60 eV, as shown in Fig. 5.11(b).

Optimizing the ALE process for these non-ideal conditions involves selecting step times which both remove a consistent amount of material over the required range of aspect ratios, and which minimize the material removed by continuous etching processes. To investigate the pulse time parameter space, simulations were performed for  $T_P$  from 5 ms to 105 ms, and  $T_I$  from 0.1 s to 1.4 s. The results indicate that for any given  $T_P$  there is some  $T_I$  which will remove 1 ML of material per cycle, or EPC = 1 ML.

These trends are shown in Fig. 5.12, where the solid lines are for conditions that produce  $EPC = 1$  ML, and the shaded areas indicate the range of  $0.9 < EPC < 1.1$  ML. Results are shown for aspect ratios of 2, 4 and 6. There are regions where EPC is near 1 ML and which are nearly independent of  $T_I$  (nearly vertical in Fig. 5.12), depending dominantly on  $T_P$ . These regions might be described as radical-starved for a continuous etch. Other regions where EPC is near 1 ML are almost independent of  $T_P$  (nearly horizontal in Fig. 5.12), depending dominantly on  $T_I$ . These regions might be described as ion-starved for a continuous etch. The width of the window for which  $0.9 < EPC < 1.1$  ML is largest at the transition between these two limiting regimes, indicating more tolerance to process variation. The largest overlap of process conditions for different AR that produce  $EPC \approx 1$  is also in this transition region.

These trends imply that operating in this region will have the largest window for etching features that have different aspect ratios, however there is a limit to this process window. There is little overlap between the shaded ALE windows for AR = 2 and AR = 6 case. This disparity indicates that the non-idealities for these conditions are severe enough to preclude obtaining a constant etch depth per cycle over this range of AR when using a single set of pulse times. To maintain a constant etch depth per cycle over this range (or even wider ranges) of AR during a single etch,  $T_P$  and  $T_I$  would need to be adjusted as the AR of the feature increases. While a constant EPC over a wide range of AR is a requirement for many applications, maintaining  $EPC = 1$  ML does not necessarily imply ideal ALE.

ALE synergy,  $\mathcal{S}_y$ , also depends on ALE step times. For example,  $\mathcal{S}_y$  is shown in Fig. 5.13(a) for AR = 4 as a function of  $T_I$  for three values of  $T_P$  (44 ms, 66 ms, 88 ms). For short  $T_I$  ( $< 0.15$  s), a large fraction of the passivated Si which covers the surface of the feature is not removed during the ion bombardment step. The continuous etching produced by ions in the

passivation phase then makes a significant contribution to the total rate of etching, which then lowers  $\mathcal{S}_y$ . For long  $T_I$  ( $> 1$  s), the passivated Si covering the feature is completely removed and the now bare silicon is exposed to ion bombardment for an extended time. The continuous etching produced during the ion bombardment step by the presence of chlorine radicals and physical sputtering then accounts for a significant portion of the EPC, which then lowers  $\mathcal{S}_y$ . The  $T_I$  which results in the maximum  $\mathcal{S}_y$  minimizes these non-idealities and maximizes the etching occurring due to the synergy between the ion bombardment and passivation steps. Due to the continuous etching which may occur during each of the ALE steps, the conditions which produce the highest  $\mathcal{S}_y$  do not necessarily result in an EPC = 1 ML. Rather, the pulse times which result in the maximum  $\mathcal{S}_y$  usually result in an EPC  $< 1$  ML. A similar maximum occurs in  $\mathcal{S}_y$  as a function of  $T_P$  (for any given ion bombardment time) for similar reasons.

The relationships of ALE synergy and EPC to both  $T_I$  and  $T_P$  are shown in Fig. 5.13(b) for an AR = 4. The contours are values of  $\mathcal{S}_y$  and the solid black line corresponds to an EPC = 1 ML. The maximum value of  $\mathcal{S}_y$  (95%) in this parameter space occurs with short pulse times ( $T_I = 0.11$  s,  $T_P = 14$  ms), which results in an EPC on only 0.3 ML. If an EPC = 1 is required, the maximum  $T_I = 0.59$  s and  $T_P = 43$  ms.

In general, to minimize non-idealities during ALE, the optimized process should use the shortest pulse times which result in  $\approx 1$  ML material removal per cycle for the largest AR feature being etched. These optimized process times will be given by the point closest to the origin on the solid line in Fig. 5.13(b). These conditions also correspond to the smallest contribution of continuous chemical sputtering, and will result in the smoothest surface and widest processing window in terms of AR.

Optimizing  $\mathcal{S}_y$  reduces the influence of non-ideal reactions on the ALE process, but the resulting feature profiles can also depend on factors not captured by this metric. For instance, bowing of feature side-walls is caused by interactions with off-axis ions, and is therefore directly proportional to  $T_I$ . As an example, simulations were performed using non-ideal ALE to etch features with ARs of 2 and 6, using  $T_I = 0.63$  and 1.03 s, respectively. Passivation pulse times were also adjusted to produce an EPC of  $\approx 1.1$  ML. These pulsing conditions result in a  $\mathcal{S}_y$  of 86% for the AR 2 feature and 90% for AR = 6. Despite its higher ALE synergy, the increase in feature width due to bowing after 100 ALE pulses was 10% for AR = 6, significantly more than in the AR = 2 case (5% increase in width). Other than the differences in bowing the profiles were essentially the same, demonstrating that the ALE process is resistant to profile changes due to AR.

#### 5.4. Gate Etch Using ALE

The investigation of the effects of non-self-limited reactions in the ALE process was performed for simple trench structures. To test whether these trends extend to more complicated structures, the etching of a finFET-like geometry was used as a case study. This test is demanding as it requires low damage and high selectivity to stop on a thin stopping layer, but also often has need for long over-etch times to clear the 3-d corners at the base of the fins.

The geometry used for this case study consists of a periodic array of vertical crystalline silicon fins each with a width of 10 nm and height of 42 nm, set at a pitch of 42 nm, as shown in Fig. 5.14. The fins are covered with an etch stop layer ( $\text{SiO}_2$  in our model) with a thickness of about 1 nm on the sides, with a thicker (10 nm) blocking layer on the top to prevent damage to the fin. The fin structures are then covered with a thick, conformal poly-silicon layer. This poly-Si layer is masked perpendicular to the direction of the fins, to create the gate structure upon

anisotropic etching. The model includes a recess in the poly layer, as would be produced by a well behaved main etch which was stopped just before exposing the tops of the fins. This structure was etched using both a low ion energy continuous etching process and using our optimized non-ideal ALE process for comparison.

To compare the results from ALE with continuous etching, while still meeting the selectivity and low damage requirements of the gate etch, simulations were performed using the HPEM of a plasma with a feed-gas of  $\text{Ar}/\text{Cl}_2 = 70/30$  and an RF bias of 30 V. The resulting fluxes to the wafer were  $8.7 \times 10^{17}$ ,  $9.1 \times 10^{15}$ ,  $3.6 \times 10^{15}$  and  $4.5 \times 10^{14} \text{ cm}^{-2}\text{s}^{-1}$  for  $\text{Cl}$ ,  $\text{Cl}_2^+$ ,  $\text{Cl}^+$  and  $\text{Ar}^+$ . The resulting ion energies are almost identical to those in Fig. 5.12(b) for the ALE ion bombardment phase, and should therefore produce comparably high selectivity and low damage for a given fluence.

The profiles resulting from using the continuous etch conditions are shown in Fig. 5.15(a-c) for over-etch of 0, 25 and 100%. (Here over-etch is defined as the additional etch time after first exposing the bottom  $\text{SiO}_2$  surface divided by the time required to reach the bottom.) The profile in Fig. 5.15(a) is shown just before the etch-front touches the underlying  $\text{SiO}_2$  layer. At this point, the profile has significantly tapered away from the trench sidewalls formed by the fins. The etch-front shows some micro-trenching, or deeper etch features at the base of the vertical walls, produced by ions (or hot neutrals) having been specularly reflected from the tapered sidewalls. After a 25% over-etch, a large area of the  $\text{SiO}_2$  has been exposed at the bottom of the feature. However, a significant amount of Si remains in the corners and on the sides of the fins. Even after an over-etch of 100%, there is still silicon remaining in the corners which would require even longer etch times to remove.

Profiles produced using the ALE pulsing scheme are shown in Fig. 5.15(d-f) for over-etch of 0%, 25% and 100% , with a passivation time of 42 ms and an ion bombardment time of 0.55 s. Choosing optimum pulse times is difficult for this test structure as there is no strict definition of aspect ratio in 3-d features. If the purpose of this etch was to clear the poly-Si from between the fins with no masking, the etch feature would look like a trench with an AR slightly more than 1. For these conditions, one might benefit from shorter pulse times for optimal etching. The pulse times used in this demonstration would be optimum for feature with an AR  $\approx$  4 to account for the higher effective aspect ratio in the 3-d corners.

The profile of the feature etched by ALE just before exposing the SiO<sub>2</sub> is shown in Fig. 5.15(d). The etch front is slightly concave, likely due to the continuous etching enabled by the radicals in the ion bombardment phase. However, the concavity is less than that produced during continuous etching. There is little or no silicon left on the side of the fins whereas silicon did persist on the sidewalls in the continuous etch case. After 25% over-etch, the bottom SiO<sub>2</sub> surface has been almost completely cleared, with little residue in the corners. Continuing to 100% over-etch results in little change to the profile.

Comparing the results of etching the finFET gate structure using ALE with the continuous etch, there is a distinct advantage to using ALE despite the non-ideal processing conditions. The reduction in over-etch from >100% to  $\approx$ 25%, with similar ion energies, should reduce plasma damage. The etch times reported here for the ALE process are active process times, and do not include the time required to purge and refill gases between pulses. To clear the feature using ALE required  $\approx$  200 pulses. The purge times will depend on hardware considerations[130], but assuming each pulse requires 5 s of purge time the ALE process would require a total process time of  $\approx$  15-20 min to clear the feature. This is a significant increase in

total process time over the continuous etch ( $\approx 2$  min). However, the active (plasma on) time to completely clear the feature is comparable between the ALE and continuous etching, and so the reduced over-etch time required by ALE potentially results in less damage. It is also possible that combining a continuous main etch until reaching the bottom of the feature followed by ALE steps to clear the feature could reduce the number of ALE pulses required, thereby reducing the total processing time without losing the over-etch benefits of ALE.[129]

## 5.5. Concluding Remarks

As demands for plasma etch fidelity increase, atomic resolution is rapidly becoming a necessity, and atomic layer etching is one option to achieve that resolution. In our computational investigation of ALE, two main conclusions can be drawn regarding the use of ALE to meet this goal. First, even small deviations from perfectly self-limited reactions significantly compromise the ideality of the ALE process. For example, having as little as 10 ppm  $\text{Cl}_2$  residual gas in the reactor during the ion bombardment phase produced non-idealities in the ALE. Introducing any source of continuous chemical etching into the ALE process leads to the onset of ARDE and roughening of the etch front. These trends have significant implications for both the design of specialized reactors which intend to utilize ideal ALE for atomic level fidelity, and also for the use of ALE to control uniformity.

A second conclusion is that non-ideal ALE processes, such as those that might occur in typical ICP reactors, may offer significant advantages over continuous etching. As demonstrated a 3-d gate etch, a non-ideal ALE process, with optimized pulse times, was able to clear 3-d corners more efficiently (less over-etch) than the equivalent continuous etch. This results in less plasma exposure time which may minimize damage to the devices. The concept of over-etch, and its possible relationship with plasma damage will be discussed again in more detail in

Chapter 6. These advantages come at the trade-off of having one more process parameter, pulse time, which must be carefully controlled, along with the longer processing times related to the ALE pulsing scheme. The gate etch does not necessarily require that the etch depth per cycle be the same for the entire etch depth, as other applications may. For applications in which EPC must be constant for a wide range of AR pulse times may need to be adjusted as aspect ratios increase with etch time.

The conclusions here, while based on the ALE of silicon using Ar/Cl<sub>2</sub> plasmas, are expected to be applicable to other ALE systems as well, particularly for other halogen ALE processes.[132] The ALE of SiO<sub>2</sub>, on the other hand, will have a different set of physical pathways that introduce continuous, non-self-limited processes. Some of the effects of non-ideal continuous etching on the ALE of SiO<sub>2</sub> will be discussed in Chapter 7. The results of our simulations of the ALE of silicon indicate that the presence of continuous etching mechanisms will affect surface roughening, and that any non-ideal process which relies on ion/neutral synergy will introduce ARDE.

## 5.6. Figures

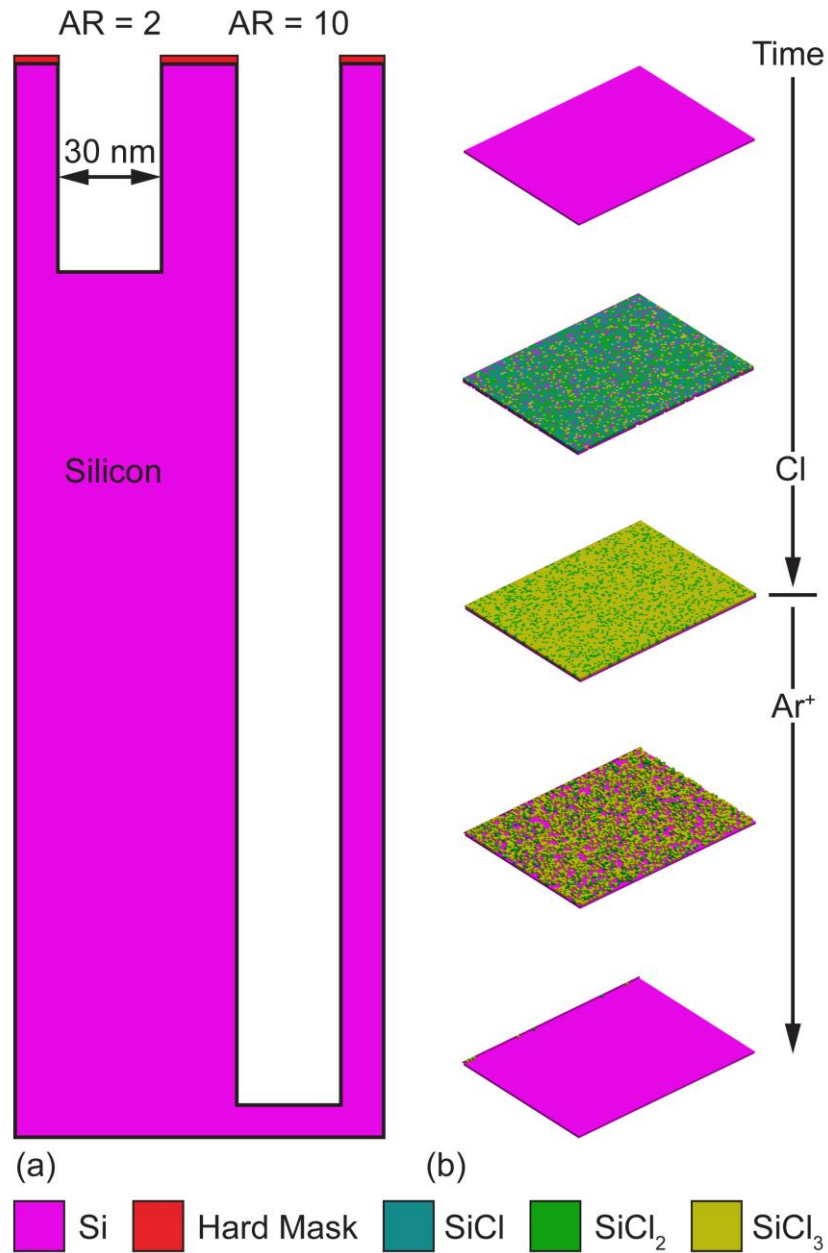


Fig. 5.1 Schematic of the ideal ALE process. (a) Schematic of the initial trench geometry used for ideal ALE simulations. (b) View of the etch front at multiple times, with different colors representing different materials. Time increases from top to bottom, but not with equal steps between images.

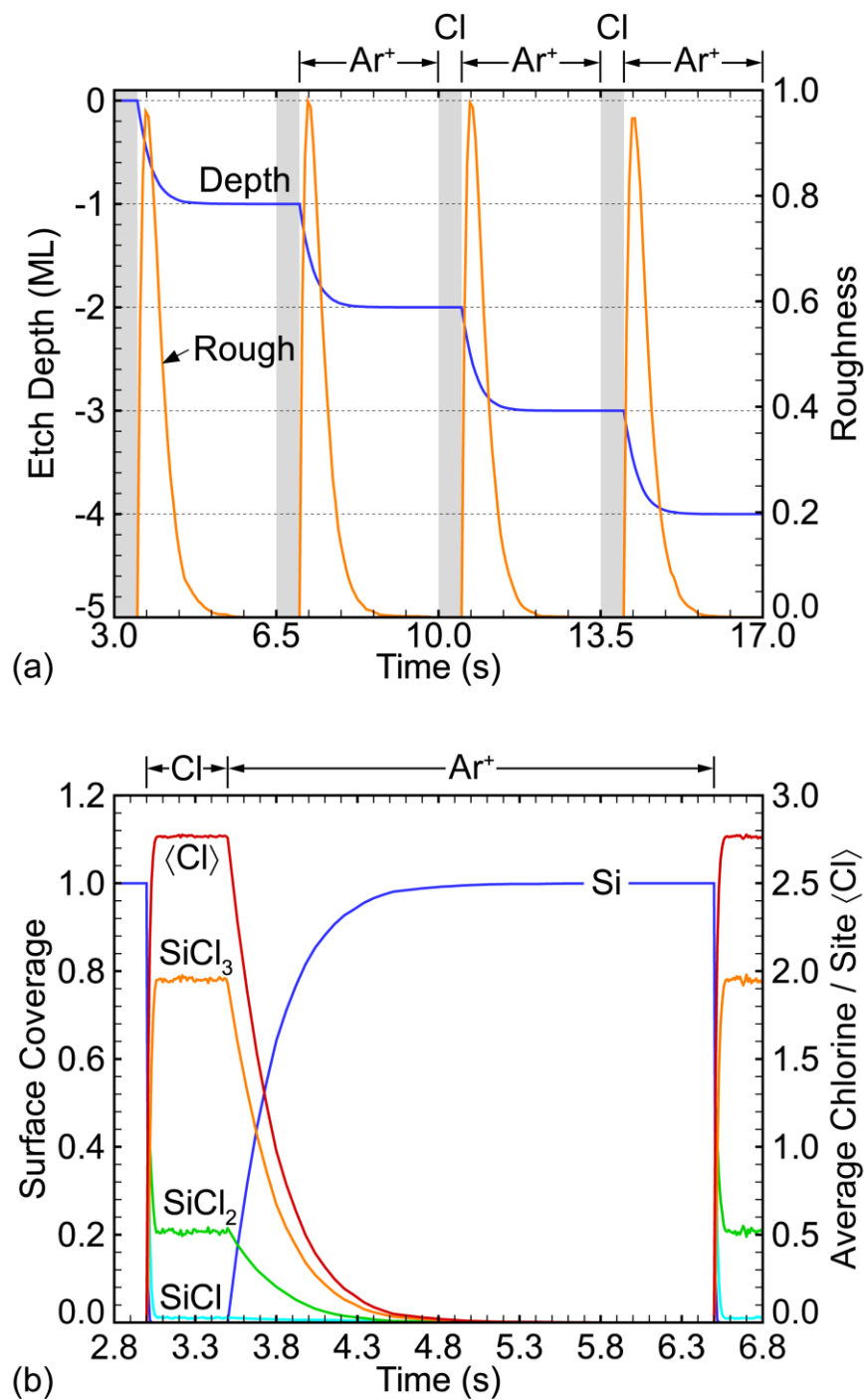


Fig. 5.2 Etch front characteristics during ideal ALE etching. (a) Etch depth and surface roughness as a function of time for the second through fifth ALE pulses. The different sub-cycles (Cl = passivation, Ar<sup>+</sup> = ion bombardment) are shown at the top for reference, with passivation phases being highlighted by grey bands in the figure. Four pulse periods are shown in total. (b) Surface coverage of Si, SiCl, SiCl<sub>2</sub>, SiCl<sub>3</sub> and average chlorine per site at the etch front as a function of time for the second pulse.

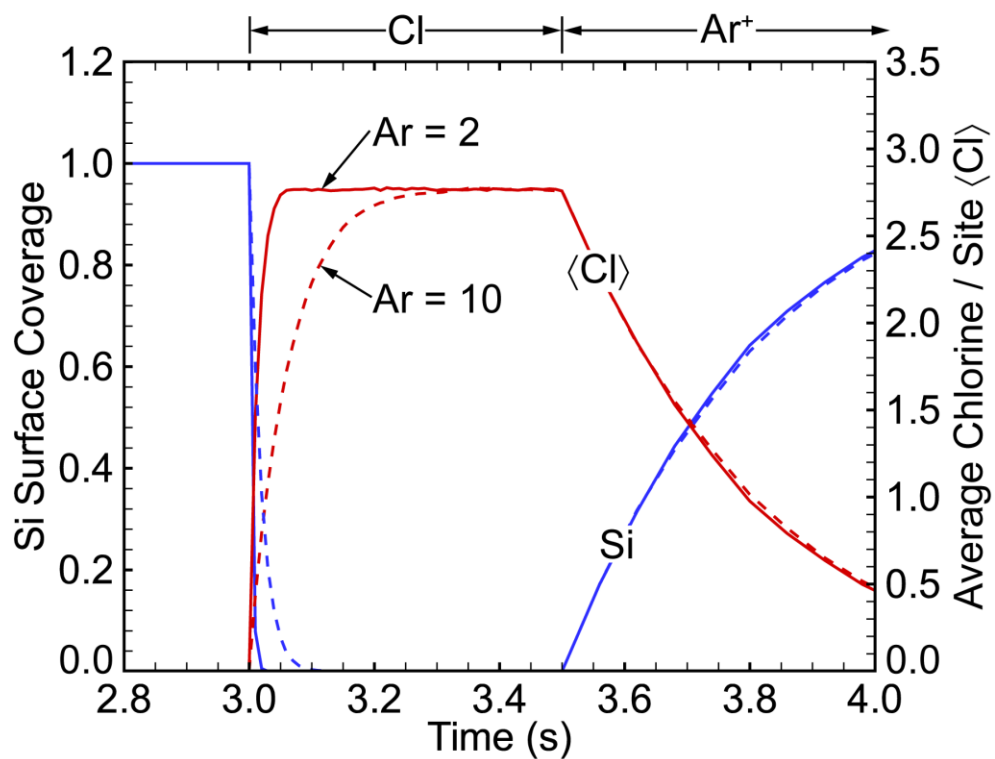


Fig. 5.3 Surface coverage of Si and average chlorine per site at the etch front for ideal ALE as a function of time for the second ALE pulse for AR = 2 and 10 trenches.

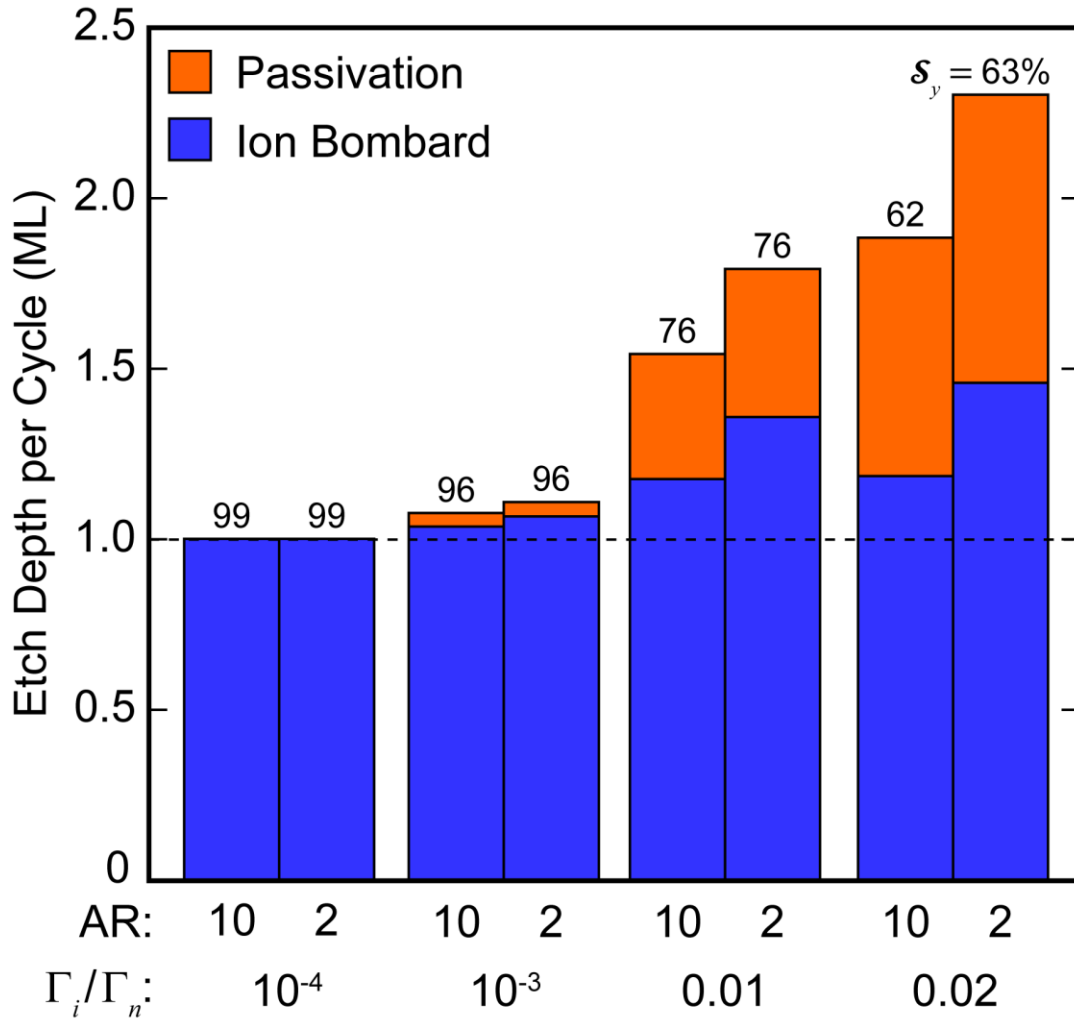


Fig. 5.4 Etch depth per cycle in the passivation and ion bombardment phase for values of  $\Gamma_i/\Gamma_n = 0.02, 0.01, 10^{-3}$  and  $10^{-4}$  in the passivation step, for both AR = 2 and 10 trenches. The dotted line represents ideal ALE, with an etch depth per cycle of 1 ML.

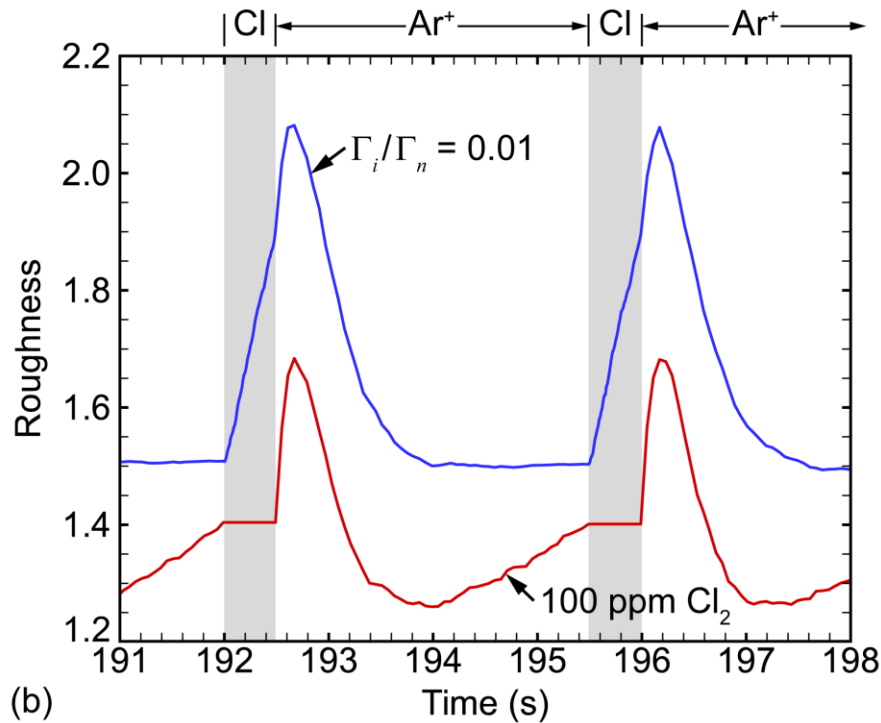
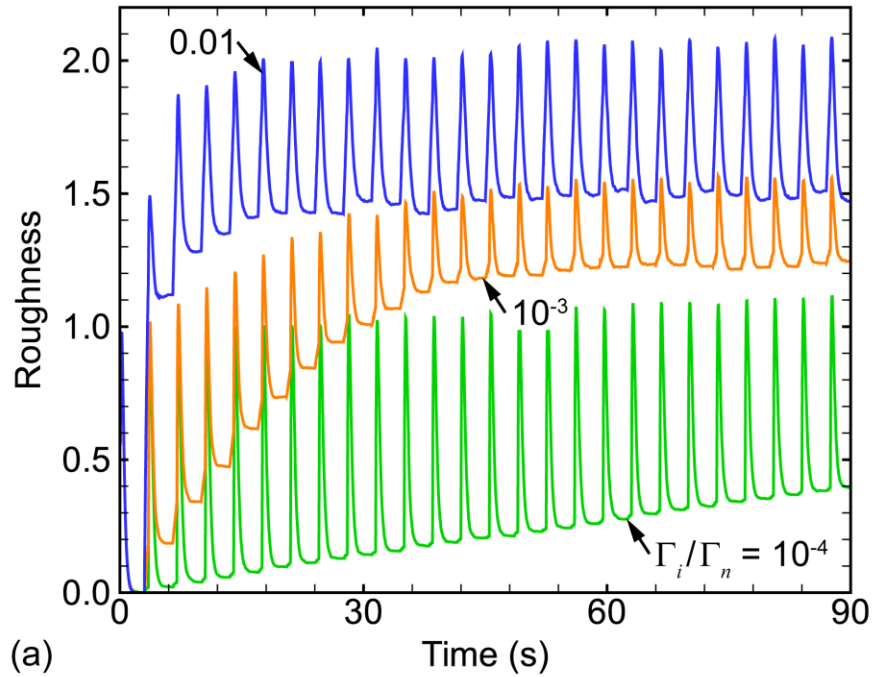


Fig. 5.5 Surface roughness as a function of time. (a) First 25 pulses for  $\Gamma_i/\Gamma_n = 0.02$ ,  $0.01$ ,  $10^{-3}$  and  $10^{-4}$  in the passivation step, showing the transient roughening at early etch times. (b) Sub-cycle roughening behavior at steady-state ( $55^{\text{th}}$  pulse) for  $\Gamma_i/\Gamma_n = 0.01$  in the passivation phase and  $100 \text{ ppm Cl}_2$  in the ion bombardment phase. ALE sub-cycles are listed at the top, with the passivation phase highlighted with grey in the figure.

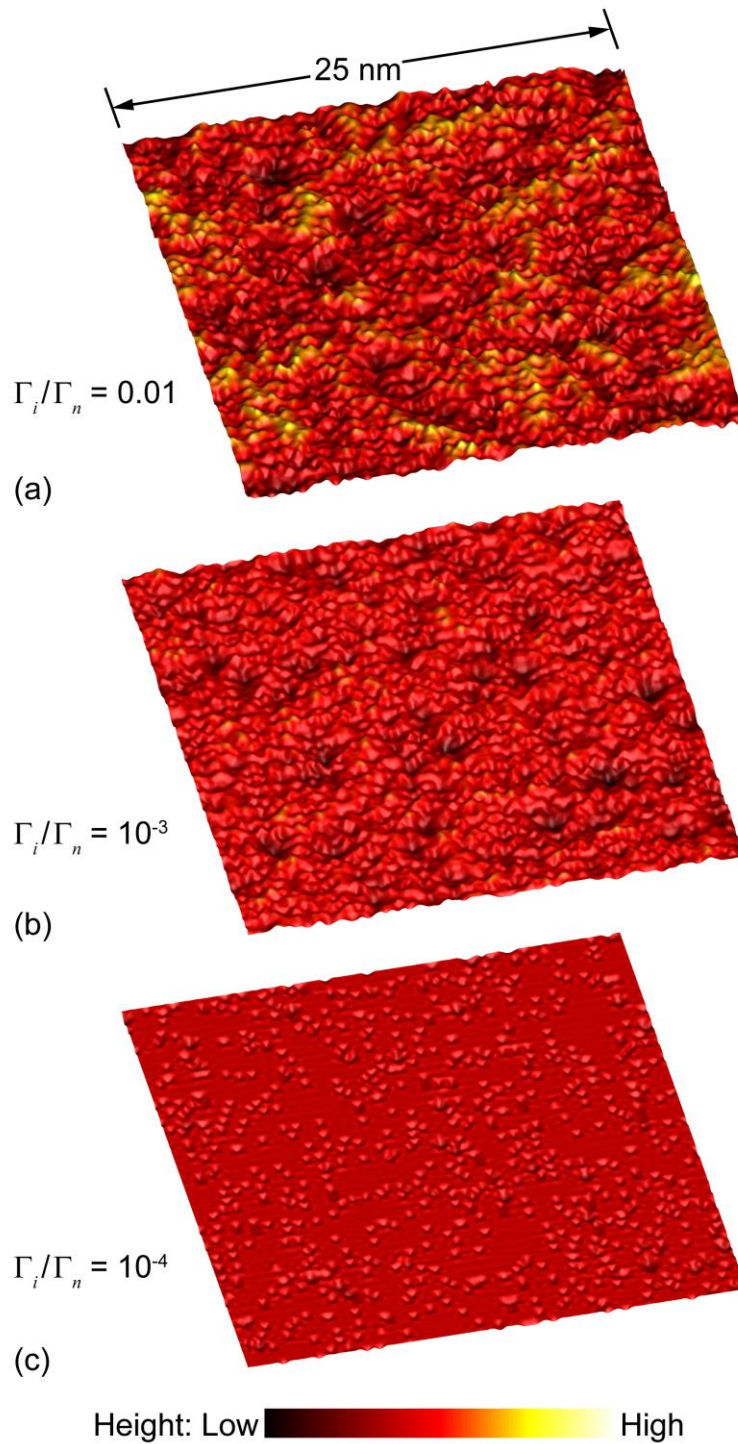


Fig. 5.6 Surface morphology of the trench bottom for  $\Gamma_i/\Gamma_n =$  (a) 0.01, (b)  $10^{-3}$  and (c)  $10^{-4}$  in the passivation step after 25 pulses (87.5 s etch time). Color represents the profile height, with black being deeper etching, red representing the average etch depth and yellow/white being higher features.

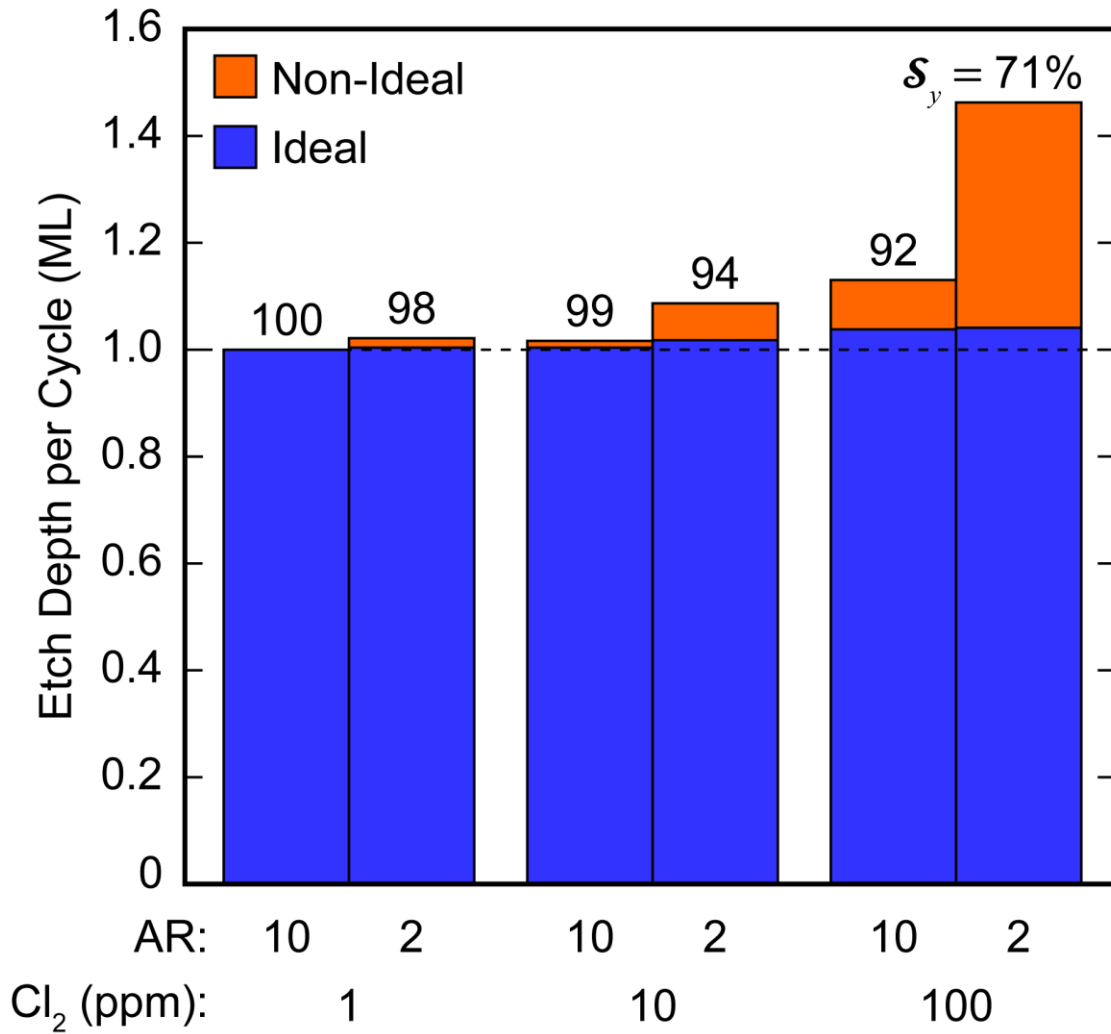
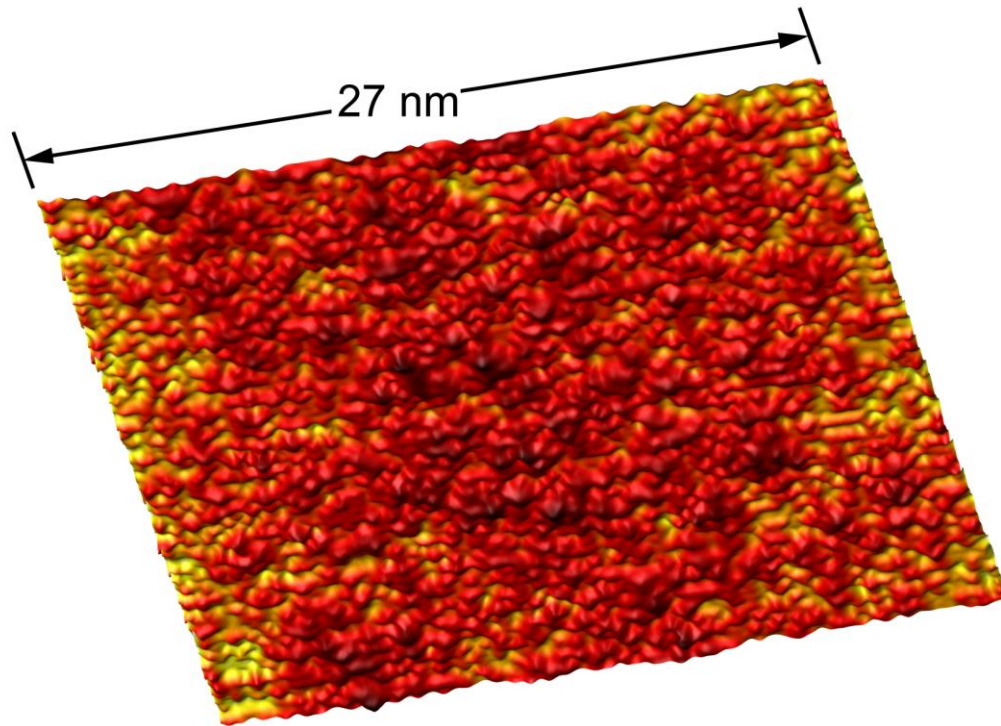


Fig. 5.7 Etch depth per cycle due to ideal (reactions which occur through ALE synergy) and non-ideal (continuous) etching for cases with 1, 10 and 100 ppm Cl<sub>2</sub> in the ion bombardment step, for both AR = 2 and 10 trenches. The dotted line represents ideal ALE, with an etch depth per cycle of 1 ML.



$\text{Cl}_2$  (ppm) = 100

Height: Low  High

Fig. 5.8 Surface morphology of the trench bottom with 100 ppm  $\text{Cl}_2$  in the ion bombardment step after 25 pulses (32 s etch time). Color represents the profile height, with black being deeper etching, red representing the average etch depth and yellow/white being higher features.

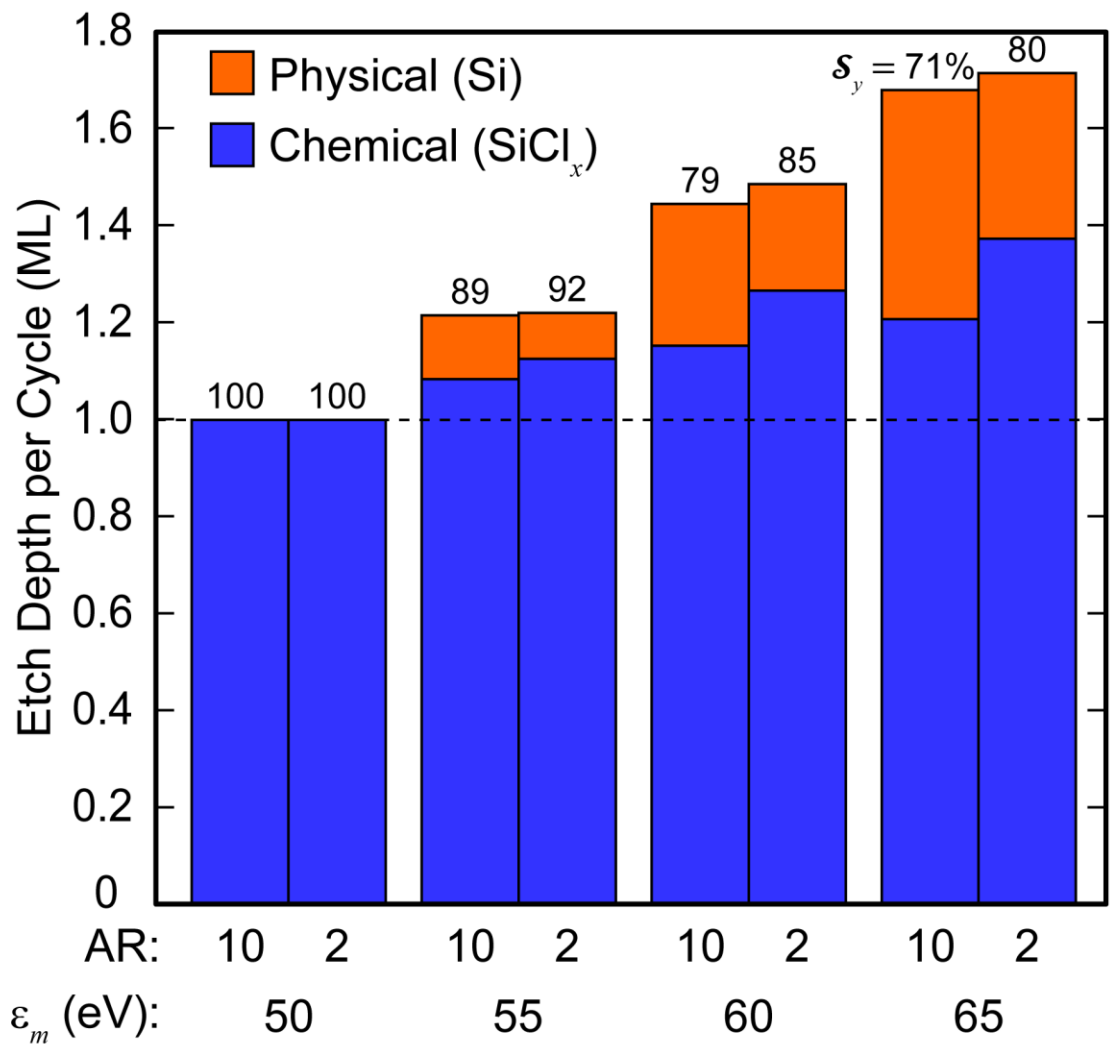


Fig. 5.9 Etch depth per cycle for physical and chemical sputtering processes for values of  $\epsilon_m = 50, 55, 60$  and  $65$  in the ion bombard step, for both  $AR = 2$  and  $10$  trenches. The dotted line represents ideal ALE, with an etch depth per cycle of  $1$  ML.

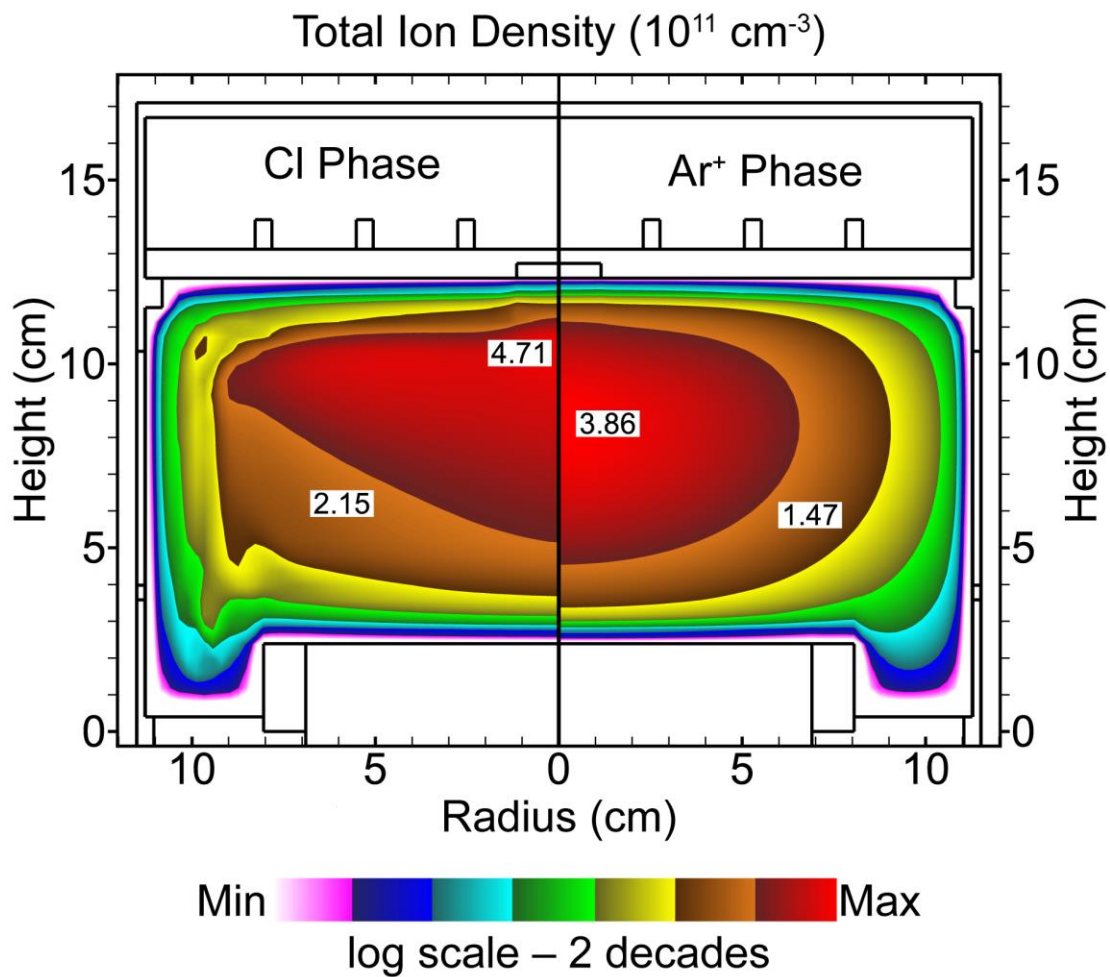


Fig. 5.10 Reactor geometry and total ion densities in the (left) Cl passivation phase and (right) Ar<sup>+</sup> ion bombardment phase. A log scale showing two decades is used.

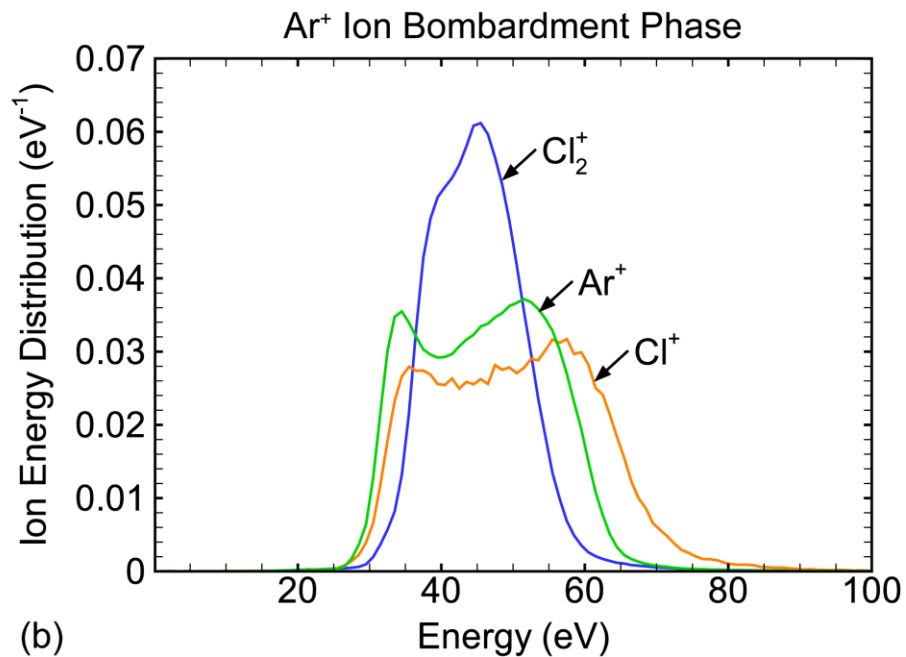
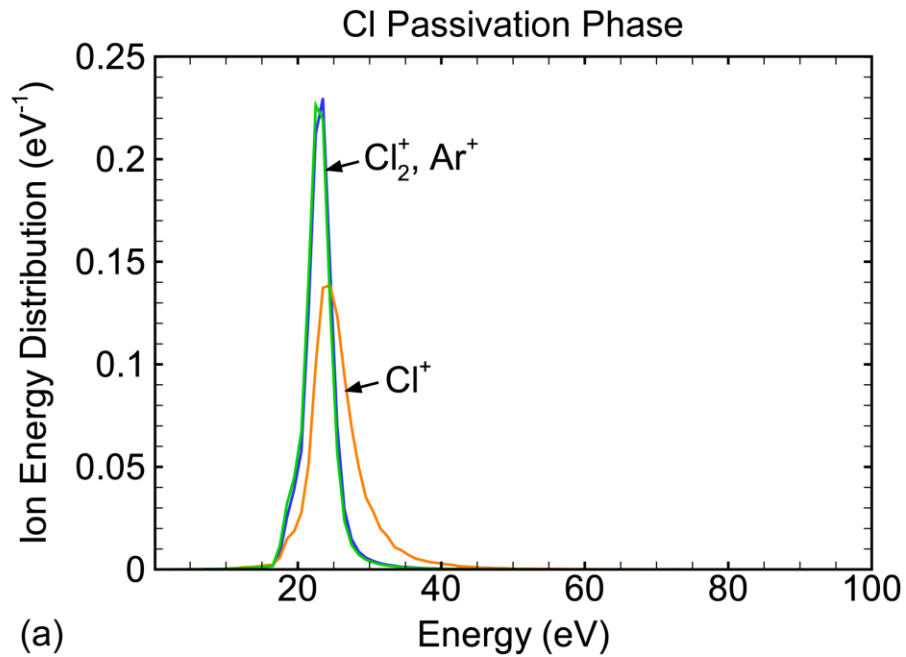


Fig. 5.11 Ion energy distribution for  $\text{Cl}^+$ ,  $\text{Cl}_2^+$  and  $\text{Ar}^+$  in the (a) passivation and (b) ion bombardment phases. Each ion energy distribution is a probability density function for that ion, and is normalized such that integrating the function in energy results in a value of 1 regardless of the total flux of that ion.

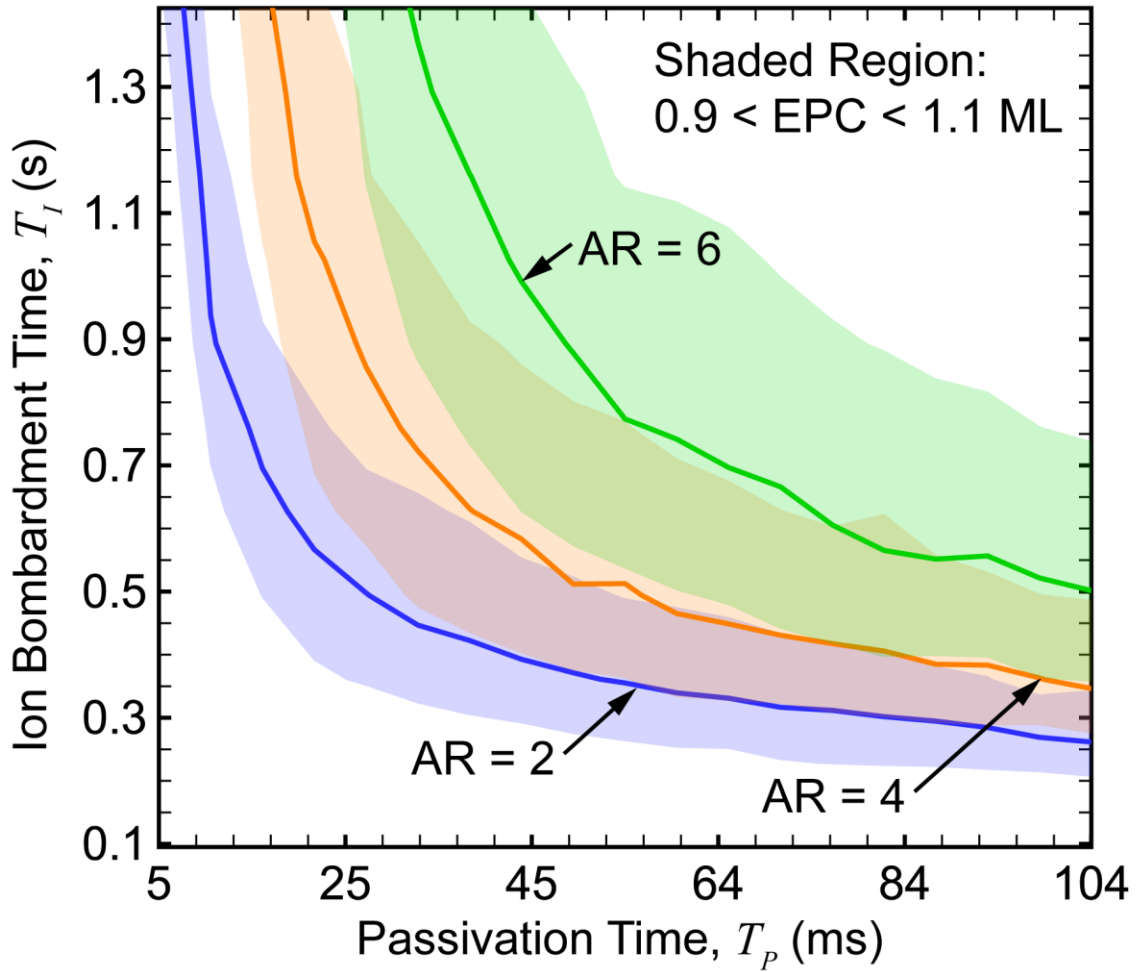


Fig. 5.12 Trend of etch depth per cycle (EPC) as a function of ion bombardment time ( $T_I$ ) and passivation time ( $T_P$ ). The solid line represents an EPC of 1, and the shaded region is the window from  $0.9 < \text{EPC} < 1.1$ .

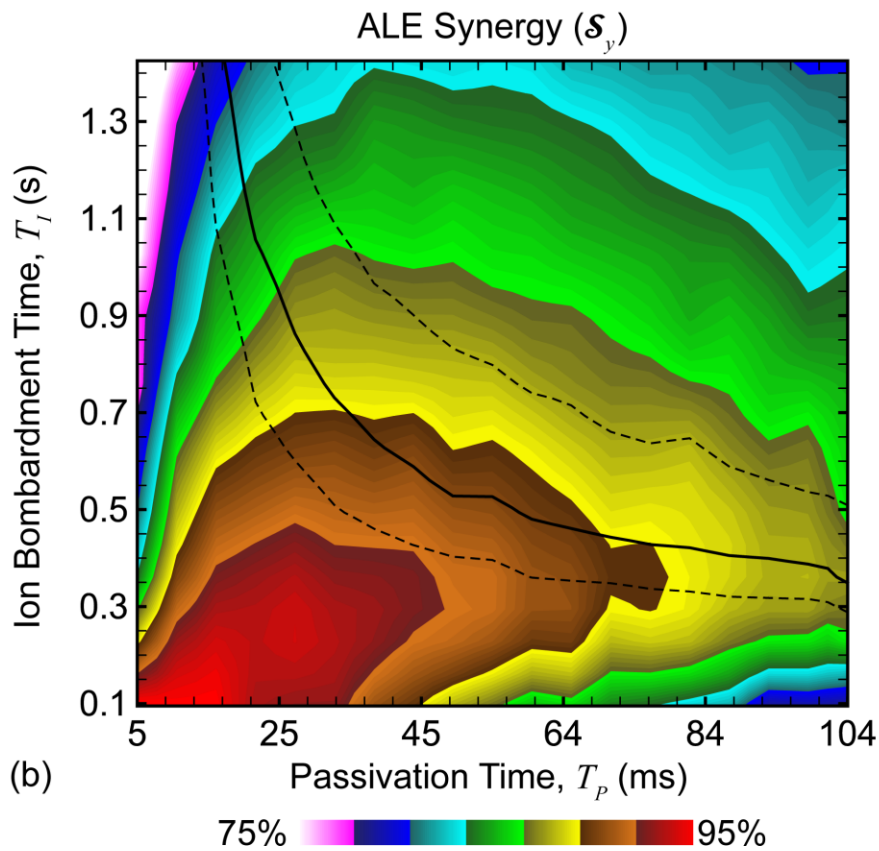
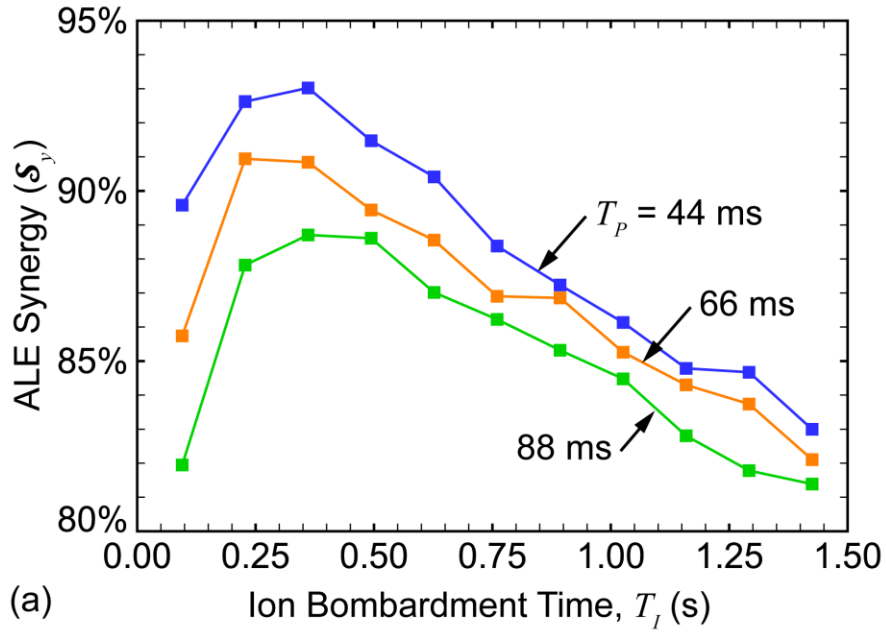


Fig. 5.13 Trends in the ALE synergy ( $\mathcal{S}_y$ ) as a function of pulse times for an AR of 4. (a)  $\mathcal{S}_y$  as a function of ion bombardment time ( $T_l$ ) for three values of passivation time ( $T_p$ ). (b)  $\mathcal{S}_y$  as a function of  $T_l$  and  $T_p$ . The solid black line represents  $EPC = 1$  and the dotted lines bound the range  $0.9 < EPC < 1.1$ .

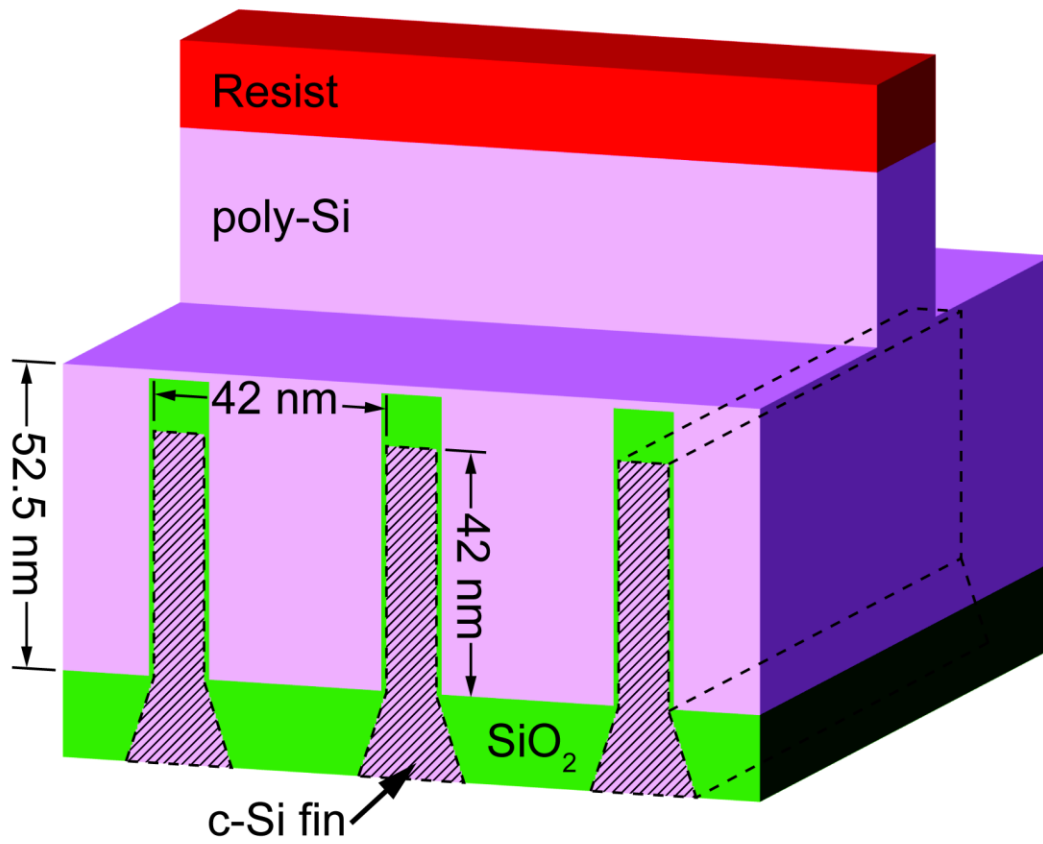


Fig. 5.14 Initial geometry used for the gate etch case study. The crystalline silicon (c-Si) fin travels back into the page, as indicated by the dotted lines. The resist (red) masks the polysilicon gate structure, which is pre-etched to a depth just above the top of the fins.



## Chapter 6 WAFER SCALE UNIFORMITY

### 6.1. Introduction

As discussed in Chapter 1.4, the wafer scale uniformity of plasma etching processes is critically important to semiconductor fabrication.[8] As feature sizes and film thicknesses shrink, conventional techniques to obtain uniform reactant fluxes and etch rates are being challenged to meet process demands. Atomic layer etching (ALE) processes, which rely on self-limited reactions, are less sensitive to the uniformity of reactant fluxes and may increase the wafer scale etching uniformity in many applications.[133,134]

Plasma based ALE, described in Chapter 5, is a self-limiting two-step process capable of removing single atomic layers in each cycle.[127] The first step of the cycle passivates the surface in a manner that naturally stops when the top surface layer is fully passivated. This step is ideally performed with an ion-free flux of neutral radicals. In the second step, the passivated layer is selectively removed by, ideally, a radical free flux of energy-controlled ions that chemically sputters the top passivated layer but is not energetic enough to sputter the underlying unpassivated atoms. When the fluence of reactants is large enough to fully saturate both of the self-limited half-reactions, the etch depth per cycle (EPC) should be constant. In this saturated regime, the etch rate should also be independent of small non-uniformities in the reactant fluxes. The adoption of ALE techniques may then offer a way to obtain atomic scale uniformity over large areas without the need for having correspondingly uniform reactant fluxes.

Although ALE of several materials has been demonstrated [123,135,136], silicon is often used as the test case to demonstrate ALE principles as its passivation and etch steps are perhaps

the most clear. In the ALE of silicon, chlorine containing plasmas are often used for the passivation step. Following passivation of the silicon surface, a rare gas plasma, often argon, is used for the removal step.[121] In the passivation phase, Cl radicals passivate Si sites to form  $\text{SiCl}_x$  ( $x \leq 3$ ). This process is inherently self-limited due to the strength of the Si-Cl bond, and the low solubility and diffusivity of Cl into the bulk silicon. The removal of passivated silicon by ion bombardment can be made self-limited by controlling ion energies to be above the sputtering threshold of  $\text{SiCl}_x$  and below that of bare Si, as shown in Chapter 5.

Self-limiting behavior is necessary to improve wafer scale uniformity in the presence of non-uniform reactant fluxes, but it is not clear what the relationship is between the uniformity enabled by ALE and process saturation. Most ALE processes are not perfectly self-limited [132], and it is difficult to estimate the effect of non-ideal etching reactions on process uniformity, as shown in Chapter 5. The following discussion focuses on the consequences of saturation during the ion bombardment phase of ALE on wafer-scale uniformity, however the same trends hold true for the passivation phase as well.

Assuming a Langmuir kinetic model for the desorption of passivated surface sites during ion bombardment, and perfect self-limited behavior, the EPC at radius  $r$  on the wafer of an ALE process can be estimated as

$$EPC(r) \sim 1 - e^{-\Gamma_i(r)T_i/\Phi_c} \quad (\text{ML/cycle}), \quad (6.1)$$

where  $\Gamma_i(r)$  is the ion flux at radius  $r$ ,  $T_i$  is the ion bombardment time and  $\Phi_c$  is the characteristic ion fluence characterizing the saturation behavior. The units of EPC, ML/cycle, are monolayers of material per ALE cycle. To obtain uniform etch rates when ion fluxes to the wafer are not uniform, the smallest ion fluence onto the wafer must be large compared to  $\Phi_c$ ,

$$\Phi_i(r) = \Gamma_i(r)T_i \gg \Phi_c. \quad (6.2)$$

This relationship specifies the minimum value of  $T_i$  that will produce saturated ALE behavior across the entire wafer.

In this chapter, results are discussed from a computational investigation of the wafer-scale uniformity of ALE in inductively coupled plasmas (ICPs) sustained in Ar/Cl<sub>2</sub> mixtures when the reactant fluxes are non-uniform. It was found that ALE can reduce the sensitivity of the etch rate to the uniformity of the incident ion flux, even when the process is not fully non-self-limited (non-ideal ALE). The sensitivity of etch uniformity to the uniformity of the ion flux increases when the ALE process is operated in the sub-saturation regime, but remains sub-linear. Finally, the ALE process was found to expose the surface to a higher ion fluence than continuous etching for a given etch depth. The models used in this investigation are described in detail in Chapter 2. A discussion of ALE enabled uniformity is given in Chapter 6.2. Our concluding remarks are in Chapter 6.3.

## **6.2. Scaling of ALE with Uniformity of Fluxes**

The plasma etching reactor used for this study was 53.4 cm in diameter, with a 3 turn radio frequency (RF) antenna located behind a quartz window 9.5 cm above the 30 cm diameter wafer. The radial position of this antenna was varied to produce three patterns of ion flux onto the wafer. Antenna A1 is located close to the edge of the reactor, A2 is centered in the reactor radius and A3 is close to the center of the reactor. The geometry, antenna configurations, and the resulting plasma density profiles are shown in Fig. 6.1. This reactor was intentionally given a somewhat wider aspect ratio and narrower antenna pattern than is typical for devices optimized for uniformity of reactant fluxes to the wafer. These configurations result in plasma non-uniformity which is exaggerated from best practice to clearly show the differences between

continuous etching and ALE, as well as to explore the limits of how much flux non-uniformity ALE is capable of compensating for.

For each of the three antenna configurations, simulations were performed using an Ar/Cl<sub>2</sub> = 90/10 mixture (for continuous etching), a pure Cl<sub>2</sub> mixture (for ALE passivation) and Ar contaminated with 10 ppm of Cl<sub>2</sub> (for ALE ion bombardment). The antenna was powered at 10 MHz, the RF bias on the substrate was 10 MHz and gas flow rate was 600 sccm held at a pressure of 10 mTorr using a feedback controlled gate valve. The wafer was divided into five regions – evenly spaced in radius – and statistics for the distribution of ion energies and incident angles were separately collected for each region. Combined with fluxes of each reactant species (Ar<sup>+</sup>, Cl<sup>+</sup>, Cl<sub>2</sub><sup>+</sup> and Cl), a piecewise assessment of the consequences of non-uniformity in reactant fluxes, ion energies and angular distributions can be taken into account in the etching model.

The introduction of 10 ppm Cl<sub>2</sub> contamination in the argon feedstock gas during the ion bombardment phase of ALE is intended to represent the residual chlorine in the system from incomplete purging of the gas lines, adsorption of Cl on the reactor walls or dissociation of Cl containing etch products by electron impact. The results of simulating the Cl<sub>2</sub> contaminated argon plasma indicate a finite ion-to-neutral ratio ( $90 < \Gamma_i/\Gamma_n < 650$ ) during the ion bombardment phase. The  $\Gamma_i/\Gamma_n$  ratio changes with both position on the wafer and antenna configuration. The presence of chlorine during the ion bombardment phase introduces an etching reaction which is not fully self-limited. The high energy tails of the ion energy distribution also extend slightly beyond the 50 eV threshold set for physical sputtering of the underlying silicon, which introduces another continuous, non-self-limited etching pathway during the ion bombardment phase. These combined pathways result in the amount of material removed in the ion

bombardment phase not being fully self-limited and therefore dependent on the ion bombardment step time ( $T_i$ ).

The ion fluxes to the wafer as a function of radius are shown in Fig. 6.2 for the three antenna configurations. The same radial dependence occurs for both continuous etching using the Ar/Cl<sub>2</sub> = 90/10 mixture, and during the ion bombardment phase of ALE using the Ar with Cl<sub>2</sub> contamination. Using antenna A1 results in an ion flux which increases from the center of the wafer to the edge. The ion flux generated by antenna A2 has a local minimum at the center of the wafer with a local maximum at a radius of  $\approx 10$  cm. Antenna A3 has a maximum in ion flux at the center of the wafer, decreasing monotonically with increasing radius.

In addition to the non-uniform ion flux, using constant ICP power for each antenna configuration results in there being different magnitudes of fluxes to the wafer between antennas. To make comparisons between the antennas, the power was scaled roughly with the radiating area of each antenna, which approximately matches the power per unit volume, and results in a similar ion flux at the center of the wafer for each antenna. The powers were 600 W for antenna A1, 300 W for A2 and 111 W for A3. The different plasma density profiles generated by each antenna also produced a different dc bias on the substrate. As a result, the average ion energy reaching the wafer was different for each antenna even with the same RF bias amplitude applied to the substrate. To compensate and ensure that the average ion energy incident onto the wafer was consistent from antenna to antenna, the RF bias was adjusted such that the average ion energy at the center of the wafer was 30 eV. The same ICP power and RF bias voltage was used for both gas mixtures.

The reactor scale model also predicts non-uniformity in several plasma properties, other than ion flux, which are relevant to etching. The ion energy distribution (IED), particularly the

maximum energy, varies with position on the wafer. This dependence of peak ion energy as a function of radius is caused by the variation in sheath width interacting with the finite transit time of ions accelerating through the sheath. Radii having lower plasma density resulted in a wider sheath at the surface of the wafer requiring a longer ion transit time. The longer transit time averages the ion trajectory over a larger portion of the 10 MHz cycle thereby reducing peak energy. The ratio of the flux of ions to reactive neutrals can also depend on antenna configuration and radial position. Since Cl radicals are produced by electron impact dissociation reactions, the non-uniformity of ICP power deposition results in a non-uniform radical flux, particularly in Cl<sub>2</sub> lean conditions. These non-uniformities in Cl radical flux and IEDs were included modeling of etch rates, however they were found to be of secondary importance.

The pure Cl<sub>2</sub> plasma was used only for passivation of Si sites in this study, and so the conditions for the passivation step were selected separately from those for the Ar/Cl<sub>2</sub> plasmas to optimize the passivation process. The Cl<sub>2</sub> plasma was sustained using 300 W of ICP power at 10 MHz, with no RF bias applied to the wafer. The resulting plasma conditions have a high neutral to ion ratio ( $\Gamma_n/\Gamma_i=300-1200$ ), and ion energies which were lower than the lowest sputtering threshold in the surface reaction mechanism. The fluxes of Cl radicals were fairly uniform for all conditions, resulting in little difference in passivation rates and outcomes between different antenna configurations.

To establish a baseline for comparing to ALE processing, continuous etching was simulated using the Ar/Cl<sub>2</sub> = 90/10 gas mixture. Continuous etching of blanket (un-patterned) silicon was simulated for each of five radial positions on the wafer using each of the three antenna configurations. The position dependent etch rates, shown as solid lines in Fig. 6.2(a), are nearly directly proportional to the total ion flux, indicating etching is operating in the ion-

starved regime [22]. Etch rates for antenna A1 increase by 89% across the wafer, marginally more than the increase in the ion flux,  $\Gamma_i$  (82%). The more rapid increase in etch rate compared to  $\Gamma_i$  is due to an increase in ion energy at the edge of the wafer where the sheath is thinner. The etch rates for antennas A2 and A3 also scale nearly linearly with ion flux. This linear dependence on  $\Gamma_i$  indicates that non-uniformities in other etch factors, such as IED and radical flux, are of secondary importance for these conditions, as appropriate in the ion-starved regime.

Atomic layer etching was modeled for the same reactor by cycling between exposure to the fluxes produced by the  $\text{Cl}_2$  plasma without a bias to passivate the surface with Cl radicals, and to the Ar plasma with an RF bias providing moderately energetic ion bombardment to etch the passivated surface. Since the  $\text{Cl}_2$  plasma used for passivation was in direct contact with the wafer, some non-ideal flux of ions was incident onto the wafer during passivation. This resulted in a small amount of continuous etching, but the dominant radical flux was essentially uniform. For this reason, the focus of this investigation will be limited to the effect of non-uniformity of the ion flux during the ion bombardment phase. For all cases, the passivation time was constant at 45 ms, which was long enough to fully saturate the silicon surface with chlorine.

The ion fluxes during the ion bombardment phase of the ALE cases are shown as a dotted line in Fig. 6.2(b) for each antenna. The radial dependence of the ion fluxes are similar to the continuous etching case, but with larger non-uniformities than in the  $\text{Cl}_2$  plasma. With antenna A1 there is an increase of 130% in ion flux from the center of the wafer to the edge.

ALE using an ion bombardment time of 3 s produced significantly more uniform etch rates than continuous etching, with only a small positive correlation between etch rate and ion flux, as shown in Fig. 6.2(b). For antenna A1, the etch rate –measured here in monolayers of

computational cells ( $3 \text{ \AA}$ ) per cycle – increased by 17 % from the center of the wafer to the edge, significantly less than the increase in  $\Gamma_i$  (133%). This improvement in etch uniformity compared to  $\Gamma_i$  indicates a fully saturated self-limited ALE reaction. Non-ideal continuous etching mechanisms result in some dependence of etch rate on  $\Gamma_i$ , and produce the remaining non-uniformity in etch rate.

While the ALE process significantly improved the etch rate uniformity for antenna A1 and A2 when compared to continuous etching, the results for antenna A3 are less improved. This result indicates that the ion fluence at the center of the wafer, which is similar for each antenna, is only just large enough to saturate the ion bombardment reaction. For the A1 and A2 antennas, the ion flux and fluence increase with radius. Given that both the passivation and ion phases are both fully saturated, the increasing fluence at larger radius does not produce a significantly higher etch rate. However, in the case of antenna A3, the ion fluence drops below saturation as the radius increases, causing the etch rate to depend more strongly on ion flux which decreases with radius.

The ICP power used for antenna A3 was chosen to result in similar ion flux at the center of the wafer as antennas A1 and A2. This choice of ion flux resulted in sub-saturation behavior at large radius where ion fluxes are the lowest when processed using the same ion bombardment time as A1 and A2. If the ion fluence was increased for case A3 so that the entire wafer was within the saturation regime, either by increasing the ICP power (resulting in a larger ion flux) or by increasing  $T_i$ , a similar increase in uniformity could be obtained for A3.

For plasma conditions which have been optimized for uniformity of the ion flux, the most effective way to change the ion fluence during ALE is to change the length of the ion bombardment phase,  $T_i$ . The ALE rates as a function of radius for values of  $T_i$  from 1.5 s to 6 s

are shown in Fig. 6.3 for antenna A2. The ion flux and rates for continuous etching are also shown for reference. The maximum ion flux is 20% larger than at the center and edge of the wafer. The etch rate with continuous etching (using the Ar/Cl<sub>2</sub> = 90/10 gas mixture) follows the radial trend of  $\Gamma_i$ , increasing by 30% from the center of the wafer to its maximum. The larger increase in etch rate compared to ion flux is due to radial non-uniformities in the ratio of ion to neutral fluxes,  $\Gamma_i/\Gamma_n$ , and ion energy.

All values of  $T_i$  produce ALE rates that are more uniform as a function of radius than the ion flux. The ALE rates become more uniform, and less sensitive to changes in ion flux, with increasing  $T_i$ . As saturation increases with increasing  $T_i$ , the dependence of etch rate on  $\Gamma_i$  decreases and the etch rate becomes more uniform. Since saturation has not been achieved in all cases, the EPC is different for each case at 1.5 cm radius. The EPC increases from 1.13 ML/cycle at  $T_i = 1.5$  s to 1.37 ML/cycle at  $T_i = 3$  s and 1.60 ML/cycle at  $T_i = 6$  s. These differences in etch rate near the center of the wafer have been normalized out of the result in Fig. 3 to aid comparison between ALE cases, ion flux and continuous etch rates. Increasing  $T_i$  once full saturation has been achieved across the entire wafer ( $\approx 6$  s) does not continue to improve etch rate uniformity, due to the presence of continuous etching mechanisms.

Completely saturated ideal self-limited reactions would result in an etch rate completely independent of the magnitude of the local ion flux, as implied by Eq. 6.1. This independence can be achieved using ideal ALE conditions (that is, no ions in the passivation phase and no radical in the ion bombardment phase), as shown in Fig. 6.4. Here, ALE rate for each antenna and radial location for  $T_i = 1.5, 3$  and 6 s are plotted as a function of ion fluence. For ideal ALE, once the critical ion fluence has been reached ( $\approx 10^{16}$  cm<sup>-2</sup>), the etch rate (ML/cycle) is constant in spite of the significantly different conditions with different antennas. This trend reinforces the

importance of ion flux non-uniformity (in the ion-starved regime) over other sources of non-uniformity in the model. Similar trends occur for non-ideal ALE, a saturation in the etch rate as the critical fluence is reached. However, for non-ideal ALE there is a finite positive slope in the etch rate as a function of ion fluence in the saturation region which results from continuous etching due to non-ideal reactions during ion bombardment. By removing the chlorine contamination from the ion bombardment phase, the ideal fluence-independent behavior in the saturation region is restored. This behavior is indicated by the horizontal line accurately fitting the etch rate of the ideal data for fluence greater than  $0.3 \times 10^{17} \text{ cm}^{-2}$  in Fig. 4. In addition to providing an etch rate which is less dependent on ion fluence (in the saturation regime), ideal ALE reaches saturation at a lower ion fluence than performing ALE with non-ideal reactant fluxes. The larger characteristic fluence required to saturate the non-ideal ALE is due to the competition between the removal of passivated silicon by ion bombardment and the re-passivation of the underlying silicon by radical chlorine contamination.

The ALE synergy parameter ( $\mathcal{S}_y$ ), is a measure of the ideality of the ALE process.[132] The  $\mathcal{S}_y$  parameter is the total etch rate during an ALE process, minus the contributions from continuous etching, divided by the total rate. A value of  $\mathcal{S}_y=1.0$  indicates ideal, self-limited ALE while  $\mathcal{S}_y=0$  indicates etching in the absence of self-limited processes. Here,  $\mathcal{S}_y$  was calculated by running three different simulations, one with only the ion bombardment conditions (no passivation phase), one with only the passivation conditions (no ion bombardment) and one for the complete cyclic ALE process. The tolerance of the ALE rate to non-uniformities in the ion flux is not directly related to  $\mathcal{S}_y$ . With there being chlorine contamination during ion bombardment and ions with above threshold energies during passivation,  $\mathcal{S}_y$  tends to decrease with increasing ion fluence, as shown in Fig 6.4(b). This results in decreasing  $\mathcal{S}_y$  with increasing

$T_i$ , due to the increased time during which continuous etching can occur. The greatest tolerance to non-uniform ion fluxes obtained for high ion fluence occurs when  $\mathcal{S}_y$  is smallest (under these conditions). This behavior is less an indication that high saturation and uniformity correlates to smaller values of  $\mathcal{S}_y$  but rather it is an indication that the ALE synergy metric, as applied here, does not capture the saturation behavior.

These results indicate that in order for ALE rates to be insensitive (or less sensitive) to the uniformity of reactant fluxes, ALE surface reactions must be both self-limited and fully saturated. Ideally self-limited reactions will not provide benefits in improving uniformity if the reactions are not allowed to saturate. On the other hand, continuous etching during non-ideal ALE will also limit the benefits to uniformity. It is possible to have high values for  $\mathcal{S}_y$  for under-saturated conditions, while such conditions will not improve uniformity over that of the ion fluxes. As the ion bombardment phase reaches saturation the sputtering probability of an impinging ion should decrease due to the lack of passivated sites, converging to zero for ideal ALE. This is in contrast to continuous etching where each ion should have approximately equal sputtering probability throughout the etch time. To obtain saturation, and therefore improved uniformity, an abundance of ions with low (chemical) sputtering probability is required. These ions are required for saturation, but they do not contribute to etching. In some sense, this is an inefficient use of ions. This means that in order to obtain saturation the ALE process must intentionally over-expose the wafer to ions compared to the continuous case. Meanwhile, the reactions must be strongly self-limited to prevent continuous etching.

Possible side-effects of this over-exposure to ions during ALE to gain uniformity include increased mask erosion and damage to stopping layers. For example, simulations of etching Si features over  $\text{SiO}_2$  with an erodible photoresist mask (by physical sputtering) were performed for

continuous etching and ALE using antenna A1. Reactant fluxes were used for two radii – 1.5 cm (low fluxes) and 13.5 cm (high fluxes). The ALE cases use  $T_i = 3$  s. The resulting profiles are shown in Fig. 6.5 at the time when the underlying  $\text{SiO}_2$  is first exposed at the wafer edge (13.5 cm). The difference in etch depth from the edge to the center of the wafer is smaller for ALE processing compared to continuous etching, indicating a more uniform process. While the silicon is etched predominantly through ALE self-limited reactions, the mask erodes through non-self-limited physical sputtering. Therefore, the high ion fluence required to provide etch rate uniformity can reduce the mask selectivity and increase the fluence of ions reaching the  $\text{SiO}_2$  etch stop layer during the over-etch. Due to the uniformity of the ALE process, only 4 additional ALE cycles were needed to clear the 3D ‘L’ feature at the inner radius (low ion fluxes) after exposing the stopping layer at the wafer’s edge (high ion fluxes). This amounted to a 16% over-etch (defined as time to completely clear the feature divided by the time to first expose the stopping layer). A 92% over-etch was required to clear the slowest etching features in the continuous etch case. This result is comparable to the reduction in over-etch time presented in Chapter 5.4. Another measure of over-etch is the total fluence of ions striking the  $\text{SiO}_2$  stopping layer. This fluence can be directly calculated in the MCFPM by summing the ions incident onto  $\text{SiO}_2$  material cells. Despite the reduction in over-etch as a percentage of the total etch time, during ALE etching the stopping layer was exposed to 33 times more ions at the edge of the wafer than at the center. For continuous etching, the stopping layer at the edge of the wafer was exposed to 4 times more ions than at the center.

In addition to etch depth uniformity, critical dimension (CD) uniformity is also important in plasma processing. In the test feature shown in Fig. 5, the CD is the linewidth of the two positive “L” shaped features. During anisotropic ALE processing, the feature sidewalls remain

passivated throughout the ion bombardment period. The presence of off-axis ions in the ion angular distribution results in exposure of the passivated sidewalls to ion bombardment in both continuous and ALE processing. Due to the increased total ion fluence in ALE processing, more mask undercut is observed than continuous etching for similar etch depths. In continuous etching the re-deposition of radical etch products can lead to tapering between features, the opposite of mask undercut. This tapering can be removed by extended over-etch, but if the over-etch is continued for too long mask undercut will eventually result. When the etch times shown in Fig. 5 were extended (over-etched) to produce features with vertical sidewalls at a radius 1.5 cm, the linewidth of the two positive “L” shaped features at radius 13.5 cm was decreased by 50% due to mask undercut. The observed undercut, and the resulting decrease in linewidth, was similar between continuous etch and ALE. The amount of mask undercut which occurs during ALE is related to  $T_i$ . As long as off-axis ions are present, longer  $T_i$  will result in more undercutting, regardless of how self-limited the surface reactions are. This indicates that, while ALE can improve etch depth uniformity as previously shown, it is less obvious that similar improvements in CD uniformity will automatically result.

### **6.3. Concluding Remarks**

ALE processing, when operated in a saturated, ion starved regime, can significantly improve the uniformity in etch rate across a wafer compared to continuous etching when the ion fluxes are not uniform. The ability of the self-limiting surface reactions to reject reactive species in over-exposed areas – either locally in a feature or globally across the wafer – can result in surface saturated reactions and uniform etch rates. This uniformity comes at the expense of over-exposing the wafer to ions (large ion fluences) compared to continuous etching. This overexposure may require careful consideration of mask and etch stop materials.

## 6.4. Figures

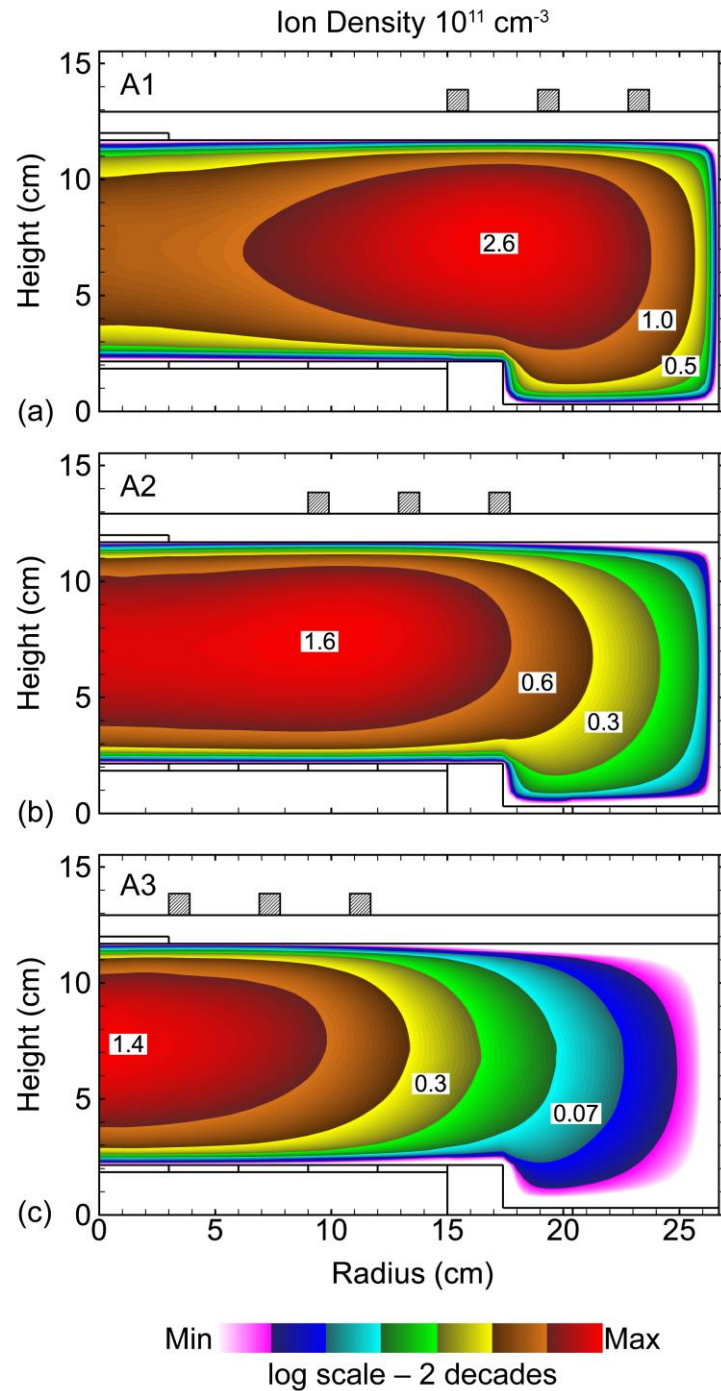


Fig. 6.1 Reactor geometry and total ion density for three different antenna configurations. Antennas, from top to bottom are: (a) A1, (b) A2 and (c) A3. The ion densities are for the argon plasma used in ion bombardment during ALE – Ar/Cl<sub>2</sub> = 100/10 ppm, 10 mTorr. Powers were adjusted to provide the same ion flux to the center of the wafer.

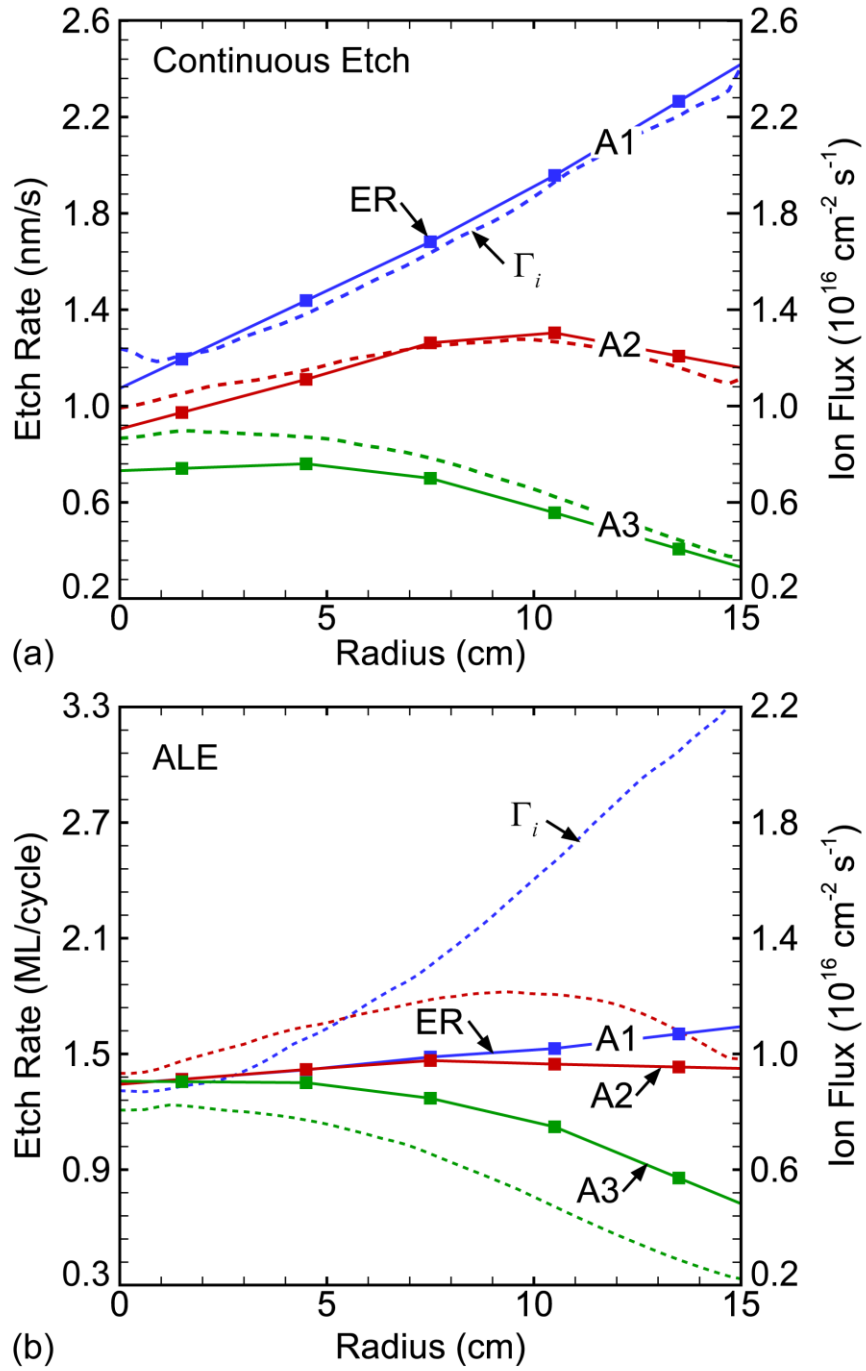


Fig. 6.2 Etch rate and ion flux to the wafer as a function radius for three antennas, A1, A2 and A3. (a) Continuous etching ( $\text{Ar}/\text{Cl}_2 = 90/10$ ) with etch rate in nm/s. (b) Ion fluxes from argon plasma with 10 ppm  $\text{Cl}_2$  contamination with ALE rate in ML/cycle.

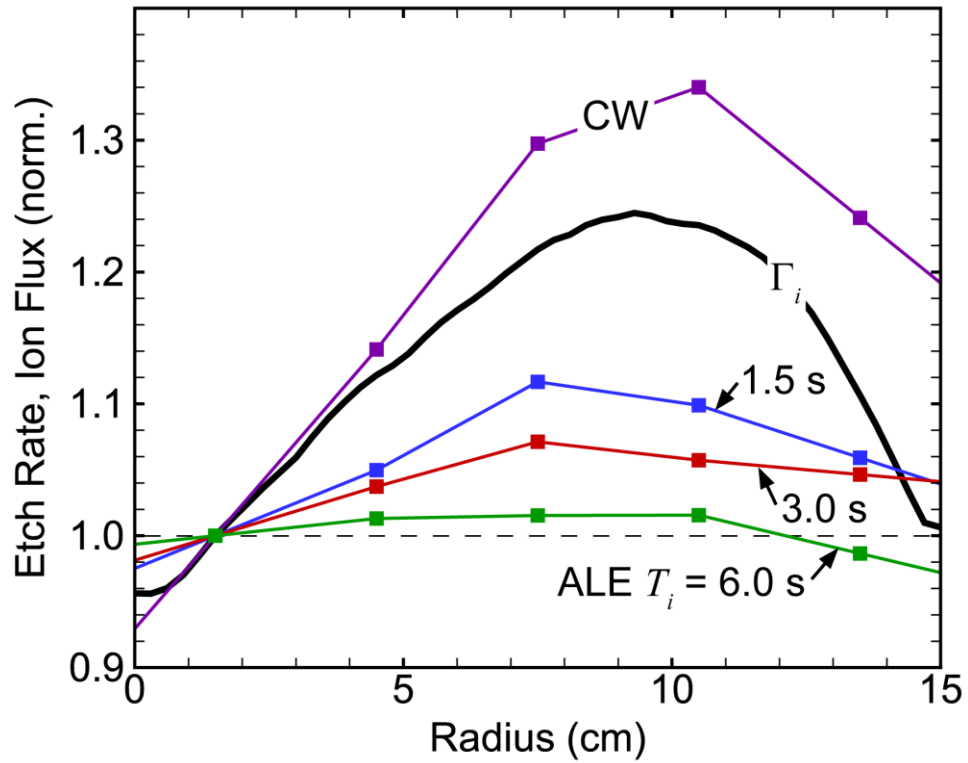


Fig. 6.3 Etch rate and ion flux normalized to their values at a radius of 1.5 cm for different ion bombardment times ( $T_i = 1.5, 3.0$  and  $6.0$  s) for antenna A2. “CW” indicates the continuous etching rate.

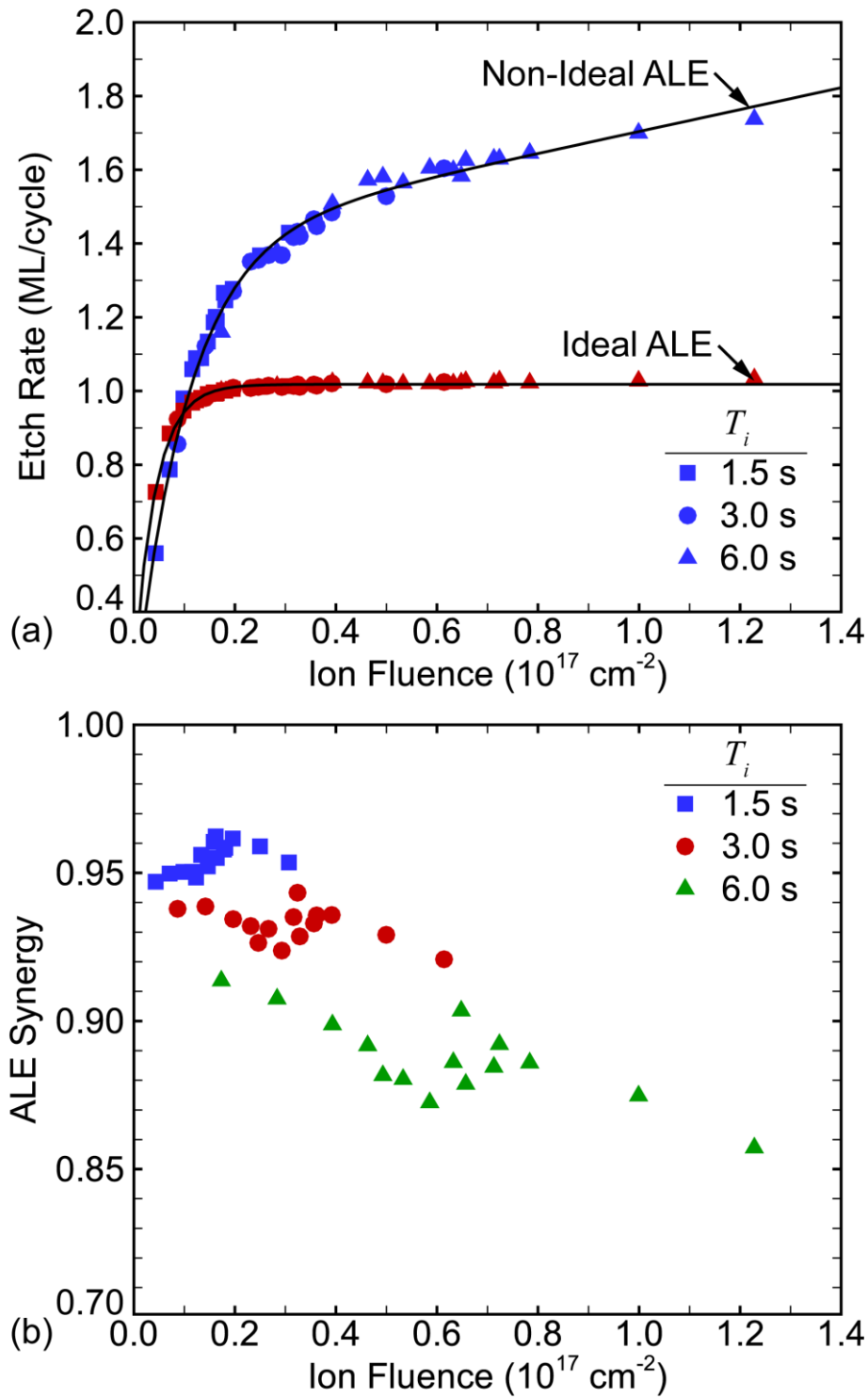


Fig. 6.4 Data points from three ion bombardment times  $T_i$  are shown using different symbols (squares:  $T_i = 1.5 \text{ s}$ ; circles:  $T_i = 3 \text{ s}$ ; triangles:  $T_i = 6 \text{ s}$ ). For each  $T_i$ , data from all three antenna configurations is shown without differentiation. (a) Etch rate. (b) ALE synergy  $\mathcal{S}_y$ .

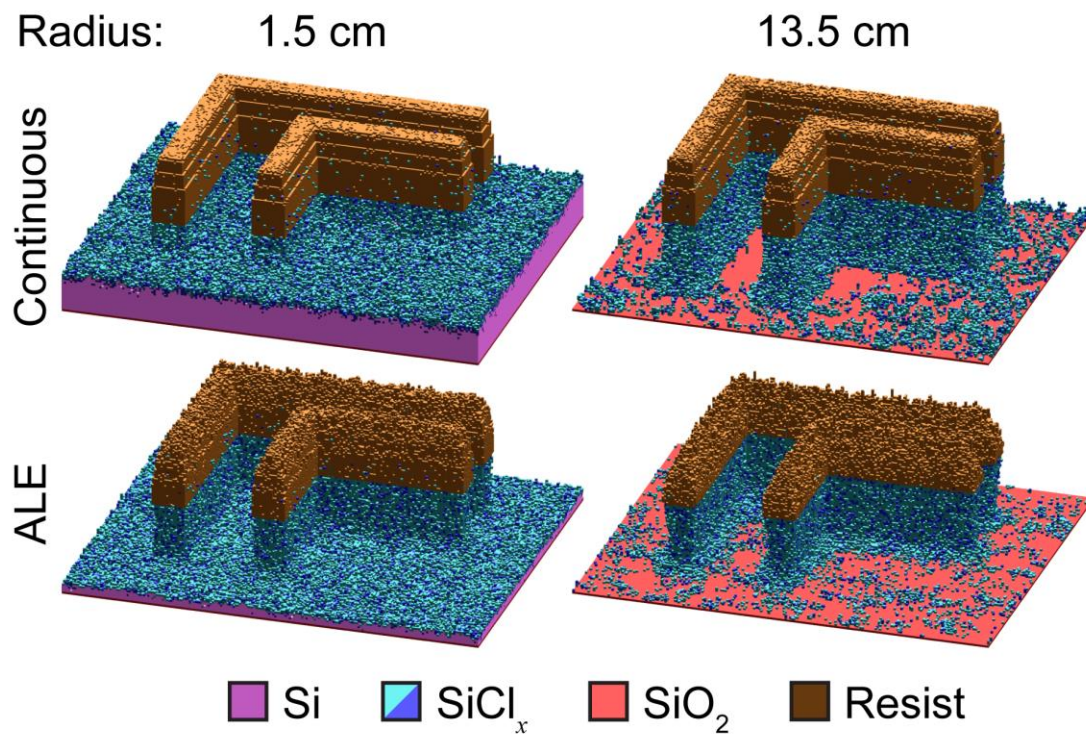


Fig. 6.5 Predicted etch profiles for using antenna A1 for (top) continuous etching and (bottom) ALE at radii of (left) 1.5 cm and (right) 13.5 cm.  $T_i = 3$  s for ALE cases. The two radial positions are etched for the same time, representing the non-uniformity on the wafer just before clearing the feature at the wafer edge.

## **Chapter 7 ATOMIC LAYER ETCHING USING FLUOROCARBON GASES**

### **7.1. Introduction**

Plasma based atomic layer etching (ALE) is a technique which can provide significant advantages over conventional etching.[118] The benefits of ALE arise from separating the etch mechanism into two half reactions. In ideal ALE, each of these half reactions are fully self-limited and would produce no continuous etching if individually employed. Only by cycling between the half-reactions does etching occur. The most basic ALE process is separated into a passivation phase and an etching phase. In plasma based ALE, the passivation and etching phases occur in separated pulsed plasmas, typically produced by exchanging gases. Passivation, which lowers the chemical sputtering threshold energy, is typically accomplished by diffusive transport of neutral radical species through the feature to the etch front. Etching is then accomplished using ion bombardment, in which low energy ions preferentially etch the passivated species after anisotropically transporting through the feature. This separation of passivation and ion bombardment enables the fluxes of radicals and ions to be separately optimized despite their different transport methods. The use of self-limited reactions for each of these phases allows for over-exposure to increase uniformity on the macro (wafer) and micro scale. An important example of micro-scale non-uniformity is the aspect ratio dependent etching (ARDE) effect.[104] ALE offers a method for improving both the macro and micro scale uniformities, while also possibly improving selectivity and reducing damage.

Plasma based ALE processes have been developed for several materials. In particular, materials which can be passivated by halogen radicals result in strong self-limiting

behavior.[132] Halogen passivation using, for example, a  $\text{Cl}_2$  or  $\text{Br}_2$  containing plasma, is ideal for ALE due to the covalent interaction between the halogen radicals produced in the plasma and the underlying material which results in rapidly producing a tightly bound passivation layer. Once the top surface of the underlying material is fully passivated, that is saturated, the inability for thermal halogen radicals to penetrate through the passivation layer prevents underlying layers from reacting with the halogen. The strength of the halogen bond can weaken the binding energy of the surface atoms with the underlying lattice, creating an energy window where incoming ions can sputter passivated surface atoms, but do not have enough energy to remove un-passivated bare material sites. This energy window enables a carefully controlled ion energy distribution (IED) of the ion flux to preferentially remove the passivated surface layer, a process that terminates when that layer is removed, resulting in self-limiting behavior in the ion bombardment phase.

Atomic layer etching of  $\text{SiO}_2$  has been experimentally demonstrated using fluorocarbon radical species for surface passivation instead of pure halogen passivation.[137] The carbon is required to remove the oxygen due to the lack of a strong fluorine-oxygen bond. Unfortunately, this passivation process is not self-limited as C-C bonds allow for the accumulation of a fluorocarbon polymer on the surface. For the conditions of interest, this fluorocarbon polymer deposition is a continuous process which does not saturate in time. The end result is a fluorocarbon polymer overlayer thickness that depends on the total fluence of fluorocarbon radicals during the passivation phase. The polymer overlayer thickness therefore depends on duration of the passivation phase and, locally, on the uniformity of the passivation fluxes in the feature. These dependencies could diminish some of the benefits of ALE of  $\text{SiO}_2$ .

## 7.2. C<sub>4</sub>F<sub>8</sub> Inductively Coupled Plasmas

The HPEM was used to investigate the properties of inductively coupled plasmas sustained in Ar/C<sub>4</sub>F<sub>8</sub> mixtures for a reactor measuring 54 cm in diameter. In this reactor design, a 300 mm wafer is mounted on a substrate biased with a radio frequency (RF) power supply at 10 MHz. A four turn coil antenna is located 16.5 cm above the wafer, behind a quartz window. RF current (at 10 MHz) is passed through this antenna, which delivers power to the plasma by inductive coupling. The reactor is maintained at 20 mTorr, regulated by a feedback controlled gate valve, with flow of 600 sccm of feedstock gas.

To simulate the two-step ALE process, passivation and ion bombardment, simulations were performed with two different feedstock gases; an Ar/C<sub>4</sub>F<sub>8</sub> = 95/5 mixture and Ar with trace (100 ppm) C<sub>4</sub>F<sub>8</sub> contamination. For the remainder of this paper, the Ar/C<sub>4</sub>F<sub>8</sub> = 95/5 mixture will be referred to as *FC gas*, and the argon gas with 100 ppm C<sub>4</sub>F<sub>8</sub> will be referred to as *impure argon*. The C<sub>4</sub>F<sub>8</sub> contamination in the impure argon gas is intended to model the fluorocarbon impurities which can originate from incomplete purging of gas lines or desorption of fluorocarbon species from the walls during the ion bombardment phase of ALE pulsing. The FC gas mixture will be used to model both continuous etching and passivation during ALE pulsing.

The FC gas mixture was investigated using inductive powers of 300 W and 1200 W. Since the pressure and feedstock flow rate were kept constant, the higher power case produced significantly more dissociation of the C<sub>4</sub>F<sub>8</sub> molecule and larger fluxes of CF<sub>x</sub> fluorocarbon radicals to the substrate. The total dissociation fraction (measured as the reactor averaged number of carbon atoms in dissociated fragments divided by the total number of carbon atoms in the reactor) in the 1200 W case was 0.44, compared to 0.18 in the 300 W plasma. The flux of neutral species to the wafer, shown in Fig. 7.1(a), indicates fluxes of F and CF<sub>x</sub> radicals generally

increase at 1200 W relative to 300 W due to the larger rate of dissociation of  $C_4F_8$ , while the flux of  $C_2F_4$  decreases, a primary dissociation product of  $C_4F_8$ . This trend indicates that the higher power is also dissociating the primary dissociation products of  $C_4F_8$ , that then contributes to the flux of  $CF_x$  as well as F. The ratio of radical fluorine to polymerizing fluorocarbon radicals ( $F/CF_{(2)}$ ) is therefore higher in the 1200 W plasma (0.47) than in the 300 W plasma (0.2).

The energy of ions impinging on the wafer can be adjusted by applying a RF bias voltage to the chuck without significantly perturbing other plasma parameters. By varying  $V_{RF}$  from 20 to 100 V, values relevant to ALE processes, the DC bias changes from -6 V to -70 V, producing average ion energies of 21 eV to 85 eV at the wafer. The natural sheath potential results in an average ion energy of 14 eV with  $V_{RF} = 0$ . Due to the large range of ion masses (a low of 19 AMU for  $F^+$  to 131 AMU for  $C_3F_5^+$ ), the ion energy distribution (IED) becomes bi-modal as  $V_{RF}$  increases. The shape of the IED is important in ALE applications. Even though the average ion energy may be within the ALE window, maximum energy of the IED may exceed the ALE window which has important implications on ALE processing. The fluxes of reactant species do not significantly change when applying the bias. The power deposition by the RF bias voltage (44 W in the case of 100 V) is dominantly dissipated in ion acceleration and additional dissociation. The total ion flux varies only slightly from  $3.0 \times 10^{15}$  to  $3.4 \times 10^{15} \text{ cm}^{-2} \text{ s}^{-1}$  for a range of  $V_{RF}$  from 0 to 100 V, with the primary ions being  $C_3F_5^+$  and  $C_2F_4^+$ . Reactant neutral fluxes also change little (< 7%) with  $V_{RF}$ .

While continuous etching and ALE surface passivation can be conducted using the FC mixture, ALE ion bombardment is usually performed in pure inert gas, often argon. Unfortunately, it is difficult to completely purge the reactor of fluorocarbon gas after the passivation phase due to incomplete purging of gas from fore-lines and desorption from the

reactor walls under ion bombardment.[95,130,138,139] Such fluorocarbon contamination in the ion bombardment phase may have significant effects on ALE performance. To model this contamination the ion bombardment phase of ALE will be conducted in the impure argon gas mixture. The impure argon plasma was sustained with 600 W of ICP power. The pressure and feed-gas flow rate were 20 mTorr and 600 sccm. These conditions result in an  $\text{Ar}^+$  flux to the wafer of  $6.9 \times 10^{15} \text{ cm}^{-2} \text{ s}^{-1}$ . The flux of polymerizing radicals is  $2.2 \times 10^{15} \text{ cm}^{-2} \text{ s}^{-1}$ , and that of fluorine radicals is  $1.3 \times 10^{15} \text{ cm}^{-2} \text{ s}^{-1}$ . RF biases from 40 V to 100 V were investigated. A bias of  $V_{\text{RF}} = 45 \text{ V}$  results in an average ion energy of 34 eV delivered to the substrate in a bimodal energy distribution having a high energy peak at 42 eV. This IED fits well into the ALE window, as shown in Fig. 7.1(b), and will be used for all cases unless otherwise noted.

Continuous etching of  $\text{SiO}_2$ ,  $\text{Si}_3\text{N}_4$  and Si can be achieved using the FC gas mixture and modest bias voltages, as shown in Fig. 7.2. Continuous etching is not the focus of this investigation, but it is important to evaluate the new polymer etching mechanism against known trends in continuous etching. Etching simulations were conducted using the FC gas mixture for the 1200 W ICP. Blanket etching was simulated using a small ( $18 \text{ nm} \times 18 \text{ nm}$ ) un-patterned initial mesh. The mesh resolution (for all simulations presented here) is  $\Delta x = 0.3 \text{ nm}$ , resulting in a  $60 \times 60$  mesh. The etch rate, calculated as the change in height of the top solid surface (averaged over the computational domain) with respect to time, is shown in Fig. 7.2(a). This etch rate is negative (indicating net polymer deposition) for  $V_{\text{RF}} \leq 20 \text{ V}$  for all materials. As  $V_{\text{RF}}$  is increased and the IED extends to higher energies, the plasma activation of the polymer becomes less efficient, reducing the polymer deposition rate and favoring thinner polymer layers. Polymer sputtering also increases with increasing ion energy, but at these energies still contributes little of the polymer loss mechanism. As ion energies and implant ranges increase

with increasing  $V_{RF}$ , ions begin interacting more strongly with the etch front at the interface between the polymer and the underlying material. When etching begins, the  $\text{SiO}_2$  consumes more polymer than  $\text{Si}_3\text{N}_4$  or bare silicon due to the larger number of C-O bonds in the selvedge, which produces a thinner layer of polymer on the  $\text{SiO}_2$  than  $\text{Si}_3\text{N}_4$  or Si for  $V_{RF} > 20$  V, as shown in Fig. 7.2(b). This difference in polymer thickness results in selective etching of  $\text{SiO}_2$  over  $\text{Si}_3\text{N}_4$  and Si. These general trends have been experimentally observed for similar etching conditions.[29]

Attempting continuous etching using the FC gas mixture with 300 W ICP power results in net deposition for all bias voltages. The increased polymer deposition is due to the lower  $\text{F}/\text{CF}_{(2)}$  ratio for the lower power deposition. Since the total flux of polymerizing  $\text{CF}_{(2)}$  radicals to the surface is larger for the 1200 W plasma, the polymer loss term in Eqn. (1.18) is being dominated by fluorine etching under these conditions. While all biases explored here (up to  $V_{RF} = 120$  V) resulted in net deposition, the deposition rate decreased slightly with increasing ion energy due to less polymer activation at higher energies. At higher ion energies, where polymer sputtering by ions becomes a significant loss mechanism, these polymerizing fluxes may result in continuous etching conditions, but such energies are probably not of interest for ALE applications.

### **7.3. ALE blanket etching**

Using the ALE, alternate pulsing scheme allows for more control of the passivation conditions over a wider range of operating conditions. ALE simulations of  $\text{SiO}_2$  were conducted using the FC gas mixture for the passivation phase and impure argon for the ion bombardment. The passivation phase was 300 W ICP power and 0 V RF bias. The resulting plasma conditions are highly polymerizing, resulting in little continuous etching. During this phase, the plasma

potential results in an ion energy of 14 eV, as shown in Fig. 7.1(b), in spite there being no applied RF bias voltage. This energy is marginally larger than threshold energies of etching, technically placing the IED within the ALE window. In spite being within the ALE window, these low energy ions can only etch exposed surface sites. Even thin polymer overlayers result in negligible etching during the passivation phase due to the inability of the 14 eV ions to penetrate the passivation, resulting in low rates of non-ideal continuous etching during the passivation phase. The ion bombardment phase uses 600 W ICP power and 45 V RF bias in impure argon gas. The ion energies during this phase are well contained in the ALE window. However, the presence of passivating radical species during this phase (due to  $C_4F_8$  contamination) does result in some non-ideal continuous etching at a rate of 0.5 nm/min.

Before modeling the complete ALE cycle for  $SiO_2$  using realistic fluxes, idealized ALE was investigated. The fluxes and IEADs from the HPEM were used for the passivation phase. However, fluorocarbon radical fluxes were removed during the ion bombardment phase, leaving only fluxes of  $Ar^+$  ions. With this modification, little continuous etching was produced during either the ion bombardment or passivation phases.

These ideal ALE conditions were used to perform simulations of  $SiO_2$  blanket etching with passivation times,  $T_p$ , ranging from 50 ms to 35 s for three different ion bombardment times ( $T_i = 10, 20$  and  $30$  s). Periodic behavior occurs for all conditions, but not all conditions resulted in steady state pulse-periodic etching. For example, the height of the topmost layer of material is shown in Fig. 7.3(a). Etching with  $T_i = 30$  s and  $T_p = 7$  s resulted in a pulsed steady state etching condition. With each FC plasma pulse using these pulse times, 0.8 nm of polymer is deposited, shown by the increase in height. With each argon plasma pulse, the polymer is essentially fully removed, resulting in etching of 0.7 nm of  $SiO_2$ , shown by the decrease in height. Since the

polymer deposition phase is not inherently self-limited, larger values of  $T_p$  result in a thicker polymer layer at the end of the passivation phase. For values of  $T_p = 21, 25$  and  $25$  s, the polymer layer becomes too thick to entirely clear during the ion bombardment phase, eventually terminating the etching process and resulting in net deposition per cycle. This critical thickness is approximately the ion penetration depth, slightly more than 1 nm for these conditions. For the longer passivation times which have net deposition in the steady state, there is initially net etching which occurs before the polymer thickness increases above the critical thickness. The transition between net etching (pulse-periodic decrease in height) to net deposition (pulse-periodic increase in height) occurs at earlier times as  $T_p$  increases.

The surface kinetics of SiO<sub>2</sub> ALE, shown in Fig. 7.3(b,c), indicate two processes which erode the SiO<sub>2</sub>. The first process results from the conversion of the base SiO<sub>2</sub> material to the selvedge material by exposure to CF<sub>(2)</sub> fluxes during the passivation phase. Since each SiO<sub>2</sub> surface site can only be converted once this process is self-limited in the absence of energetic ion bombardment. After converting the surface to the selvedge material, further CF<sub>(2)</sub> fluxes result in polymer buildup on top of the selvedge layer, continuously increasing the total overlayer thickness. When a significant portion of the surface is bare SiO<sub>2</sub> at the beginning of the passivation phase (as is the case for  $T_p = 7$  s, shown in Fig. 7.3(b)) there are two distinct polymer deposition rates. The initial rate is higher than later in the deposition phase due to the higher sticking coefficient of CF<sub>(2)</sub> on SiO<sub>2</sub> than other polymer species. Once the entire surface is covered with polymer, the polymer deposition rate decreases due to this lower sticking coefficient. Kaler et al. have also observed this effect, and proposed that it may be utilized to produce pseudo-self-limiting behavior.[98]

The second process which results in the erosion of  $\text{SiO}_2$  occurs during the ion bombardment phase. This erosion occurs as  $\text{SiO}_2$  is converted to selted species by mixing with polymer when activated by ions penetrating through the polymer capping layer. Since all of the overlying polymer must be consumed during the ion bombardment phase in order for ALE to reach a pulse-periodic steady state, the amount of etching which occurs through this reaction channel is proportional to the initial polymer thickness. This results in an *etch-per-cycle* (EPC) which depends on polymer thickness, which in turn depends on  $T_p$ . Once all of the polymer is consumed, this erosion of  $\text{SiO}_2$  terminates and the etch rate returns to zero. If  $T_p$  is sufficiently long with low ion energies, the larger thickness of polymer is not completely consumed during the ion bombardment phase (Fig. 7.3(c)). The self-limited nature of the ion bombardment phase is then not exercised, and some of the benefits of ALE may not be as pronounced as a result.

The pulse-periodic steady state EPCs for different ion bombardment times,  $T_i$ , as a function of passivation time,  $T_p$ , are shown in Fig. 7.4. Using ideal  $\text{SiO}_2$  ALE conditions, shown as dotted lines in Fig. 7.4(a), there is a wide range of passivation times which result in a EPC. The EPC shown here are measured after the system has reached a pulse-periodic steady state. Only conditions that completely clear the polymer from the surface during ion bombardment will have a positive EPC. Conditions which do not completely clear the polymer will eventually transition to a net deposition condition in the steady state. For each  $T_i$ , there is a  $T_p$  is above which pulse-periodic ALE cannot be achieved. This critical value of  $T_p$  increases with increasing  $T_i$  and represents the thickest polymer deposit which can be removed in the during the bombardment period. Above the critical  $T_p$ , the system results in polymer deposition during each step. With the ion bombardment conditions being ideal, the EPC has little dependence on  $T_i$  as long as  $T_p$  is below the critical value as once the polymer is cleared, there is no additional

continuous etching. Despite the ideal conditions, there remains a dependence of EPC on  $T_p$ , increasing from 0.4 nm/cycle at  $T_p = 1$  s to 0.8 nm/cycle at  $T_p = 11$  s.

Similar simulations were conducted using the actual fluxes from the HPEM, representing realistic, non-ideal ALE conditions. Under these conditions the steady state EPC of SiO<sub>2</sub>, shown as solid lines in Fig. 7.4(a), has significant dependence on  $T_i$ , particularly at low values of  $T_p$ . There is a slightly reduced dependence on  $T_p$ , with the non-ideal and ideal results converging as  $T_p$  increases. The dependence of EPC on  $T_i$  is due to the non-ideal etching occurring during the ion bombardment phase due to the fluorocarbon contamination in the chamber. After the polymer deposited during the passivation phase is removed and exposed the underlying SiO<sub>2</sub>, the small flux of CF<sub>(2)</sub> due to contaminating C<sub>4</sub>F<sub>8</sub> enables continuous etching.

The reduced dependence of EPC on  $T_p$  with non-ideal conditions is a result of the polymer overlayer masking some of the non-ideal etching for longer  $T_p$ . With longer  $T_p$ , the polymer overlayer persists for a larger portion of the ion bombardment phase. This effect results in the EPC for ideal and non-ideal conditions converging as  $T_p$  increases, implying a larger portion of the total EPC is a result of the synergistic relationship between the two half-reactions as opposed to continuous etching. The trends for EPC with non-ideal fluxes have the same saturation behavior as the ideal conditions, where above a critical value of  $T_p$  the steady state etching stops and the system transitions to net deposition. The critical values of  $T_p$  are similar for ideal and non-ideal conditions, within the resolution of this study ( $\Delta T_p = 2$  s). This indicates that continuous etching does not significantly affect this process.

Evaluating the ALE quality for this process is more complex than halogen based ALE systems which leverage well defined self-limited processes. *ALE synergy* ( $\mathcal{S}_y$ ) has been proposed as a metric for ALE processes.[132] The ALE synergy is the fraction of total etching which

occurs due to the synergy between the two half-reactions, as opposed to continuous etching during one phase or the other. For this metric to reach unity, etching cannot occur during either of the half-reaction processes. Only by cycling between the two half-reactions does etching occur. With halogen etching systems it is possible to estimate  $\mathcal{S}_y$  by measuring the etch rate of each half-reaction separately and evaluating  $\mathcal{S}_y$  as

$$\mathcal{S}_y = \frac{EPC - (a + b)}{EPC}. \quad (7.1)$$

where  $\alpha$  and  $\beta$  are the continuous etch rates in during the passivation and ion bombardment phases multiplied by  $T_p$  and  $T_i$ , respectively. This method works well in halogen plasma ALE, where passivation layers are not much thicker than one monolayer. In fluorocarbon ALE processes, this method for estimating  $\mathcal{S}_y$  does not apply. Under the conditions discussed here, for instance, the ion bombardment phase has a continuous etch rate of 0.5 nm/min on SiO<sub>2</sub> due to the C<sub>4</sub>F<sub>8</sub> impurity. The fluorocarbon fluxes from the plasma have a larger probability of sticking to bare SiO<sub>2</sub> than on a polymer surface. Therefore, when the surface is fully covered with polymer the continuous etch rate would be less than on a bare SiO<sub>2</sub> surface. As the SiO<sub>2</sub> surface transitions from polymer covered to bare during each ALE pulse, it is difficult to directly evaluate  $\beta$ .

Given these difficulties, synergy will be estimated by comparing the non-ideal EPC directly to the EPC obtained with idealized ALE fluxes. Synergy is calculated as

$$\mathcal{S}_y = \frac{EPC_i}{EPC}, \quad (7.2)$$

Where  $EPC_i$  refers to ideal conditions. The ALE synergy, calculated using Eqn (7.2), is shown in Fig 7.4(b) with the steady state EPC for ideal and non-ideal etching for  $T_p < 3$  s. The ion bombardment time is  $T_i = 20$  s. The contribution of non-ideal etching to EPC is fairly constant in

this range. As the EPC decrease with smaller  $T_p$ , this constant contribution by continuous etching becomes a larger fraction of the total etching, which reduces  $\mathcal{S}_y$  as  $T_p$  decreases. At  $T_p = 0$  s etching can only occur due to non-ideal process during ion bombardment and so the etch rate for ideal etching is zero. The non-ideal conditions produce etching of 0.16 nm/cycle, resulting in  $\mathcal{S}_y = 0$ . Synergy increases rapidly as  $T_p$  increases until reaching 0.8 at  $T_p = 1.5$  s. After that point,  $\mathcal{S}_y$  increases slowly to a value of 0.9 at  $T_p = 7$  s. For larger values of  $T_p$ , the system transitions to net deposition in the pulse-periodic steady state.

In principle, the ALE of  $\text{Si}_3\text{N}_4$  should follow that same trends as the ALE of  $\text{SiO}_2$ . In our mechanism, the distinguishing factor between fluorocarbon plasma etching of  $\text{Si}_3\text{N}_4$  compared to  $\text{SiO}_2$  is that etching of  $\text{Si}_3\text{N}_4$  consumes less polymer during etching than  $\text{SiO}_2$ . Due to this lower rate of polymer consumption, for the same reactive fluxes from the plasma, only values of  $T_p < 1$  s resulted in pulse-periodic steady-state etching of  $\text{Si}_3\text{N}_4$ . This narrower window for ALE of  $\text{Si}_3\text{N}_4$  suggests that there is a correspondingly large window in  $T_p$  where the selectivity to  $\text{SiO}_2$  over nitride is large in the steady state. For  $T_p$  large enough to enter the net deposition regime, both materials perform identically.

While ALE may offer the possibility of high etch selectivity of  $\text{SiO}_2$  over  $\text{Si}_3\text{N}_4$  in the steady state, this selectivity is based on the buildup of polymer to levels that terminate etching of  $\text{Si}_3\text{N}_4$ , which requires several pulses to occur. Before the polymer layers become thick enough to enable selectivity there is a transient period where the selectivity is less than the steady state value. This transient period may result in significant etching of masking materials such as  $\text{Si}_3\text{N}_4$  before reaching the steady state, which may be a limiting factor in some applications. For example, the heights of ALE etching  $\text{SiO}_2$ , and  $\text{Si}_3\text{N}_4$  are shown in Fig 7.5(a) for  $T_i = 30$  s and  $T_p = 5$  s. These conditions produce a pulse-periodic steady state etching for  $\text{SiO}_2$ , however

significant etching of  $\text{Si}_3\text{N}_4$  stops after approximately 15 cycles. For  $\text{SiO}_2$  ALE, the polymer overlayer is nearly completely removed by the end of each cycle, as shown in Fig 7.5(b). During the first few cycles of ALE of  $\text{Si}_3\text{N}_4$ , a residual layer of polymer remains at the end of each cycle. This overlayer increases in thickness cycle to cycle, shown in Fig 7.5(c), which reduces the EPC of the  $\text{Si}_3\text{N}_4$ . In spite of the fairly thick overlayer, the  $\text{Si}_3\text{N}_4$  continues to etch with each cycle until the overlayer grows to about 2 nm, at which point  $\text{Si}_3\text{N}_4$  etching essentially stops while the polymer layer continues to thicken.

While the thickness of the overlayer provides insights to the pulse-periodic characteristics of the surface kinetics, the distribution of selvedge species at the interface better reflects the kinetics of the surface reactions. The thickness of these species are shown in Fig. 7.6 as a function of time for ALE of  $\text{SiO}_2$  and  $\text{Si}_3\text{N}_4$  for  $T_i = 30$  s and  $T_p = 5$  s (same conditions as Fig. 7.5).

For ALE of  $\text{SiO}_2$ , there are three selvedge species,  $\text{SiO}_2\text{C}_x\text{F}_{y(s)}$ ,  $\text{SiOC}_x\text{F}_{y(s)}$  and  $\text{SiF}_{x(s)}$ . At the beginning of the passivation phase, the surface is predominantly bare  $\text{SiO}_2$ . When exposed to passivating radicals the  $\text{SiO}_2$  surface is rapidly converted to  $\text{SiO}_2\text{C}_x\text{F}_{y(s)}$ , as shown in Fig 7.6(a). Due to the small number of low energy ions in the passivation phase, a small fraction of these  $\text{SiO}_2\text{C}_x\text{F}_{y(s)}$  sites begin to be converted to  $\text{SiOC}_x\text{F}_{y(s)}$  during passivation. Since the probability of de-oxygenating the  $\text{SiOC}_x\text{F}_{y(s)}$  site is similar to the  $\text{SiO}_2\text{C}_x\text{F}_{y(s)}$  site, it is likely that some of the  $\text{SiOC}_x\text{F}_{y(s)}$  is also being converted to  $\text{SiF}_{x(s)}$ , but this species is rapidly consumed by the abundant radical fluorine in the CF plasma. This is the dominant pathway of continuous etching during the passivation phase. However, this continuous etching is quite slow due to the average ion energy being below threshold for the two de-oxygenation reactions after implanting through the overlayer.

During the ion bombardment phase the  $\text{SiO}_2\text{C}_x\text{F}_y$  species are rapidly converted to  $\text{SiF}_{x(s)}$ . However, since the fluxes of radical fluorine are low during this phase,  $\text{SiF}_{x(s)}$  is removed by sputtering as opposed to thermal etching. The polymer thickness grows during the passivation phase and is rapidly removed during the ion bombardment phase. The amount of polymer which is removed during ion bombardment is large because each de-oxygenation reaction from the  $\text{SiO}_2$  also removes a carbon atom polymer, represented in the model as removing a polymer site. With moderate ion bombardment times, the polymer becomes thin enough that the  $\text{SiF}_{x(s)}$  species can be fully removed from the surface by sputtering.

The surface reactions are qualitatively different on  $\text{Si}_3\text{N}_4$  compared to  $\text{SiO}_2$ . The  $\text{Si}_3\text{N}_4$  etching mechanism only includes two selvedge species,  $\text{SiNC}_x\text{F}_{y(s)}$  and  $\text{SiF}_{x(s)}$ . During ion bombardment, some of the  $\text{SiNC}_x\text{F}_{y(s)}$  is converted to  $\text{SiF}_{x(s)}$ , as shown in Fig 7.6(b) starting the fifth ALE pulse. This process does not remove as much polymer as converting an  $\text{SiO}_2\text{C}_x\text{F}_{y(s)}$  to  $\text{SiF}_{x(s)}$ , so conditions which produce pulse-periodic steady state ALE on  $\text{SiO}_2$  do not completely clear the polymer on  $\text{Si}_3\text{N}_4$ . With this thicker polymer layer, the ion penetration depth during the ion bombardment phase for  $\text{Si}_3\text{N}_4$  is comparable to the polymer thickness. This results in ions reaching the etch front having low average energy which precludes sputtering of the  $\text{SiF}_{x(s)}$ . During the passivation phase the abundance of radical fluorine rapidly etches the  $\text{SiF}_{x(s)}$  surface species, providing additional etching during this phase. The result is that etching is nearly continuous, as shown in Fig. 7.5(c), in spite the modulation of polymer thickness during the ALE cycle. The total polymer thickness continues to increase with each pulse, as shown in Fig. 7.6(b). This process of accumulating polymer with each pulse continues from pulse to pulse until the polymer thickness is large enough to completely stop the etching reactions on  $\text{Si}_3\text{N}_4$  (Fig. 7.5(a)).

The total changes in height of the substrate material for SiO<sub>2</sub> ( $\Delta H_O$ ) and Si<sub>3</sub>N<sub>4</sub> ( $\Delta H_N$ ) after 15 pulses as a function of passivation time for different  $T_i$  are shown in Fig. 7.7. The value of  $\Delta H$  indicates the removal of substrate material (SiO<sub>2</sub> or Si<sub>3</sub>N<sub>4</sub>), and is therefore always positive (the thickness of SiO<sub>2</sub> is never increased during etching). These results demonstrate the transient etching effect in Si<sub>3</sub>N<sub>4</sub>, as shown in Fig. 7.7. For short  $T_p$ , the polymer deposited on the Si<sub>3</sub>N<sub>4</sub> during each ALE cycle is small, resulting in a longer period of transient etching before polymer buildup terminates etching. The result is that low values of  $T_p$  result in larger  $\Delta H$  for Si<sub>3</sub>N<sub>4</sub> than SiO<sub>2</sub>. As  $T_p$  increases the  $\Delta H$  in SiO<sub>2</sub> increases (more net etching) due to the thicker polymer layer fueling the etch longer during the ion bombardment phase. In Si<sub>3</sub>N<sub>4</sub>,  $\Delta H$  monotonically decreases as  $T_p$  increases due to the shorter transient etching period associated with longer passivation times. For each  $T_i$ , there is a transition from steady state etching conditions at low  $T_p$  to steady state net deposition conditions at higher  $T_p$ . This transition occurs at larger  $T_p$  for longer  $T_i$ . The metric  $\Delta H$  shows a measurable change in height for most of these conditions. However, etching may have completely ended for both SiO<sub>2</sub> and Si<sub>3</sub>N<sub>4</sub> by the end of 15 pulses, which is not captured in this metric alone.

Selectivity for etching SiO<sub>2</sub> compared to Si<sub>3</sub>N<sub>4</sub>, defined as  $\Delta H_O/\Delta H_N$ , after 15 cycles is shown in Fig. 7.8(a). The results indicate that there is a trend of increasing maximum selectivity with increasing  $T_i$ . The  $T_p$  which produces the maximum selectivity also increases with  $T_i$ . For each  $T_i$  investigated, the peak selectivity occurs with a  $T_p$  that would not produce continuous pulse-periodic etching in the steady state. This indicates that conditions which do not result in a pulse-periodic ALE may be useful for increasing selectivity in short etches, or when used as a pre-etch followed by conditions which would transition back into a pulse-periodic steady state etch condition.

Transient etching effect plays an important role in the selectivity of SiO<sub>2</sub> compared to Si<sub>3</sub>N<sub>4</sub> in a fluorocarbon plasma ALE process. As a result, the number of pulses required to complete the etch can change the resulting selectivity. For example, selectivity is shown in Fig. 7.8(b) as a function of  $T_p$  for  $T_i = 20$ s. Fewer etch cycles results in decreased maximum selectivity for a given  $T_i$ . This occurs because the Si<sub>3</sub>N<sub>4</sub> removal occurs mostly in the first 3-5 cycles for these conditions, resulting in a constant etch contribution for 5, 10 and 15 cycles. The SiO<sub>2</sub> removal still scales linearly with the number of cycles in this range. Accordingly, the constant  $\Delta H_N$  results in the peak selectivity decreasing from 21 at 15 cycles, to only 9 at 5 cycles. Depending on the film thickness to be removed, the transient etching behavior may be a limiting factor in process development.

#### 7.4. Feature etching

To demonstrate the influence of transient etching in ALE of SiO<sub>2</sub>, simulations were performed of a self-aligned contact (SAC) geometry, shown in Fig. 7.9. In this plasma etching process, SiO<sub>2</sub> is removed from a high aspect ratio trench between Si<sub>3</sub>N<sub>4</sub> features. The initial geometry is shown in Fig. 7.9(a). The gap between gate features is 14 nm, and the computational domain is 78 nm ( $x$ )  $\times$  6 nm ( $y$ )  $\times$  187.5 nm ( $z$ ). With a mesh resolution of  $\Delta x = 0.3$  nm, this results in  $3.25 \times 10^6$  computational cells. Feature profiles for etching using a continuous process with RF bias of 40 V and 100 V are shown in Fig. 7.9(b,c). Continuous etching processes with similar conditions to those of ALE have difficulty etching this feature. Using the FC gas mixture with  $V_{RF} = 40$  V results in high selectivity to SiO<sub>2</sub> during continuous etching, as shown in Fig. 7.2(a). Applying these conditions to the SAC geometry does result in little etching of the Si<sub>3</sub>N<sub>4</sub>, however but the tapering in the trench quickly leads to an etch stop in which the polymerization is too thick to allow etching to continue. The etch stop can be avoided

by applying a larger bias of  $V_{RF} = 100$  V. Using these conditions, the selectivity for  $\text{SiO}_2$  significantly decreases, and the  $\text{Si}_3\text{N}_4$  shoulders are eroded before the etch reaches the contact point at the bottom of the feature. These plasma conditions were not specifically optimized for this particular etch application. It is likely that other plasma etch conditions will perform better in this application.

Using ALE allows more control over the polymerization and selectivity of this process than continuous etching. Plasma conditions which could not complete the SAC etch using continuous etching prove to be effective for ALE. Etch profiles are shown in Fig 7.9(d-f) using ALE with passivation times of  $T_p = 3.5, 4.5$  and  $5.5$  s. The ion bombardment time was 20 s for all cases with the same ion energy distribution as previously used in blanket etching ( $V_{RF} = 45$  V). The tapering of the feature is measured as *critical dimension (CD) loss*, which is the change in width of the trench between the  $\text{Si}_3\text{N}_4$  features from the top to a point 90% of the way down the feature, measured in nm. This CD loss is a measure of how much  $\text{SiO}_2$  remains in the SAC feature near the bottom contact point. The width of the actual contact patch is not used to calculate CD loss here because it is affected by the properties of the etch stop material, which is not calibrated in this case. The  $\text{Si}_3\text{N}_4$  *shoulder loss* will also be measured in nm, from the initial  $\text{Si}_3\text{N}_4$  surface to the etched surface after the SAC feature has been cleared. The CD loss and shoulder loss are shown in Fig. 7.10 as a function of  $T_p$  after 166 cycles. The results indicate two trends – increasing  $T_p$  results in a decreased shoulder loss while producing increased CD loss. The decrease in shoulder loss is a direct result of larger  $T_p$  having higher selectivity, as discussed for blanket etching. With the higher  $T_p$ , the polymer layer reaches an etch stop thickness on  $\text{Si}_3\text{N}_4$  more quickly, resulting in less transient etching. Comparing the profiles in Fig. 7.9(d-f) the polymer layer protecting the  $\text{Si}_3\text{N}_4$  is visibly thicker for larger  $T_p$ .

Critical dimension loss in the SAC feature is a multi-dimensional phenomenon, meaning that it cannot exist in a 1-d blanket etch scenario, and its root causes cannot be inferred from blanket results. While ALE can help obtain ideal, non-tapered, feature profiles [8], the underlying fluorocarbon plasma etch process has a strong propensity for generating tapered features, as shown in Fig 7.9(b). This taper can be related to ion energy, polymerization on the sidewalls, the angular dependence of sputtering yield and the re-deposition of radical etch products within the feature.[140–142] The reason the feature taper persists in the ALE case is related to a low ion sputtering yield of SiO<sub>2</sub> for near-grazing ion impacts on the tapered walls. In the halogen plasma ALE of silicon, the selvedge layer which is to be removed during ion bombardment, is directly exposed to the plasma and to ion bombardment. Direct plasma exposure increases sputtering yield when compared to sputtering through a thick passivation layer, but the total yield is still low at grazing and near grazing angles. Because of this, a larger  $T_i/T_p$  ratio is needed to clear passivated surface sites on tapered sidewalls. This effect was observed previously using our model when clearing residual silicon from the tapered sidewalls between fins during gate etching in a Cl<sub>2</sub>/Ar plasma ALE of silicon.[143]

In fluorocarbon plasma ALE of SiO<sub>2</sub>, sensitivity to the angular dependence of sputtering yield during the ion bombardment phase is exacerbated by polymer buildup on the walls. Ions striking the tapered sidewall at a near-grazing angle must penetrate the polymer layer to interact with the underlying selvedge layer. This is less likely at near-grazing incidence than normal incidence. First, the straight line path to the selvedge layer is longer for near-grazing ions than normal ions, assuming the same polymer thickness. Second, even small angle scattering as the ion implants through the polymer layer can result in a large portion of near-grazing impacts re-emerging into the plasma. On the other hand, normal incidence ions would have to undergo

$>90^\circ$  of total scattering before they could emerge from the polymer layer, making it much less likely to occur before interacting with the selvedge layer. This makes ions interacting with the selvedge layer less likely with a polymer overlayer than without. The main source of polymer etching during the ion bombardment phase is the consumption of the polymer layer by ions interacting with the selvedge layer. This depletion mechanism results in a polymer overlay which is more difficult to remove from tapered sidewalls than horizontal surfaces, and encourages tapering of the feature. From this perspective, larger  $T_p$  producing thicker polymer layers will result in a more tapered feature for a given  $T_i$ .

### **7.5. Role of Polymer in Dielectric Plasma ALE**

The results of blanket and SAC feature plasma ALE using FC gas mixtures ALE indicate that controlling polymer thickness is an essential aspect of the process. ALE offers an opportunity to control polymer thickness that is not available when using continuous plasma processing. Unfortunately, polymer deposition is not a fully self-limited process, making some of the benefits of ALE processing difficult to obtain. The selectivity, EPC, ALE synergy and CD loss all depend on polymer thickness, which in turn depend on fluxes of polymerizing species, fluxes of polymer etching radicals, fluxes of ions and ion energies (due to ion activation of the polymer layer and sputtering). This strong coupling of most or all of the important quality metrics to polymer thickness, along with the lack of a truly self-limited polymer deposition reaction, provide a dilemma for ALE process design.

Running an ALE process in the thick polymer regime, close to where the system will transition to net deposition, can provide several benefits. As shown in Fig 7.4(a) the EPC quasi-saturates at higher passivation times, indicating that in this regime the EPC is less dependent on polymer thickness. As  $T_p$  increases the EPC for ideal and non-ideal ALE fluxes converge.

These trends indicate that the thick polymer regime has a higher ALE synergy by suppressing continuous etching during the ion bombardment phase. Having higher ALE synergy and lower dependence of EPC on polymer thickness implies that operating with these conditions would result in lower aspect ratio dependent etch rates (ARDE). Unfortunately, these benefits only occur at the edge of continuous etching conditions, where the polymer layer is only just removed during each ALE cycle. This is, in some ways, an unstable steady-state condition. If conditions in the reactor change towards higher polymer deposition per cycle, either as a result of reactor wall seasoning or changing conditions with increasing aspect ratio in the feature, it is possible to rapidly transition to a net deposition condition.

While many of the benefits of ALE seem to be optimized by operating in a thick polymer regime, etching of the SAC demonstrates that there is a tradeoff between selectivity and CD loss (tapering) for these conditions. The results shown in Fig. 7.10 indicate that CD loss increases with increasing polymerization time  $T_p$  up to 6.5 s. For  $T_p \geq 7$  s, an etch-stop occurred before reaching the bottom contact material due to excessive polymer buildup in a fully tapered feature. The blanket ALE results, shown in Fig. 7.4(a), indicate that steady-state etching can be achieved with  $T_p = 7$  s for  $T_i = 20$  s, slightly longer polymerization time than was possible in the high aspect ratio feature. The high aspect ratio feature may impose a stricter limit on polymer deposition before etch-stop occurs compared to blanket etching. Another consideration when evaluating the ALE of high aspect ratio features is over-etch. (Over-etch refers to the additional time that etching proceeds following any point in the feature reaching the etch stop bottom layer.) The results presented in Fig. 7.10 are for the same number of ALE pulses, which represent about a 10% over-etch for  $T_p = 6.5$  s. Using the same number of pulses enabled a side-by-side comparison of the different conditions. If the over-etch is increased for each set of

conditions, the CD loss can be reduced. In fact, if the over etch is extended to 90% (285 cycles) the CD loss can be reduced, without dramatically increasing the shoulder loss, shown as dotted lines in Fig. 7.10. For instance, at  $T_p = 6$  s the CD loss decreased from 6.2 nm to 1.6 nm, while the shoulder loss increased from 2.5 nm to 2.8 nm. The increase in over-etch has a larger effect on shoulder loss at lower passivation times. For larger passivation times, the over etch does not significantly increase shoulder loss because the majority of  $\text{Si}_3\text{N}_4$  etching was during the short transient period at the beginning of the etch. If evaluated during the last several cycles of the process when the over-etch actually occurs, the selectivity to  $\text{SiO}_2$  would be essentially infinite.

## 7.6. Concluding Remarks

Atomic layer etching represents an opportunity to control polymer deposition during etching of  $\text{SiO}_2$  in fluorocarbon plasmas, which in turn enables finer control over selectivity, etch rate and profile propagation compared to continuous etching for comparable conditions. The results from our computational investigation indicate that ALE using cyclic pulses of a polymerizing  $\text{C}_4\text{F}_8$  containing plasma, and an argon plasma for ion bombardment of the passivated surface, can result in stable pulse-periodic steady-state ALE of  $\text{SiO}_2$ . Being able to achieve this steady state is in part due to the consumption of polymer during the  $\text{SiO}_2$  etch cycle, which can effectively clear the  $\text{SiO}_2$  surface of polymer in spite the use of low energy non-reactive species for ion bombardment. For the same conditions, it is difficult to completely clear the polymer overlayer from  $\text{Si}_3\text{N}_4$  surfaces during the ion bombardment phase, which eventually leads to polymer buildup and an etch stop. This leads to effectively infinite selectivity of  $\text{SiO}_2$  over  $\text{Si}_3\text{N}_4$  for ALE in the pulse-periodic steady state.

Transient etching effects before the polymer overlay has fully developed have an important role in the ALE of  $\text{SiO}_2$ , and particularly in its selectivity over  $\text{Si}_3\text{N}_4$ . Conditions

which will eventually lead to an etch stop on  $\text{Si}_3\text{N}_4$  can also produce significant etching in the first several ALE cycles before the overlayer is thick enough to prevent further etching. For many applications, including the SAC etch process described above, this initial transient etching of  $\text{Si}_3\text{N}_4$  can be a limiting factor on the selectivity of  $\text{SiO}_2$  over  $\text{Si}_3\text{N}_4$  the process. For etching of thinner films, for example those requiring less than 10 ALE cycles, the limitations on the selectivity of the ALE pulsing scheme used here may be insurmountable, requiring additional techniques such as pre-dosing the passivation phase to achieve a thicker initial polymer layer to preserve the selectivity of  $\text{SiO}_2$  over  $\text{Si}_3\text{N}_4$  achievable in the pulse-periodic steady state.

## 7.7. Figures

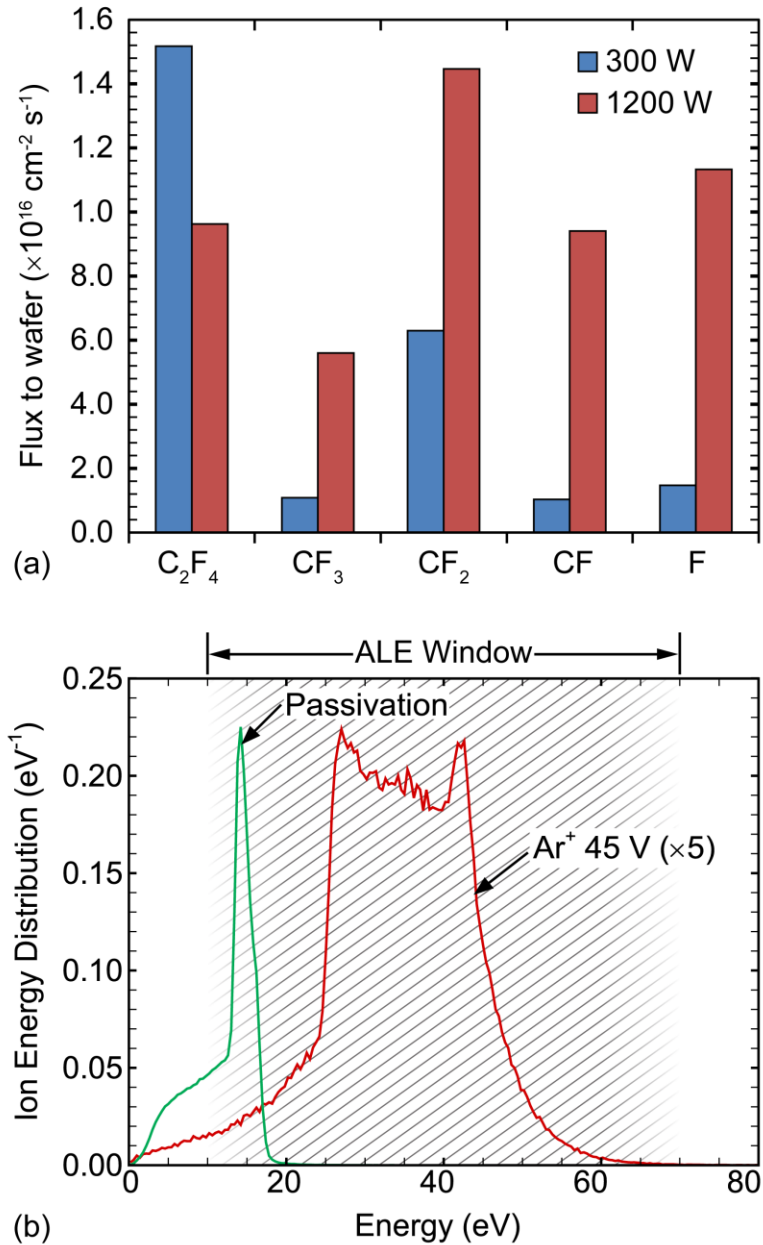
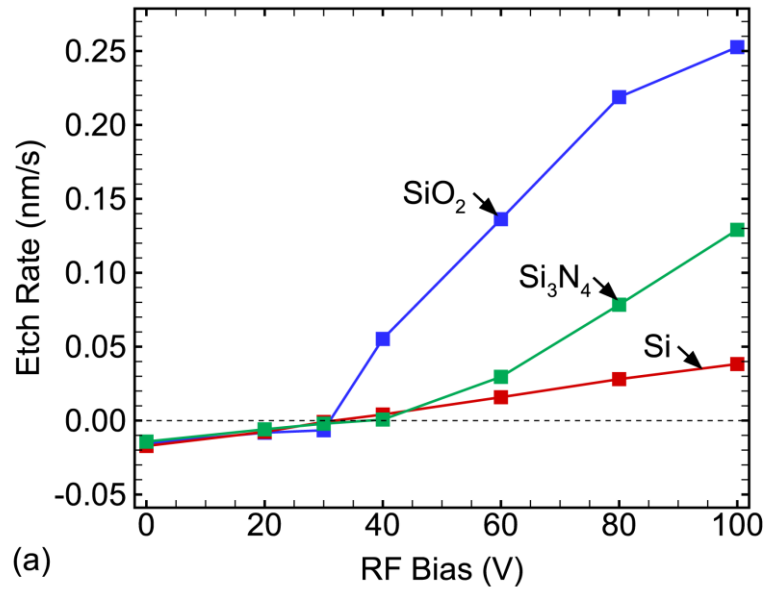
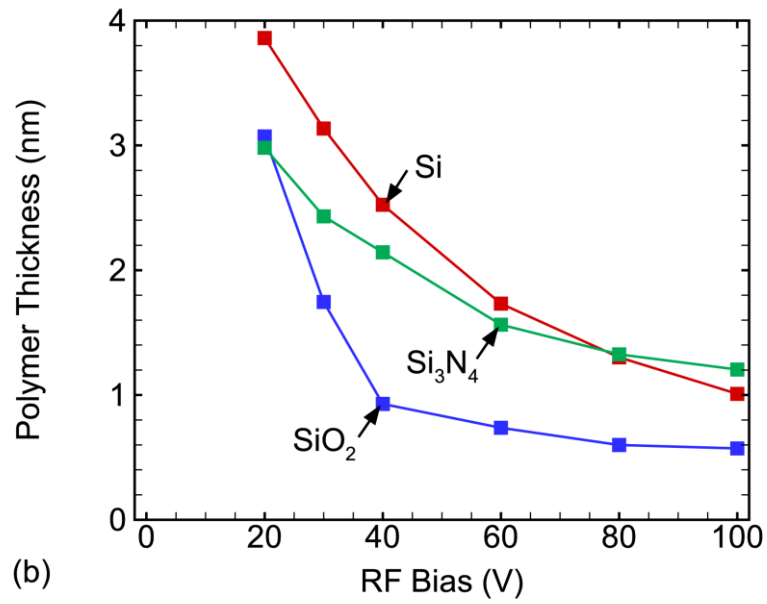


Fig. 7.1 Plasma conditions used in continuous and ALE processing. (a) Ratios of fluxes of  $\text{C}_4\text{F}_8$  dissociation products incident onto the wafer for ICP powers of 300 W and 1200 W. (b) Ion energy distributions reaching the surface during the passivation (VRF = 0 V) and ion bombardment (VRF = 45 V) phases.



(a)



(b)

Fig. 7.2 Continuous etching properties of Si, SiO<sub>2</sub> and Si<sub>3</sub>N<sub>4</sub> using the FC gas mixture as a function of RF bias voltage. (a) Etch rate where positive values represent continuous etching and negative values are the average polymer deposition rate for the first 200 s. (b) Steady-state polymer thickness.

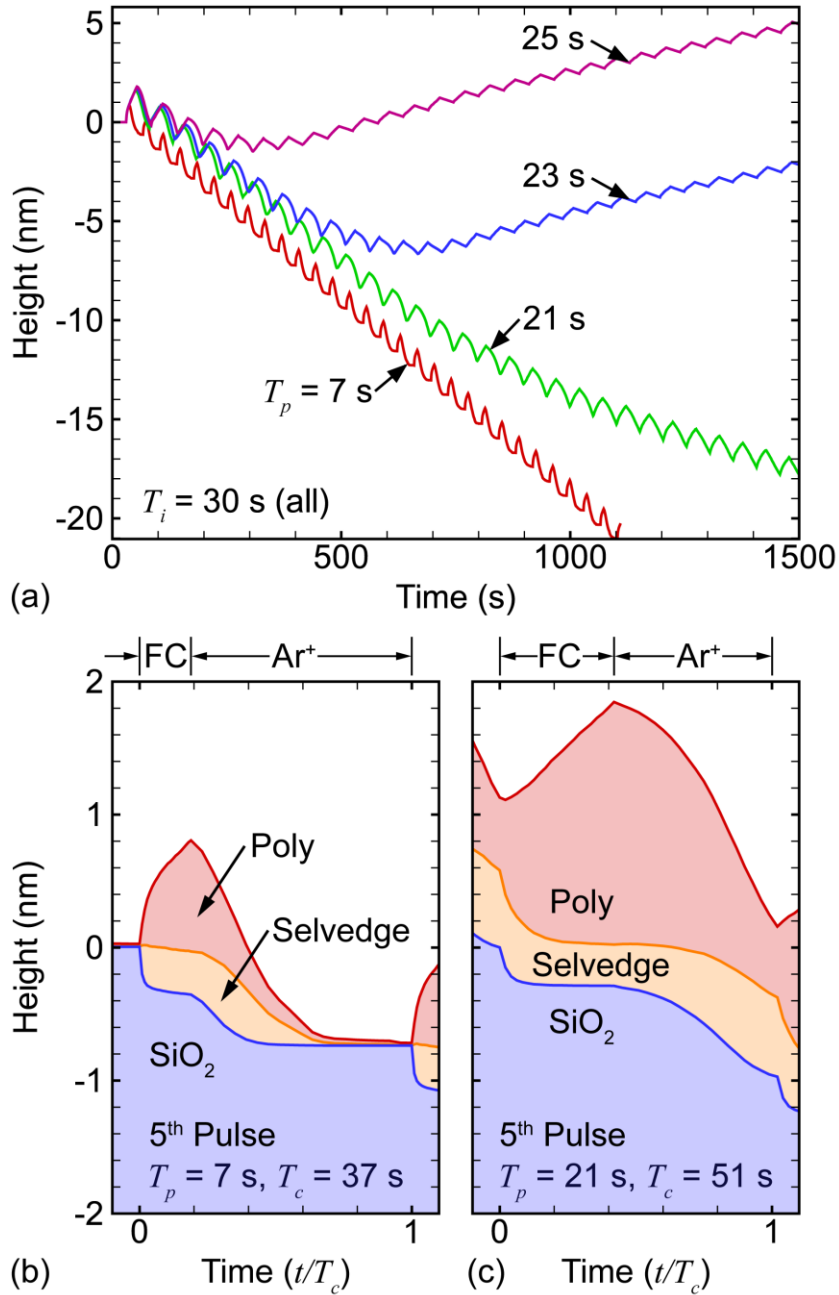
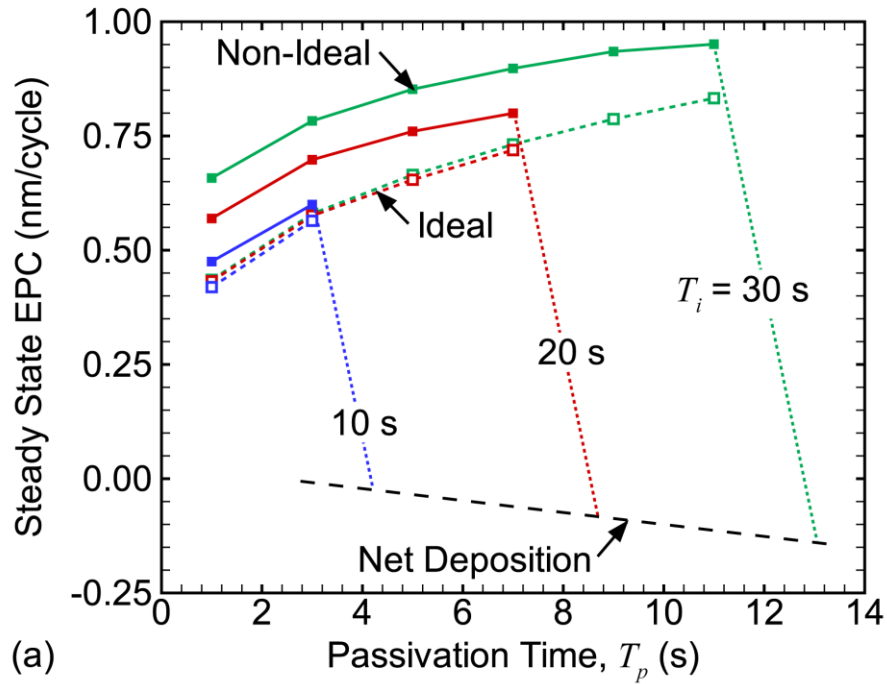
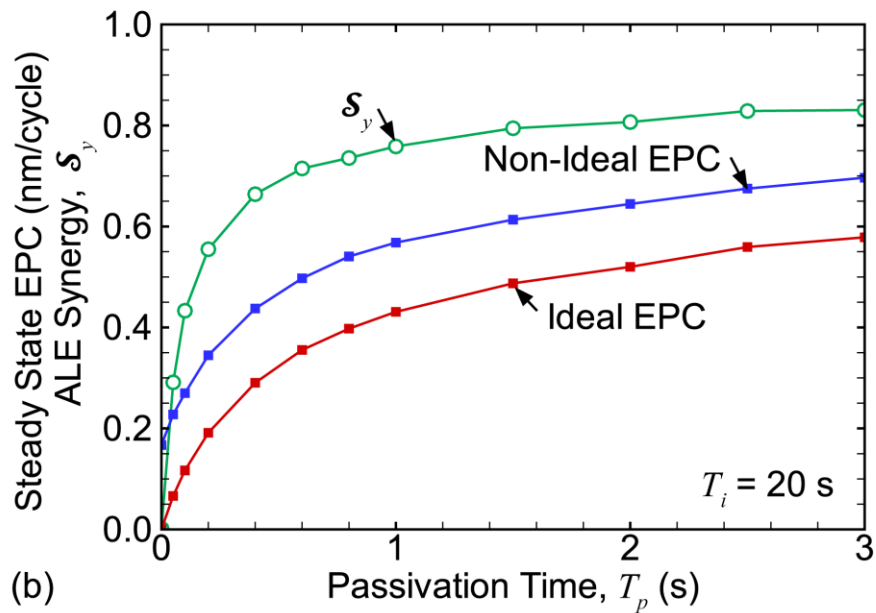


Fig. 7.3 Properties of SiO<sub>2</sub> ALE. (a) Change in total height (including polymer) as a function of time for polymerization times of  $T_p = 7, 21, 23$  and  $27$  s. All cases use  $T_i = 30$  s. Height of individual material layers during the 5<sup>th</sup> ALE pulse for (b)  $T_p = 7$  s and (c)  $T_p = 21$  s. The total ALE cycle time,  $T_c$ , is in each frame.



(a)



(b)

Fig. 7.4 Comparison of non-ideal and ideal  $\text{SiO}_2$  ALE properties. (a) Pulse-periodic steady state etch per cycle (EPC) as a function of  $T_p$ , for  $T_i = 10, 20$  and  $30$  s for ideal (dotted lines) and non-ideal (solid lines) reactive fluxes. (b) ALE synergy and steady state EPC for small values of  $T_p$  with  $T_i = 20$  s. Values are shown for ideal and non-ideal fluxes.

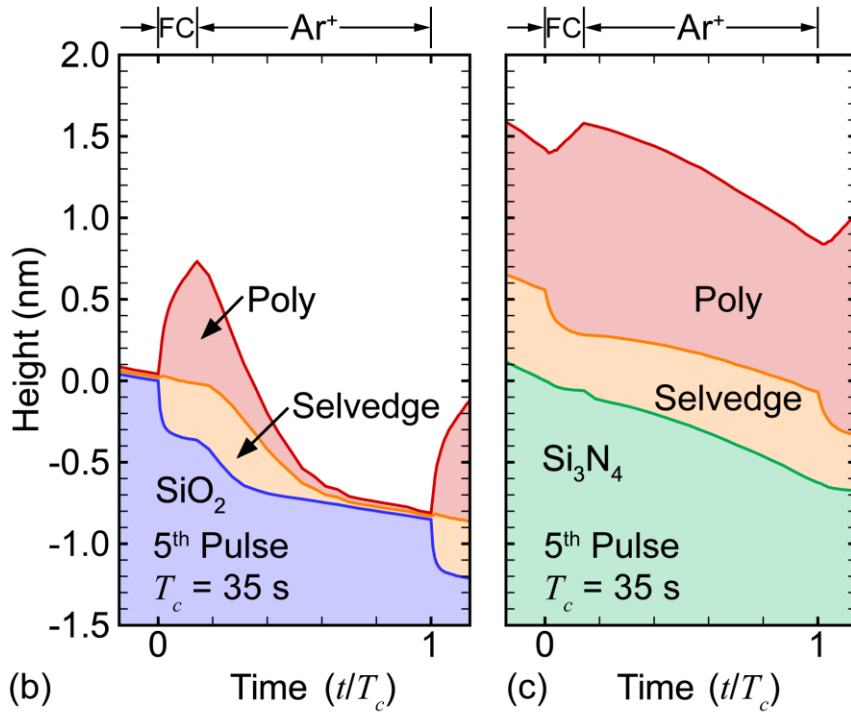
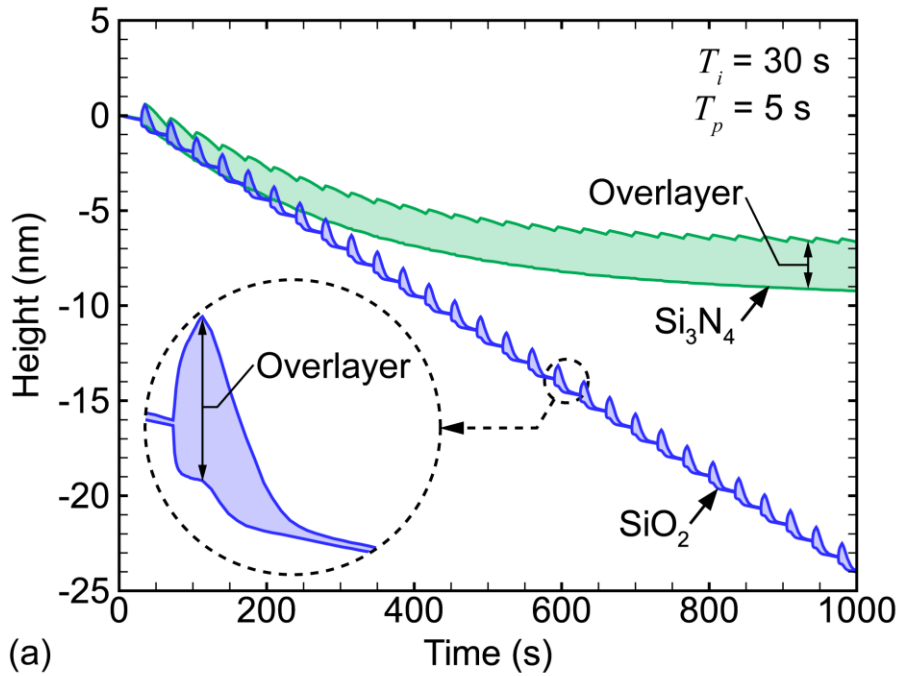


Fig. 7.5 ALE of  $\text{SiO}_2$  and  $\text{Si}_3\text{N}_4$  using non-ideal fluxes. (a) Change in total height (including polymer) as a function of time for  $\text{SiO}_2$  and  $\text{Si}_3\text{N}_4$ . The shaded regions represent the overlayer thickness, comprised of both the selvedge and polymer layers. Height of individual material layers during the 5<sup>th</sup> ALE pulse for (b)  $\text{SiO}_2$  and (c)  $\text{Si}_3\text{N}_4$ .

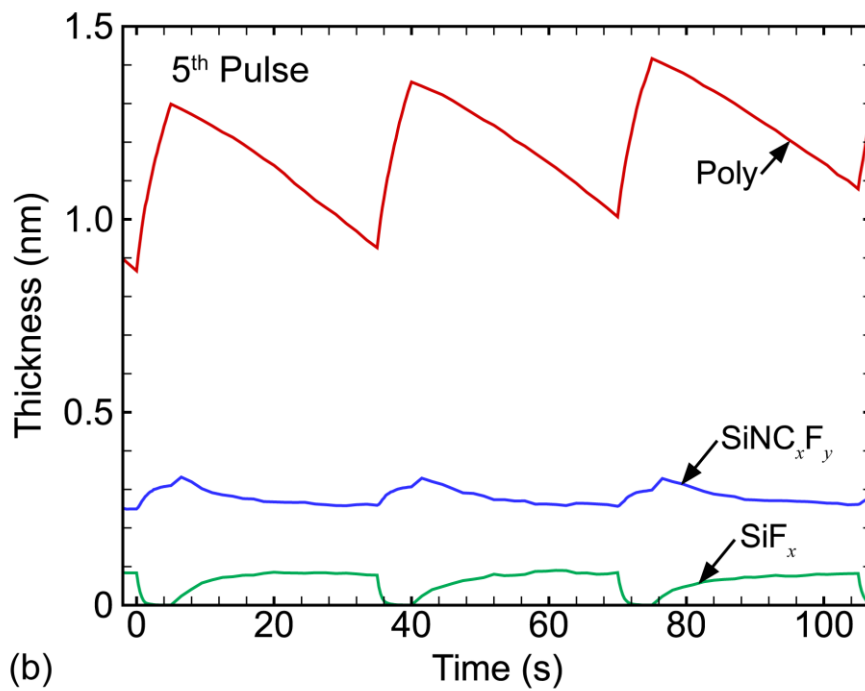
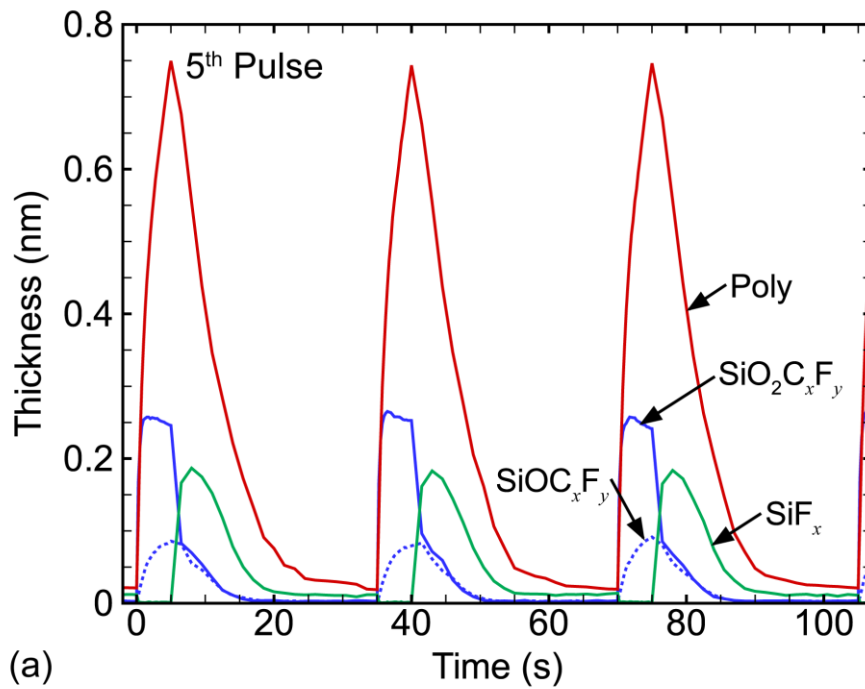


Fig. 7.6 Thickness of each overlayer species as a function of time during three ALE pulses ( $t = 0$  is the start of the 5<sup>th</sup> pulse) for (a)  $\text{SiO}_2$  and (b)  $\text{Si}_3\text{N}_4$ .

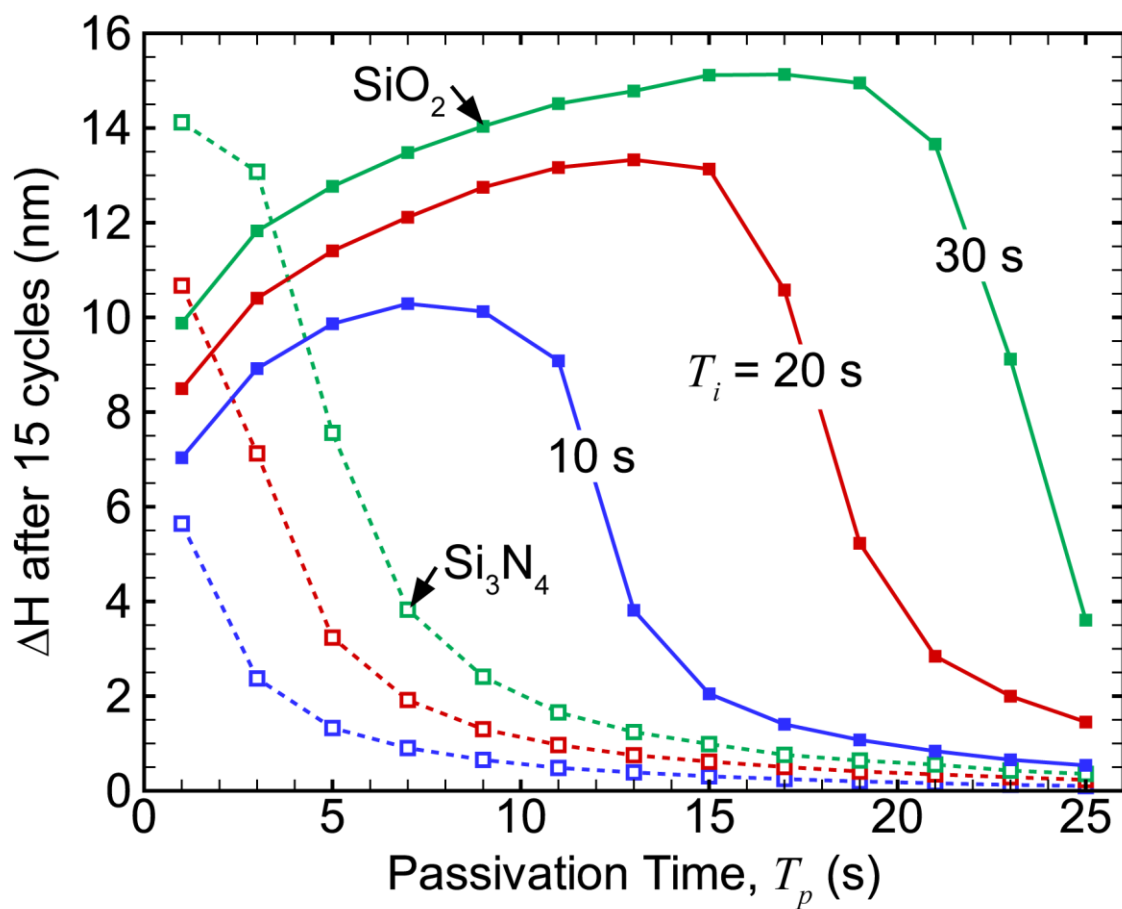
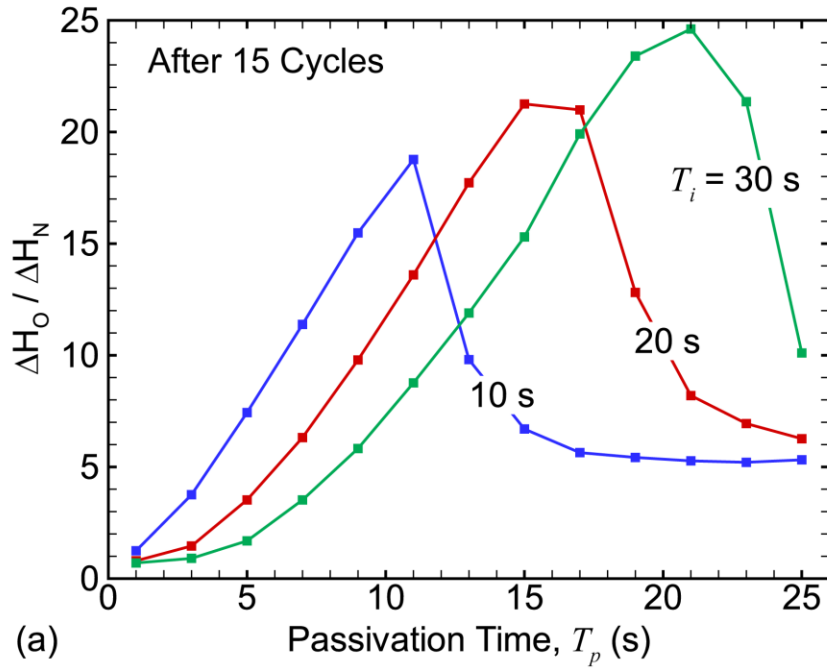
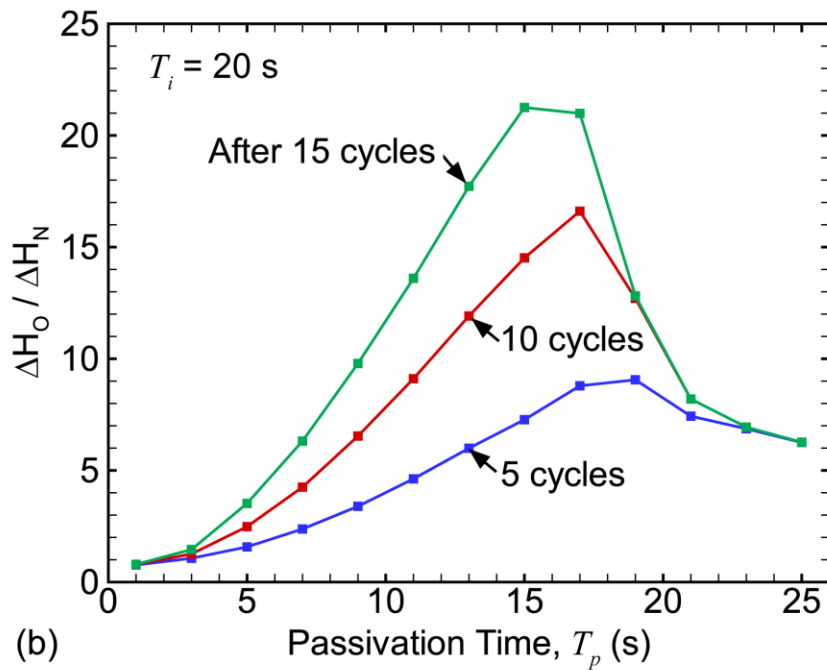


Fig. 7.7 Total change in height ( $\Delta H$ ) of the surface of  $\text{SiO}_2$  or  $\text{Si}_3\text{N}_4$  (not including overlayer) after 15 ALE cycles as a function of passivation time ( $T_p$ ) for ion bombardment times ( $T_i$ ) of 10, 20 and 30 s.  $\text{SiO}_2$  ALE is shown as solid lines,  $\text{Si}_3\text{N}_4$  as dotted lines.



(a)



(b)

Fig. 7.8 Selectivity of ALE of  $\text{SiO}_2$  over  $\text{Si}_3\text{N}_4$ . (a) Selectivity after 15 cycles as a function of passivation time ( $T_p$ ) for ion bombardment times ( $T_i$ ) of 10, 20 and 30 s. (b) Selectivity as a function of  $T_p$  for three different etch durations (5, 10 and 15 cycles) using  $T_i = 20$  s.

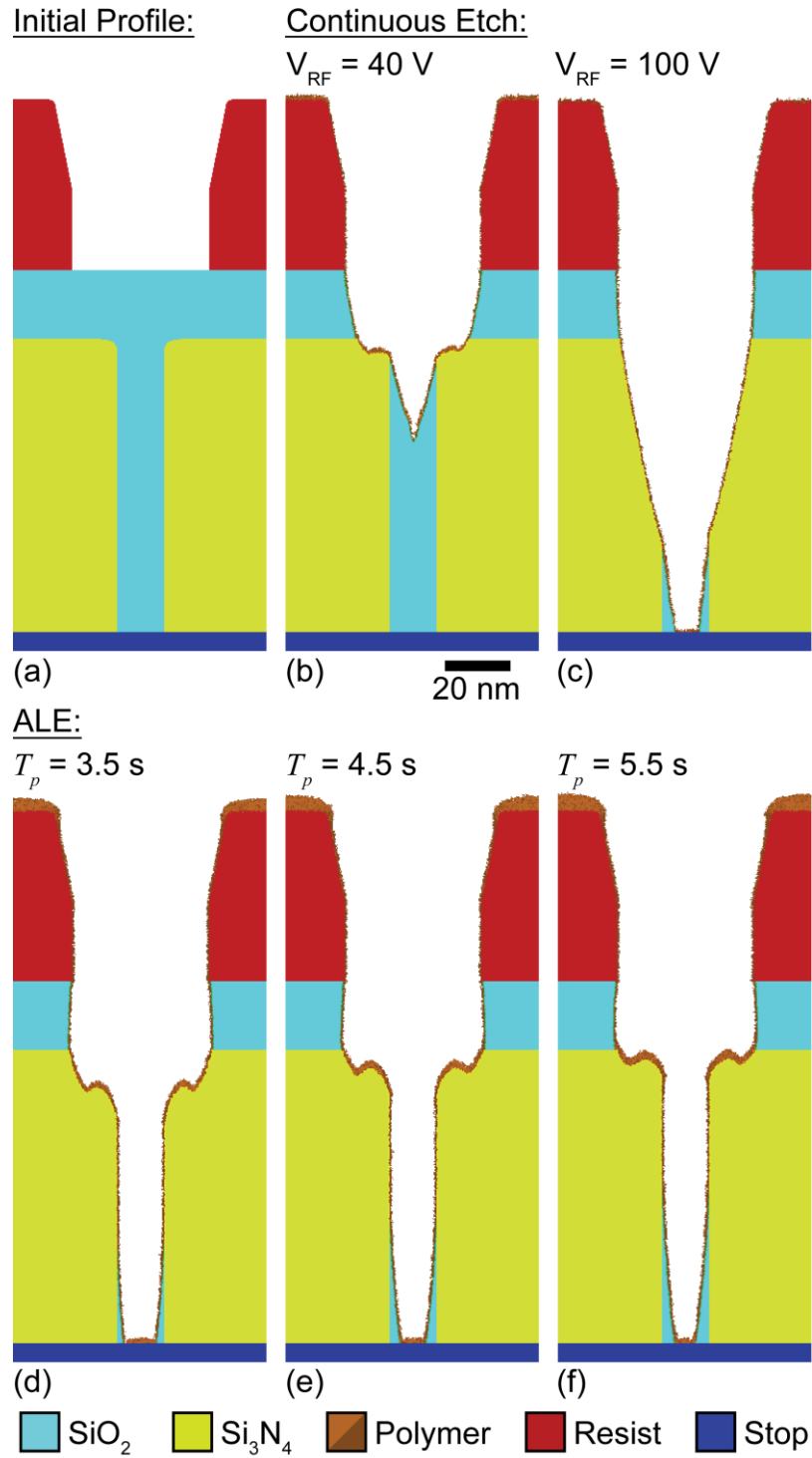


Fig. 7.9 Self-aligned-contact etch profiles for continuous etching and ALE. (a) Initial profile. Continuous etch using the FC gas mixture with 1200 W ICP power for (b)  $V_{RF} = 40 \text{ V}$  and (c)  $V_{RF} = 100 \text{ V}$ . ALE profiles after 165 cycles using  $T_i = 20 \text{ s}$  and  $T_p =$  (d) 3.5 s, (e) 4.5 s and (f) 5.5 s.

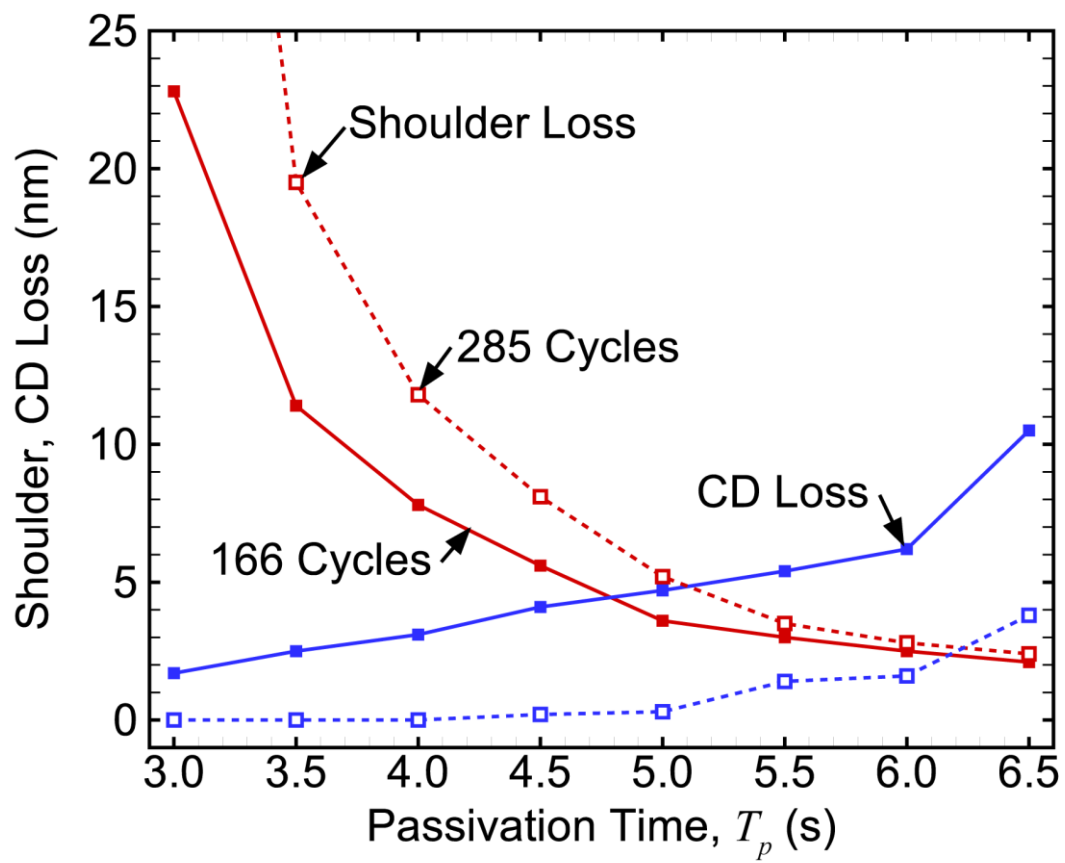


Fig. 7.10 Shoulder loss and CD loss as a function of passivation time for the SAC feature with  $T_i = 20$  s.

## **Chapter 8 SUMMARY AND FUTURE WORK**

In this thesis, a new feature scale model of the plasma etching process was described and used to elucidate the physical mechanisms and scaling relations involved in several industry relevant etching applications. In order to do this several new models were developed and described, as illustrated schematically in Fig. 2.6. The main purpose of this work was to develop and use feature scale modeling as a tool to better understand the underlying physics which link reactor scale conditions to final etched profiles.

### **8.1. Summary**

Chapter 1 introduces the idea of plasma etching and conveys background knowledge required to understand the following studies. A brief review of plasma physics was given, focusing particularly on how high energy and reactivity species are created in the plasma. The basic physical mechanisms of the interaction between these high energy species with surfaces was reviewed. A review of some of the challenges currently facing the plasma etching community, including aspect ratio dependent etching and uniformity was given. A discussion was also presented on the techniques and goals of feature scale modeling, including a review of previously published models.

In Chapter 2, the details of the Monte Carlo Feature Profile Model (MCFPM) were described. Several new physical models were incorporated into the MCFPM in order to describe the physics involved in fluorocarbon plasma etching. The new models developed include 3d ion implantation (including several new reaction pathway types), neutral diffusion and diffusion of physisorbed species on 3d surfaces, as illustrated in Fig. 2.6. These new models are essential to

capture the scaling of etching processes in the presence of a fluoropolymer overlayer. In addition to the new models, a description of the basic MCFPM algorithm is given, including code layout and parallelism techniques used.

Chapter 3 includes a detailed description of the workings of the two surface reaction mechanisms used in this thesis:  $\text{Cl}_2$  and  $\text{C}_4\text{F}_8$  (both in argon) for use in the MCFPM. In addition to describing the reaction pathways involved in each of these mechanisms, justification is given for the choice of reaction probabilities based on experimental evidence wherever possible.

In Chapter 4 results are presented from a study on the role neutral transport plays in the aspect ratio dependence of the etch rate when etching silicon in a chlorine containing plasma. It was found that the aspect ratio dependence of neutral transport is the main source for the aspect ratio dependent etch rate in these conditions. By increasing the total neutral flux, and driving the system towards a neutral saturated regime, the dependence on aspect ratio was postponed to higher aspect ratio, but not eliminated. Several 3d results were also presented showing that it is difficult to describe a 3d feature with a single aspect ratio. Instead it is useful to think of the feature as having an effective aspect ratio which varies depending on position in the 3d feature.

Results presented in Chapter 5 demonstrate that atomic layer etching (ALE) can provide significant benefits over continuous etching. In this work, ALE of silicon is performed by alternating between exposure to a chlorine containing plasma, to passivate the surface, and an argon plasma to preferentially remove the passivated surface sites. An ideal model was constructed, showing that, in the absence of continuous etching pathways, the ALE technique can provide aspect ratio independence and smooth and flat etch surfaces. Results were then presented using realistic reactant fluxes from an inductively coupled plasma reactor, including some non-ideal fluxes. These non-ideal fluxes introduced continuous etching pathways into the

passivation and ion bombardment phases. With the addition of this continuous etching the ability of the ALE process to provide aspect ratio independence was diminished. Surface roughening was also observed when using non-ideal fluxes. A technique for optimizing the ALE pulse times to minimize the effect of non-ideal fluxes was presented. Finally, this technique is used to clear features in a gate etch application with significantly less over-etch than a similar continuous etching process.

In Chapter 6, the use of ALE to improve wafer scale etching uniformity is discussed. Results show that fully saturated self-limited surface reactions can lead to very high wafer scale uniformity, even in the presence of highly non-uniform ion fluxes. Continuous etching, on the other hand, suffered from an etch rate which had a much stronger dependence on ion flux, and therefore was highly non-uniform. If the ALE reactions were not allowed to fully saturate the benefits of ALE were diminished, as the etch per cycle began to depend on the local ion flux. When using fully saturated reactions the total ion fluence to the wafer is significantly higher than when etching using a continuous process. This requires strongly self-limiting reactions, and highly ideal ALE conditions.

In Chapter 7, the ALE technique is applied to the etching of  $\text{SiO}_2$  and  $\text{Si}_3\text{N}_4$  in a fluorocarbon containing plasma. Unlike ALE of silicon using chlorine, the fluorocarbon passivation reaction is not self-limited, resulting in a continuous deposition process. The results indicate that the polymer overlayer acts a fuel for the etching reaction, and couples the polymer thickness with the etch per cycle. This results in an ALE process where the etch per cycle depends on the total fluence of polymerizing species during the passivation phase, which is not ideal. This ALE process can offer very high selectivity to  $\text{SiO}_2$  over  $\text{Si}_3\text{N}_4$  in the steady state, but results indicate that there is a transient period at the start of etching where the selectivity is

not as high. This transient etching effect can dominate the selective etching behavior in a wide variety of processes, including the self-aligned contacts used as an example application in this chapter.

## **8.2. Future work**

The MCFPM has been incrementally improved over the course of many years. In this way, it can be seen as a work in progress. Many additional improvements can be imagined for the MCFPM which could improve the physics of the of the model. Two examples will be outlined here.

By implementing a binary collision model to simulate the impact of gas phase particles on the solid surface the MCFPM could link the energy lost during a collision with the reaction probabilities. Currently, the energy lost during reflections is deterministic, depending on the initial ion energy and angle of impact. The probability of most energy dependent (sputtering) reactions also depends on impact angle deterministically. By implementing a binary collision routine with a randomly chosen impact parameter it may be possible to add a non-deterministic element to the energy loss, while coupling the energy deposited into the solid to the reaction probabilities for that collision.

In order to accurately model the high ion energy regime, the MCFPM should be modified to allow for sputtering yields larger than one. Currently, particles are assumed to react with mesh cells in a 1:1 way. Each collision can, at most, react with only one cell in the mesh. This assumption holds for thermal reactions and low energy ion processes, but at higher energies the measured yield (sputtered atoms/ion) can exceed one. In order to model this in the MCFPM some method for allowing an ion to interact with multiple cells in the mesh.

### 8.3. Concluding Remarks

The models developed in this thesis demonstrate that computational modeling of the plasma etching process can be of vital importance to the semiconductor industry. As logic elements continue to shrink, the demands on process engineering become increasingly more difficult (and expensive) to meet using only conventional design-of-experiments techniques. Modeling of the plasma etching process offers a compelling method to improve process design, complimenting experimental techniques.

The first possible benefit of incorporating plasma etch modeling into the process design workflow is cost. Individual simulation runs are very inexpensive, while each experimental run carries considerable cost. Furthermore, with current trends in parallel computing, tens of thousands of simulation jobs can be processed simultaneously if necessary. This allows users to probe a much larger portion of the parameter space in a much shorter time when compared to running experiments on a small number of (very expensive) etching machines, even if the time required for one simulation is significantly longer than the time required to process a wafer. The large number of simulations that can be performed generate data which can then be used as the input for machine-learning, artificial intelligence and “big data” processing to discover subtle but important trends.

Another benefit of including modeling in the process design workflow is access to portions of the parameter space which are inaccessible to experimental techniques. An example of this capability is presented in Chapters 5.2 and 7.3, where models of ideal ALE conditions were used. Once an ideal baseline was established using the model, deviations from ideal conditions could easily be studied. Since it is difficult to obtain ideal ALE conditions using

actual plasma equipment, this technique offers a very important method for studying the effect of non-ideal conditions on the benefits of ALE.

Finally, modeling can offer a method to decouple parameters which are closely coupled in a physical reactor. This technique was used in Chapter 4.3, where the ratio of reactive neutral to ion species fluxes was varied independently from other parameters. In experiments, this ratio is difficult or impossible to control without simultaneously changing other parameters. By decoupling this parameter in the model important information was learned about the role of neutral to ion flux ratios on the aspect ratio dependence of etch rates.

Each of these use cases demand that the etch model be calibrated and predictive. In order to obtain a model which can be calibrated over a wide range of parameters, and predictive outside of the calibrated range, the model must accurately capture the important physics of the etching process, as opposed to a simple empirical fitting of experimental data. The new plasma etching model presented here uses Monte-Carlo techniques to track energetic particles and radical species as they implant or diffuse through the polymer capping layer which forms during etching in fluorocarbon plasmas. By combining this physically based modeling technique with calibration data from experiments the new fluorocarbon etching model can be used to explore etching regimes significantly outside of the calibrated range.

The computational results presented in this thesis show that atomic layer etching can be used to overcome some of the limitations to traditional continuous etching. Utilizing self-limited reactions allows for decoupling neutral passivation reactions from the ion driven etching reactions. The results presented here demonstrate that the atomic layer etching technique can result in benefits by improving uniformity, by minimizing aspect ratio dependence, and producing smoother etched surfaces. In order to provide these benefits, it was shown here that

two conditions must be met: etching must be dominated by self-limited reactions, and surface reactions must be allowed to fully saturate. The results in this thesis demonstrate that one of these conditions without the other will not result in the full benefits of atomic layer etching.

Computational modeling, based on physics as opposed to empirical fitting, can provide significant insights into the plasma etching process, as demonstrated by this thesis. The modeling techniques presented here are general in nature and can be expanded and used to investigate a wide variety of problems not addressed here. Furthermore, the results from this model offer useful insights into the parameter space trade-offs involved in the atomic layer etching process.

## REFERENCES

- [1] M. P. Lepselter, "Beam-Lead Technology", *Bell Syst. Tech. J.* **45**, 233 (1966).
- [2] P. D. Davidse, "RF Sputter Etching—A Universal Etch", *J. Electrochem. Soc.* **116**, 100 (1969).
- [3] H. Seidel, L. Csepregi, A. Heuberger and H. Baumgärtel, "Anisotropic Etching of Crystalline Silicon in Alkaline Solutions", *J. Electrochem. Soc.* **137**, 3612 (1990).
- [4] K. R. Williams and R. S. Muller, "Etch rates for micromachining processing", *J. Microelectromechanical Syst.* **5**, 256 (1996).
- [5] Gordon Moore, "Cramming More Components onto Integrated Circuits", *Electronics* 114 (1965).
- [6] C. Svensson, "Forty years of feature-size predictions (1962-2002)", in *IEEE International Solid-State Circuits Conference (ISSCC)* **1**, 35 (2003).
- [7] R. P. Feynman, "Plenty of Room at the Bottom", (1959).
- [8] C. G. N. Lee, K. J. Kanarik and R. A. Gottscho, "The grand challenges of plasma etching: a manufacturing perspective", *J. Phys. D. Appl. Phys.* **47**, 273001 (2014).
- [9] J. Gregório and L. C. Pitchford, "Updated compilation of electron-Cl<sub>2</sub> scattering cross sections", *Plasma Sources Sci. Technol.* **21**, 32002 (2012).
- [10] E. Kawamura, V. Vahedi, M. A. Lieberman and C. K. Birdsall, "Ion energy distributions in rf sheaths; review, analysis and simulation", *Plasma Sources Sci. Technol.* **8**, R45 (1999).
- [11] R. T. C. Tsui, "Calculation of Ion Bombarding Energy and Its Distribution in rf Sputtering", *Phys. Rev.* **168**, 107 (1968).
- [12] J. W. Coburn and E. Kay, "Positive- ion bombardment of substrates in rf diode glow discharge sputtering", *J. Appl. Phys.* **43**, 4965 (1972).
- [13] P. Sigmund, "Theory of Sputtering. I. Sputtering Yield of Amorphous and Polycrystalline Targets", *Phys. Rev.* **184**, 383 (1969).
- [14] C. Steinbrüchel, "A simple formula for low-energy sputtering yields", *Appl. Phys. A Solids Surfaces* **36**, 37 (1985).
- [15] C. Steinbrüchel, "Universal energy dependence of physical and ion- enhanced chemical etch yields at low ion energy", *Appl. Phys. Lett.* **55**, 1960 (1989).
- [16] J. Orloff, M. Utlaut and L. Swanson, in *High Resolution Focused Ion Beams: FIB and its Applications 205* (Springer US, 2003).
- [17] H. M'saad, J. Michel, J. J. Lappe and L. C. Kimerling, "Electronic passivation of silicon

- surfaces by halogens", *J. Electron. Mater.* **23**, 487 (1994).
- [18] M. Balooch, M. Moalem, W.-E. Wang and A. V. Hamza, "Low-energy Ar ion-induced and chlorine ion etching of silicon", *J. Vac. Sci. Technol. A Vacuum, Surfaces, Film.* **14**, 229 (1996).
- [19] C. C. Cheng, K. V. Guinn, V. M. Donnelly and I. P. Herman, "In situ pulsed laser-induced thermal desorption studies of the silicon chloride surface layer during silicon etching in high density plasmas of Cl<sub>2</sub> and Cl<sub>2</sub>/O<sub>2</sub> mixtures", *J. Vac. Sci. Technol. A Vacuum, Surfaces, Film.* **12**, 2630 (1994).
- [20] M. W. Radny, P. V. Smith and P. L. Cao, "An ab initio Hartree-Fock/density functional study of the cluster simulated Si(111)7 × 7:Cl adsorption system", *Surf. Sci.* **365**, 15 (1996).
- [21] J. W. Coburn and H. F. Winters, "Ion- and electron- assisted gas- surface chemistry— An important effect in plasma etching", *J. Appl. Phys.* **50**, 3189 (1979).
- [22] J. P. Chang, J. Arnold, G. Zau, H.-S. Shin and H. H. Sawin, "Kinetic study of low energy argon ion-enhanced plasma etching of polysilicon with atomic/molecular chlorine", *J. Vac. Sci. Technol. A Vacuum, Surfaces, Film.* **15**, 1853 (1997).
- [23] J. P. Chang and H. H. Sawin, "Kinetic study of low energy ion-enhanced polysilicon etching using Cl, Cl<sub>2</sub>, and Cl<sup>+</sup> beam scattering", *J. Vac. Sci. Technol. A Vacuum, Surfaces, Film.* **15**, 610 (1997).
- [24] J. P. Chang and H. H. Sawin, "Molecular-beam study of the plasma-surface kinetics of silicon dioxide and photoresist etching with chlorine", *J. Vac. Sci. Technol. B Microelectron. Nanom. Struct.* **19**, 1319 (2001).
- [25] C. M. Huard, Y. Zhang, S. Sriraman, A. Paterson and M. J. Kushner, "Role of neutral transport in aspect ratio dependent plasma etching of three-dimensional features", *J. Vac. Sci. Technol. A Vacuum, Surfaces, Film.* **35**, 05C301 (2017).
- [26] W. Steckelmacher, "Knudsen flow 75 years on: the current state of the art for flow of rarefied gases in tubes and systems", *Reports Prog. Phys.* **49**, 1083 (1986).
- [27] H. Ohta and S. Hamaguchi, "Molecular dynamics simulation of silicon and silicon dioxide etching by energetic halogen beams", *J. Vac. Sci. Technol. A Vacuum, Surfaces, Film.* **19**, 2373 (2001).
- [28] M. J. Barela, H. M. Anderson and G. S. Oehrlein, "Role of C<sub>2</sub>F<sub>4</sub>, CF<sub>2</sub>, and ions in C<sub>4</sub>F<sub>8</sub>/Ar plasma discharges under active oxide etch conditions in an inductively coupled GEC cell reactor", *J. Vac. Sci. Technol. A Vacuum, Surfaces, Film.* **23**, 408 (2005).
- [29] M. Schaepkens, T. E. F. M. Standaert, N. R. Rueger, P. G. M. Sebel, G. S. Oehrlein and J. M. Cook, "Study of the SiO<sub>2</sub>-to-Si<sub>3</sub>N<sub>4</sub> etch selectivity mechanism in inductively coupled fluorocarbon plasmas and a comparison with the SiO<sub>2</sub>-to-Si mechanism", *J. Vac. Sci. Technol. A Vacuum, Surfaces, Film.* **17**, 26 (1999).
- [30] T. E. F. M. Standaert, C. Hedlund, E. A. Joseph, G. S. Oehrlein and T. J. Dalton, "Role of fluorocarbon film formation in the etching of silicon, silicon dioxide, silicon nitride, and amorphous hydrogenated silicon carbide", *J. Vac. Sci. Technol. A Vacuum, Surfaces, Film.* **22**, 53 (2004).

- [31] T. E. F. M. Standaert, M. Schaepkens, N. R. Rueger, P. G. M. Sebel, G. S. Oehrlein and J. M. Cook, "High density fluorocarbon etching of silicon in an inductively coupled plasma: Mechanism of etching through a thick steady state fluorocarbon layer", *J. Vac. Sci. Technol. A Vacuum, Surfaces, Film.* **16**, 239 (1998).
- [32] Y. J. Lee, F. J. Hou, S. S. Chuang, F. K. Hsueh, K. H. Kao, P. J. Sung, W. Y. Yuan, J. Y. Yao, Y. C. Lu, K. L. Lin, C. T. Wu, H. C. Chen, B. Y. Chen, G. W. Huang, H. J. H. Chen, J. Y. Li, Y. Li, S. Samukawa, T. S. Chao, T. Y. Tseng, W. F. Wu, T. H. Hou and W. K. Yeh, "Suspended Diamond-Shaped Nanowire With Four {111} Facets for High-Performance Ge Gate-All-Around FETs", *IEEE Trans. Electron Devices* **63**, 3837 (2016).
- [33] H. Mertens, R. Ritzenthaler, A. Hikavy, M. S. Kim, Z. Tao, K. Wostyn, S. A. Chew, A. De Keersgieter, G. Mannaert, E. Rosseel, T. Schram, K. Devriendt, D. Tsvetanova, H. Dekkers, S. Demuynck, A. Chasin, E. Van Besien, A. Dangol, S. Godny, B. Douhard, N. Bosman, O. Richard, J. Geypen, H. Bender, K. Barla, D. Mocuta, N. Horiguchi and A. V. Thean, "Gate-All-Around MOSFETs based on Vertically Stacked Horizontal Si Nanowires in a Replacement Metal Gate Process on Bulk Si Substrates", 2016 IEEE Symp. VLSI Technol. Honolulu, HI, 2016, pp. 1-2
- [34] K. J. Kuhn, U. Avci, A. Cappellani, M. D. Giles, M. Haverty, S. Kim, R. Kotlyar, S. Manipatruni, D. Nikonov, C. Pawashe, M. Radosavljevic, R. Rios, S. Shankar, R. Vedula, R. Chau and I. Young, "The ultimate CMOS device and beyond", 2012 IEEE Int. Electron Devices Meet. San Fr. CA, 2012, pp. 8.1.1-8.1.4
- [35] V. M. Donnelly and A. Kornblit, "Plasma etching: Yesterday, today, and tomorrow", *J. Vac. Sci. Technol. A Vacuum, Surfaces, Film.* **31**, 50825 (2013).
- [36] C. G. N. Lee, K. J. Kanarik and R. A. Gottscho, "The grand challenges of plasma etching: a manufacturing perspective", *J. Phys. D. Appl. Phys.* **47**, 273001 (2014).
- [37] R. L. Bates, M. J. Goeckner and L. J. Overzet, "Correction of aspect ratio dependent etch disparities", *J. Vac. Sci. Technol. A Vacuum, Surfaces, Film.* **32**, 51302 (2014).
- [38] S. Hwang and K. Kanarik, "Evolution of across-wafer uniformity control in plasma etch", *Solid State Technology* (2016).
- [39] X.-Y. Sun, Y.-R. Zhang, X.-C. Li and Y.-N. Wang, "Modulations of the plasma uniformity by low frequency sources in a large-area dual frequency inductively coupled plasma based on fluid simulations", *Phys. Plasmas* **22**, 53508 (2015).
- [40] K. Zhao, Y.-X. Liu, F. Gao, G.-H. Liu, D.-M. Han and Y.-N. Wang, "Experimental investigations of the plasma radial uniformity in single and dual frequency capacitively coupled argon discharges", *Phys. Plasmas* **23**, 123512 (2016).
- [41] P. G. Jung, S. S. Hoon, C. C. Wook and C. H. Young, "On the plasma uniformity of multi-electrode CCPs for large-area processing", *Plasma Sources Sci. Technol.* **22**, 55005 (2013).
- [42] X. A. Cao, S. J. Pearton, A. P. Zhang, G. T. Dang, F. Ren, R. J. Shul, L. Zhang, R. Hickman and J. M. Van Hove, "Electrical effects of plasma damage in p-GaN", *Appl. Phys. Lett.* **75**, 2569 (1999).
- [43] S. Fang and J. P. McVittie, "Thin-oxide damage from gate charging during plasma

- processing", *IEEE Electron Device Lett.* **13**, 288 (1992).
- [44] P. Brichon, E. Despiau-Pujo, O. Mourey and O. Joubert, "Key plasma parameters for nanometric precision etching of Si films in chlorine discharges", *J. Appl. Phys.* **118**, 53303 (2015).
- [45] H. Ito, T. Kuwahara, K. Kawaguchi, Y. Higuchi, N. Ozawa and M. Kubo, "Tight-binding quantum chemical molecular dynamics simulations for the elucidation of chemical reaction dynamics in SiC etching with SF<sub>6</sub>/O<sub>2</sub> plasma", *Phys. Chem. Chem. Phys.* **18**, 7808 (2016).
- [46] H. Ito, T. Kuwahara, K. Kawaguchi, Y. Higuchi, N. Ozawa, S. Samukawa and M. Kubo, "Tight-Binding Quantum Chemical Molecular Dynamics Simulations of Mechanisms of SiO<sub>2</sub> Etching Processes for CF<sub>2</sub> and CF<sub>3</sub> Radicals", *J. Phys. Chem. C* **118**, 21580 (2014).
- [47] B. A. Helmer and D. B. Graves, "Molecular dynamics simulations of Cl<sub>2</sub><sup>+</sup> impacts onto a chlorinated silicon surface: Energies and angles of the reflected Cl<sub>2</sub> and Cl fragments", *J. Vac. Sci. Technol. A Vacuum, Surfaces, Film.* **17**, 2759 (1999).
- [48] B. A. Helmer and D. B. Graves, "Molecular dynamics simulations of Ar<sup>+</sup> and Cl<sup>+</sup> impacts onto silicon surfaces: Distributions of reflected energies and angles", *J. Vac. Sci. Technol. A Vacuum, Surfaces, Film.* **16**, 3502 (1998).
- [49] T. Tatsumi, M. Matsui, M. Okigawa and M. Sekine, "Control of surface reactions in high-performance SiO<sub>2</sub> etching", *J. Vac. Sci. Technol. B Microelectron. Nanom. Struct.* **18**, 1897 (2000).
- [50] E. Gogolides, P. Vauvert, G. Kokkoris, G. Turban and A. G. Boudouvis, "Etching of SiO<sub>2</sub> and Si in fluorocarbon plasmas: A detailed surface model accounting for etching and deposition", *J. Appl. Phys.* **88**, 5570 (2000).
- [51] S. Osher and J. A. Sethian, "Fronts propagating with curvature-dependent speed: Algorithms based on Hamilton-Jacobi formulations", *J. Comput. Phys.* **79**, 12 (1988).
- [52] O. Ertl and S. Selberherr, "Three-dimensional level set based Bosch process simulations using ray tracing for flux calculation", *Microelectron. Eng.* **87**, 20 (2010).
- [53] T. Shimada, T. Yagisawa and T. Makabe, "Modeling of Feature Profile Evolution in SiO<sub>2</sub> as functions of Radial Position and Bias Voltage under Competition among Charging, Deposition, and Etching in Two-Frequency Capacitively Coupled Plasma", *Jpn. J. Appl. Phys.* **45**, 8876 (2006).
- [54] A. P. Mahorowala and H. H. Sawin, "Etching of polysilicon in inductively coupled Cl<sub>2</sub> and HBr discharges. II. Simulation of profile evolution using cellular representation of feature composition and Monte Carlo computation of flux and surface kinetics", *J. Vac. Sci. Technol. B Microelectron. Nanom. Struct.* **20**, 1064 (2002).
- [55] W. Guo, B. Bai and H. H. Sawin, "Mixing-layer kinetics model for plasma etching and the cellular realization in three-dimensional profile simulator", *J. Vac. Sci. Technol. A Vacuum, Surfaces, Film.* **27**, 388 (2009).
- [56] W. Guo and H. H. Sawin, "Etching of SiO<sub>2</sub> in C<sub>4</sub>F<sub>8</sub>/Ar plasmas. I. Numeric kinetics modeling and Monte Carlo simulation in a three-dimensional profile simulator", *J. Vac. Sci. Technol. A Vacuum, Surfaces, Film.* **28**, 250 (2010).

- [57] P. J. Stout, S. Rauf, A. Nagy and P. L. G. Ventzek, "Modeling dual inlaid feature construction", *J. Vac. Sci. Technol. B Microelectron. Nanom. Struct.* **24**, 1344 (2006).
- [58] Y. Osano and K. Ono, "An Atomic Scale Model of Multilayer Surface Reactions and the Feature Profile Evolution during Plasma Etching", *Jpn. J. Appl. Phys.* **44**, 8650 (2005).
- [59] Y. Osano and K. Ono, "Atomic-scale cellular model and profile simulation of poly-Si gate etching in high-density chlorine-based plasmas: Effects of passivation layer formation on evolution of feature profiles", *J. Vac. Sci. Technol. B Microelectron. Nanom. Struct.* **26**, 1425 (2008).
- [60] K. Ono, N. Nakazaki, H. Tsuda, Y. Takao and K. Eriguchi, "Surface morphology evolution during plasma etching of silicon: roughening, smoothing and ripple formation", *J. Phys. D. Appl. Phys.* **50**, 414001 (2017).
- [61] S. Takagi, S. Onoue, K. Nishitani, T. Shinmura and Y. Shigesato, "Comparison of CF<sub>4</sub> and C<sub>4</sub>F<sub>8</sub> gas etching profiles by multiscale simulation", *Jpn. J. Appl. Phys.* **54**, 36501 (2015).
- [62] S. Takagi, S. Onoue, K. Iyanagi, K. Nishitani, T. Shinmura, M. Kanoh, H. Itoh, Y. Shioyama, T. Akiyama and D. Kishigami, "Predictable topography simulation of SiO<sub>2</sub> etching by C<sub>5</sub>F<sub>8</sub> gas combined with a plasma simulation, sheath model and chemical reaction model", *Plasma Sources Sci. Technol.* **12**, S64 (2003).
- [63] D. O. S. Melville, A. E. Rosenbluth, A. Waechter, M. Millstone, J. Tirapu-Azpiroz, K. Tian, K. Lai, T. Inoue, M. Sakamoto, K. Adam and A. Tritchkov, "Computational lithography: Exhausting the resolution limits of 193-nm projection lithography systems", *J. Vac. Sci. Technol. B, Nanotechnol. Microelectron. Mater. Process. Meas. Phenom.* **29**, 06FH04 (2011).
- [64] L. V. Zavyalova, L. Luan, H. Song, T. Schmoeller and J. P. Shiely, "Combining lithography and etch models in OPC modeling", in **9052**, 905222 (International Society for Optics and Photonics, 2014).
- [65] C. Auth, A. Aliyarukunju, M. Asoro, D. Bergstrom, V. Bhagwat, J. Birdsall, N. Bisnik, A. Yeoh, et al., "A 10nm high performance and low-power CMOS technology featuring 3<sup>rd</sup> generation FinFET transistors, Self-Aligned Quad Patterning, contact over active gate and cobalt local interconnects", in 2017 IEEE International Electron Devices Meeting (IEDM) 29.1.1 (IEEE, 2017).
- [66] M. J. Kushner, "Hybrid modelling of low temperature plasmas for fundamental investigations and equipment design", *J. Phys. D. Appl. Phys.* **42**, 194013 (2009).
- [67] "Mark Kushner Group - Publications", Online at: <http://uigelz.eecs.umich.edu/publications.html>
- [68] D. Zhang and M. J. Kushner, "Surface kinetics and plasma equipment model for Si etching by fluorocarbon plasmas", *J. Appl. Phys.* **87**, 1060 (2000).
- [69] A. Agarwal and M. J. Kushner, "Seasoning of plasma etching reactors: Ion energy distributions to walls and real-time and run-to-run control strategies", *J. Vac. Sci. Technol. A Vacuum, Surfaces, Film.* **26**, 498 (2008).
- [70] C. C. Battaile, D. J. Srolovitz and J. E. Butler, "A kinetic Monte Carlo method for the

- atomic-scale simulation of chemical vapor deposition: Application to diamond", *J. Appl. Phys.* **82**, 6293 (1998).
- [71] S. A. Islam, "Math Notes-Least Squares Plane",
- [72] L. N. Trefethen and D. Bau, "*Numerical linear algebra*", (Society for Industrial and Applied Mathematics, 1997).
- [73] G. E. Farin and D. Hansford, "*Practical linear algebra : a geometry toolbox*", (2013).
- [74] H. D. Hagstrum, "Theory of Auger Neutralization of Ions at the Surface of a Diamond-Type Semiconductor", *Phys. Rev.* **122**, 83 (1961).
- [75] F. Celestini and F. Mortessagne, "Cosine law at the atomic scale: toward realistic simulations of Knudsen diffusion.", *Phys. Rev. E* **77**, 21202 (2008).
- [76] C. Steinbrüchel, "Universal energy dependence of physical and ion-enhanced chemical etch yields at low ion energy", *Appl. Phys. Lett.* **55**, 1960 (1989).
- [77] T. E. F. M. Standaert, M. Schaepkens, N. R. Rueger, P. G. M. Sebel, G. S. Oehrlein and J. M. Cook, "High density fluorocarbon etching of silicon in an inductively coupled plasma: Mechanism of etching through a thick steady state fluorocarbon layer", *J. Vac. Sci. Technol. A Vacuum, Surfaces, Film.* **16**, 239 (1998).
- [78] R. A. Fisher and F. Yates, "*Statistical tables for biological, agricultural and medical research.*", Statistical tables for biological, agricultural and medical research. (Oliver and Boyd, Edinburgh, 1949).
- [79] J. F. Ziegler, M. D. Ziegler and J. P. Biersack, "SRIM – The stopping and range of ions in matter (2010)", *Nucl. Instruments Methods Phys. Res. Sect. B Beam Interact. with Mater. Atoms* **268**, 1818 (2010).
- [80] C. T. Rettner, J. A. Barker and D. S. Bethune, "Angular and velocity distributions characteristic of the transition between the thermal and structure regimes of gas-surface scattering", *Phys. Rev. Lett.* **67**, 2183 (1991).
- [81] S. Matteson, "Atomic mixing in ion impact: A collision cascade model", *Appl. Phys. Lett.* **39**, 288 (1981).
- [82] N. Metropolis, A. W. Rosenbluth, M. N. Rosenbluth, A. H. Teller and E. Teller, "Equation of State Calculations by Fast Computing Machines", *J. Chem. Phys.* **21**, 1087 (1953).
- [83] P. Clausing, "The Flow of Highly Rarefied Gases through Tubes of Arbitrary Length", *J. Vac. Sci. Technol.* **8**, 636 (1971).
- [84] Y. Zhang, C. Huard, S. Sriraman, J. Belen, A. Paterson and M. J. Kushner, "Investigation of feature orientation and consequences of ion tilting during plasma etching with a three-dimensional feature profile simulator", *J. Vac. Sci. Technol. A Vacuum, Surfaces, Film.* **35**, 21303 (2017).
- [85] N. Layadi, V. M. Donnelly and J. T. C. Lee, "Cl<sub>2</sub> plasma etching of Si(100): Nature of the chlorinated surface layer studied by angle-resolved x-ray photoelectron spectroscopy", *J. Appl. Phys.* **81**, 6738 (1997).
- [86] G. P. Kota, J. W. Coburn and D. B. Graves, "The recombination of chlorine atoms at surfaces", *J. Vac. Sci. Technol. A Vacuum, Surfaces, Film.* **16**, 270 (1998).

- [87] R. Khare, A. Srivastava and V. M. Donnelly, "Cl atom recombination on silicon oxychloride layers deposited on chamber walls in chlorine–oxygen plasmas", *J. Vac. Sci. Technol. A Vacuum, Surfaces, Film.* **30**, 51307 (2012).
- [88] G. Cunge, D. Vempaire, R. Ramos, M. Touzeau, O. Joubert, P. Bodard and N. Sadeghi, "Radical surface interactions in industrial silicon plasma etch reactors", *Plasma Sources Sci. Technol.* **19**, 34017 (2010).
- [89] M. E. Barone and D. B. Graves, "Molecular dynamics simulations of plasma - surface chemistry", *Plasma Sources Sci. Technol.* **5**, 187 (1996).
- [90] J. M. Lane, K. H. A. Bogart, F. P. Klemens and J. T. C. Lee, "The role of feedgas chemistry, mask material, and processing parameters in profile evolution during plasma etching of Si(100)", *J. Vac. Sci. Technol. A Vacuum, Surfaces, Film.* **18**, 2067 (2000).
- [91] J. A. Levinson, E. S. G. Shaqfeh, M. Balooch and A. V. Hamza, "Ion-assisted etching and profile development of silicon in molecular chlorine", *J. Vac. Sci. Technol. A Vacuum, Surfaces, Film.* **15**, 1902 (1997).
- [92] G. Cunge, M. Kogelschatz and N. Sadeghi, "Production and loss mechanisms of  $\text{SiCl}_x$  etch products during silicon etching in a high density  $\text{HBr} / \text{Cl}_2 / \text{O}_2$  plasma", *J. Appl. Phys.* **96**, 4578 (2004).
- [93] G. Cunge, R. L. Inglebert, O. Joubert, L. Vallier and N. Sadeghi, "Ion flux composition in  $\text{HBr} / \text{Cl}_2 / \text{O}_2$  and  $\text{HBr} / \text{Cl}_2 / \text{O}_2 / \text{CF}_4$  chemistries during silicon etching in industrial high-density plasmas", *J. Vac. Sci. Technol. B Microelectron. Nanom. Struct.* **20**, 2137 (2002).
- [94] C. Petit-Etienne, M. Darnon, P. Bodart, M. Fouchier, G. Cunge, E. Pargon, L. Vallier, O. Joubert and S. Banna, "Atomic-scale silicon etching control using pulsed  $\text{Cl}_2$  plasma", *J. Vac. Sci. Technol. B Microelectron. Nanom. Struct.* **31**, 11201 (2013).
- [95] G. Cunge and J. P. Booth, " $\text{CF}_2$  production and loss mechanisms in fluorocarbon discharges: Fluorine-poor conditions and polymerization", *J. Appl. Phys.* **85**, 3952 (1999).
- [96] H. Chae, S. A. Vitale and H. H. Sawin, "Silicon dioxide etching yield measurements with inductively coupled fluorocarbon plasmas", *J. Vac. Sci. Technol. A Vacuum, Surfaces, Film.* **21**, 381 (2003).
- [97] G. S. Oehrlein, Y. Zhang, D. Vender and M. Haverlag, "Fluorocarbon high-density plasmas. I. Fluorocarbon film deposition and etching using  $\text{CF}_4$  and  $\text{CHF}_3$ ", *J. Vac. Sci. Technol. A Vacuum, Surfaces, Film.* **12**, 323 (1994).
- [98] S. S. Kaler, Q. Lou, V. M. Donnelly and D. J. Economou, "Atomic layer etching of silicon dioxide using alternating  $\text{C}_4\text{F}_8$  and energetic  $\text{Ar}^+$  plasma beams", *J. Phys. D. Appl. Phys.* **50**, 234001 (2017).
- [99] S. B. Wainhaus, E. A. Gislason and L. Hanley, "Determination of Activation Energies for Ion Fragmentation by Surface-Induced Dissociation", *J. Am. Chem. Soc.* **119**, 4001 (1997).
- [100] E. R. Fuoco and L. Hanley, "Large fluorocarbon ions can contribute to film growth during plasma etching of silicon", *J. Appl. Phys.* **92**, 37 (2002).

- [101] L. Meng, J. Li, C. Zhao and J. Yan, "Aspect Ratio Dependent Analytic Model and Application in Deep Silicon Etch", *ECS Solid State Lett.* **3**, Q25 (2014).
- [102] J. W. Coburn and H. F. Winters, "Conductance considerations in the reactive ion etching of high aspect ratio features", *Appl. Phys. Lett.* **55**, 2730 (1989).
- [103] A. Beskok and G. E. Karniadakis, "Report: A Model for Flows in Channels, Pipes and Ducts at Micro and Nano Scales", *Microscale Thermophys. Eng.* **3**, 43 (1999).
- [104] R. A. Gottscho, C. W. Jurgensen and D. J. Vitkavage, "Microscopic uniformity in plasma etching", *J. Vac. Sci. Technol. B Microelectron. Nanom. Struct.* **10**, 2133 (1992).
- [105] J. S. Han, J. P. McVittie and J. Zheng, "Profile modeling of high density plasma oxide etching", *J. Vac. Sci. Technol. B Microelectron. Nanom. Struct.* **13**, 1893 (1995).
- [106] J. Hoang, C.-C. Hsu and J. P. Chang, "Feature profile evolution during shallow trench isolation etch in chlorine-based plasmas. I. Feature scale modeling", *J. Vac. Sci. Technol. B Microelectron. Nanom. Struct.* **26**, 1911 (2008).
- [107] A. D. Bailey, M. C. M. van de Sanden, J. A. Gregus and R. A. Gottscho, "Scaling of Si and GaAs trench etch rates with aspect ratio, feature width, and substrate temperature", *J. Vac. Sci. Technol. B Microelectron. Nanom. Struct.* **13**, 92 (1995).
- [108] M. A. Vyvoda, H. Lee, M. V. Malyshev, F. P. Klemens, M. Cerullo, V. M. Donnelly, D. B. Graves, A. Kornblit and J. T. C. Lee, "Effects of plasma conditions on the shapes of features etched in Cl<sub>2</sub> and HBr plasmas. I. Bulk crystalline silicon etching", *J. Vac. Sci. Technol. A Vacuum, Surfaces, Film.* **16**, 3247 (1998).
- [109] M. A. Vyvoda, M. Li, D. B. Graves, H. Lee, M. V. Malyshev, F. P. Klemens, J. T. C. Lee and V. M. Donnelly, "Role of sidewall scattering in feature profile evolution during Cl<sub>2</sub> and HBr plasma etching of silicon", *J. Vac. Sci. Technol. B Microelectron. Nanom. Struct.* **18**, 820 (2000).
- [110] N. C. M. Fuller, I. P. Herman and V. M. Donnelly, "Optical actinometry of Cl<sub>2</sub>, Cl, Cl<sup>+</sup>, and Ar<sup>+</sup> densities in inductively coupled Cl<sub>2</sub>-Ar plasmas", *J. Appl. Phys.* **90**, 3182 (2001).
- [111] S. Samukawa, K. Sakamoto and K. Ichiki, "High-efficiency neutral-beam generation by combination of inductively coupled plasma and parallel plate DC bias", *Jpn. J. Appl. Phys.* **40**, L779 (2001).
- [112] S. Noda, H. Nishimori, T. Ida, T. Arikado, K. Ichiki, T. Ozaki and S. Samukawa, "50 nm gate electrode patterning using a neutral-beam etching system", *J. Vac. Sci. Technol. A Vacuum, Surfaces, Film.* **22**, 1506 (2004).
- [113] S. Samukawa, "Ultimate Top-down Etching Processes for Future Nanoscale Devices: Advanced Neutral-Beam Etching", *Jpn. J. Appl. Phys.* **45**, 2395 (2006).
- [114] N. Kuboi, T. Tatsumi, M. Fukasawa, T. Kinoshita, J. Komachi, H. Ansai and H. Miwa, "Effect of open area ratio and pattern structure on fluctuations in critical dimension and Si recess", *J. Vac. Sci. Technol. A Vacuum, Surfaces, Film.* **31**, 61304 (2013).
- [115] X. Li, X. Hua, L. Ling, G. S. Oehrlein, M. Barela and H. M. Anderson, "Fluorocarbon-based plasma etching of SiO<sub>2</sub>: Comparison of C<sub>4</sub>F<sub>6</sub>/Ar and C<sub>4</sub>F<sub>8</sub>/Ar discharges", *J. Vac. Sci. Technol. A Vacuum, Surfaces, Film.* **20**, 2052 (2002).

- [116] O. Joubert, G. S. Oehrlein and M. Surendra, "Fluorocarbon high density plasma. VI. Reactive ion etching lag model for contact hole silicon dioxide etching in an electron cyclotron resonance plasma", *J. Vac. Sci. Technol. A Vacuum, Surfaces, Film.* **12**, 665 (1994).
- [117] G. S. Oehrlein, D. Metzler and C. Li, "Atomic Layer Etching at the Tipping Point: An Overview", *ECS J. Solid State Sci. Technol.* **4**, N5041 (2015).
- [118] K. J. Kanarik, T. Lill, E. a. Hudson, S. Sriraman, S. Tan, J. Marks, V. Vahedi and R. a. Gottscho, "Overview of atomic layer etching in the semiconductor industry", *J. Vac. Sci. Technol. A Vacuum, Surfaces, Film.* **33**, 20802 (2015).
- [119] C. Carver, J. Plombon, P. Romero, S. Suri, T. Tronic and R. Turkot, "Atomic Layer Etching: An Industry Perspective", *ECS J. Solid State Sci. Technol.* **4**, N5005 (2015).
- [120] N. A. Kubota, D. J. Economou and S. J. Plimpton, "Molecular dynamics simulations of low-energy (25–200 eV) argon ion interactions with silicon surfaces: Sputter yields and product formation pathways", *J. Appl. Phys.* **83**, 4055 (1998).
- [121] S. U. Engelmann, R. L. Bruce, M. Nakamura, D. Metzler, S. G. Walton and E. A. Joseph, "Challenges of Tailoring Surface Chemistry and Plasma/Surface Interactions to Advance Atomic Layer Etching", *ECS J. Solid State Sci. Technol.* **4**, N5054 (2015).
- [122] T. Matsuura, J. Murota, Y. Sawada and T. Ohmi, "Self-limited layer-by-layer etching of Si by alternated chlorine adsorption and Ar<sup>+</sup> ion irradiation", *Appl. Phys. Lett.* **63**, 2803 (1993).
- [123] S. Tan, W. Yang, K. J. Kanarik, T. Lill, V. Vahedi, J. Marks and R. A. Gottscho, "Highly Selective Directional Atomic Layer Etching of Silicon", *ECS J. Solid State Sci. Technol.* **4**, N5010 (2015).
- [124] H. Shin, W. Zhu, L. Xu, V. M. Donnelly and D. J. Economou, "Control of ion energy distributions using a pulsed plasma with synchronous bias on a boundary electrode", *Plasma Sources Sci. Technol.* **20**, 55001 (2011).
- [125] M. D. Logue, H. Shin, W. Zhu, L. Xu, V. M. Donnelly, D. J. Economou and M. J. Kushner, "Ion energy distributions in inductively coupled plasmas having a biased boundary electrode", *Plasma Sources Sci. Technol.* **21**, 65009 (2012).
- [126] T. Gu, M. Okandan, O. O. Awadelkarim, J. F. Rembetski, P. Aum and Y. D. Chan, "Impact of Polysilicon Dry Etching on 0.5  $\mu\text{m}$  NMOS Transistor Performance: The Presence of Both Plasma Bombardment Damage and Plasma Charging Damage", *IEEE Electron Device Lett.* **15**, 48 (1994).
- [127] S. D. Athavale and D. J. Economou, "Realization of atomic layer etching of silicon", *J. Vac. Sci. Technol. B Microelectron. Nanom. Struct.* **14**, 3702 (1996).
- [128] A. Ranjan, M. Wang, S. D. Sherpa, V. Rastogi, A. Koshiishi and P. L. G. Ventzek, "Implementation of atomic layer etching of silicon: Scaling parameters, feasibility, and profile control", *J. Vac. Sci. Technol. A Vacuum, Surfaces, Film.* **34**, 31304 (2016).
- [129] A. Agarwal and M. J. Kushner, "Plasma atomic layer etching using conventional plasma equipment", *J. Vac. Sci. Technol. A Vacuum, Surfaces, Film.* **27**, 37 (2009).

- [130] A. Goodyear and M. Cooke, "Atomic layer etching in close-to-conventional plasma etch tools", *J. Vac. Sci. Technol. A Vacuum, Surfaces, Film.* **35**, 01A105 (2017).
- [131] O. Mourey, C. Petit-Etienne, G. Cunge, M. Darnon, E. Despiau-Pujo, P. Brichon, E. Lattu-Romain, M. Pons and O. Joubert, "Roughness generation during Si etching in Cl<sub>2</sub> pulsed plasma", *J. Vac. Sci. Technol. A Vacuum, Surfaces, Film.* **34**, 41306 (2016).
- [132] K. J. Kanarik, S. Tan, W. Yang, T. Kim, T. Lill, A. Kabansky, E. A. Hudson, T. Ohba, K. Nojiri, J. Yu, R. Wise, Y. Pan, J. Marks and R. A. Gottscho, "Predicting Synergy in Atomic Layer Etching (ALE)", *J. Vac. Sci. Technol. A* **35**, 5 (2017).
- [133] V. D. Parkhe, K. Makhratchev, M. Ono and Z. Guo, "Pixilated cooling, temperature controlled substrate support assembly", U.S. Patent Application 20150228513 (2015).
- [134] K. W. Gaff, H. Singh, K. Comendant and V. Vahedi, "Adjusting substrate temperature to improve cd uniformity", U.S. Patent 8642480 B2 (2014).
- [135] D. Metzler, C. Li, S. Engelmann, R. L. Bruce, E. A. Joseph and G. S. Oehrlein, "Fluorocarbon assisted atomic layer etching of SiO<sub>2</sub> and Si using cyclic Ar/C<sub>4</sub>F<sub>8</sub> and Ar/CHF<sub>3</sub> plasma", *J. Vac. Sci. Technol. A Vacuum, Surfaces, Film.* **34**, 01B101 (2016).
- [136] S. D. Sherpa and A. Ranjan, "Quasi-atomic layer etching of silicon nitride", *J. Vac. Sci. Technol. A Vacuum, Surfaces, Film.* **35**, 01A102 (2017).
- [137] D. Metzler, R. L. Bruce, S. Engelmann, E. A. Joseph and G. S. Oehrlein, "Fluorocarbon assisted atomic layer etching of SiO<sub>2</sub> using cyclic Ar/C<sub>4</sub>F<sub>8</sub> plasma", *J. Vac. Sci. Technol. A Vacuum, Surfaces, Film.* **32**, 20603 (2014).
- [138] M. Schaepkens, R. C. M. Bosch, T. E. F. M. Standaert, G. S. Oehrlein and J. M. Cook, "Influence of reactor wall conditions on etch processes in inductively coupled fluorocarbon plasmas", *J. Vac. Sci. Technol. A Vacuum, Surfaces, Film.* **16**, 2099 (1998).
- [139] K. Miyata, M. Hori and T. Goto, "CF<sub>x</sub> radical generation by plasma interaction with fluorocarbon films on the reactor wall", *J. Vac. Sci. Technol. A Vacuum, Surfaces, Film.* **14**, 2083 (1996).
- [140] M. Tuda and K. Ono, "Mechanisms for Microscopic Nonuniformity in Low-Pressure, High-Density Plasma Etching of Poly-Si in Cl<sub>2</sub> and Cl<sub>2</sub> / O<sub>2</sub> Mixtures", *Jpn. J. Appl. Phys.* **36**, 2482 (1997).
- [141] M. Tuda, K. Shintani and H. Ootera, "Profile evolution during polysilicon gate etching with low-pressure high-density Cl<sub>2</sub>/HBr/O<sub>2</sub> plasma chemistries", *J. Vac. Sci. Technol. A Vacuum, Surfaces, Film.* **19**, 711 (2001).
- [142] T. Ohiwa, K. Horioka, T. Arikado, I. Hasegawa and H. Okano, "SiO<sub>2</sub> Tapered Etching Employing Magnetron Discharge of Fluorocarbon Gas", *Jpn. J. Appl. Phys.* **31**, 405 (1992).
- [143] C. M. Huard, Y. Zhang, S. Sriraman, A. Paterson, K. J. Kanarik and M. J. Kushner, "Atomic layer etching of 3D structures in silicon: Self-limiting and nonideal reactions", *J. Vac. Sci. Technol. A Vacuum, Surfaces, Film.* **35**, 31306 (2017).